UNIVERSITÀ DEGLI STUDI DI TRIESTE

XXIX CICLO DEL DOTTORATO DI RICERCA IN

Ingegneria industriale e dell'informazione

Modeling and analysis of special electrical machines for distributed generation

Settore scientifico-disciplinare: ING-IND/32

DOTTORANDO:
MAURO BORTOLOZZI

COORDINATORE:
PROF. DIEGO MICHELI

SUPERVISORE DI TESI:
PROF. ALBERTO TESSAROLO

ANNO ACCADEMICO 2015/2016

Summary

ABSTRACT

Nowadays, the pollution caused by the massive use of fossil fuel is a well-known critical issue makes the design of the electrical machines a crucial task because the vast majority of the industrial or household applications are integrated with this kind of technology; hence improving the efficiency of electric motors is expected to result in an extraordinary benefit in terms of energy saving. On the other side, the increasing use of renewable energies (like wind energy, hydropower, tidal energy), combined with the distributed generation concept, call for new electric machine technology and for new design approaches.

The improvement in motor and generator efficiency is not only a matter of technology but has also various important implications in terms of scientific research.

This doctoral thesis summarizes some of the main results obtained during my Ph.D. period. The research activity has been mainly focused on finding analytical procedures to model and analyze some types of electrical machines which are of interest for renewable and distributed generation. The use of analytical approaches is, in some cases, fundamental because numerical methods, mostly based on Finite Element Analysis (FEA), are very inefficient in terms of required time and computation resources.

The types of electrical machines considered in this work are various. The attention is first placed on the slotless surface permanent magnet (SPM) topology (with different types of rotor magnetization), which is very promising for small-power distributed wind generation plants required to operate with weak-wind conditions. Wound-field synchronous generators are then considered as they represent the traditional and most common choice for power generation. Machines with multiphase stator winding are finally taken into account due their importance in DC distributed generation, e.g. in shipboard power systems employing a DC distribution. For the various kinds of the machines taken into account, some modeling, design and analysis studies have been conducted in the attempt to fill some gaps in the existing technical literature.

After some general introductive notes on electromagnetic field analysis, in the first part of the thesis (chapter 2) the purely analytical modeling of slotless SPM machines is addressed. Slotless permanent-magnet machines are attractive in some modern high-efficiency high-performance drives as well as in distributed power generation where a minimized cogging torque is needed (e.g. for small wind turbines required to operate at low torque and power). In the work, it has been considered how the stator slotless design can be combined with different surface permanent magnet rotor topologies. The main efforts of the study have been addressed to the purpose of finding an explicit analytical expression to compute slotless machine torque and no-load back-EMF, covering all the SPM rotor topologies of interest. The analytical formulas are derived by treating rotor permanent magnets as equivalent current distributions and considering the interaction of such equivalent currents with the radial component of the armature reaction field. A similar approach is also employed to derive explicit analytical expressions for the no-load back-EMF. The obtained results for the torque, in particular, are an original fully-analytical alternative to the traditional way to compute the torque through Maxwell stress tensor integral formula, which includes both the air-gap field component and requires numerical integration. The explicit torque and back-EMF expressions obtained in this way are extensively validated against finite element analysis (FEA). The proposed formulations are a very computationally efficient alternative to FEA especially when it comes to rapidly compare different design solutions, particularly for optimization purposes. To illustrate this, in the last part of the third chapter, two application examples are provided in which the presented method is adopted to optimize the machine cross section under different design constraints.

The subsequent part of the thesis (chapter 3) is about the analytical computation of end-coil leakage inductance in concentric windings. The electrical machine windings, with a concentric structure, are quite common in various applications (stator winding of slotless machines, field windings of round-rotor synchronous generators). For a good dynamic modeling of these machines, it is useful that their mathematical model is implemented and that model parameters are identified with good accuracy. One of the main challenges in parameter estimation is the determination of the inductance component due to the leakage flux around the end windings. As an application example, the end-winding leakage determination for the field circuit of a real wound-rotor synchronous generator is addressed. The proposed technique shows a very good accordance compared with a 3D FEA simulation and is also validated though tests conducted on a dedicated experimental set-up.

Multiphase machines are attractive for many energy-saving fault-tolerant applications thanks to their higher efficiency and intrinsic resilience to faults. They are also interesting for distributed generation in DC power systems, e.g. in shipboard applications. A challenging task in the modeling of multiphase machines for design and simulation is identifying the self and mutual inductances due to leakage fluxes. Chapter 4 presents a new approach for the leakage inductance determination in multiphase machines based on routine tests combined with very simple 2D magnetostatic FEA simulations. The procedure is, in particular, applied to 9-phase salient-pole synchronous generators and is experimentally validated in this case. The proposed approach is valuable as it relies on very simple tests which are usually conducted on the built machine and does not require either 3D simulation or tests with the rotor removed.

Chapter 5 is about the design of wound-field synchronous generators specifically required to operate in a distributed generation system where significant fluctuations are known to frequently occur in both voltage and frequency. Design provisions are investigated to improve the generator resilience to these grid disturbances.

In Chapter 6 the attention is focused on multiphase alternators interfaced to DC distribution systems through multiple rectifiers, which is a design adopted in some DC distribution systems. As a new finding presented as a part of this investigation, it is shown that a short circuit fault occurring on AC/DC rectifier terminals generates a strongly oscillatory behavior with much larger current peaks than could be predicted with conventional models regarding short circuit transients in DC networks.

Most of the work presented in this thesis has been published in IEEE journals (Chapters 3, 4 and 5) or presented at IEEE-sponsored or IEEE-cosponsored conferences (Chapters 6 and 7).

INTRODUZIONE

Oggigiorno, il problema dell'inquinamento causato dal massiccio uso di energia derivante da fonti non rinnovabili è una questione fondamentale nel panorama odierno. Il progetto di macchine elettriche gioca un ruolo fondamentale in quanto, queste, sono utilizzate in tantissime applicazioni che vanno da utilizzatori industriali di grande potenza a piccole macchine per applicazioni domestiche. Un miglioramento dell'efficienza delle macchine elettriche è quindi fondamentale per minimizzare il consumo di combustibili fossili. Da un altro punto di vista, fonti energetiche rinnovabili (energia eolica, energia solare, energia idroelettrica) combinate al concetto di generazione distribuita sono altrettanto importanti in quanto non prevedono lo sfruttamento di combustibili inquinanti. Anche in questo tipo di produzione energetica, un progetto più consapevole delle macchine elettriche risulta essere necessario per ottimizzare il processo produttivo.

In questo lavoro di tesi, si è cercato di trovare degli approcci analitici che andassero a modellizzare e descrivere il comportamento di alcune macchine elettriche di particolare interesse per la generazione distribuita. L'uso di formulazioni analitiche è in molti casi il metodo più conveniente per affrontare la modellizzazione dei fenomeni fisici caratteristi delle macchine elettriche. Questo perché altri approcci, quali possono essere le simulazioni agli elementi finiti (FEA) o metodi numerici in genere, richiedono molte risorse computazionali.

I tipi di macchine elettriche affrontate in questo lavoro sono molteplici. Innanzitutto l'attenzione è stata focalizzata sulle macchine sincrone a magneti permanenti superficiali (SPM) con statori di tipo di tipo slotless. Le macchine di questo tipo sono utilizzate e offrono ottime prestazioni ad esempio in sistemi di generazione distribuita basati su piccole turbine eoliche, che devono operare anche in condizioni di bassa ventosità. Gli altri tipi di macchine considerati in questo lavoro sono i generatori sincroni a rotore avvolto. Data la loro importanza nella generazione di energia elettrica si è deciso di analizzare sia strutture trifase che strutture multifase. Questa diversa architettura di statore è molto importante in applicazioni come la generazione distribuita in corrente continua (ad esempio in sistemi di distribuzione implementati a bordo di navi di medie e grandi dimensioni). Per tutti i vari tipi di macchine affrontate sono stati effettuati degli studi sulla modellizzazione e sul design di tali architetture con l'obbiettivo di riempire eventuali mancanze trovate nella letteratura tecnica specializzata.

Dopo una parte introduttiva sulle leggi fondamentali del campo elettromagnetico e sull'analisi vettoriale, nella prima parte della tesi si è ricavato un modello analitico completo per le macchine SPM di tipo slotless. Questo tipo di macchine risulta essere fondamentale in tutte quelle applicazioni dove si richiedono altissimi valori di efficienza ad alte velocità e ridottissimi fenomeni parassiti come cogging torque o oscillazioni di coppia in genere (piccole turbine eoliche o macchine ad altissima velocità). In questa parte del lavoro di tesi si è inoltre considerato il fatto che le macchine SPM possono essere equipaggiate in generale con vari tipi di rotori. La parte principale di questo studio si è concentrata nel trovare una formulazione analitica per la coppia istantanea della macchina, e per la tensione generata ai morsetti da questa, in condizioni di assenza di carico. Una formulazione analitica per la coppia è stata possibile grazie al fatto che i magneti permanenti sono stati modellizzati come delle distribuzioni lineari di correnti. Grazie a questo fatto poi è stato possibile derivare l'andamento della coppia nel tempo valutando l'interazione tra queste distribuzioni di corrente e la componente radiale del campo magnetico genato dalle correnti di statore. Un approccio analogo è stato utilizzato per valutare anche la tensione a vuoto di macchina.

Un approccio di questo tipo per il calcolo della coppia è da considerarsi innovativo, in quanto alternativo alle classiche tecniche utilizzate in letteratura che coinvolgono metodi come il tensore degli sforzi di Maxwell o metodi basati sulla valutazione dell'energia magnetica. Tutte le formule trovate sono state ampiamente validate con apposite applicazioni costruite utilizzando gli elementi finiti. Gli approcci proposti hanno dimostrato una perfetta corrispondenza e un'ottima efficienza computazionale. Il calcolo per la valutazione delle prestazioni di macchina è praticamente istantaneo, quindi ottimo per essere inserito in processi di ottimizzazione. Per mostrare questa caratteristica, nell'ultima parte dello stesso capitolo, sono riportate due possibili ottimizzazioni che sfruttano le metodologie proposte con diverse ipotesi di partenza.

Nella parte successiva della tesi (capitolo 3), è stato affrontato il calcolo dell'induttanza di dispersione in testata di avvolgimenti concentrici. Questo tipo di avvolgimento è in uso in vari tipi di macchine elettriche come: lo statore delle macchine slotless e l'avvolgimento di campo delle macchine sincrone a rotore isotropo. Per una buona modellizzazione dinamica di un qualsiasi sistema è necessario definire un modello matematico e determinare in modo molto accurato i parametri di tale modello. Una delle maggiori sfide nella stima dei parametri delle macchine elettriche è proprio la determinazione della componente della reattanza di dispersione dovuta alle testate degli avvolgimenti. A questo proposito in questa tesi si è proposto un metodo innovativo per la valutazione di tale componente con un approccio completamente analitico che sfrutta la teoria degli integrali di Neumann. La metodologia proposta ha mostrato un'ottima corrispondenza sia con simulazioni agli elementi finiti tridimensionali, che con apposite misure effettuate su setup sperimentali dedicati. Anche in questo caso l'approccio analitico ha mostrato chiari vantaggi in termini di tempi computazionali e risorse necessarie.

Le macchine elettriche con l'avvolgimento di statore multifase (maggiore di tre), sono di particolare interesse in tutti quei settori dove gli alti valori di efficienza e la resistenza ai guasti sono dei requisiti fondamentali. Un altro settore dove questo tipo di architettura emerge in modo importante è la generazione distribuita in corrente continua. Sempre nell'ottica di costruire un modello matematico accurato, un parametro difficile da determinare in questo tipo di macchine, è la reattanza di dispersione di fase. Nel capitolo 4, si propone un nuovo approccio per la determinazione della reattanza di dispersione di fase basato su alcuni test sperimentali di routine per le macchine elettriche, e su alcune semplici simulazioni agli elementi finiti bidimensionali. Tutta la procedura è stata applicata a un generatore a poli salienti a tripla terna e confrontata sperimentalmente con le normali procedure trovate in letteratura.

Il capitolo 5 descrive i risultati di un progetto di un generatore sincrono a rotore avvolto per applicazioni dove è richiesta una particolare resistenza alle fluttuazioni di rete. Tale resistenza è tipicamente richiesta quando il generatore si trova ad operare in reti di generazione distribuita dove le fluttuazioni possono coinvolgere sia la tensione che la frequenza della rete. Per assicurare che il generatore rispetti determinati standard, si è deciso di operare determinate scelte di progetto descritte in questa parte di elaborato. In design finale così ottenuto è stato quindi confrontato con una macchina equivalente in termini di requisiti standard di progetto ma senza nessun accorgimento riguardo il comportamento dinamico ai disturbi.

L'ultimo capitolo di questa tesi è incentrato sull'analisi di generatori multifase interfacciati con reti in corrente continua mediante ponti raddrizzatori. Il presente lavoro ha sottolineato il fatto che, in caso di guasto, nella rete in corrente continua (ad esempio un corto circuito) si possono instaurare pericolose oscillazioni di corrente ben maggiori di quelle stimabili con i modelli standard. A tal proposito sono state effettuate delle simulazioni utilizzando l'ambiente di sviluppo Matlab-Simulink combinato ad appositi modelli costruiti ad hoc per investigare come e in che entità queste oscillazioni si presentano nella rete.

La maggior parte dei lavori presentati in questa tesi sono stati pubblicati su riviste specialistiche dell' IEEE(capitoli 2,3 e 4) o presentati a conferenze sempre sponsorizzate o co-sponsorizzate dell'IEEE (capitoli 5 e 6)

1 NOTES ON ELECTROMAGNETIC FIELDS

The aim of this chapter is to recall some basic concepts of multivariable advanced calculus and electromagnetic fields [1]. This introductive part is not a complete dissertation about these arguments but only a short summary to help the reader to understand the following chapters.

1.1 BRIEF INTRODUCTION TO MULTIVARIABLE CALCULUS

In a three-dimensional space (R^3) let *V*=*V*(*P*) be a scalar function that defines a scalar field, and *A*=*A*(*P*) a vector function that defines a vector field. The point *P* dependency can be expressed by using three different coordinate systems: Cartesian (*x*, *y*, *z*), Cylindrical (r, θ, z) and spherical (r, θ, ϕ).

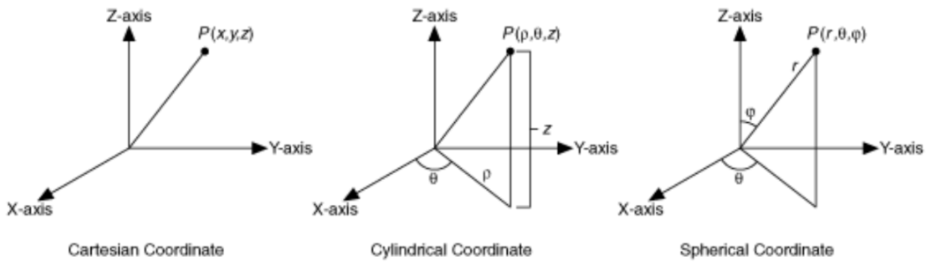

Figure 1: Reference coordinate systems in a three dimensional space

In general, all of the quantities composing the scalar or vector field can be a function of time, therefore the correct definition of the fields would be: $A = A(P,t)$ and $V = V(P,t)$ however, for the sake of clarity the explicit notation that identifies the dependency of various quantities on the position and time is omitted in the following sections.

1.1.1 OPERATIONS BETWEEN VECTORS

Assuming **C** and **D** two vectors in a three-dimensional space, with $|\mathbf{C}|$ and $|\mathbf{D}|$ their magnitude, and γ the angle between their oriented directions.

- The scalar product is defined as:

$$\mathbf{C} \cdot \mathbf{D} = |\mathbf{C}||\mathbf{D}|\cos(\gamma) \tag{1.1}$$

- The vector product as:

$$\mathbf{C} \times \mathbf{D} = (|\mathbf{C}||\mathbf{D}|\sin(\gamma))\,\boldsymbol{n}_{CD} \tag{1.2}$$

  where $\boldsymbol{n}_{CD}$ is the unity vector normal to the plane identified by **C** and **D**. The resultant vector from (1.2) is normal to both starting vectors, and its direction corresponds do the direction of advancement of a right screw rotating from **C** to **B** as shown in Figure 2a.

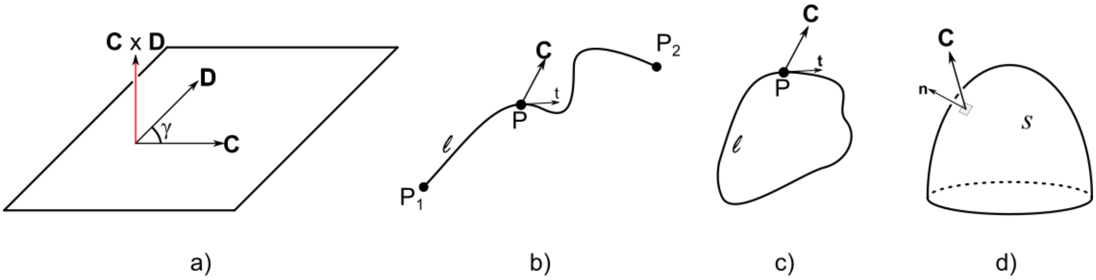

Figure 2: Basic operations with vectors

Using Cartesian coordinates, the two vectors involved in these two operations can be defined as:

$$\mathbf{C} = (C_x, C_y, C_z) = (C_x\boldsymbol{u_x} + C_y\boldsymbol{u_y} + C_z\boldsymbol{u_z})$$

$$\mathbf{D} = (D_x, D_y, D_z) = (D_x\boldsymbol{u_x} + D_y\boldsymbol{u_y} + \mathrm{D}_z\boldsymbol{u_z})$$

where $\boldsymbol{u_x}$, $\boldsymbol{u_y}$, $\boldsymbol{u_z}$ are the coordinate unity vectors. The scalar and vector products become respectively:

$$\mathbf{C}\cdot\mathbf{D} = C_xD_x + C_yD_y + C_zD_z \qquad 1.3$$

$$\mathbf{C}\times\mathbf{D} = \begin{vmatrix} \boldsymbol{u_x} & \boldsymbol{u_y} & \boldsymbol{u_z} \\ C_x & C_y & C_z \\ D_x & D_y & D_z \end{vmatrix} = \qquad 1.4$$

$$= (C_yD_z - C_zD_y)\boldsymbol{u_x} + (C_zD_x - C_xD_z)\boldsymbol{u_y} + (C_xD_y - C_yD_x)\boldsymbol{u_z}$$

Scalar and vector products properties:

$$\begin{aligned} \mathbf{C}\cdot\mathbf{C} &= |\mathbf{C}|^2 & \mathbf{C}\cdot(\mathbf{D}+\mathbf{E}) &= \mathbf{C}\cdot\mathbf{D} + \mathbf{C}\cdot\mathbf{E} \\ \mathbf{C}\cdot\mathbf{D} &= \mathbf{D}\cdot\mathbf{C} & \mathbf{C}\times(\mathbf{D}+\mathbf{E}) &= \mathbf{C}\times\mathbf{D} + \mathbf{C}\times\mathbf{E} \\ \mathbf{C}\times\mathbf{D} &= -\mathbf{D}\times\mathbf{C} & \mathbf{C}\times(\mathbf{D}\times\mathbf{E}) &= (\mathbf{C}\cdot\mathbf{E})\,\mathbf{B} - (\mathbf{C}\cdot\mathbf{D})\,\mathbf{C} \end{aligned} \qquad 1.5$$

1.1.2 DEFINITION OF LINEAR INTEGRAL AND FLUX OF A VECTOR FIELD

The *linear integral* of a vector field **A** along an open curve $\boldsymbol{\ell}$, starting from point P_1 to point P_2 and oriented in every point in the same way as the vector **t** tangent to the curve in every point (Figure 2b) can be expressed as follows:

$$\Gamma_{12} = \int_{P_1}^{P_2} \boldsymbol{A}\cdot\boldsymbol{t}\ dl \qquad 1.6$$

The *closed loop integral* of a vector field **A** along a closed loop $\boldsymbol{\ell}$ oriented tangentially in every point (Figure 2c) can be expressed as follows:

$$\Gamma = \oint \boldsymbol{A}\cdot\boldsymbol{t}\, dl \qquad 1.7$$

The flux of a vector field **A** across a general surface *S* and oriented as the normal unity vector **n**, can be expressed as follows (Figure 2d):

$$\Phi = \int_S \boldsymbol{A} \cdot \boldsymbol{n}\, ds \qquad 1.8$$

1.1.3 Differential operators

Considering a scalar field *V*, the *gradient* is a vector function defined in each point *P* by a direction corresponding to the maximum directional derivative of *V* (defined by the unity vector $\mathbf{u}_{\mathbf{max}}$), and by a magnitude equal to this derivative, therefore the *gradient* can be expressed as:

$$grad(V) = \nabla V = \max\left(\frac{\partial V}{\partial l}\right) \boldsymbol{u_{max}} \qquad 1.9$$

Along any direction defined by the unity vector **u**, the scalar product of ∇V by **u** gives the derivative of *V* along the direction of **u**, which is:

$$\nabla V \cdot \boldsymbol{u} = \left.\frac{\partial V}{\partial l}\right|_{\mathbf{u}} \qquad 1.10$$

The *divergence* of a vector field **A** is a scalar function defined in each point *P* by the ratio between the flux of **A** going through a closed surface S_c and the volume τ contained by S_c when this volume tends to zero, which is:

$$\operatorname{div}(\mathbf{A}) = \nabla \cdot \mathbf{A} = \lim_{\tau \to 0} \frac{\oint_{S_c} \boldsymbol{A} \cdot \boldsymbol{n}\, ds}{\tau} \qquad 1.11$$

The infinitesimal flux $d\Phi$ of a vector **A** going out a closed surface, that contains the infinitesimal volume $d\tau$, is given by $d\Phi = \nabla \cdot \boldsymbol{A}\, d\tau$. Then the divergence of **A** is greater than zero in a point where the lines of the field **A** generate, while the divergence of **A** is less than zero in a point where the lines of the field terminate (Figure 3).

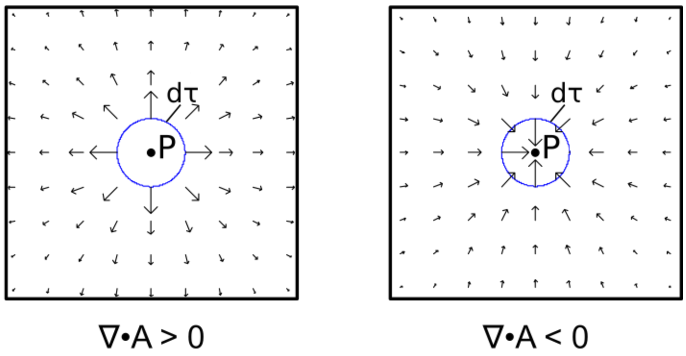

Figure 3: Vector field in the region of a specific point P with two different divergence cases

Considering again a vector field **A**, the *curl* is a vector function defined in each point *P* by the ratio between the integral of **A** along a closed loop l and the surface *S* bordered by l when this surface tends to zero, which is:

$$\operatorname{curl}(\mathbf{A}) = \nabla \times \mathbf{A} = \lim_{S \to 0} \frac{\oint_l \boldsymbol{A} \cdot \boldsymbol{t}\, dl}{S} \qquad 1.12$$

The infinitesimal loop integral $d\Gamma$ of the vector **A** along a closed loop l that borders the infinitesimal surface dS, oriented by **n** is given by $\nabla\times A\,\boldsymbol{n}\,dS$, then the curl of the vector represents the vortices around which the lines of the vector field go around.

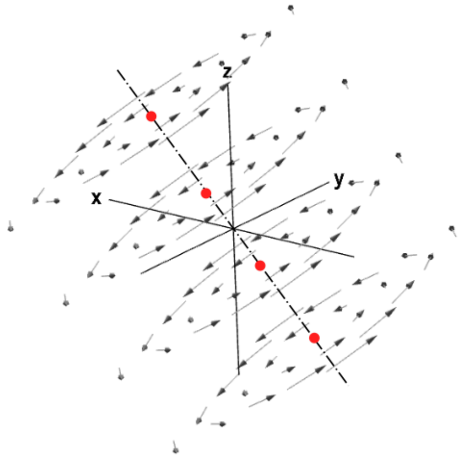

Figure 4: Example of 3D rotational Field

In Figure 4 a rotating vector field is represented. If the vector field is interpreted as velocity of fluid flow, the fluid appears to flow in circles. From the graphical perspective, the fluid appears to circulate along its axis of rotation (dash-dotted line). Looking at this graph there are some red points along the axis of rotation. These dots are representations of vectors of zero length, as the velocity is zero there.

The *laplacian* of a scalar field *V* is given by the divergence of the vector gradient of the scalar function *V*, as:

$$\nabla^2 V = \nabla \cdot (\nabla V) \qquad 1.13$$

The *laplacian* of a vector field **A** is given by:

$$\nabla^2 \mathbf{A} = \nabla(\nabla \cdot \mathbf{A}) - \nabla\times(\nabla\times\mathbf{A}) \qquad 1.14$$

Referring to the differential operators defined above there are different integral and derivative properties, however, for the sake of brevity, in this summary these properties are omitted.

1.1.4 Expression of differential operators using different coordinate systems.

Cartesian coordinates

Using Cartesian coordinates, the point P, in a three dimensional space, is given by P(*x, y, z*) and the reference versors are $(\boldsymbol{u_x},\ \boldsymbol{u_y},\ \boldsymbol{u_z})$.

$$\nabla V = \frac{\partial V}{\partial x}\boldsymbol{u}_x + \frac{\partial V}{\partial y}\boldsymbol{u}_y + \frac{\partial V}{\partial z}\boldsymbol{u}_z \qquad 1.15$$

$$\nabla \cdot \mathbf{A} = \frac{\partial A_x}{\partial x} + \frac{\partial A_y}{\partial y} + \frac{\partial A_z}{\partial z} \qquad 1.16$$

$$\nabla\times\mathbf{A}=\begin{vmatrix}\boldsymbol{u}_x & \boldsymbol{u}_y & \boldsymbol{u}_z\\ \dfrac{\partial}{\partial \mathrm{x}} & \dfrac{\partial}{\partial \mathrm{y}} & \dfrac{\partial}{\partial \mathrm{z}}\\ A_x & A_y & A_z\end{vmatrix}=\left(\frac{\partial A_z}{\partial y}-\frac{\partial A_y}{\partial z}\right)\boldsymbol{u_x}+\left(\frac{\partial A_x}{\partial z}-\frac{\partial A_z}{\partial x}\right)\boldsymbol{u_y}+\left(\frac{\partial A_y}{\partial x}-\frac{\partial A_x}{\partial y}\right)\boldsymbol{u_z} \qquad 1.17$$

$$\nabla^2 V=\nabla\cdot(\nabla V)=\frac{\partial^2 V}{\partial x^2}+\frac{\partial^2 V}{\partial y^2}+\frac{\partial^2 V}{\partial z^2} \qquad 1.18$$

$$\begin{aligned}\nabla^2\mathbf{A}=\nabla(\nabla\cdot\mathbf{A})-\nabla\times(\nabla\times\mathbf{A})&=\nabla^2 A_x\boldsymbol{u_x}+\nabla^2 A_y\boldsymbol{u_y}+\nabla^2 A_z\boldsymbol{u_z}\\ &=\left(\frac{\partial^2 A_x}{\partial x^2}+\frac{\partial^2 A_x}{\partial y^2}+\frac{\partial^2 A_x}{\partial z^2}\right)\boldsymbol{u_x}\\ &+\left(\frac{\partial^2 A_y}{\partial x^2}+\frac{\partial^2 A_y}{\partial y^2}+\frac{\partial^2 A_y}{\partial z^2}\right)\boldsymbol{u_y}\left(\frac{\partial^2 A_z}{\partial x^2}+\frac{\partial^2 A_z}{\partial y^2}+\frac{\partial^2 A_z}{\partial z^2}\right)\boldsymbol{u_z}\end{aligned} \qquad 1.19$$

Cylindrical coordinates

Using Cylindrical coordinates, the point *P*, in a three-dimensional space, is given by *P* $(r,\ \theta,\ z)$ and the reference versors are $(\boldsymbol{u_r},\ \boldsymbol{u_\theta},\ \boldsymbol{u_z})$.

$$\nabla V=\frac{\partial V}{\partial r}\boldsymbol{u}_r+\frac{1}{r}\frac{\partial V}{\partial\theta}\boldsymbol{u}_\theta+\frac{\partial V}{\partial z}\boldsymbol{u}_z \qquad 1.20$$

$$\nabla\cdot\boldsymbol{A}=\frac{1}{r}\frac{\partial(rA_r)}{\partial r}+\frac{1}{r}\frac{\partial A_\theta}{\partial\theta}+\frac{\partial A_z}{\partial z} \qquad 1.21$$

$$\nabla\times\mathbf{A}=\left(\frac{1}{r}\frac{\partial A_z}{\partial\theta}-\frac{\partial A_\theta}{\partial z}\right)\boldsymbol{u_r}+\left(\frac{\partial A_r}{\partial z}-\frac{\partial A_z}{\partial r}\right)\boldsymbol{u_\theta}+\frac{1}{r}\left(\frac{\partial(rA_\theta)}{\partial r}-\frac{\partial A_r}{\partial\theta}\right)\boldsymbol{u_z} \qquad 1.22$$

$$\nabla^2 V=\nabla\cdot(\nabla V)=\frac{1}{r}\frac{\partial}{\partial \mathrm{r}}\left(r\frac{\partial V}{\partial r}\right)+\frac{1}{r^2}\frac{\partial^2 V}{\partial\theta^2}+\frac{\partial^2 V}{\partial z^2}=\frac{1}{r}\frac{\partial V}{\partial r}+\frac{\partial^2 V}{\partial r^2}+\frac{1}{r^2}\frac{\partial^2 V}{\partial\theta^2}+\frac{\partial^2 V}{\partial z^2} \qquad 1.23$$

$$\begin{aligned}\nabla^2\mathbf{A}&=\nabla(\nabla\cdot\mathbf{A})-\nabla\times(\nabla\times\mathbf{A})\\ &=\left(\frac{\partial^2 A_r}{\partial r^2}+\frac{1}{r^2}\frac{\partial^2 A_r}{\partial\theta^2}+\frac{\partial^2 A_r}{\partial z^2}+\frac{1}{r}\frac{\partial A_r}{\partial r}-\frac{2}{r^2}\frac{\partial A_\theta}{\partial\theta}-\frac{A_r}{r^2}\right)\boldsymbol{u_r}\\ &+\left(\frac{\partial^2 A_\theta}{\partial r^2}+\frac{1}{r^2}\frac{\partial^2 A_\theta}{\partial\theta^2}+\frac{\partial^2 A_\theta}{\partial z^2}+\frac{1}{r}\frac{\partial A_\theta}{\partial r}-\frac{2}{r^2}\frac{\partial A_r}{\partial\theta}-\frac{A_\theta}{r^2}\right)\boldsymbol{u_\theta}\\ &+\left(\frac{\partial^2 A_z}{\partial r^2}+\frac{1}{r^2}\frac{\partial^2 A_z}{\partial\theta^2}+\frac{1}{r}\frac{\partial A_z}{\partial r}+\frac{\partial^2 A_z}{\partial z^2}\right)\boldsymbol{u_z}\end{aligned} \qquad 1.24$$

Spherical coordinates

Using Spherical coordinates, the point P, in a three dimensional space, is given by *P*$(r,\ \theta,\ \varphi)$ and the reference versors are $(\mathbf{u}_{\boldsymbol{r}},\ \mathbf{u}_{\boldsymbol{\theta}},\ \mathbf{u}_{\boldsymbol{\varphi}})$.

$$\nabla V=\frac{\partial V}{\partial r}\boldsymbol{u}_r+\frac{1}{r}\frac{\partial V}{\partial\theta}\boldsymbol{u}_\theta+\frac{1}{r\sin(\theta)}\frac{\partial V}{\partial\varphi}\boldsymbol{u}_\varphi \qquad 1.25$$

$$\nabla \cdot \boldsymbol{A} = \frac{1}{r^2}\frac{\partial(r^2 A_r)}{\partial r} + \frac{1}{r\sin(\theta)}\frac{\partial(sin(\theta)\ A_\theta)}{\partial\theta} + \frac{1}{r\sin(\theta)}\frac{\partial A_\varphi}{\partial\varphi} \quad 1.26$$

$$\nabla\times\boldsymbol{A} = \frac{1}{r\sin(\theta)}\left(\frac{\partial(\sin(\theta)\,A_\varphi)}{\partial\theta} - \frac{\partial A_\theta}{\partial\varphi}\right)\boldsymbol{u_r} + \frac{1}{r\sin(\theta)}\left(\frac{\partial A_r}{\partial\varphi} - \frac{\partial(\sin(\theta)\,\mathrm{r}A_\varphi)}{\partial \mathrm{r}}\right)\boldsymbol{u_\theta} + \frac{1}{r}\left(\frac{\partial(rA_\theta)}{\partial r} - \frac{\partial A_r}{\partial\theta}\right)\boldsymbol{u_\varphi} \quad 1.27$$

$$\nabla^2 V = \nabla\cdot(\nabla V) = \frac{1}{r^2}\frac{\partial}{\partial \mathrm{r}}\left(r^2\frac{\partial V}{\partial r}\right) + \frac{1}{r^2\sin(\theta)}\frac{\partial}{\partial\theta}(\sin(\theta)\frac{\partial V}{\partial\theta}) + \frac{1}{r\sin(\theta)^2}\frac{\partial^2 \mathrm{V}}{\partial\varphi^2} \quad 1.28$$

The *laplacian* of a vector field **A** using spherical coordinates is not reported here but it can be found in [2].

1.1.5 Conservative, Irrotational, Solenoidal and Harmonic Fields

A vector field **B** is conservative if it exhibits a null loop integral along each closed line in the domain of definition. Consequently, the linear integral of **B** along a generic open line results dependent only on the end points of the line and not on its path. It is possible to combine a *scalar potential* ϕ with a conservative field **B**. The potential of a conservative field is defined so that:

$$\mathbf{B} = -\nabla\phi + C \quad 1.29$$

where C is an arbitrary constant. The surfaces where ϕ assumes an equal value are equipotential areas and they are always normal to the field flux lines.

A vector field **B** is *irrotational* if its curl is null in all the domain of definition. A conservative field is irrotational. Conversely an irrotational field is conservative only if it is defined in a simply connected domain (a domain is simply connected when each closed line along which the integral is computed may be reduced to a point remaining always within the domain).

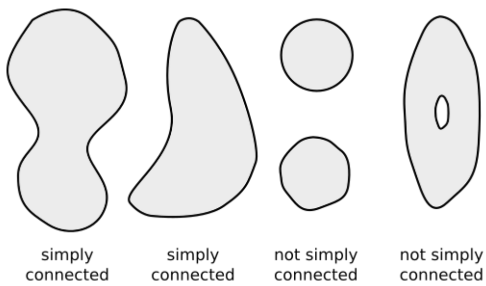

Figure 5: Examples of simply connected and not simply connected domains in a 2D space

A vector field **B** is *solenoidal* if its divergence is null in the whole domain of definition. Therefore, the flux of **B** along any closed surface is null. It is possible to express a solenoidal field **B** by means of a curl of a vector potential **A**. This vector potential **A** is defined so that:

$$\mathbf{B} = \nabla(A + C) \quad 1.30$$

where C is an arbitrary irrotational vector field. It follows that the loop integral of the vector potential along a closed line l is equal to the flux of the solenoidal field through any surfaces bordered by l.

A scalar field ϕ is *harmonic* if it satisfies the Laplace equation:

$$\nabla^2\phi = \nabla \cdot (\nabla\phi) = 0 \tag{1.31}$$

Then a vector field **B** that is obtained as gradient of harmonic scalar field ϕ, i.e., $\boldsymbol{B} = \nabla\phi$, is irrotational, since $\nabla\times(\nabla\phi) = 0$, and solenoidal.

A vector field **A** is harmonic if it is irrotational and solenoidal. Hence, it results:

$$\nabla^2\mathbf{A} = 0 \tag{1.32}$$

Then, the vector field **B** obtained as a curl of a harmonic vector field **A**, i.e., $\boldsymbol{B} = \nabla\times\boldsymbol{A}$ is solenoidal because $\nabla \cdot (\nabla\times\boldsymbol{A}) = 0$, irrotational.

1.1.6 FIELDS TIME DEPENDENCY

Up to now, the scalar fields and vector fields have been considered as a function exclusively of the points of the space. However, they may be also a function of time. Of course, the space variables and the time variable t are considered separately. Then, it is possible to write the following expressions:

$$\nabla\frac{\partial V}{\partial t} = \frac{\partial}{\partial t}\nabla V \qquad \nabla\cdot\frac{\partial \mathbf{A}}{\partial t} = \frac{\partial}{\partial t}\nabla\cdot\mathbf{A}$$
$$\nabla\times\frac{\partial \mathbf{A}}{\partial t} = \frac{\partial}{\partial t}\nabla\times\mathbf{A} \qquad \nabla^2\frac{\partial \mathbf{A}}{\partial t} = \frac{\partial}{\partial t}\nabla^2\mathbf{A} \tag{1.33}$$

1.2 OUTLINE ON ELECTROMAGNETIC FIELDS

The aim of this section is to give a brief outline of the electromagnetic fields basic concepts. Some of these concepts will be used in the following parts of the thesis.

1.2.1 ELECTRIC CHARGE AND ELECTRIC CHARGE DENSITY

The electric charges in one region of a selected domain may be distinguished as free and polarization charges. The phenomena of attraction and repulsion between the various bodies, on which the electric charge are placed, are generated by the total charge, the sum of the free charges and of those of polarization. Only the free charges are dealt with hereafter, while the charges of polarization are considered by defining conveniently the characteristics of the media. In any point of the space, where the infinitesimal volume $\Delta\tau$ contains the (free) charge Δq, it is possible to define a volume density of (free) charge ρ as:

$$\rho = \lim_{\Delta\tau \to 0} \frac{\Delta q}{\Delta\tau} \qquad 1.34$$

This quantity is measured in $(\mathrm{C/m^3})$ and in general can be variable with time. If the element where the charge is distributed, is characterized by one dimension being much smaller than the others (e.g. a parallelepiped where the height is much larger than width and depth), it is possible to define a surface density of charge ρ_s measured in $(\mathrm{C/m^2})$:

$$\rho_s = \lim_{\Delta s \to 0} \frac{\Delta q}{\Delta s} \qquad 1.35$$

1.2.2 ELECTRIC DISPLACEMENT FIELD

The spatial description of the effects due to the free electric charges that are in restricted regions is represented by the vector field **D** (electric displacement field). The unit of its magnitude is (C/m^2). The fundamental property of the field **D**, in differential form and in integral form respectively, is:

$$\nabla \cdot \mathbf{D} = \rho \qquad 1.36$$

$$\oint_{S_c} \mathbf{D} \cdot \mathbf{n}\, ds = q \qquad 1.37$$

Equation 1.37 represents the well-known Gauss law. This relationship indicates that the flux of the vector **D** going out through the closed surface S_c, oriented by the unity vector **n** normal to the surface (external direction), is equal to the free charge q that is contained by the surface S_c itself.

1.2.3 CURRENT DENSITY FIELD

The movement of the electric charges is described by means of the electric current density. Referring to a volume charge density ρ moving with velocity $\mathbf{v}_p$, the electric current density vector **J** can be defined as:

$$\mathbf{J} = \rho\, \boldsymbol{v}_p \qquad 1.38$$

whose reference positive direction is that of the positive charges. Its magnitude is measured in $(\mathrm{A/m^2})$. The vector $\boldsymbol{J}$ defines a vector field, called the current density field. Let S be an open surface, with normal unity vector n, then the current intensity *i* measured in (A) is given by:

$$i = \int_S \mathbf{J} \cdot \mathbf{n}\, ds \qquad 1.39$$

Considering the current density field, it is possible to define the continuity equation in a differential form as:

$$\nabla \cdot \mathbf{J} = -\frac{\Delta\rho}{\Delta t} \qquad 1.40$$

In integral form, the current intensity leaving a closed surface S_c oriented with a normal vector $\mathbf{n}$ in the time interval Δt corresponds to the variation of the electric charge Δq in the volume enclosed by S_c, which is:

$$i_{out} = \oint_{S_c} \mathbf{J} \cdot \mathbf{n} \, ds = -\frac{\Delta q}{\Delta t} \tag{1.41}$$

It is also possible to define the total current density vector:

$$\mathbf{J}_{tot} = \mathbf{J} + \frac{\partial \mathbf{D}}{\partial t} \tag{1.42}$$

which is the sum of the current density vector $\mathbf{J}$ and the displacement current density vector. Considering equation 1.36 about **D** and the continuity equation 1.40, the current field $\mathbf{J}_{tot}$ is solenoidal.

1.2.4 MAGNETIC FLUX DENSITY FIELD

The movement of the electric charges causes effects in the points of the surrounding space, so that it is possible to define the magnetic flux density field **B**. Its magnitude is measured in (T). One can also observe that if there is a test charge moving within the magnetic flux density field **B** at a velocity $\mathbf{v}_q$ that charge is subjected to a Force given by:

$$\delta \mathbf{F} = \delta q \, \mathbf{v}_q \times \mathbf{B} \tag{1.43}$$

This force is called Lorentz's force and will be described in a following section. The fundamental property of the field B is that it is a solenoidal field, that is, the flux of **B** through any closed surface S_c is null. Thus, we have:

$$\nabla \cdot \mathbf{B} = 0 \tag{1.44}$$

$$\oint_{Sc} \mathbf{B} \cdot \mathbf{n} \, ds = 0 \tag{1.45}$$

1.2.5 VECTOR MAGNETIC POTENTIAL FIELD

Since the magnetic flux density field **B** is solenoidal in the whole space, it is suitable to define a vector magnetic potential field **A**, such as:

$$\mathbf{B} = \nabla \times \mathbf{A} \tag{1.46}$$

This relationship defines the field $\mathbf{A}$ apart from a generic irrotational field. The divergence of $\mathbf{A}$ can be defined in an arbitrary way; the positions that are commonly adopted are as follows:

- *Coulomb's position:* mainly used in stationary or quasi-stationary magnetic fields and also used in the rest of the thesis:

$$\nabla \cdot \mathbf{A} = 0 \tag{1.47}$$

- *Lorentz position:* that is well used in rapidly variable magnetic fields:

$$\nabla \cdot \mathbf{A} = -\mu\varepsilon \frac{\partial V}{\partial t} \qquad 1.48$$

1.2.6 Magnetic field Intensity

Together with the flux density vector **B**, the magnetic field strength vector field **H** is introduced. The measure unit of its magnitude is (A/m). The two vector fields are linked by the constitutive law:

$$\mathbf{B} = \mu\, \mathbf{H} \qquad 1.49$$

where, μ is the magnetic permeability of the material. Within a uniform medium, the two fields **B** and **H** are proportional (i.e., they have same direction and proportional amplitude), while in an anisotropic medium their link exhibits a "tensor" nature.

The fundamental property of the field **H** is the definition of its curl (General *Ampere's law*)

$$\nabla \times \mathbf{H} = \mathbf{J} + \frac{\partial \mathbf{D}}{\partial t} \qquad 1.50$$

In stationary or quasi stationary magnetic condition, i.e., when the displacement current density may be neglected, the previous equation can be reduced to (*Ampere's law*):

$$\nabla \times \mathbf{H} = \mathbf{J} \qquad 1.51$$

In an integral form, the Ampere's law is expressed by equating the line integral of **H** along an oriented closed line l to the current intensity i flowing through the surface enclosed by the line l itself, which is:

$$\oint_l \mathbf{H} \cdot \mathbf{t}\, dl = i \qquad 1.52$$

In Figure 6 two classic examples are reported of the Ampere circuit law application. The first example is the infinite wire model where the ampere circuital law condition can be expressed as shown in (1.52); the solenoid case needs some attention, because here there are multiple currents passing through a surface contoured by *l*, so (1.52) has to be modified as follows:

$$\oint_l \mathbf{H} \cdot \mathbf{t}\, dl = \sum_{i=0..n} i_n \quad if \quad (i_1 = i_2 = \cdots i_n = i) \;\rightarrow\; \oint_l \mathbf{H} \cdot \mathbf{t}\, dl = N\, i \qquad 1.53$$

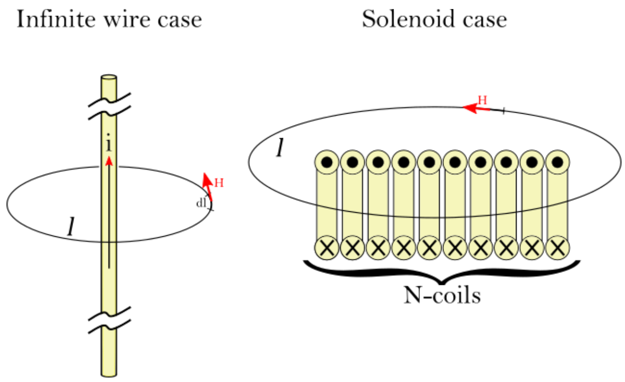

Figure 6: Infinite wire ad solenoid case regarding the Ampere circuital law application

The integral of **H** along an oriented open line σ define the magneto-motive force between the line end points.

$$\int_P^Q \mathbf{H}\cdot\mathbf{t}\,dl = \Psi_{PQ} \qquad 1.54$$

If the magnetic field is irrotational in a simply connected region, it is possible to define a scalar magnetic potential Ψ *as* follows:

$$\mathbf{H} = -\nabla\Psi \qquad 1.55$$

1.2.7 Lorentz force in a current-carrying wire

The Lorentz force is the force applied on a particle with a charge *q* moving with velocity *v* through an electric (**E**) and magnetic (**B**) field. The general formulation of this force can be expressed as follows:

$$\mathbf{F} = q\mathbf{E} + qv\times\mathbf{B} \qquad 1.56$$

The first term is contributed by the electric field. The second term is the magnetic force and has a direction perpendicular to both the velocity and the magnetic field. If a rigid current-carrying wire with a current I is placed only in an external magnetic field **B** (Figure 7)**,** the wire is subjected to an external force F.

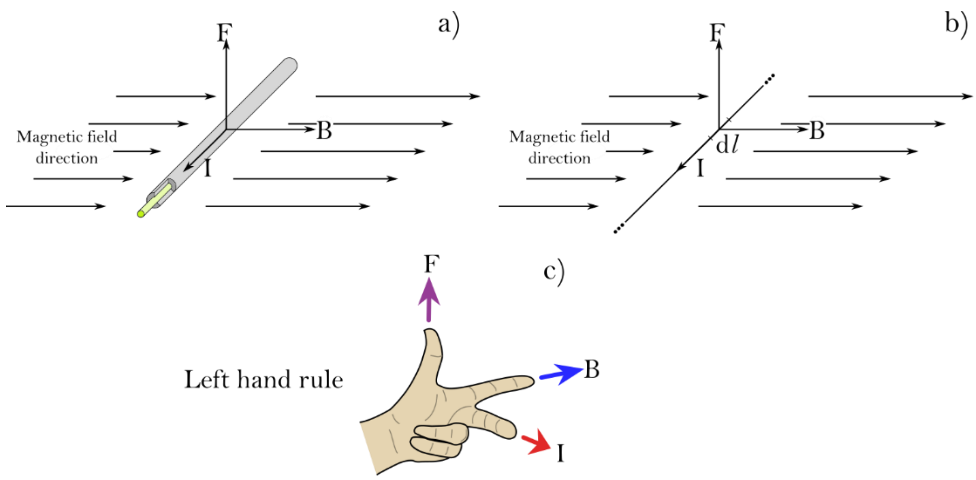

Figure 7: a, b) Generic current-carrying wire in a magnetic field B c) left hand rule for the force direction determination

This fact can be connected to the Lorenz force because the current represents a movement of charges in the wire and the Lorentz force acts on the moving charges. Because these charges are bound to the conductor, the magnetic forces on the charges are transferred to the wire. By combining the Lorentz force and the electric current definition (as the variation of charge over time) the force acting in a small portion of the wire dl can be expressed as follows (Figure 7):

$$\mathbf{dF} = i\ \mathbf{dl}\times\boldsymbol{B} \qquad 1.57$$

and extended to the whole wire using an integral definition:

$$\mathbf{F} = i \int_l \mathbf{dl}\times\boldsymbol{B} \qquad 1.58$$

The force vector has a direction perpendicular to both **B** and I (to identify the direction of the force there is a practical rule called *left hand rule* shown in Figure 7).

1.3 SUMMARY OF THE FUNDAMENTAL EQUATION FOR THE ELECTRO-MAGNETIC FIELD:

Main vectors acting in electromagnetic fields:

Vector	Name	Unit of measurement
B(*P*, *t*)	Magnetic flux density	[T]
D(*P*, *t*)	Electric displacement	[C/m^2]
E(*P*, *t*)	Electric field	[V/m]
H(*P*, *t*)	Magnetic field	[A/m]
J(*P*, *t*)	Current density	[A/m^2]

where *P* indicates the action point of the vector, in other words the spatial dependency, and *t* represents the time dependency.

1.3.1 MAXWELL EQUATIONS

The relationships between these vector fields are the Maxwell equations:

Differential form

Name	Differential form	meaning
General Ampere's law	$\nabla\times\mathbf{H}(P,t) = \mathbf{J}(p,t) + \dfrac{\partial\mathbf{D}(P,t)}{\partial t}$	The magnetic field induced around a closed loop is proportional to the electric current added to displacement current (rate of change of electric field) it encloses.
Maxwell-faraday Equation	$\nabla\times\mathbf{E}(P,t) = -\dfrac{\partial\mathbf{B}(P,t)}{\partial t}$	The voltage induced in a closed circuit is proportional to the rate of change of the magnetic flux it encloses.

Gauss's law for magnetism	$\nabla \cdot \mathbf{B}(P,t) = \mathbf{0}$	There are no magnetic monopoles; the total magnetic flux through a closed surface is zero.
Gauss's law	$\nabla \cdot \mathbf{D}(P,t) = \rho(P,t)$	The electric flux leaving a volume is proportional to the charge inside.

Integral form

Name	Differential form	meaning
General Amperes law	$\oint_{\partial S} \mathbf{B} \cdot \mathbf{dl} = \mu \iint_S \mathbf{J}(P,t) dS + \mu\varepsilon \frac{d}{dt} \iint_S \mathbf{E} \cdot \mathbf{ds}$	The magnetic field induced around a closed loop is proportional to the electric current added to displacement current (rate of change of electric field) it encloses.
Maxwell-faraday Equation	$\oint_{\partial S} \mathbf{E} \cdot \mathbf{dl} = -\frac{d}{dt} \iint_S \mathbf{B}\, dS$	The voltage induced in a closed circuit is proportional to the rate of change of the magnetic flux it encloses.
Gauss's law for magnetism	$\oiint_{\partial\Omega} \mathbf{B}\, dS = 0$	There are no magnetic monopoles; the total magnetic flux through a closed surface is zero.
Gauss's law	$\oiint_{\partial\Omega} \mathbf{E} \cdot \mathbf{n}\, dS = \frac{1}{\varepsilon} \iiint_{\Omega} \rho(P,t)\, dV$	The electric flux leaving a volume is proportional to the charge inside.

where:

- $\rho(P.t)$ is the free charge density;
- S is a generic surface in the domain and ∂S its frontier;
- Ω is a generic volume in the domain and $\partial\Omega$ its frontier;
- μ, ε, σ are respectively: the magnetic permeability, electric permittivity and conductivity of the domain material

1.3.2 CONSTITUTIVE LAWS AND CONTINUITY LAW

In the following the constitutive equations for the electromagnetic field are reported:

	Equation
Flux density & Magnetic field	$\mathbf{B}(P,t) = \mu(P)\,\mathbf{H}(P,t)$
Electric displacement & Electric field	$\mathbf{D}(P,t) = \varepsilon(P)\,\mathbf{E}(p,t)$
Current density & Electric field	$\mathbf{J}(P,t) = \sigma(P)\,\mathbf{E}(P,t)$

And the continuity law:

$$\nabla \cdot \mathbf{J}(P,t) = -\frac{\partial \rho(P,t)}{\partial t} \qquad 1.59$$

If the material shows an anisotropic nature all the linking constants $(\mu, \varepsilon, \sigma)$ must be expressed using the tensorial notation, therefore in three dimensions that is:

$$\mu = \begin{bmatrix} \mu_x & 0 & 0 \\ 0 & \mu_y & 0 \\ 0 & 0 & \mu_z \end{bmatrix} \qquad \varepsilon = \begin{bmatrix} \varepsilon_x & 0 & 0 \\ 0 & \varepsilon_y & 0 \\ 0 & 0 & \varepsilon_z \end{bmatrix} \qquad \sigma = \begin{bmatrix} \sigma_x & 0 & 0 \\ 0 & \sigma_y & 0 \\ 0 & 0 & \sigma_z \end{bmatrix} \qquad 1.60$$

These three quantities, in some non-homogenous materials, are also variable through the *i* (with *i=x, y, z*) direction and dependent on the value of the applied field (**H** or **E** respectively).

1.3.3 LAPLACE, POISSON, HELMHOLTZ EQUATIONS

For the sake of simplicity, the following equations are reported for the static case, so all the time derivatives are equal to zero. With the *Coulomb Position (*1.47*)* for the magnetic vector potential **A**, the magnetic field problem can be expressed using the following quasi-harmonic equation:

$$\nabla\times(\frac{1}{\mu}\nabla\times\mathbf{A}) = \mathbf{J} \qquad 1.61$$

Equation 1.61 in a homogenous domain, where μ is constant with the position, can be simplified into the *Poisson* equation for the magnetostatic field:

$$\nabla^2 \mathbf{A} = -\mu \mathbf{J} \qquad 1.62$$

If the considered domain exhibits a null current density **J** in all its points, the problem is represented by the *Laplace* equation for the magnetostatic field.

$$\nabla^2 \mathbf{A} = 0 \qquad 1.63$$

In some applications, it is necessary to consider the magnetic and current field variation with time, and their mutual coupling. Supposing that the time variations of the field quantities are well represented by sinusoids it is possible to represent such variables using complex notation:

$$A(t) = A_m \cos(\omega\, t + \alpha) \xrightarrow[\text{notation}]{\text{complex}} \dot{A} = A_m\, e^{j\alpha} = A^r + jA^i = A_m \cos(\alpha) + j\, A_m \sin(\alpha) \qquad 1.64$$

Considering also a homogeneous material and the time derivative of **D**=0 the only electric force acting in the domain is the electric field **E**. Under these hypotheses the current density **J** can be expressed as the sum of the external current density $\mathbf{J_s}$ and the induced current density $\mathbf{J_i}$ given by:

$$\dot{\mathbf{J}} = \sigma\, \dot{\mathbf{E}} = -\sigma \frac{\partial \dot{\mathbf{A}}}{\partial t} = -j\omega\sigma\dot{\mathbf{A}} \qquad 1.65$$

where ω is the pulsation of the field quantities. Substituting 1.65 into 1.62 generates the so-called *Helmholtz* equation, that represents the spatial variations of **A** with its time variations:

$$\nabla^2 \dot{\mathbf{A}} - j\omega\sigma\dot{\mathbf{A}} = -\mu\dot{\mathbf{J}} \qquad 1.66$$

1.4 METHOD OF IMAGES FOR THE MAGNETIC FIELD

The solution of the magnetic field distribution caused by a given set of currents in the presence of magnetic materials with different permeabilities is not as common as the corresponding electrostatic case. Though the principles can be formulated in a rather similar manner, the actual application frequently does not lend itself to a simple adaptation of a known electrostatic solution because of the restrictions which one must impose upon the scalar magnetostatic potential.

It must be also kept in mind that the mirror image of the electrostatic field of a positive charge in front of a conductive plane, is a negative charge; the mirror image of the magnetic field of a positive current (placed in front of an infinite permeable surface) is, instead, a positive current.

1.4.1 IMAGES WITH RESPECT TO IDEALLY PLANAR EQUIPOTENTIAL BOUNDARIES

The solution for the magnetic field of any line current in air near a planar magnetic material of infinite permeability with a planar surface is found by replacing the magnetic material with a suitable image of the line currents. This is analogous to the procedure on a planar conducting surface in electrostatics with the appropriate change in sign of the source image.

If a long straight line current flows in the proximity of such an ideal magnetic boundary, as in Figure 8a, the field in air is the combination of two equivalent line currents, both placed in air, as show in Figure 8b. In the new configuration (Figure 8b), the field distribution is now easy to determine using analytical methods.

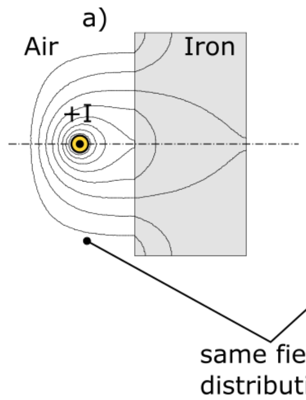

Figure 8: a: Infinite long conductor in a proximity to an infinite permeable magnetic plate, b: Method of magnetic images applied to the situation reported in a

A first and simple application of this method is to analyze the self-inductance variation of a parallel pair of long transmission line wires running close to a ferromagnetic plate with infinite permeability. This situation is represented in Figure 9a and the equivalent representation using the image method in Figure 9b.

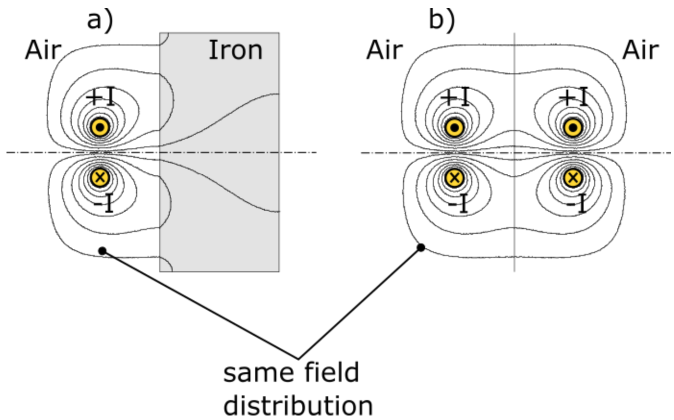

Figure 9: a: Couple of Infinitely long conductors in the proximity of an infinitely permeable magnetic plate, b: Method of magnetic images applied to the situation reported in a

The proximity of the magnetic material increases the self-inductance of the conductor system; this increase can be computed from the flux produced by the image conductors and linked with the original loop. As reported in [3] this variation can be calculated as follows:

$$\Delta L = \frac{\mu_0}{2\pi} \cdot \ln\left(1 + \left(\frac{c}{d}\right)^2\right) \qquad 1.67$$

where *c* is the semi-distance between the conductors and *d* is the distance of the conductors from the magnetic plate.

Obviously, as *d* decreases, ΔL increases, reaching the maximum external inductance when the conductors touch the surface.

The same procedure can be used for any linear current loop, so that the well-known formulas for the magnetic field evaluation are usable to solve the problem. For uniform current densities, this method can be extended to conductors of finite cross sections, subdividing them into current elements $J\ dS$ and applying the imaging method to each of them.

All these considerations are possible also if the magnetic plate permeability is a finite quantity. In that case, the "image current" value is different from the imposed one ([3]), and more precisely equal to:

$$\mathrm{I}' = \frac{\mu_{iron}-\mu_{air}}{\mu_{iron}+\mu_{air}}\mathrm{I} \tag{1.68}$$

1.4.2 METHOD OF IMAGES APPLIED TO A GENERIC-SHAPED COIL

The method of magnetic images briefly explained in the previous chapters, can be used also to model complex systems. For this purpose, let us consider a coil geometry as reported in Figure 10a where the conductors are partly embedded in the iron region.

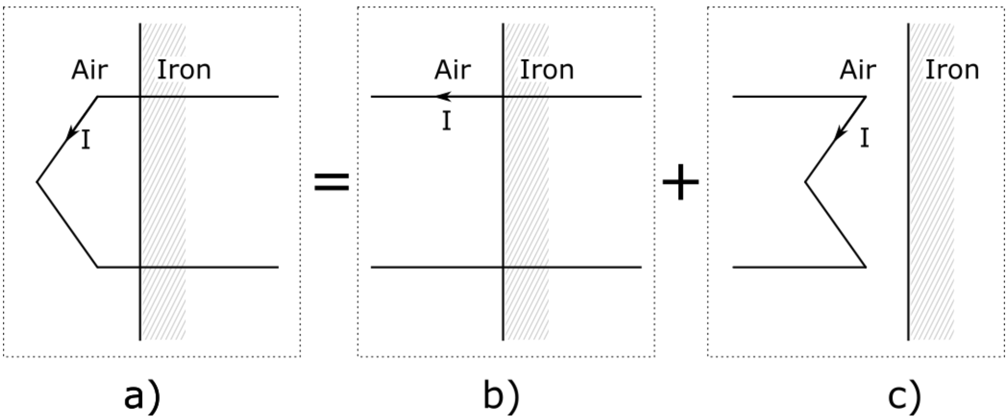

Figure 10: a) Coil geometry with conductors passing through the iron region; b) and c) superposition principle applied to the initial coil geometry

The geometric model of the coil is clear looking at Figure 10. Before every other consideration, it is necessary to make some starting assumptions:

- The permeability of the iron core is constant and infinite ($\mu = \infty$).
- The iron core surface extends infinitely and fills the entire half-space.
- The coils are represented by infinitely thin conductors.

In this case, the method of images [3] is applied to take into account the influence of the magnetic plate on the magnetic field distribution in the air region. The basic model of the coil is shown in Figure 10a. This model can be constructed out of the circuits shown in Figure 10b and Figure 10c applying the superposition principle.

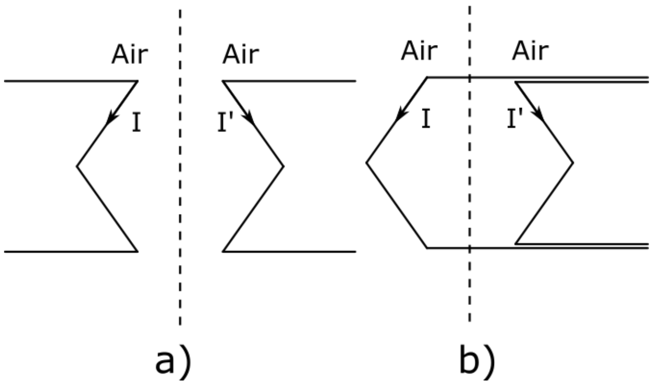

Figure 11: a) and b) Method of magnetic mirror images applied to the coil geometry reported in figure 16

The field due to the current in the circuit in Figure 10c can be determined from that circuit and its mirror image (Figure 11). The mirror image of the circuit in Figure 10b is identical to its original. The superposition of circuits shown in Figure 10b and Figure 11a yields the final circuit in Figure 11b. The current that flows in the mirror image of the circuit in Figure 10c is determined by the permeability of the iron and is calculated according to 1.68.

The idea of the circuit reported in Figure 11b can be used for the end winding inductance determination in some electrical machine stator windings [4].

1.5 REFERENCES

[1] N. Bianchi, “Electrical machine analysis using finite elements”, CRC Taylor & Francis, 1-24, 1953

[2] Moon, P. and Spencer, D. E. "The Meaning of the Vector Laplacian." J. Franklin Inst. 256, 551-558, 1953.

[3] E. Weber, “Electromagnetic fields Theory and Applications”, John Wiley & Sons, Inc., New York Chapman & Hall, Limited, London

[4] D. Ban, D. Zarko and I. Mandic, "Turbogenerator end-winding leakage inductance calculation using a 3-D analytical approach based on the solution of Neumann Integrals," in IEEE Transactions on Energy Conversion, vol. 20, no. 1, pp. 98-105, March 2005.

2 DESIGN AND ANALYSIS OF SLOTLESS SPM MACHINES WITH ANALYTICAL TECHNIQUES

Nowadays, the well-known world-wide environmental issues relating to the still massive use of polluting fossil fuel is being approached in several ways. The two most important and promising strategies consist of a growing employment of renewable energy sources and on the implementation of effective energy-saving policies. In this scenario, electric machines play a crucial role: on one side, in fact, the vast majority (around 80%) of the worldwide power consumption results from the use of electric motors in industrial, household and vehicle traction applications; hence improving the efficiency of electric motors is expected to result in extraordinary benefits in terms of saved energy. On the other side, the use of renewable energy sources (like photovoltaics, wind energy, tidal energy, hydropower, etc.) calls for a radical change in the electric generator technology. For instance, electric generators suitable for being coupled to wind turbines or to buoys for tidal energy exploitation strongly differ from conventional alternators that have been used for decades in power stations based on steam and/or gas turbines.

The advance in motor and generator technology to improve their efficiency and to make their design fit for new green generation needs is not only a matter of technology but has also some important implications in terms of scientific research and basic physical knowledge. In fact, the development of new technologies (carried out in specialized industrial environment) is necessarily founded on deep and extensive theoretical investigations to which the scientific community can make a significant contribution.

2.1 SLOTLESS SPM MACHINE

In conventional electric machines, the stator windings are embedded in stator core slots and retained by appropriate wedges. The presence of a slotted stator bore, however, is known to produce parasitic effects like cogging torques and rotor eddy-current losses [1]. In some applications, it is convenient to overcome these issues by resorting to a slotless stator design, wherein the stator windings are directly attached to a smooth cylindrical stator bore surface [2]-[6].

Application examples of slotless architecture are:

- High-performance motors used to drive gas compressors which require a perfectly smooth ripple-free driving torque;
- Wind generators designed to operate also in presence of very weak wind (thus requiring practically null parasitic torques [7]);
- High-efficiency high-speed motors and generators where the extremely high rotor speed would make eddy-current losses due to slotting effects potentially harmful in terms of rotor overheating [8]-[10];
- Wind generators where torque pulsations are to be minimized in order to reduce possible mechanical fatigue issues as well as mechanical resonance problems relating to the gear-box.

For all these kinds of applications (all relating to energy saving and distributed generation), slotless machines are expected to gain a growing importance over the next few years.

Investigations into the electromagnetic design and analysis of this machinery have been then started [2][3]. The main purpose of these investigations is to work out a fully analytical model to very rapidly study slotless permanent-magnet machines with various rotor surface permanent magnet topologies without the need to use time-consuming finite-element analysis (FEA) tools. This has been already achieved with respect to radially magnetized surface permanent-magnet rotor topologies. In this chapter the performance investigation will be extended to the case of Halbach-array rotor designs as well as to permanent magnets with parallel magnetization. Comparative performance evaluations will be carried out based on the analytical computation tools which have been prepared. The availability of a fully analytical algorithm to accurately predict the performance of slotless permanent magnet machines will be a key advantage compared to the present state-of-the-art especially when it comes to design the machine through design optimization tools. In fact, these tools require a huge number (hundreds or thousands) of design variants to be analyzed and compared in search for the optimum and, if all computations are performed by FEA, the optimization results in an extraordinarily heavy computational burden; conversely, analytical models produce the same results as FEA with the same accuracy almost instantaneously, with dramatic computational savings.

2.1.1 Brief introduction on slotless SPM machines

Surface Permanent Magnet (SPM) machines may be equipped with either a slotted or slotless stator core [4][5][6]. In the latter case, the stator laminations are obtained from a ferromagnetic hollow cylinder whose inner surface is smooth. Stator coils are attached to this surface (Figure 12), instead of being embedded in slots as in the ordinary construction.

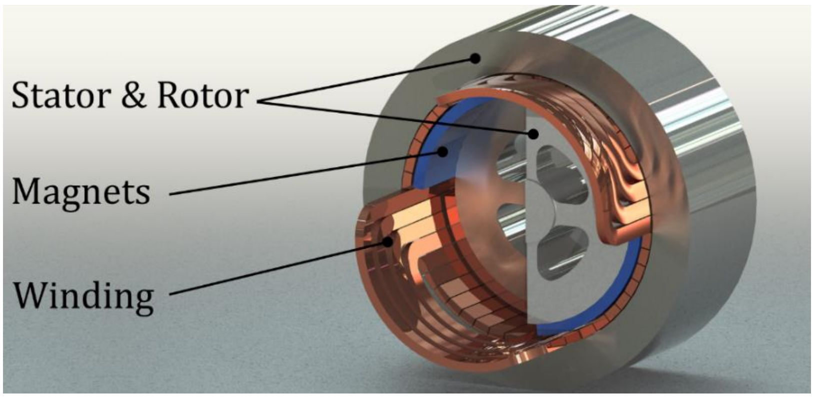

Figure 12: Rendering of a slotless SPM machine (some parts are omitted or cut for the sake of clarity)

Thanks to the absence of teeth, slotless SPM machine geometry allows for a relatively easy analytical solution for the magnetic fields in active parts [2]. Formulations of the magnetic field in the air-gap due to both permanent magnets and armature windings have been already presented in the literature [8]-[13]. In this chapter, an analytical exact formulation is derived for the load torque and the back EMF of slotless SPM machines with different rotor magnetization patterns. An analytical formulation of the problem has the advantage of explicitly showing how machine torque relates to every single construction detail. Therefore, it can be of practical usefulness in the dimensioning and design optimization stage as a fast alternative to time-consuming Finite Element (FE) analysis [7][8].

With respect to the existing literature, the method proposed in this chapter for torque computation does not rely on Maxwell's stress tensor technique [4]-[6] (which is known to lead to quite involved formulation) but employs an alternative approach where rotor permanent magnets are modeled as a combinations of equivalent current sheets [11]. Such a modeling makes it possible to compute the force acting on them (and thus the rotor torque) from the vector product of the armature reaction field and the equivalent current density representing permanent magnets through (1.57).

2.1.2 SLOTLESS-STATOR ARCHITECTURE

In common slotted configurations, stator conductors are retained and cooled by embedding them in laminated cores inside slots; although mechanically and thermally advantageous, slotted design gives rise to parasitic phenomena due to the magnetically anisotropic air-gap structure, such as rotor additional losses caused by flux pulsations and cogging torques (as said in the previous section). In addition to the iron losses in the teeth, the amount of rotor losses which result from slotting effects can be not negligible, especially at high speeds, also considering that rotor losses are the most difficult to remove. Thanks to the availability of high energy density permanent magnets, in view of high efficiency and reliability targets, a slotless motor design can be an appropriate choice, where single-layer resin-encapsulated stator coils are directly fixed on a smooth stator bore surface (Figure 13).

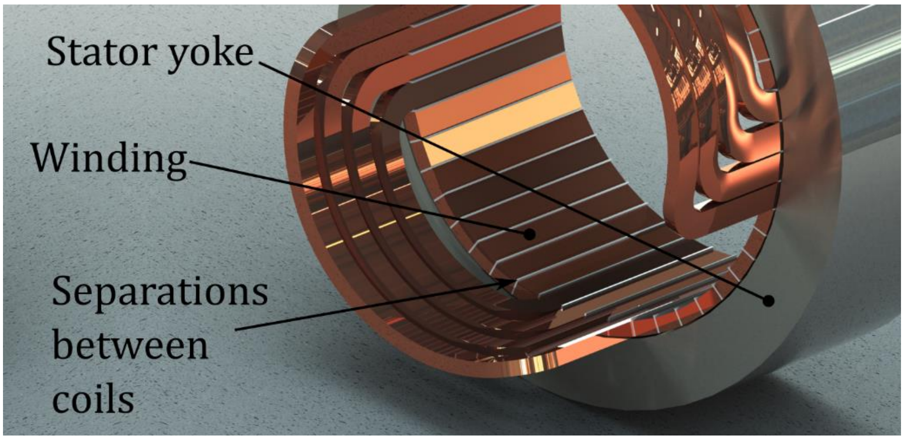

Figure 13: Rendering of stator winding distribution in a slotless machine

In Figure 13 a zoomed view is represented of the stator of a slotless machine with concentric single layer winding. The picture also shows the end-windings of one phase. It can be seen that the end windings of these kind of machines are "Cylinder-shaped" (this fact will be used in the following chapters where an analytical formula for the end winding inductance calculation is proposed).

For winding conductors, Litz-wire technology is sometimes necessary in order to limit eddy current losses. This means that each conductor is constituted by a bundle of parallel-connected thin wires, properly twisted so that they link the same integral flux and no circulation currents arise among them.

The sides of the coils are anchored by means of thin dielectric (ceramic) spacers (Figure 13, Figure 14) wedged into the stator bore. Spacers are designed to withstand tangential electrodynamic forces and to transfer the heat due to resistive copper losses from the winding into laminations. The end coils are epoxy-resin impregnated and encapsulated for mechanical consolidation and thermal exchange purposes. Employment of a very low-loss electric steel material with high silicon content is mandatory to limit the core losses at supply frequency. Another critical point in this sense is the appropriate selection of the maximum flux density level in stator yoke in motor dimensioning or optimization.

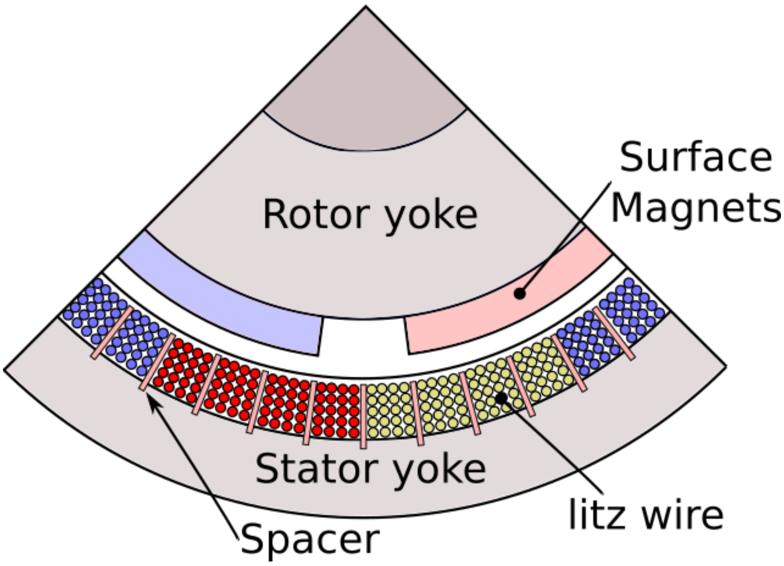

Figure 14: Cross section of a slotless SPM machine

With respect to the winding scheme, the most common solution for this kind of machines, is the three-phase single layer winding (sometimes a multi three phase scheme can be used). This means that the winding is distributed as shown in the following table (for a 4 poles machine with four coils per-pole per-phase). In the table, for the sake of brevity, only the winding distribution for two poles has been reported.

Table I: Three phase single layer winding

POLE	**POLE1**												**POLE2**											
COIL	1	2	3	4	5	6	7	8	9	10	11	12	13	14	15	16	17	18	19	20	21	22	23	24
PHASE	a+	a+	a+	a+	c-	c-	c-	c-	b+	b+	b+	b+	a-	a-	a-	a-	c+	c+	c+	c+	b-	b-	b-	b-

In table I, coils sections are called a+, b+, c+ for the positive sides and a-, b-, c-, for the negative parts. It can be seen that there are four coils per pole per phase. Another example is reported in table II, where a double three phase winding is provided:

Table II: Double-three phase single layer winding

POLE	**POLE1**												**POLE2**											
COIL	1	2	3	4	5	6	7	8	9	10	11	12	13	14	15	16	17	18	19	20	21	22	23	24
PHASE	a1+	a1+	a2+	a2+	c1-	c1-	c2-	c2-	b1+	b1+	b2+	b2+	a1-	a1-	a2-	a2-	c1+	c1+	c2+	c2+	b1-	b1-	b2-	b2-

In table II, the phases for the two three phase windings are called a1, b1, c1 and a2, b2, c2 respectively. In this case, there are two coils per pole per phase.

The choice of a dual three-phase design firstly improves system fault tolerance since a fault on one converter does not cause an immediate drive stop. Secondly, it improves torque and air-gap flux harmonic quality thanks to mutual cancellation effects among air-gap space harmonic fields produced by the two winding sections.

2.1.3 SPM ROTOR POSSIBLE ARCHITECTURES

The slotless SPM machine topologies considered in this work are shown in Figure 15, where arrows indicate the magnetization directions of the single magnet segment.

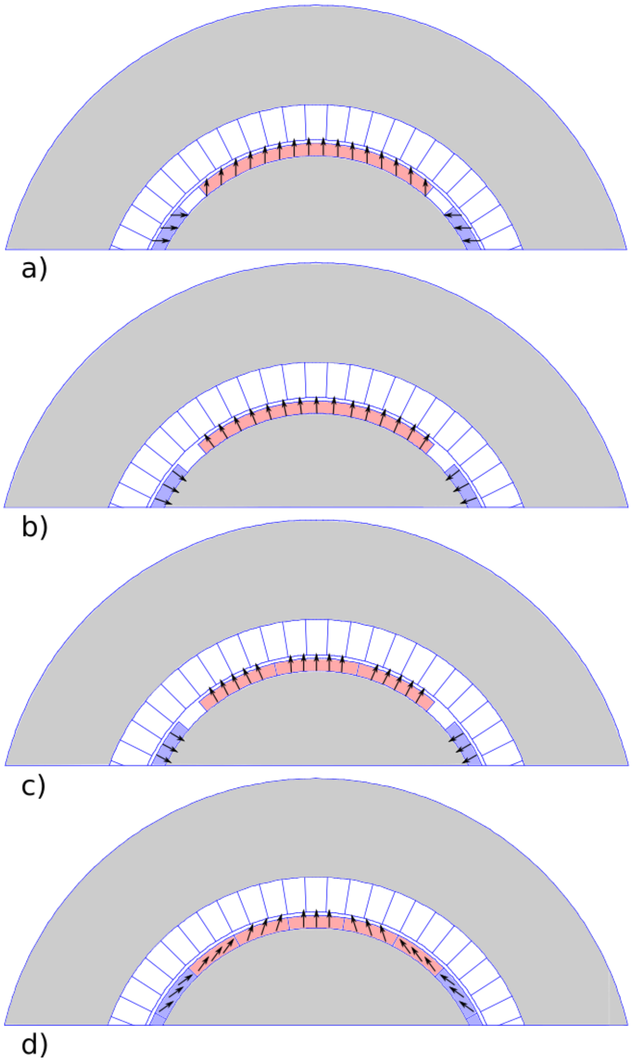

Figure 15:Slotless SPM rotor topologies: (a) parallel magnetization with single magnet per pole; (b) continuous radial magnetization; (c) discrete radial magnetization; (d) Halbach array

The most common topologies for the SPM architecture are:

- The parallel magnetization pattern with a single magnet per pole (Figure 15a);
- The continuous radial magnetization pattern (Figure 15b);
- The discrete radial magnetization pattern (Figure 15c), where each pole encompasses an arbitrary number N_{bp} of parallel-magnetized blocks;
- Halbach-array magnetization pattern with an arbitrary number N_{bp} of parallel-magnetized permanent magnet blocks per pole (Figure 15d).

Multiple parallel-magnetized permanent magnets per pole are often used in real applications to implement a discrete radial magnetization pattern (Figure 15c) as an alternative to the continuous one in order to reduce permanent magnet production costs.

2.1.3.1 *Parallel magnetization*

In the parallel magnetization pattern (Figure 15a), each pole is composed of a single parallel magnetized magnet block. This configuration is the simplest to manufacture but the mean air gap flux density harmonic content due to the rotor is generally high. This is clear looking at Figure 16 where the radial component of the flux density in the mean geometric air-gap is plotted. This means that this kind of machine can suffer from torque ripple problems, although the cogging torque component is absent.

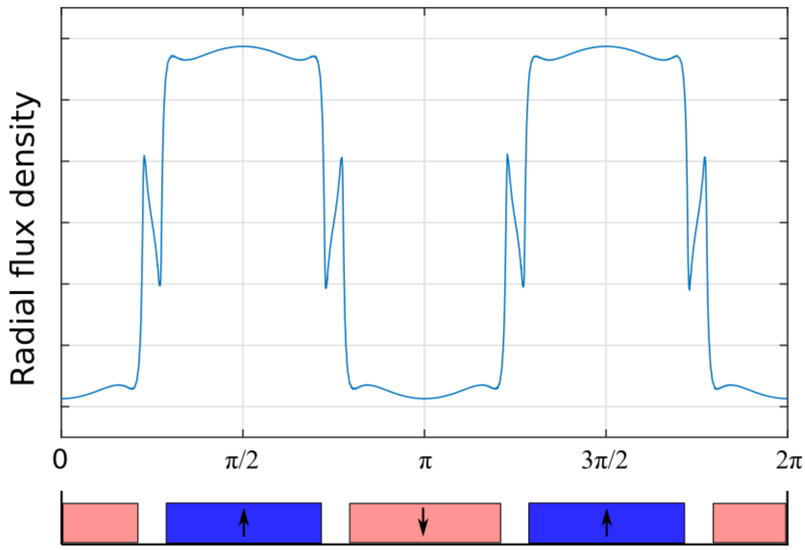

Figure 16: Radial component of the flux density due to a parallel magnetized rotor in the mean geometric air gap

2.1.3.2 *Continuous radial magnetization*

In the continuous radial magnetization pattern (Figure 15b), each pole is composed of a single radially magnetized magnet block. This configuration is hard to manufacture (because a custom magnetizer is necessary to energize the magnet) and the radial component of the mean air gap flux density is theoretically a square wave. This means that the harmonic content in the airgap is comparable to that of a parallel magnetized architecture. This means, again, that this kind of machine can suffer from torque ripple problems, although the cogging torque component is absent.

2.1.3.3 *Discrete parallel magnetization pattern*

In the discrete parallel magnetization pattern (Figure 15c), each pole is composed of a certain number of magnet blocks with parallel magnetization (Figure 17). This configuration is the simplest to manufacture and the radial component of the mean air gap flux density is midway between the radial and the single-block parallel configuration (it is obvious that the higher the number of parallel magnets blocks per pole the more this configuration looks like the radially magnetized one). The main advantage of this configuration is the possibility to use commercial smaller magnets instead of custom-shaped and magnetized elements. Figure 17 shows an example of an air gap radial flux density distribution at no load along the mean air-gap circumference. In this particular case, there are three parallel blocks per pole.

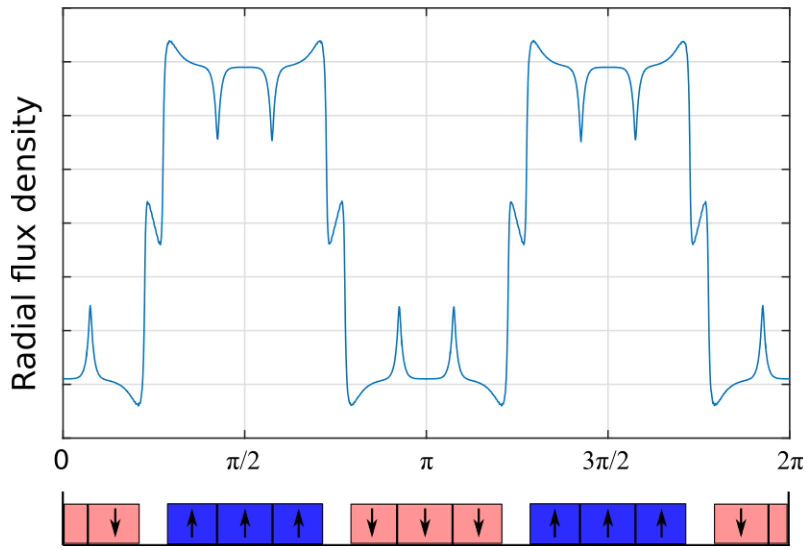

Figure 17: Radial component of the flux density due to a segmented parallel magnetized rotor

2.1.3.4 Halbach array magnetization pattern

A Halbach array magnetization pattern consists of several surface-mounted permanent magnets covering the whole rotor periphery and having a magnetization direction that changes by discrete steps along it. Figure 18 shows a sketch of the radial flux density in the mean air gap in a four-pole slotless motor with Halbach array rotor design. The example motor shown in the figure has five permanent magnet segments per pole, with an angular step of 18 degrees between the magnetizations of adjacent segments.

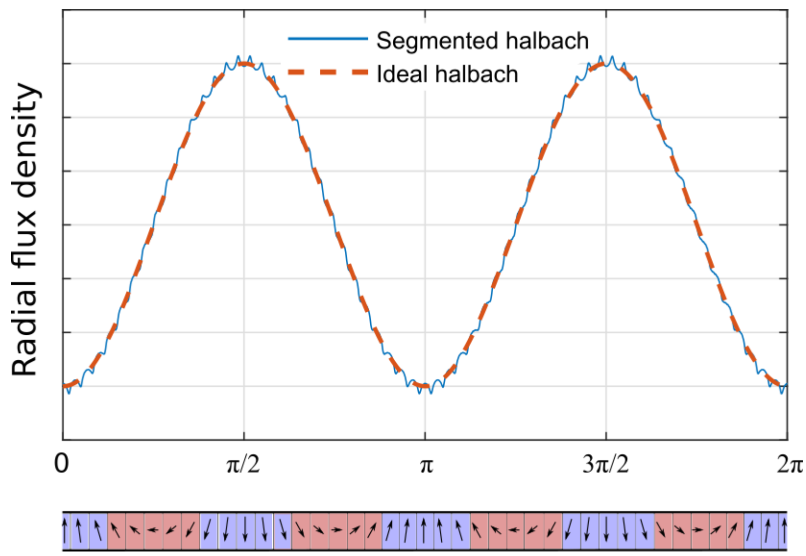

Figure 18: Radial component of the flux density due to a segmented halbach magnetized rotor

Compared to conventional SPM design, Halbach-array permanent magnet arrangement enhances the no-load air-gap flux density waveform by reducing its space harmonic content. This is clear looking at Figure 18 where the mean air-gap radial flux density is almost sinusoidal.

The main drawback of Halbach-array structures is the higher permanent magnet cost related to magnetization direction requirements. There are two different possibilities to magnetize the rotor: the first, and the most expensive, is to realize a single magnet sector (with an annular shape) and use a custom magnetizer to energize the magnet. In this case the resulting spatial distribution of the radial flux density in the mean air gap is almost a perfect sinusoid; the second methodology, and the less expensive (Figure 18), is to realize the Halbach array using N_{bp} parallel magnetized blocks per pole (the adopted simplified configuration needs only N_{bp} different magnet types to manufacture the whole rotor). In this case the resulting spatial distribution of the radial flux density is worst, compared to the previous, in terms of harmonic content, but better in terms of manufacturing cost because a custom magnetizer is not needed.

2.1.4 MAIN ADVANTAGES AND DISADVANTAGES USING SLOTLESS ARCHITECTURE

As already said in the first part of this chapter, this kind of machines are well suited for various kinds of applications where low parasitic phenomena are required. In this subsection, all the main advantages and drawbacks of the slotless machine are summarized to better understand why they are so adequate to fit all the requirements.

2.1.4.1 Low parasitic effects

At this point, it is clear that this kind of architecture reduces almost to zero the parasitic phenomena known as cogging torque (typical for the SPM slotted machines); furthermore, the joule losses due to the Eddie currents in the rotor parts are strongly reduced (due to the absence of the slot harmonics).

The absence of cogging torque is an essential feature where the machine is required to operate for most time at low torque compared to the rated one. So, it is possible that the torque oscillation introduced by this parasitic effect could cause inacceptable speed variations.

The reduction of rotor losses caused by eddy currents is a crucial feature where the machine efficiency is a main requirement. This kind of currents occur in the conductive parts of the rotor due to the air gap flux variation; adopting the slotless structure, it is possible to reduces the air-gap field harmonic content (absence of slotting harmonics) and consequently the joule losses.

2.1.4.2 Lower stator inductance

The slotless structure offers an additional advantage which is constituted by a very small stator phase inductance value (compared to the inductance of a slotted machine). The reason why the inductance is smaller than usual is due to a very large magnetic air gap.

The difference between mechanical and magnetic air gap is clear looking at Figure 14 and Figure 15 where the magnetic gap is composed by the magnet, the winding and the mechanical gap thickness.

In the hypothesis of infinitely permeable stator and rotor iron, the reactance that limits the armature reaction field is proportional to the magnetic air gap not to the mechanical one. Therefore, higher is the magnetic air gap, lower is the phase inductance.

One of the reasons why a small value of this inductance is desirable is clear looking at the phasor diagram represented in Figure 19.

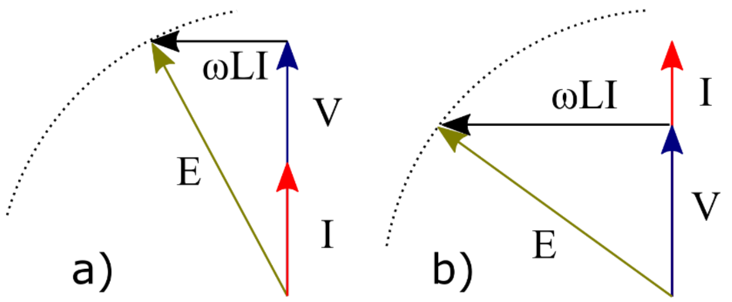

Figure 19: Simplified phasor diagram for a synchronous generator feeding two different resistive loads

In this diagram, *E* represents the open circuit voltage at pulsation ω, *V* and *I* phase voltage and current respectively and *L* is the phase inductance. The voltage drop due to the phase resistance is neglected. Looking at the voltage drop across the inductance, it is clear that the phase voltage decreases as the load increase. This reduction can be significantly limited if the machine phase inductance is low.

Another issue connected with the small phase inductance is the capability of the machine to withstand electromechanical transients. These transients (e.g. high load variations) can cause pole-slipping issues forcing the machine stop. The transient stabilizing torque is known to be directly proportional to the product of *E* and *V* and inversely proportional to the sub transient reactance X_d'':

$$T_{stab} \propto \frac{E\,V}{X_d''} = \frac{E\,V}{\omega\,L} \tag{2.1}$$

where the sub-transient reactance X_d'' in a SPM machine is equal to the synchronous reactance ωL. It is obvious that a smaller value of this reactance results in a better transient stability.

However, from the transient point of view, a small value of the machine phase reactance has a double consequence. On one side, as already said with 2.1, the stabilizing torque increases but on the other side tends to increase also the transient peak current. This current can cause harmful effects in the machine and in the power system.

From the efficiency point of view the phase inductance value can play a crucial role if the power supply system use the pulse width modulation (PWM) technique. In this case, a small inductance can increase the machine losses [14] .

2.1.4.3 Lower power/torque density compared to standard slotted machines

Compared with slotted motors, a slotless machine exhibits generally a lower power and torque density. As already proved in literature [15],[16], slotless motors have a larger rotor diameter than slotted construction for the same require torque and considering the same outside dimensions. A bigger rotor causes a higher inertia, reducing dynamic performances in terms of accelerations.

In other terms, the slotted motors are good for high torque density and high acceleration, while slotless motors are optimum for smooth operation.

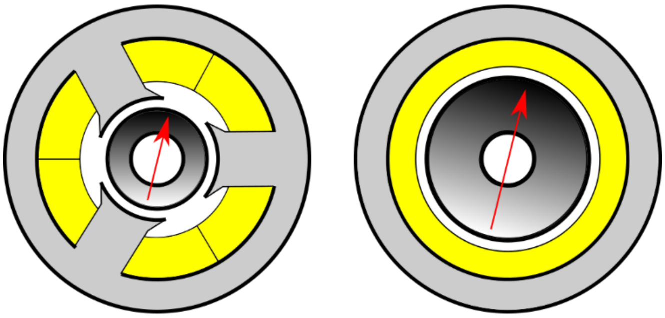

Figure 20: Examples of slotted and slotless machines studied in [15]

In the following paragraph the results of an optimization process regarding the comparison of different SPM machines are reported [15]. In this example, the machine under study is a two-pole brushless PM motor with parallel magnetization with slotted or slotless stator architecture for high speed operations (Figure 20). This optimization algorithm was carried out with given external dimensions (outer dimeter and stack length) and with given heat exchange conditions (limiting the maximum current density). Other fixed parameters are: the mechanical air-gap thickness, the shaft diameter, and the slot filling factor. The optimization war performed for various magnetic materials searching for the maximum torque value.

The attention was mainly focused on two design variables: the ratio between the stator bore diameter D and the outer stator diameter D_e and the flux density value in the machine stator yoke B_{iron}.

Slotted configuration			
PM material	Sintered NdFeB	Bonded NdFeB	Ferrite
Geometry		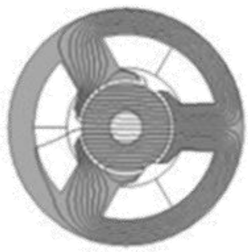	
B_{iron} [T]	0.9	1.0	1.15
D/D_e [%]	30.2	41.1	52.6
Torque [Nm]	0.37	0.36	0.32
Active Power [W]	1170	1170	1020
Current density [A/mm² rms]	8.8	8.5	8.3

Slotless configuration			
PM material	Sintered NdFeB	Bonded NdFeB	Ferrite
Geometry	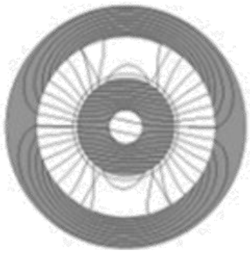	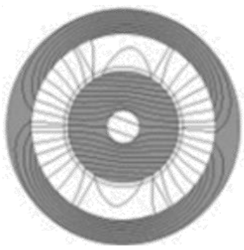	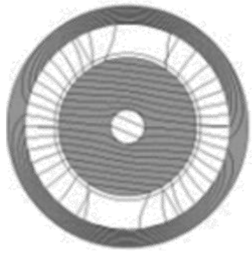
B_{iron} [T]	0.9	0.9	0.8
D/D_e [%]	43.8	50.1	58.5
Torque [Nm]	0.39	0.33	0.26
Active Power [W]	1230	1040	800
Current density [A/mm^2 rms*]*	5.5	5.7	5.8

A summary with motors designs exhibiting the maximum torque is reported in the following table. Looking at the table, and more in particular at the ratio D/D_e it is clear that the slotless machine exhibits a lower torque density compared to the slotted one.

2.1.5 SLOTLESS SPM MACHINES FABRICATION ISSUES

As said in the previous sections, the winding of slotless machines is attached to the annular stator iron core of the machine (Figure 21).

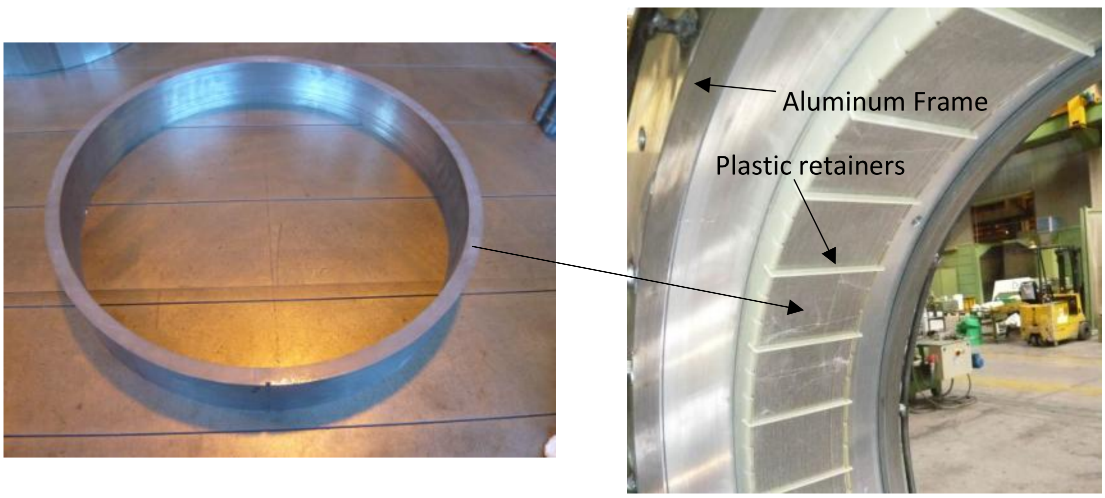

Figure 21: a) stator iron core of a slotless machine b) stator iron core of a slotless machine with some of the winding retainers

The winding needs to be very firmly retained because the exchanged torque from the whole winding and the stator bore is the electromagnetic torque of the machine. To avoid such severe consequences as the machine destruction due to winding detachment, it is a good practice to fix the spacers between coils (made of plastic or ceramic material) into stator slits as shown in Figure 21b.

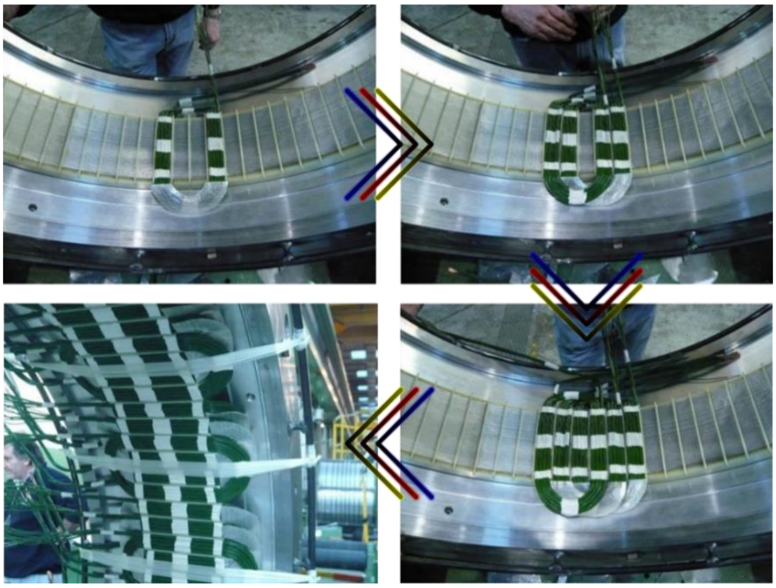

Figure 22: Stator coils assembling procedure

Considering the practical winding fabrication there are some other remarkable issues to notice. In

Figure 22 shows a possible procedure for the stator coil mounting. This manufacturing process may change from one winding type or technology to another, but in any case stator coils are distributed along all the stator bore circumference without any magnetic components between them.

After the physical mounting of all the winding components (coils and retainers) it is necessary to impregnate and encapsulate all these machine parts inside a cast resin block. This process is illustrated in Figure 23.

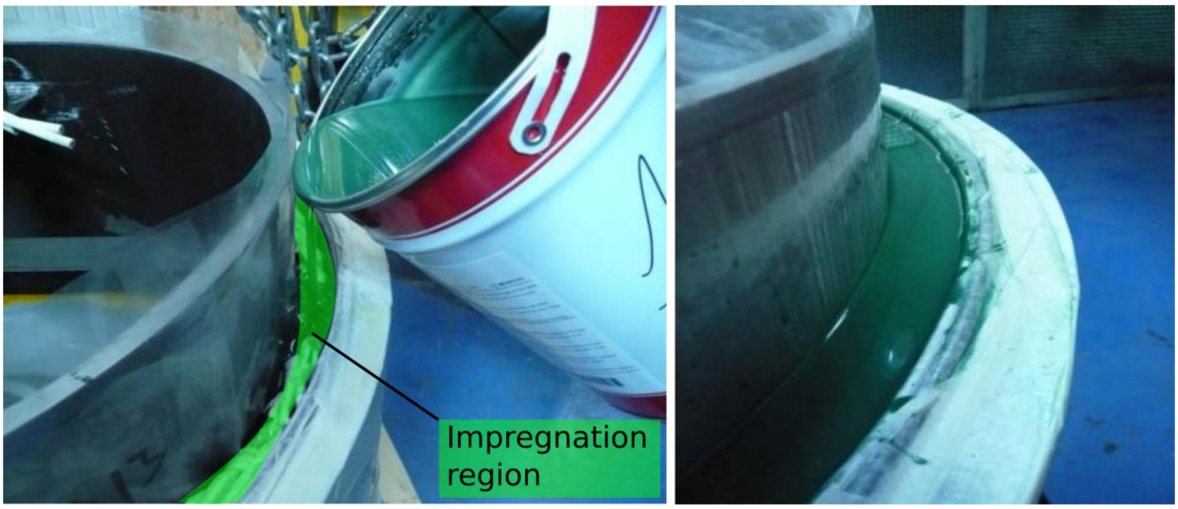

Figure 23: Stator impregnation details

As said in chapter 2.1.3 there are different types of SPM rotors, but all of them have the same geometric structure and exhibit the same manufacturing issues. In Figure 24 two stages in rotor magnet mounting are illustrated.

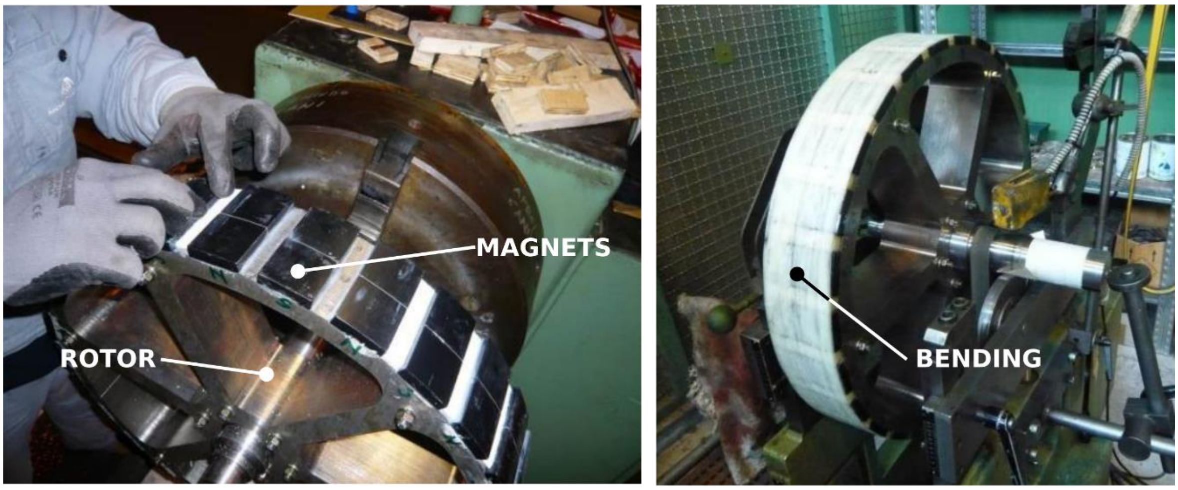

Figure 24: Rotor magnet mounting

Finally, in Figure 25 it is possible to see an example of complete slotless SPM machine with and without enclosing shields (made of aluminum).

Figure 25: Slotless SPM machine example with and without enclosing shields

2.2 SLOTLESS SPM MACHINE PERFORMANCE PREDICTION

Slotless surface permanent magnet (SPM) machines are attractive in some industrial and power generation fields where it is essential to reduce the cogging torque to the minimum possible extent, as said in the previous sections. The slotless stator design can be combined with different SPM rotor topologies, including radial, parallel or Halbach-array magnetization patterns.

The analytical solution of the magnetic field inside slotless SPM and inset permanent-magnet machines is not new and has been addressed by many previous works through the solution of Poisson's differential equation in the air-gap, winding and permanent magnet domain ([8][9][10][12][13]). Most of the literature dedicated to the topic, however, focuses on the analytical prediction of the flux density field, while the torque computation is either neglected or performed numerically using Maxwell stress tensor formula ([18][19]). Explicit analytical expressions for the torque of slotless permanent magnet machines can be actually found in [2], [12] but their validity is restricted to some specific rotor design configurations like: two-pole parallel-magnetized cylindrical permanent-magnet rotor; purely radial SPM rotor; 2-segment-per-pole Halbach array rotor.

In this section, an explicit analytical formulation of the torque for slotless permanent magnet machines is derived covering the case of SPM rotor topologies with different possible magnetization patterns, including radial, parallel and Halbach-array types (Figure 15). The treatment applies to the case when each pole encompasses an arbitrary number of permanent magnet segments. The explicit torque expression generalizes the procedure followed in [2] for the radial SPM topology, a procedure which is also reported in a following subsection, namely: the armature reaction field is firstly determined by direct solution of Poisson's equation; secondly, the flux density is integrated along the contour of each permanent magnet modelled as an equivalent surface current distribution [2][17]. This integral can be symbolically solved contrary to the integral resulting from Maxell stress tensor method, which typically requires a numerical solution [18][19].

For the sake of completeness, the treatment is also extended to the computation of the back-EMF. An explicit analytical expression is derived for this quantity, too, with the same approach used for the torque, i.e. assuming different rotor magnetization patterns along with permanent magnet segmentation into an arbitrary number of magnet units, each treated as a set of equivalent surface currents. The stator inductance computation, instead, is not covered as it does not depend on the rotor permanent magnet arrangement and magnetization and explicit analytical expressions for it are already available in the existing literature [9].

The accuracy of the obtained torque and back-EMF expressions are successfully assessed by comparison against Finite Element Analysis (FEA) for different number of poles and magnetization patterns. The availability of an explicit analytical torque computation formula makes it possible to quickly compare and optimize various possible slotless SPM machine design configurations, with different dimensions and/or rotor topologies, as it will be discussed in chapter 2.3 and 2.4

The rest of the section is organized as follows: first of all, the model geometry is introduced along with the main assumptions made to study it. After that the armature reaction field expression is derived, focusing the attention on the radial flux density component, which is the only one needed for torque computation with the proposed method. Subsequently explicit analytical expressions are derived and assessed to compute the torque and the back-EMF, respectively, for different rotor magnetization patterns.

2.2.1 MODEL GEOMETRY AND ASSUMPTIONS

The slotless SPM machine topologies addressed in this work are shown in Figure 15, where arrows indicate the magnetization of the single magnet block. The topologies being covered are: the parallel magnetization pattern with a single magnet per pole (Figure 15a); the continuous radial magnetization pattern (Figure 15b); the discrete radial magnetization pattern (Figure 15c), where each poles encompasses an arbitrary number N_{bp} of parallel-magnetized blocks; Halbach-array magnetization pattern with an arbitrary number N_{bp} of parallel-magnetized permanent magnet blocks per pole (Figure 15d).

Out of the four topologies illustrated in Figure 15, the continuous radial magnetization pattern (Figure 15b) is already addressed and assessed in [2]. All the details for explicit torque computation in this case are therefore not included in this thesis and only the most important and the final results are recalled in section 0.

The attention is therefore focused on the other three topologies, which are all characterized by a set of differently displaced parallel-magnetized blocks. The approach to the torque and back-EMF computation is based on summing the contributions due to all parallel-magnetized permanent magnet blocks. Each of these is modeled as shown in Figure 26, where the main characteristic dimensions of the machine cross section are also illustrated.

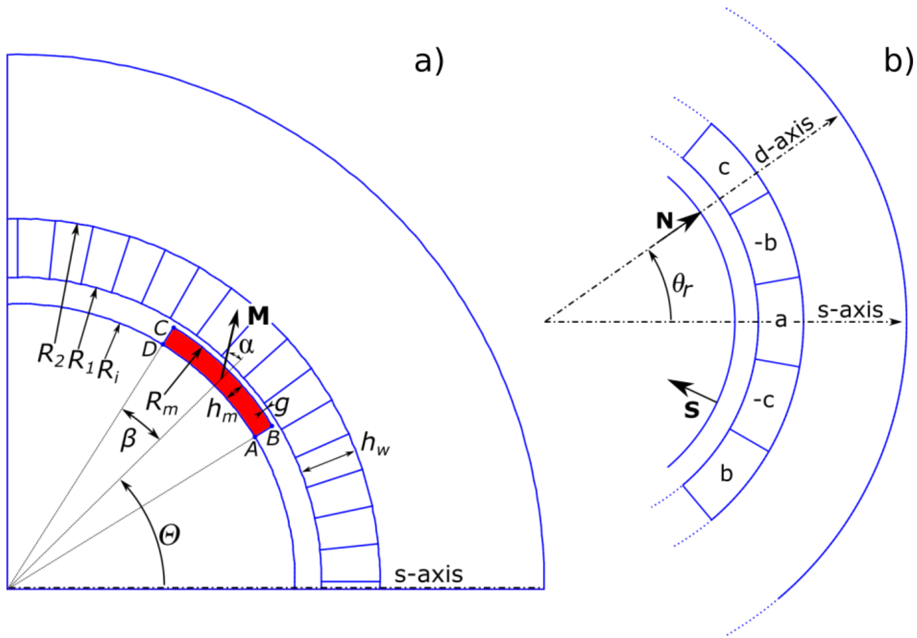

Figure 26: (a) Characteristic dimensions of the machine cross-section with a single permanent magnet block, (b) Stator-attached s-axis and rotor d-axis representation.

The machine cross section is characterized by radii R_i, R_m, R_1, R_2 (outer rotor radius, radius at permanent magnet surface, inner stator winding radius, inner stator core radius, respectively). The winding and permanent magnet heights are respectively indicated as h_w and h_m. The stator winding is supposed to be a three-phase single-layer one ([5],[6],[7]) with phases defined as *a*, *b*, *c*. Currents in phases *a, b, c* are supposed to be sinusoidal and shifted by 120 electrical degrees apart in time:

$$
\begin{aligned}
i_a(t) &= I\cos(\omega t) \\
i_b(t) &= I\cos\left(\omega t - \frac{2}{3}\pi\right) \\
i_c(t) &= I\cos(\omega t - \frac{4}{3}\pi)
\end{aligned}
\qquad 2.2
$$

The mechanical air gap width is g. As regards each single permanent magnet block (having contour ABCD in Figure 26a), it is characterized by an angular span equal to 2β and its axis is placed at an angular position Θ. By definition, the block has uniform magnetization indicated by the vector *M*, displaced by an angle α with respect to the block radial axis (Figure 26a). The angular position Θ is measured in mechanical radians with respect to a fixed *s* axis which passes through the center of a phase belt pertaining to stator phase a as illustrated in Figure 26a. With respect to the *s* axis, the position of the rotor *d* axis is identified by the angle θ_r (Figure 26b).

The machine is also characterized by the following data:

- N_c: number of turns per coil
- p: number of pole pairs
- q: number of coils per pole per phase
- I: peak phase current
- ω: stator current pulsation
- τ_p: pole pitch
- τ_{pm}: magnet span

Stator and rotor cores are assumed to have infinite magnetic permeability and the relative magnetic permeability of permanent magnets is supposed equal to unity.

End-effects are disregarded, hence the vector potential is everywhere parallel to the rotational axis, so that its axial component is always considered as a scalar quantity.

For machine field analysis, a polar coordinate system (r, θ) is introduced where a generic point *P* in the machine cross section is identified by a radius vector of length *r* starting from rotation axis and forming an angle ϑ with the reference *s* axis.

2.2.2 COMPUTATION OF THE OUTPUT TORQUE FOR ALL MAGNETIZATION PATTERNS

In this subsection, an explicit expression for the torque is derived for the various rotor magnetization patterns. For this purpose, permanent magnets are modelled as equivalent surface current distributions and the torque is computed considering the interaction between such current distributions and the armature reaction field. In particular, only the radial component of the flux density produced by the stator winding is useful for torque generation when interacting with permanent magnet equivalent current density.

2.2.2.1 Armature Reaction field computation

The armature reaction field in the air-gap domain is first computed. By air-gap domain in this context reference is made to all the machine region not occupied by ferromagnetic cores; the air gap in this sense therefore includes permanent magnet and stator winding regions as well. The armature reaction field is being computed by solving Maxwell equation for the magnetic vector potential in the air-gap domain. The field solution in the winding region ($R_1 < r < R_2$) is indicated in the following by subscript "w", while the solution in the remaining part of the air-gap (mainly occupied by permanent magnets, $R_i \le r \le R_1$) will be denoted by subscript "m". If only stator current energizes the machine, the vector potential in the winding and permanent magnet domain (A_w, A_m, respectively), satisfy the following differential equations in polar coordinates r, ϑ:

$$\nabla A_w = \frac{1}{r}\frac{\partial}{\partial r}\left(r\frac{\partial A_w}{\partial r}\right) + \frac{1}{r^2}\frac{\partial^2 A_w}{\partial^2 \theta} = -\mu_0 J(\theta,t) \qquad 2.3$$

$$\text{for} \quad R_1 < r < R_2$$

while the magnetic vector potential A_m in the region including the mechanical air gap and the permanent magnets obeys to Laplace equation:

$$\nabla A_m = \frac{1}{r}\frac{\partial}{\partial r}\left(r\frac{\partial A_m}{\partial r}\right) + \frac{1}{r^2}\frac{\partial^2 A_m}{\partial^2 \theta} = 0 \qquad 2.4$$

$$\text{for} \quad R_\mathrm{i} < r < R_1$$

where $J(\theta, t)$ is the current density distribution as a function of time t and the angular position θ.

From the solution of (2.3) and (2.5), the flux density polar components (tangential θ and radial r) in the winding region (B_{wr}, $B_{w\theta}$) and in the permanent magnet region (B_{mr}, $B_{m\theta}$) can be obtained using the definition (1.46) as:

$$B_{wr} = \frac{1}{r}\frac{\partial A_w}{\partial \theta}, \quad B_{w\theta} = -\frac{\partial A_w}{\partial r} \qquad 2.5$$

$$\text{for} \;\; R_1 \le r \le R_s$$

$$B_{mr} = \frac{1}{r}\frac{\partial A_m}{\partial \theta}, \quad B_{m\theta} = -\frac{\partial A_m}{\partial r} \qquad 2.6$$

$$\text{for} \;\; R_i \le r \le R_1$$

Definition of current density function

The current density function $J(\theta, t)$ is a piece-wise constant function that accounts for the current density being uniform over each phase belt. By simple geometric considerations, it can be shown that the function $J(\theta, t)$ can be expressed as the following series expansion [2]:

$$J(\theta,t) = \sum_{h=p,7p,13p,\dots} J_h \cos(h\theta - \omega t) + \sum_{k=5p,11p,17p,\dots} J_k \cos(k\theta + \omega t) \qquad 2.7$$

ω being the stator angular frequency. The generic Fourier coefficient J_n in (2.7) can be written as follows for any integer n [2]:

$$J_n = \frac{36 N_c I_c p^2 q \sin[n\pi/(6p)]}{\pi^2 n (R_2{}^2 - R_1{}^2)}$$

$$with:\ I_c = \sigma\, k_{fill} \cdot \frac{\pi(R_2^2 - R_1^2)}{6pq\ N_c} \qquad 2.8$$

where:

- N_c: is the number of conductor per coil;
- I_c: is the current per conductor (peak value);
- σ: is the conductor current density (peak value);
- k_{fill}: is the filling factor of the coil;
- p: is the number of pole pairs;
- q: are the number of coils per pole per phase.

Indices *k* and *h* in (2.7) respectively take odd integer values given by $k = 6q + 1$ (with q=0, 1, 2…) and $h = 6q - 1$ (with q=1, 2, 3…). Figure 27 shows the plot of current density function $J(\theta, t)$ for a four-pole machine over the whole circumference ($0 \leq \theta \leq 2\pi$) at two instants of time, namely at *t*=0 and *t*=*T*/12 where $T = 2\pi/\omega$ is the period of stator currents. The data of the sample SPM slotless machine considered to draw the plots in Figure 27 are reported in the following table.

Table I: Sample machine data for the current density plot

I_c	1194 [A]	Conductor current
p	2	Number of pole pairs
q	1	Coils per pole per phase
N_c	1	Number of conductors per coil
R_1	52 [mm]	Inner winding radius
R_2	62 [mm]	Outer winding radius

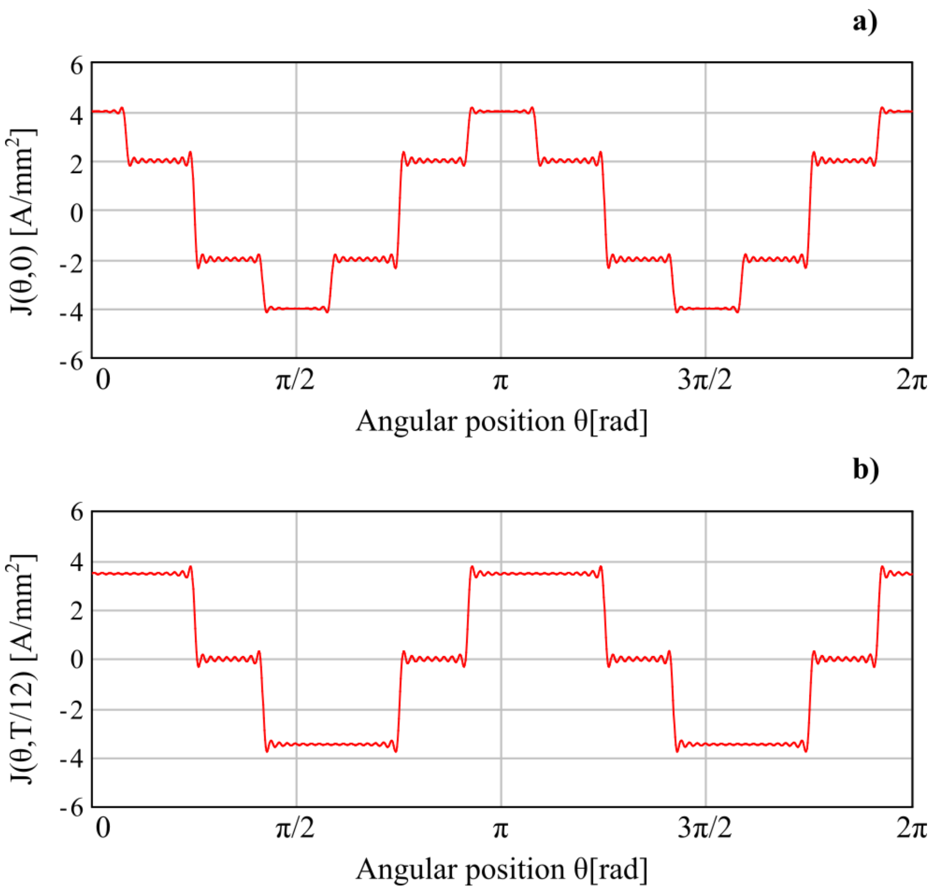

Figure 27: Current density function plot over the whole circumference at time t=0 and t=T/12

Defining boundary conditions

Once the current density function has been defined as discussed in the previous section, what is still required to solve the differential problem (2.3-2.4) is the definition of the boundary conditions.

Two homogeneous Neumann boundary conditions can be established on the outer and inner air-gap circumferences (at radii $r = R_i$ and $r = R_s$), imposing that the flux density must have zero tangential component on them (due to the assumed infinite core permeability):

$$B_{w\theta}\Big|_{r=R_s} = -\left.\frac{\partial A_w}{\partial r}\right|_{r=R_s} = 0 \qquad 2.9$$

$$B_{m\theta}\Big|_{r=R_i} = \left.\frac{\partial A_m}{\partial r}\right|_{r=R_i} = 0 \qquad 2.10$$

for any ϑ. Two further boundary conditions can be fixed by imposing that the flux density must be continuous at r=R_1 in both its radial and tangential components:

$$B_{w\theta}\Big|_{r=R_1} = -\left.\frac{\partial A_w}{\partial r}\right|_{r=R_1} = B_{m\theta}\Big|_{r=R_1} = -\left.\frac{\partial A_m}{\partial r}\right|_{r=R_1} \qquad 2.11$$

$$B_{wr}\Big|_{r=R_1} = \frac{1}{R_1}\frac{\partial A_w}{\partial \theta}\Big|_{r=R_1} = B_{mr}\Big|_{r=R_1} = \frac{1}{R_1}\frac{\partial A_m}{\partial \theta}\Big|_{r=R_1} \qquad 2.12$$

All the boundary conditions and the defined regions are summarized in Figure 28:

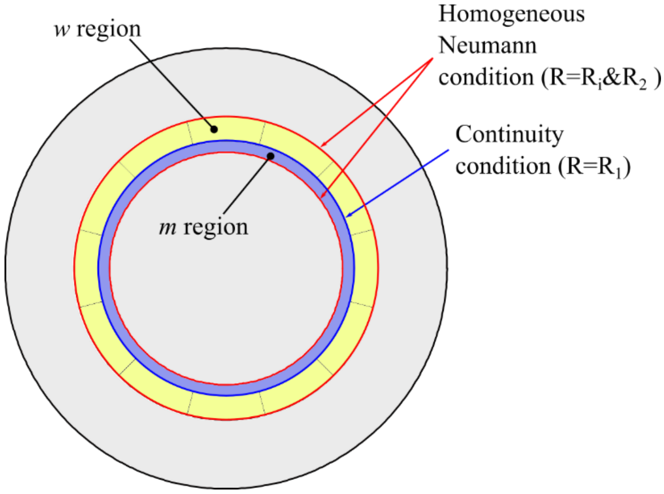

Figure 28: SPM machine cross-section with boundary conditions and defined regions

Solution in the winding region

To determine the vector potential in the winding region, boundary conditions (2.9-2.12) have to be applied to the general solutions of (2.5, 2.6). By separation of variables [2], a general solution for 2.3) can be obtained as follows:

$$A_w(r,\theta,t) = \sum_{h=p,\,7p,\,13p,\,...} w_h(r)\cos(h\theta - \omega t) + \sum_{k=5p,\,11p,\,17p,\,...} w_k(r)\cos(k\theta + \omega t) \qquad 2.13$$

where the functions w_n are the parts of the solution which account for the dependency on r according to the imposed boundary conditions (2.9-2.12) and using separation of variables [2]. For any n they are:

$$w_n(r) = \begin{cases} W_n^{+} r^{n} + W_n^{-} r^{-n} - W_n^{*} r^{2} & \text{if } n \neq 2 \\ \dfrac{\mu_0 J_2}{4}\left[\dfrac{C + Dr^4}{4r^2\left(R_i^4 - R_2^4\right)} - r^2 \ln r\right] & \text{if } n = 2 \end{cases} \qquad 2.14$$

In (2.14), coefficients C and D are given by:

$$C = R_1^4 R_2^4 - R_2^4 R_1^4 - 4R_i^4 R_2^4 \ln\left(R_2 / R_1\right) \qquad 2.15$$

$$D = R_1^4 - 2R_2^4 + R_i^4 + 4R_i^4 \ln R_1 - 4R_2^4 \ln R_2 \qquad 2.16$$

and coefficients $W_n^{+}, W_n^{-}, W_n^{*}$ are as follows:

$$W_n^{+} = \frac{\mu_0 J_n}{2n(R_2^{2n} - R_i^{2n})}\left[\frac{R_2^{n+2} - R_i^{2n} R_1^{2-n}}{2-n} + \frac{R_2^{n+2} - R_1^{2+n}}{2+n}\right] \qquad 2.17$$

$$W_n^- = \frac{\mu_0 J_n}{2n(R_i^{-2} - R_2^{-2n})}\left[\frac{R_2^{2-n} - R_i^{-2n} R_1^{2+n}}{2+n} + \frac{R_2^{2-n} - R_1^{2-n}}{2-n}\right] \tag{2.18}$$

$$W_n^* = \frac{\mu_0 J_n}{4 - n^2} \tag{2.19}$$

It is noted that the function (2.14) takes two different expressions depending on *n*; the two expressions are linked by the following limit relationship:

$$\lim_{n\to 2}\left(W_n^+ \, r^n + W_n^- \, r^{-n} - W_n^* r^2\right) = \frac{\mu_0 J_2}{4}\left[\frac{C + Dr^4}{4r^2\left(R_i^4 - R_2^4\right)} - r^2 \ln r\right] \tag{2.20}$$

Once the equation (2.13) is fully determined it is possible to define the parallel and radial flux density functions in the winding region:

$$B_{wr}(\theta, r, t) = \frac{1}{r}\frac{\partial A_w}{\partial \theta} = -\frac{1}{r}\left(\sum_{h=p,7p,13p,..} h\, w_h(r)\sin(h\theta - \omega t) + \sum_{k=5p,11p,17p,..} k\, w_k(r)\sin(k\theta + \omega t)\right) \tag{2.21}$$

$$B_{w\theta}(\theta, r, t) = -\frac{\partial A_w}{\partial r} = \sum_{h=p,7p,13p,..} w_h'(r)\cos(h\theta - \omega t) + \sum_{k=5p,11p,17p,..} w_k'(r)\cos(h\theta + \omega t) \tag{2.22}$$

where:

$$w_n'(r) = \frac{\partial w_n'(r)}{\partial r} = \begin{cases} nW_n^+ \, r^{n-1} - nW_n^- \, r^{-n-1} - 2W_n^* r & \text{if } n \neq 2 \\ -\dfrac{\mu_0 J_2}{4}\left[\dfrac{C + Dr^4}{2r^3\left(R_2^4 - R_i^4\right)} + \dfrac{rD}{R_2^4 - R_i^4} + r + 2r\ln(r)\right] & \text{if } n = 2 \end{cases} \tag{2.23}$$

Solution in the magnet region

In the magnet region, a general solution for the vector potential equation (2.4) is:

$$A_m(r, \theta, t) = \sum_{h=p,\,7p,\,13p,\,\ldots} m_h(r)\cos(h\theta - \omega t) + + \sum_{k=5p,\,11p,\,17p,\,\ldots} m_k(r)\cos(k\theta + \omega t) \tag{2.24}$$

where the functions m_n are the part of the solution which account for the dependency on r. These functions can be determined using conditions (2.9-2.12) again and the separation of variable technique; for any integer n they are given by:

$$m_n(r) = \begin{cases} M_n^+ \, r^n + M_n^- \, r^{-n} & \text{if } n \neq 2 \\ \dfrac{\mu_0 J_2\left(R_i^4 + r^4\right)\left(4R_2^4 \ln \dfrac{R_1}{R_2} + R_1^4 - R_2^4\right)}{16r^2\left(R_i^4 - R_2^4\right)} & \text{if } n = 2 \end{cases} \tag{2.25}$$

where coefficients M_m^+ and M_m^- are defined as follows:

$$M_n^+ = \frac{1}{R_1^{2n} - R_i^{2n}} \left(\frac{\mu_0 J_n R_1^{n+2}}{n^4 - 4} + W_n^+ R_1^{2n} + W_n^- \right) \qquad 2.26$$

$$M_n^- = \frac{R_i^{2n}}{R_1^{2n} + R_i^{2n}} \left(\frac{\mu_0 J_n R_1^{n+2}}{n^4 - 4} + W_n^+ R_1^{2n} + W_n^- \right) \qquad 2.27$$

It can be proved that the relationship between expressions in (2.25) is:

$$\frac{\mu_0 J_2 \left(R_i^4 + r^4\right)\left[4R_2^4 \ln\left(R_1 / R_2\right) + R_1^4 - R_2^4\right]}{16 r^2 \left(R_i^4 - R_2^4\right)} = \lim_{n \to 2} \left(M_n^+ \, r^n + M_n^- \, r^{-n} \right) \qquad 2.28$$

Once the equation (2.24) is fully determined it is possible to define the parallel and radial flux density functions in the magnet region:

$$B_{mr}(\theta, r, t) = \frac{1}{r}\frac{\partial A_m}{\partial \theta} = -\frac{1}{r}\left(\sum_{h=p,7p,13p,..} h\, m_h(r) \sin(h\theta - \omega t) + \sum_{k=5p,11p,17p,..} k\, m(r) \sin(h\theta + \omega t) \right) \qquad 2.29$$

$$B_{m\theta}(\theta, r, t) = -\frac{\partial A_m}{\partial r} = \sum_{h=p,7p,13p,..} m_h{}'(r) \cos(h\theta - \omega t) + \sum_{h=5p,11p,17p,..} m'(r) \cos(h\theta + \omega t) \qquad 2.30$$

where, for any integer *n*.

$$m'_n(r) = \frac{\partial m_n}{\partial r} = \begin{cases} n\, M_n^+ \, r^{n-1} - n\, M_n^- \, r^{-n-1} & \text{if } n \neq 2 \\ \dfrac{2\mu_0 J_2 \left(R_i^4 - r^4\right)\left(4R_2^4 \ln \dfrac{R_1}{R_2} + R_1^4 - R_2^4\right)}{16 r^3 \left(R_2^4 - R_i^4\right)} & \text{if } n = 2 \end{cases} \qquad 2.31$$

FEM validations

In order to validate (2.21, 2.22) and (2.29, 2.30) two finite elements simulation are provided with two different SPM machines (sample machines data are reported in tables II and III). Results are plotted in Figure 29 and in Figure 30.

Table II: Sample machine data for the flux density comparison: four pole machine

σ	4	[A/mm^2]	Conductors current density
p	2	\	Pole pairs
q	1	\	Coils per pole per phase
N_c	1	\	Number of conductors per coil
R_1	52	[mm]	Inner winding radius
R_2	62	[mm]	Outer winding radius
R_i	47.5	[mm]	Inner magnet radius
R_m	51	[mm]	Outer magnet radius
g	1	[mm]	Geometric Air-Gap

Table III: Sample machine data for the flux density comparison: twelve pole machine

σ	4	[A/mm^2]	Conductors current density
p	6	\	Pole pairs
q	1	\	Coils per pole per phase
N_c	1	\	Number of conductors per coil
R_1	52	[mm]	Inner winding radius
R_2	62	[mm]	Outer winding radius
R_i	47.5	[mm]	Inner magnet radius
R_m	51	[mm]	Outer magnet radius
g	1	[mm]	Geometric Air-Gap

In these figures, the flux density in the air-gap due to the stator coils is plotted along two circumferences, Γ_1 and Γ_2, with two different radii. In the Figure 29 the tangential and radial flux densities evaluated with analytical formulas are compared with 2D finite element analysis simulation results showing almost a perfect matching. In Figure 30 the same thing is done with a similar machine in terms of geometrical quantities, but with 12 poles. Also in this case the distribution resulting from the analytical approach gives good results.

The interesting quantity for the purpose of torque computation with the proposed method is the radial flux density component B_{mr} in the magnet region; from this it is possible to compute the torque contribution of the various magnet blocks as explained next.

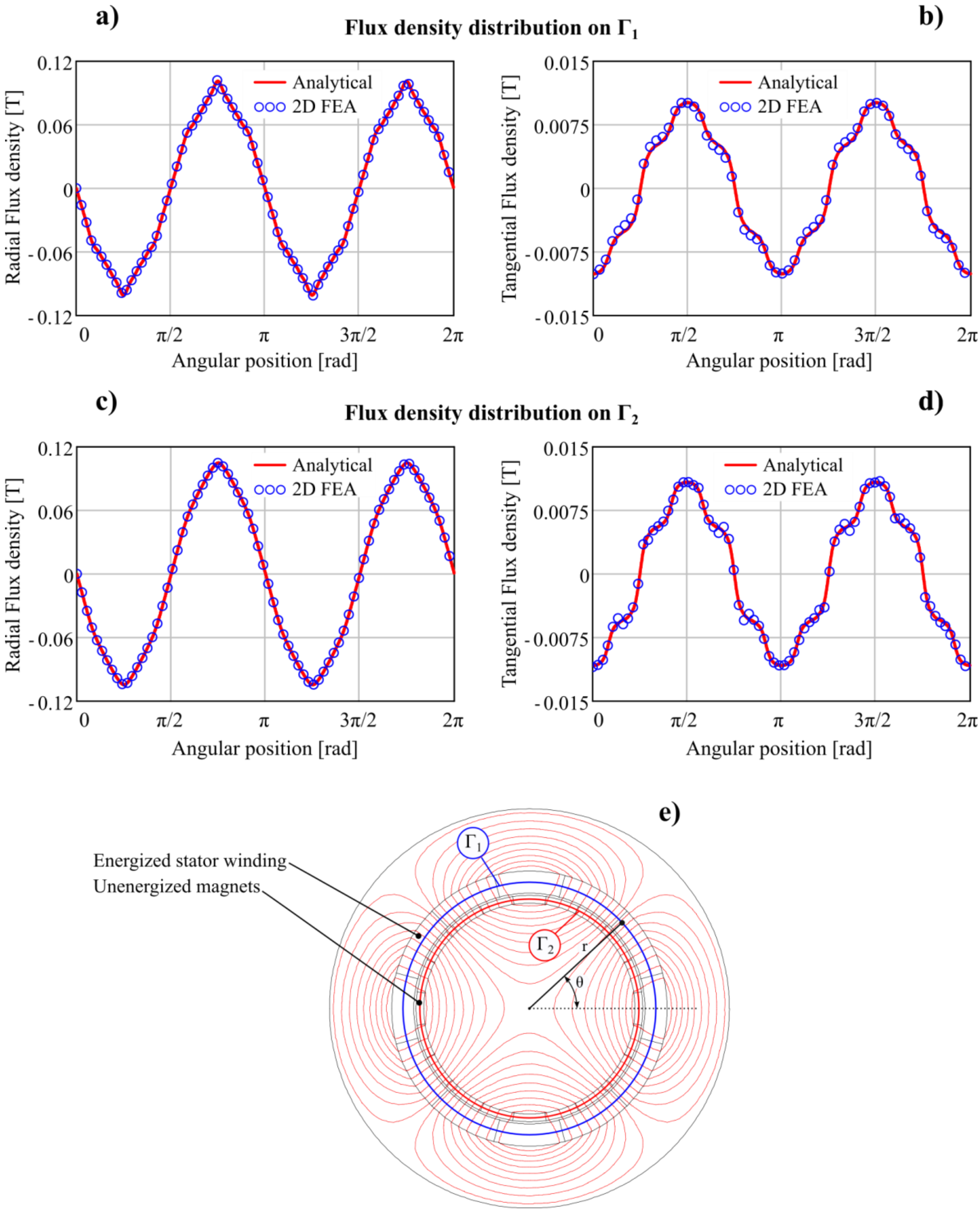

Figure 29: Flux density plot comparison between analytical computation and FEA in a four-pole machine

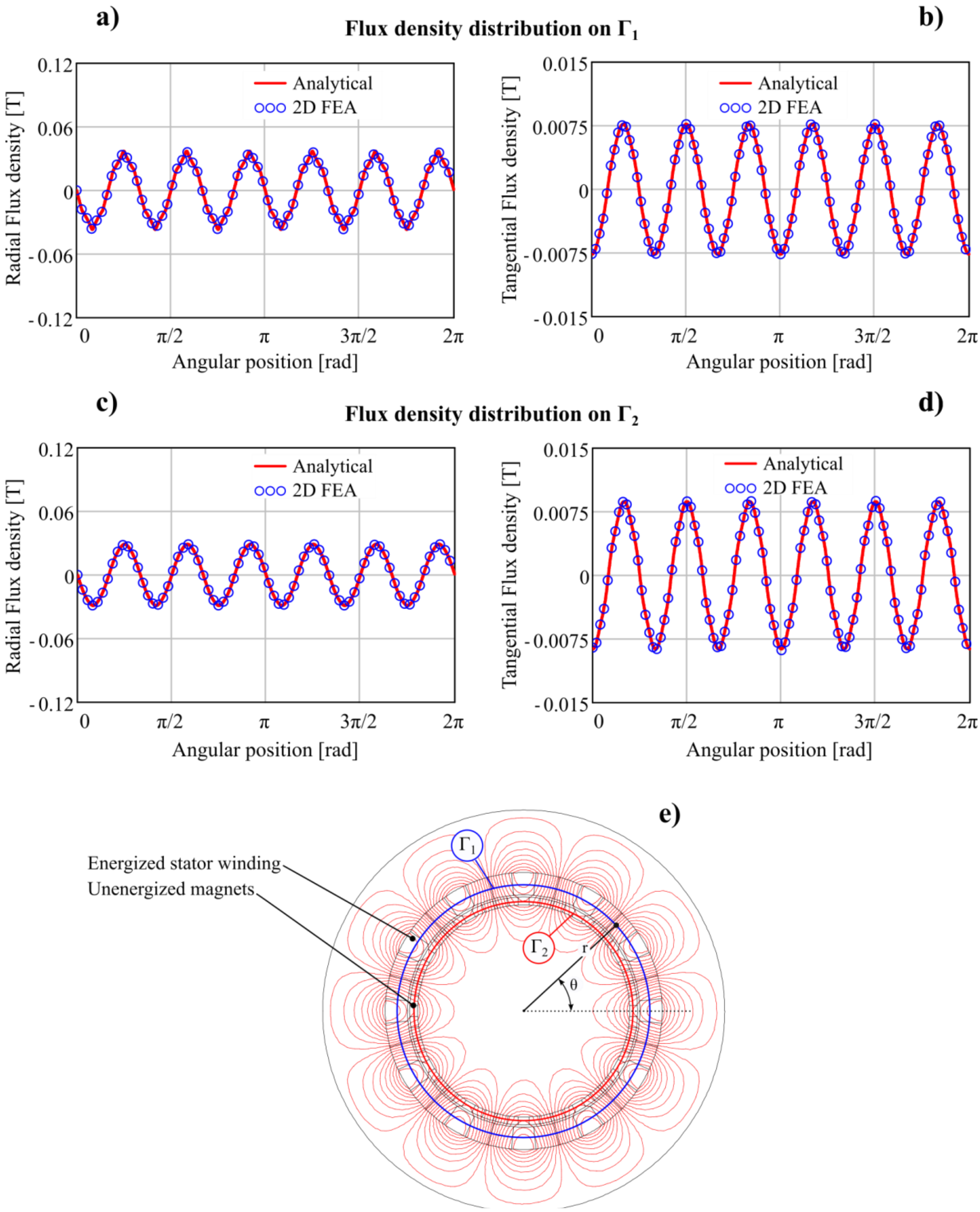

Figure 30: Flux density plot comparison between analytical computation and FEA in a twelve-pole machine

2.2.2.2 *Modeling of permanent magnets as equivalent surface current distributions*

As mentioned above, all the magnetization patterns under study can be reduced to set of elementary permanent magnet blocks with uniform parallel magnetization. In Figure 31a the basic parallel magnetized block with all the geometrical characteristics is represented.

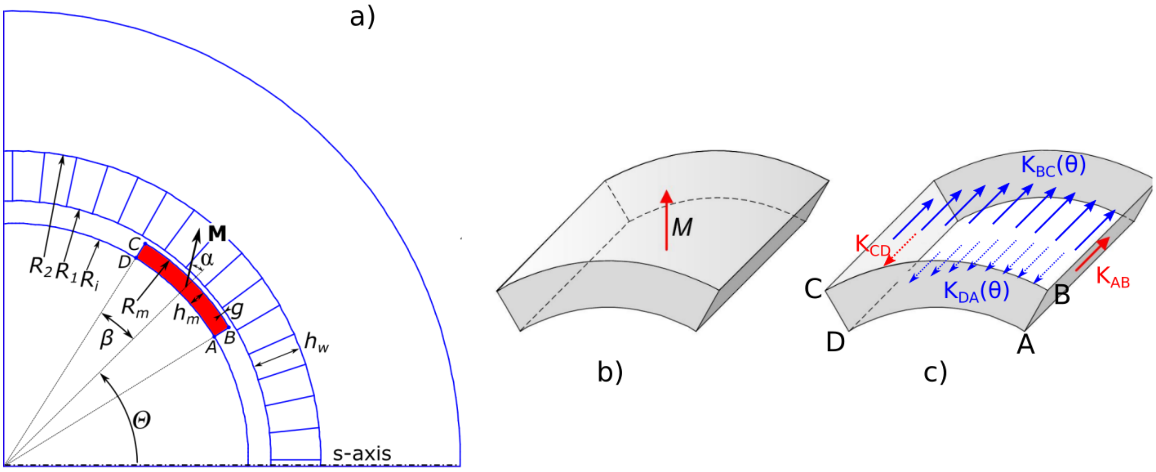

Figure 31: Parallel magnetized magnet block representation b), c) Example of radial magnetized magnet modeled with surface current distribution

The effects of this uniform magnetization are the same as those produced by a suitable current density flowing in the axial direction and distributed over the magnet block external surface (Figure 31b and c) and defined by the current density vector **K** such that:

$$\mathbf{K} = \mathbf{M} \times \hat{\mathbf{n}} \qquad 2.32$$

where $\hat{\boldsymbol{n}}$ is the unity vector locally orthogonal to the magnet surface and pointing outwards. The value of the linear current density can be computed as the projection of $\mathbf{K}$ along the axial direction. Therefore, along the straight magnet block sides AB and CD (Figure 31a), the linear current density is respectively given by:

$$K_{AB}(\alpha) = (\mathbf{M} \times \hat{\mathbf{n}}) \cdot \hat{\mathbf{u}}_z = -M \sin\left(\tfrac{\pi}{2} + \alpha + \beta\right) = -M \cos(\alpha + \beta) \qquad 2.33$$

$$K_{DC}(\alpha) = (\mathbf{M} \times \hat{\mathbf{n}}) \cdot \hat{\mathbf{u}}_z = M \sin\left(\tfrac{\pi}{2} - \gamma\right) = M \cos\gamma = M \cos(\alpha - \beta) \qquad 2.34$$

as illustrated in Figure 32 where $\gamma = \alpha - \beta$ and $\widehat{\boldsymbol{u}_z}$ is the unity vector along the axial direction.

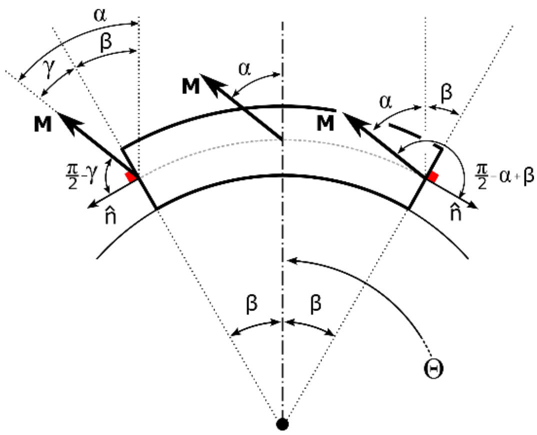

Figure 32: Schematic illustrating the computation of the equivalent surface current densities $\boldsymbol{K}_{AB}$ and $\boldsymbol{K}_{DC}$ along the straight sides AB and DC of a permanent magnet block

Similarly, along the arcs AD and BC (Figure 31a), at a generic angular position θ, the equivalent current density is respectively given by:

$$K_{AD}(\theta,\Theta,\alpha) = (\mathbf{M}\times\hat{\mathbf{n}})\cdot\hat{\mathbf{u}}_z = M\sin(\pi-(\alpha-\delta)) = M\sin(\alpha-\delta) = M\sin(\alpha-\theta+\Theta) \quad 2.35$$

$$K_{BC}(\theta,\Theta,\alpha) = (\mathbf{M}\times\hat{\mathbf{n}})\cdot\hat{\mathbf{u}}_z = -M\sin(\alpha-\delta) = -M\sin(\alpha-\theta+\Theta) \quad 2.36$$

as illustrated in Figure 33 where $\delta = \theta - \Theta$.

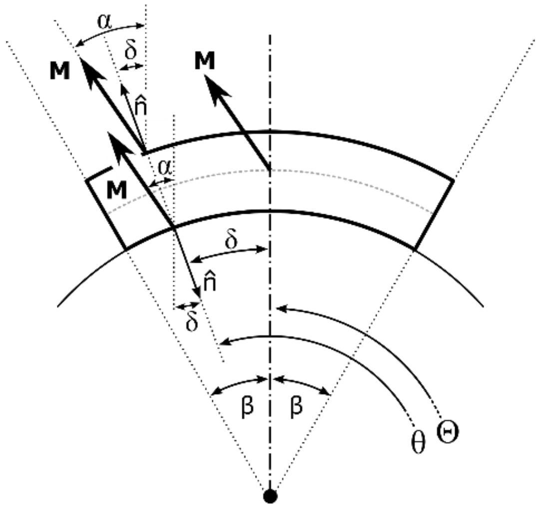

Figure 33: Schematic illustrating the computation of the equivalent surface current densities $\mathbf{K}_{BC}$ and $\mathbf{K}_{AD}$ along the arcs BC and AD of a permanent magnet block.

In both Figure 32 and Figure 33 the angle α represents the angle between the magnetization vector **M** and the magnet block axis.

2.2.2.3 Computation of the torque due to a single magnet block

The procedure for computing the overall torque starts from the evaluation of the torque due to a generic parallel-magnetized block with its axis placed at $\theta = \Theta$ (Figure 31a). Then the torque contributions of all the blocks will be summed up using the superposition principle.

At instant t, the block placed at position Θ and having the magnetization displaced by an angle α with respect to its axis contributes with the torque T_{block} given by:

$$T_{block}(\Theta,\alpha,t) = T_{AB}(\Theta,\alpha,t) + T_{DC}(\Theta,\alpha,t) + T_{AD}(\Theta,\alpha,t) + T_{BC}(\Theta,\alpha,t) \quad 2.37$$

where the four terms in the right-hand side member can be written using the Lorentz force definition (1.57) particularized to the model under study:

$$T_{AB}(\Theta,\alpha,t) = L\int_{R_i}^{R_m} r\, K_{AB}(\alpha)\, B_{mr}(r,\Theta-\beta,t)dr \quad 2.38$$

$$T_{DC}(\Theta,\alpha,t) = L\int_{R_i}^{R_m} r\, K_{DC}(\alpha)\, B_{mr}(r,\Theta+\beta,t)dr \quad 2.39$$

$$T_{BC}(\Theta,\alpha,t) = L\, R_m^{\ 2}\int_{\Theta-\beta}^{\Theta+\beta} K_{BC}(\theta,\alpha)\, B_{mr}(R_m,\theta,t)d\theta \quad 2.40$$

$$T_{AD}(\Theta,\alpha,t)=L\,R_i^{\,2}\int_{\Theta-\beta}^{\Theta+\beta}K_{AD}(\theta,\alpha)\,B_{mr}(R_i,\theta,t)d\theta \qquad 2.41$$

with L indicating the stack length.

The four terms account for the interaction of the air-gap flux density (due to the stator currents) with the equivalent current density, flowing in the axial direction and distributed along magnet block surface portions AB, DC, CB and AD, respectively. This equivalent current interacts with both $B_{m\theta}$ and B_{mr}, but the interaction with $B_{m\theta}$ results in a radial force which does not contribute to the torque. This is why only the radial flux density component B_{mr} appears in the integrals (2.38-2.41). By substituting (2.33), (2.34) and (2.29) into (2.38) and (2.39) and summing the two latter equations we obtain:

$$T_{AB}(\Theta,\alpha,t)+T_{DC}(\Theta,\alpha,t)=\sum_{\substack{k=5p,\,11p,\,17p,\,\ldots\\ h=p,\,7p,\,13p,\,\ldots}}\left[\tau'_k(\Theta,\alpha,t)+\tau'_h(\Theta,\alpha,-t)\right] \qquad 2.42$$

where the functions τ'_n for any integer n are:

$$\tau'_n(\Theta,\alpha,t)=\begin{cases}\sum\limits_{s\in\{-1,1\}}u_{n,s}(\Theta,\alpha,t)U_n & \text{if } n\neq 2\\ \sum\limits_{s\in\{-1,1\}}u_{2,s}(\Theta,\alpha,t)U^* & \text{if } n=2\end{cases} \qquad 2.43$$

having posed:

$$u_{n,s}(\Theta,\alpha,t)=\frac{L\,M\,n\cos(\alpha+s\beta)\sin(n\Theta-s\beta n+\omega t)}{R_m^{\,n-1}}\cdot \\ \cdot\left[2R_i^{\,n+1}R_m^{\,n-1}-R_m^{\,2n}(1-n)-R_i^{\,2n}(1+n)\right] \qquad 2.44$$

$$U_n=\frac{(n^2-4)\left(W_n^-+R_1^{\,2n}W_n^+\right)+R_1^{\,n+2}\mu_0 J_n}{\left(R_1^{\,2n}+R_i^{\,2n}\right)\left(n^4-5n^2+4\right)}, \qquad 2.45$$

$$U^*=\frac{\mu_0 J_2\left[4R_2^{\,4}\ln(R_2/R_1)+R_2^{\,4}-R_1^{\,4}\right]}{48\left(R_2^{\,4}-R_i^{\,4}\right)}. \qquad 2.46$$

It can be proven that the quantities U_n and U^*expressed in (2.45) and (2.46) are linked by the following relationship:

$$U^*=\lim_{n\to 2}U_n \qquad 2.47$$

From a physical point of view, $\tau'_k(\Theta,\alpha,t)$ are the harmonic torque components resulting from the interaction between the equivalent current densities along AB and CD and the armature reaction space harmonics with k=5p, 11p, 17p, etc. pole pairs, which revolve in the opposite direction with respect to the rotor. Similarly, $\tau'_h(\Theta,\alpha,-t)$ are the harmonic torque components resulting from the interaction between the equivalent current densities along AB and CD and the armature reaction space harmonics with h=1p, 7p, 13p, etc. pole pairs, which revolve in the same direction as the rotor.

Similarly, to what has been done with T_{AB} and T_{DC}, we can substitute (2.35), (2.36) and (2.29) into (2.40), (2.41) and, summing the two latter contributions, we can find:

$$T_{AD}(\Theta,\alpha,t)+T_{BC}(\Theta,\alpha,t)=\sum_{\substack{k=5p,11p,17p,\ldots\\ h=p,7p,13p,\ldots}}\left[\tau''_k(\Theta,\alpha,t)+\tau''_h(\Theta,\alpha,-t)\right] \tag{2.48}$$

where the functions τ''_n for any integer n are:

$$\tau''_n(\Theta,\alpha,t)=\begin{cases}\sum_{s\in\{-1,1\}} v_{n,s}(\Theta,\alpha,t)V_n & \text{if } n\neq 2\\ \sum_{s\in\{-1,1\}} v_{2,s}(\Theta,\alpha,t)V^* & \text{if } n=2\end{cases} \tag{2.49}$$

having posed:

$$v_{n,s}(\Theta,\alpha,t)=sLM\,\frac{\sin(\beta(n-s))\cos(\omega t+s\alpha+n\Theta)}{n-s} \tag{2.50}$$

$$V_n=\sum_{q\in\{-1,1\}}\frac{-qn\left[R_i^{\,2n}+\rho_q^{\,2n}\right]\left[(n^2-4)(W_n^-+R_1^{\,2n}W_n^+)+R_1^{\,n+2}\mu_0 J_n\right]}{\rho_q^{\,n-1}(R_1^{\,2n}+R_i^{\,2n})(n^2-4)} \tag{2.51}$$

$$V^*=\sum_{q\in\{-1,1\}}\frac{-q\mu_0(R_i^{\,4}-\rho_q^{\,4})J_2(4R_2^{\,4}\ln(R_1/R_2)+R_1^{\,4}-R_2^{\,4})}{8\rho_q(R_i^{\,4}-R_2^{\,4})} \tag{2.52}$$

$$\rho_q=\tfrac{1}{2}\left[(R_m+R_i)+q(R_m-R_i)\right] \tag{2.53}$$

It can be also proven that:

$$V^*=\lim_{n\to 2}V_n \tag{2.54}$$

From a physical viewpoint, $\tau''_k(\Theta,\alpha,t)$ are the harmonic torque components resulting from the interaction between the equivalent current densities along AD and BC and the armature reaction space harmonics with k=5p, 11p, 17p, etc. pole pairs, which revolve in the opposite direction with respect to the rotor. Similarly, $\tau''_h(\Theta,\alpha,t)$ are the harmonic torque components resulting from the interaction between the equivalent current densities along AB and CD and the armature reaction space harmonics with h=1p, 7p, 13p, etc. pole pairs, which revolve in the same direction as the rotor.

Equation (2.37), whose explicit expression is detailed by (2.42) and (2.48), gives the torque acting on a single parallel-magnetized magnet block including all the harmonics (of orders p, 5 p, 7 p, 11 p, 13 p, etc.) due to the armature reaction fields. If we take only the fundamental of the armature reaction field (corresponding to the space harmonic of order p) and neglect higher order harmonics, the sum of (2.42) and (2.48) gives:

$$\overline{T}_{block}(\Theta,\alpha,t)=\tau'_p(\Theta,\alpha,-t)+\tau''_p(\Theta,\alpha,-t) \tag{2.55}$$

which represents the average torque component provided that the rotor (and hence each single magnet block) revolves synchronously with the armature reaction field, i.e. at an electrical speed equal to the stator angular frequency ω.

The explicit expressions derived in this section for the torque acting on a single permanent magnet block will be used in the next chapter to obtain the overall torque for the various rotor magnetization patterns.

2.2.2.4 Torque expression for parallel magnetization

In this subsection, the case of a rotor with one parallel-magnetized permanent magnet block per pole is addressed. The parameter β in this case is given by:

$$\beta = (\frac{\pi}{2p} \cdot s_m) \qquad 2.56$$

where s_m is the permanent magnet span over the pole pitch ratio. The rotor arrangement includes $2p$ parallel-magnetized permanent magnet blocks. The position of the m^{th} block (for m between 0 and $2p$−1) is given by:

$$\Theta = \theta_r + m\frac{\pi}{p} \qquad 2.57$$

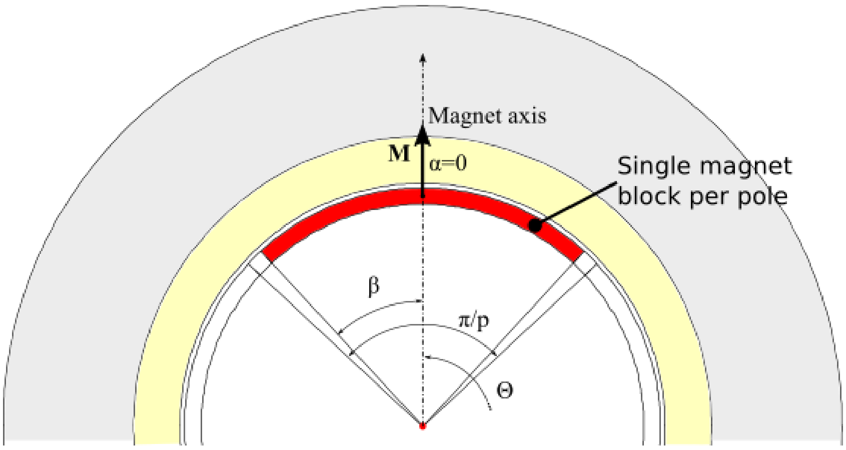

Figure 34: Four poles SPM machine with single block parallel magnetization pattern

Assuming synchronous operation, the rotor position θ_r in mechanical radians is related to the time t as follows:

$$\theta_r = (\omega t + \psi)/p \quad \Rightarrow \quad t = (p\theta_r - \psi)/\omega \qquad 2.58$$

where ψ is the initial rotor position in electrical radians for $t = 0$ with respect to the angular reference that coincides with the *s* axis (Figure 35b).

It is noted that, based on stator phase current definition (2.2), the *s* axis identifies the air gap point where the armature reaction field is zero (Figure 35). Hence, if $\psi = 0$ means that the rotor is in quadrature with the armature reaction field and this represents the operating condition where the maximum possible torque is achieved for an SPM machine.

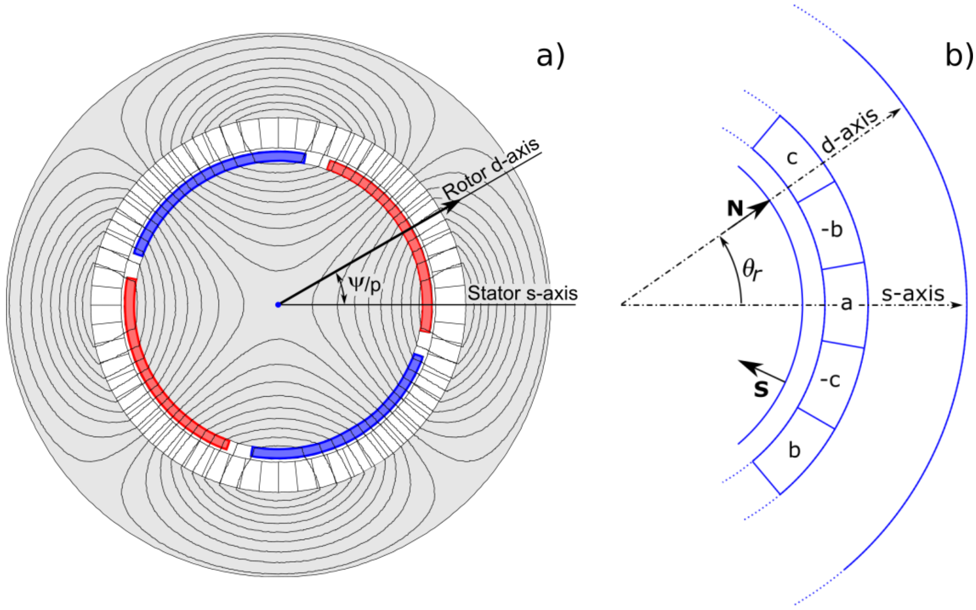

Figure 35:Example of the armature reaction field lines at t=0 and initial rotor position ψ/p. The stator s axis identifies the air-gap point where the armature reaction field is zero

The torque as a function of the rotor position angle can be found by summing all the contributions of the $2p$ magnet blocks given by (2.37), considering that: their position Θ is given by (2.57); $\alpha = 0$ for all of them; the time is given by (2.58). These conditions yield:

$$\mathrm{T}_{par}(\theta_r) = \sum_{m=0}^{2p-1} (-1)^m \, \mathrm{T}_{block}\left(\theta_r + \frac{m\pi}{p}, 0, \frac{p\theta_r - \psi}{\omega}\right) \qquad 2.59$$

With identical considerations, the average torque is obtained from (2.47) as follows:

$$\overline{\mathrm{T}}_{par} = \sum_{m=0}^{2p-1} (-1)^m \, \overline{\mathrm{T}}_{block}\left(\theta_r + \frac{m\pi}{p}, 0, \frac{p\theta_r - \psi}{\omega}\right) \qquad 2.60$$

2.2.2.5 *Torque expression for radial magnetization with segmented magnets*

In this subsection, the rotor arrangement shown in Figure 36 is addressed. In this arrangement, each pole encompasses N_{bp} parallel-magnetized blocks. Calling again s_m the overall magnet to pole pitch ratio, the parameter β is given by:

$$\beta = \frac{\pi}{2pN_{bp}} s_m \tag{2.61}$$

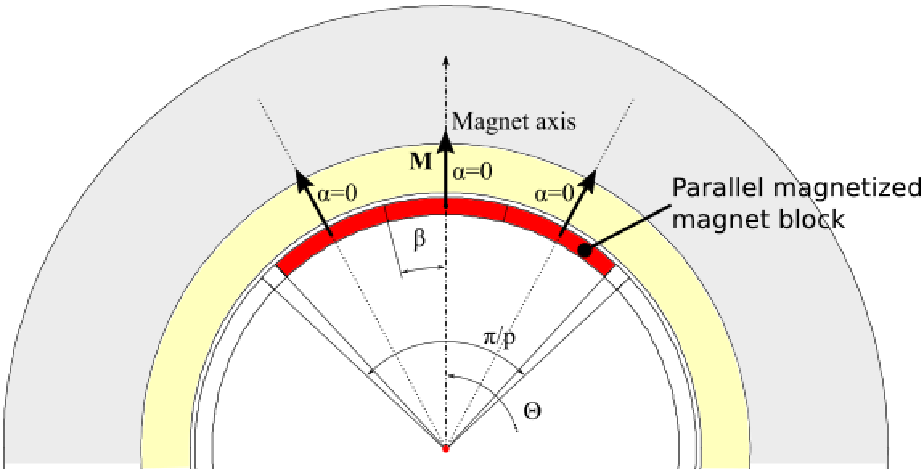

Figure 36: Four poles SPM machine with three parallel magnetized blocks per pole

The torque expression is obtained summing both over the poles (index m ranging between 0 and 2p−1) and over the blocks per pole (index b ranging between 0 and N_{bp}−1) and considering that the b^{th} block in the m^{th} pole is placed at an angular position:

$$\Theta = \theta_r + \frac{m\pi}{p} + \left(1 - N_{bp} + 2b\right)\beta \tag{2.62}$$

The overall torque is therefore obtained as:

$$T_{seg}(\theta) = \sum_{m=0}^{2p-1} \sum_{b=0}^{N_{bp}-1} (-1)^m T_{block}\left(\theta_r + \frac{m\pi}{p} + \left(1 - N_{bp} + 2b\right)\beta, 0, \frac{p\theta_r - \psi}{\omega}\right) \tag{2.63}$$

and the mean component is:

$$\overline{T}_{seg} = \sum_{m=0}^{2p-1} \sum_{b=0}^{N_{bp}} (-1)^m \overline{T}_{block}\left(\theta_r + \frac{m\pi}{p} + \left(1 - N_{bp} + 2b\right)\beta, 0, \frac{p\theta_r - \psi}{\omega}\right) \tag{2.64}$$

2.2.2.6 *Torque expression for Halbach magnetization pattern*

This subsection addresses the case of a discrete Halbach magnetization pattern (Figure 37) characterized by N_{bp} blocks per pole. The rotor then includes $2pN_{bp}$ parallel-magnetized blocks, each having a span 2β with:

$$\beta = \frac{\pi}{2pN_{bp}} \tag{2.65}$$

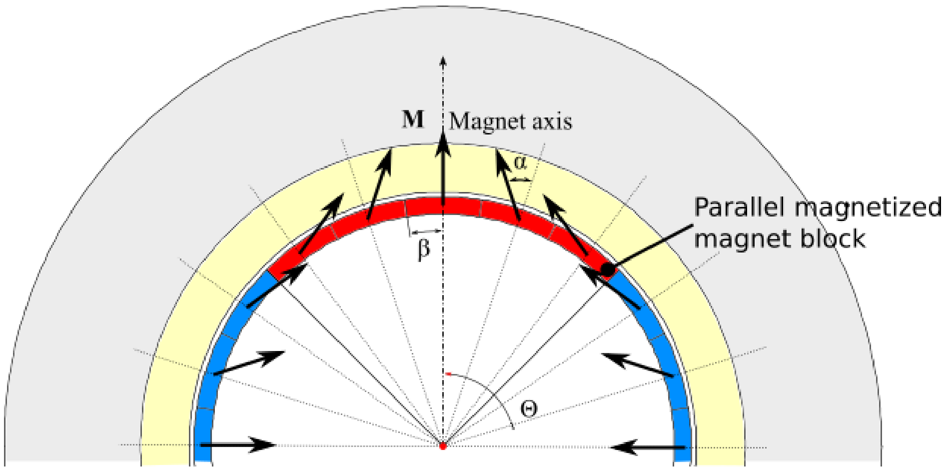

Figure 37: Four poles SPM machine with three parallel magnetized blocks per pole Halbach array

The position of the b_{th} block (with b ranging from 0 to $2pN_{bp0}$) is:

$$\Theta = \theta_r + 2b\beta \tag{2.66}$$

and the direction of its magnetization with respect to its symmetry axis is:

$$\alpha = 2pb\beta \tag{2.67}$$

Using (2.58), (2.66), (2.67) in (2.37) and (2.55) and summing over all the blocks finally gives the overall torque:

$$\mathrm{T}_{hal}(\theta) = \sum_{b=0}^{2pN_{bp}-1} \mathrm{T}_{block}\left(\theta_r + 2b\beta, 2pb\beta, \frac{p\theta_r - \psi}{\omega}\right) \tag{2.68}$$

Its mean component is:

$$\overline{\mathrm{T}}_{hal} = \sum_{b=0}^{2pN_{bp}-1} \overline{\mathrm{T}}_{block}\left(\theta_r + 2b\beta, 2pb\beta, \frac{p\theta_r - \psi}{\omega}\right) \tag{2.69}$$

2.2.2.7 Torque expression for Continuous radial magnetization pattern

In this chapter the explicit analytical torque expression for the continuous radial magnetization pattern is given for the sake of completeness. The detailed procedure to obtain this feature is omitted as it has been already addressed in [2]. The overall torque T_{rad} as a function of the rotor position θ_r results from summing the average constant value $\overline{T}_{rad}$ and the variable component T_{harm} due to the space harmonics in the armature reaction field:

$$T_{rad}(\theta_r) = \overline{T}_{rad} + T_{harm}(\theta_r) \qquad 2.70$$

The two torque components $\overline{T}_{rad}$ and T_{harm} can be expressed as follows:

$$\overline{T}_{rad} = 4p^2 ML \sin(\pi s_m/2)\cos(\psi) F_p \qquad 2.71$$

$$T_{harm}(\theta) = 2p^2 ML \left[\begin{array}{l} \displaystyle\sum_{\substack{k=5p,11p\ldots \\ s\in\{-1,1\}}} \frac{sk}{p} F_k \sin\left(\theta(k+p) + s\frac{\pi k s_m}{2p} - \psi \right) + \\ \displaystyle\sum_{\substack{h=p,7p\ldots \\ s\in\{-1,1\}}} \frac{sh}{p} F_h \sin\left(\theta(h-p) + s\frac{\pi h s_m}{2p} - \psi \right) \end{array} \right] \qquad 2.72$$

where s_m is the permanent magnet over pole span ratio, Ψ defines the rotor position for *t*=0 as explained in 2.58 , **M** is the magnetization vector magnitude, *p* is the number of pole pairs and the functions F_n for any integer n are defined as follows:

$$F_n = \begin{cases} M_n^+ (R_m^2 - R_i^2) + M_n^- \ln\left(\dfrac{R_m}{R_i}\right) & \text{if } n = 1 \\ \mu_0 J_2 \left(2R_i^3 R_m - 3R_i^4 + R_m^4\right)\left(4R_2^4 \ln\left(\dfrac{R_1}{R_2}\right) + R_1^4 - R_2^4\right) & \text{if } n = 2 \\ \dfrac{M_n^+ (R_m^{1+n} - R_i^{1+n})}{1+n} + \dfrac{M_n^- (R_m^{1-n} - R_i^{1-n})}{1-n} & \text{otherwise} \end{cases} \qquad 2.73$$

The parameters M_n^+ and M_n^- are defined according to (2.26-2.27).

2.2.3 FEA ASSESSMENT FOR THE TORQUE COMPUTATION

2.2.3.1 FEA assessments for parallel, radial segmented and halbach magnetization

The explicit torque expressions found in Section 2.2.2 are hereinafter assessed against FEA simulations. Two case studies are taken into account, including a 4-pole machine and a 12-pole machine having the geometric data given in Table IV. For both machines the three design versions respectively featuring a parallel, radial segmented and Halbach magnetization of the rotor are taken into account. Simulations are performed assuming synchronous operation in the maximum torque condition, occurring when the rotor is in quadrature with the armature reaction field, i.e. $\psi = 0$ (2.58). The comparison between analytical and FEA results for the 4-pole and the 12-pole machines and for the three magnetization patterns are shown in Figure 38 and in Figure 39. The diagrams show a good agreement between FEA and analytical results. In particular, Figure 38d and Figure 39d show that, for both the 4-pole and the 12-pole machines, the parallel magnetization of the rotor leads to lower torque values than the radial segmented one. Conversely, the Halbach magnetization pattern leads to a lower torque than the other patterns in the 4-pole machine while for the 12-pole machine it is the rotor arrangement leading to the maximum torque.

This is not the place where to investigate the physical reasons for the different behavior found for the various magnetization patterns in terms of maximum torque. However, it should be clear that having a fully analytical tool to rapidly compute the torque for any machine design (including the permanent magnet segmentations into multiple magnet units) can be of help to compare various design alternatives, possibly leading to unexpected results.

Table IV: Geometric ad electrical data of the (4-pole and 12-pole) machines used for FEA simulations

Permanent magnet coercivity	850 kA
Permanent magnet relative permeability	1.04
Stator maximum current density	4 A/mm^2
Winding fill factor k_{fill}	1
R_i	47.5 mm
R_2	62 mm
g	1 mm
h_m	10.5 mm
h_w	3 mm
L	80 mm
s_m for parallel and radial magnetization	0.95
N_{bp} for parallel magnetization	1
N_{bp} for radial magnetization	3
N_{bp} for Halbach magnetization	15

To quantify the computational advantage of the proposed analytical approach compared to FEA, the torque calculation for the four-pole machine, whose data are given in Table IV, is performed on the same computer (processor: Intel Core i5, clock frequency: 3.1 GHz; RAM size: 4Gb) using the proposed analytical formulas and FEA, with the same rotor position and stator current values. The analytical formulas are implemented in the Mathcad© (version 15) environment; the FEA is performed in the FEMM© (version 4.2) environment with an optimized number of mesh nodes equal to 81.000. The comparison between the times required by the calculation with the two methods is given in Table V. In addition to the faster computation time, the analytical procedure obviously leads to the advantage that the geometric model of the machine (required for FEA) does not need to be prepared. Finally, it is observed that the calculation time reduction (Table V) obtained with the analytical approach acquires a significant importance when the computation is to be performed several times, for example to plot the torque waveforms shown in Figure 38 and Figure 39, or in the case of machine design optimization through automated tools based on genetic algorithms.

Table V: Comparison of torque computation times with fea and analytical techniques

Method	**Tool**	**Computation time**
FEA	FEMM© v.4.2	1 m
Analytical	Mathcad© v.15	0.5 s

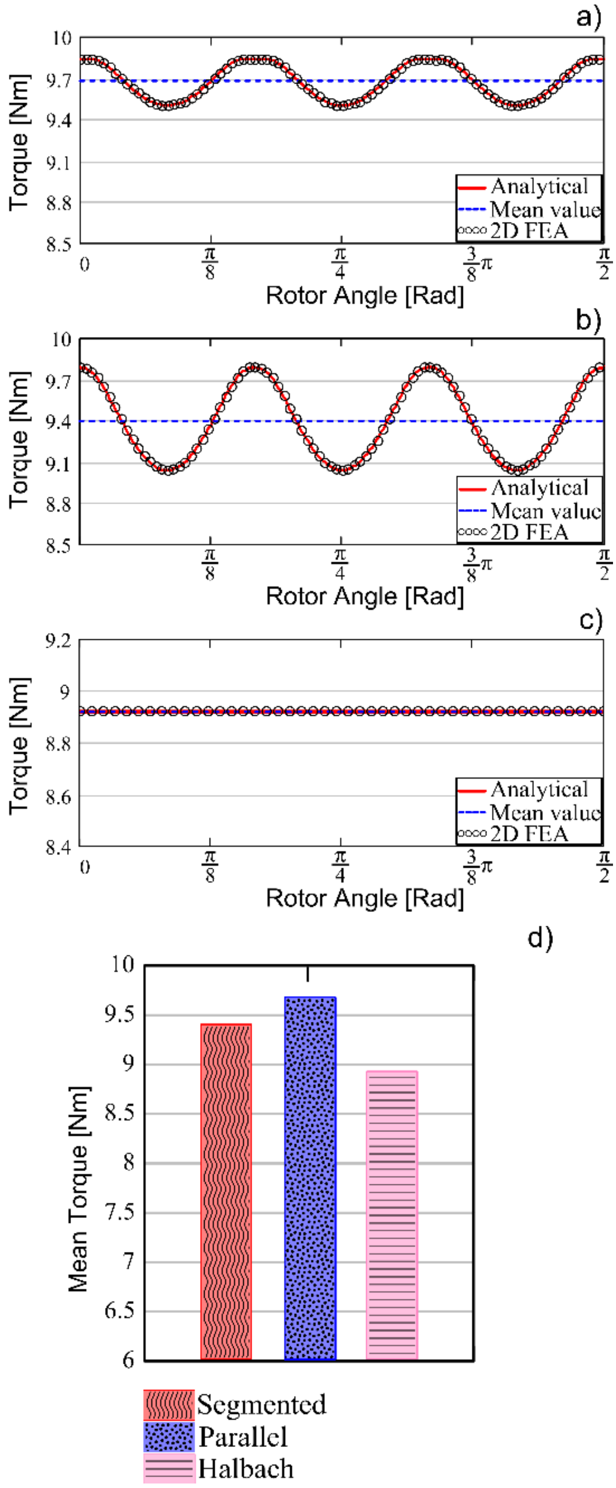

Figure 38: Torque waveforms and average value for the 4-poles machine with a) parallel magnetization b) radial segmented magnetization c) Halbach magnetization d) comparison of the average torques obtained

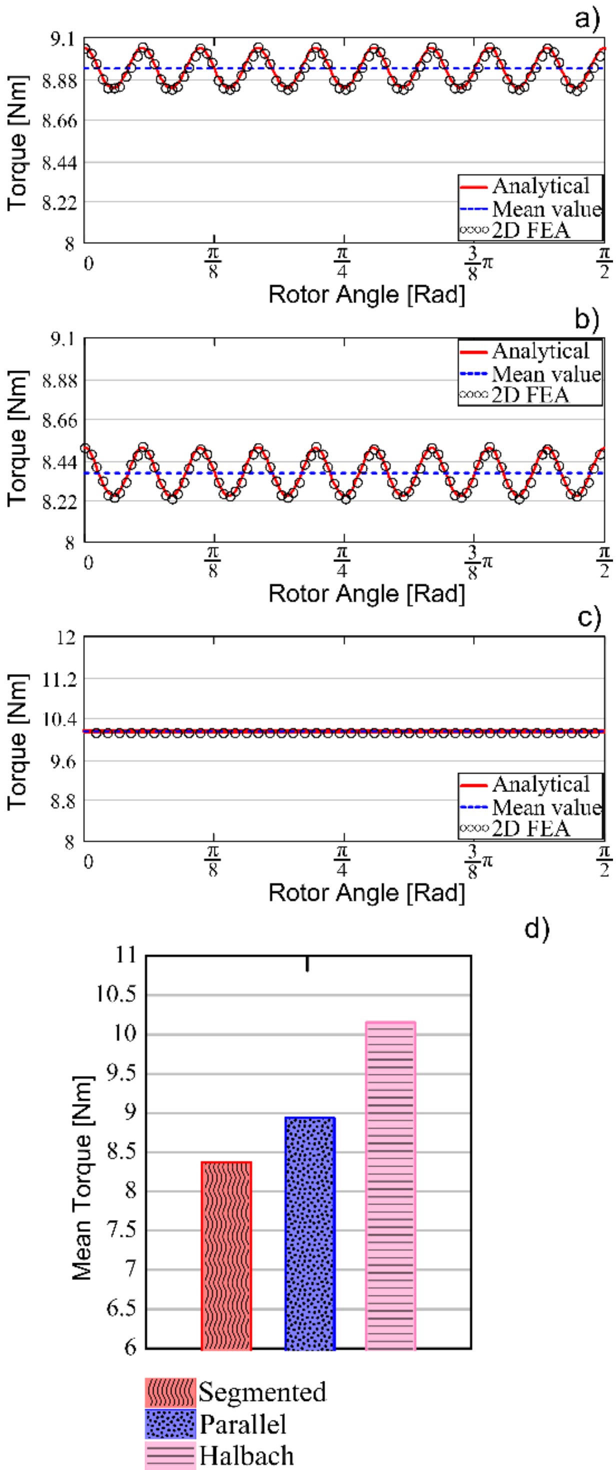

Figure 39: Torque waveforms and average value for the 12-poles machine with a) parallel magnetization b) radial segmented magnetization c) Halbach magnetization d) comparison of the average torques obtained

2.2.3.2 FEA assessments for continuous radial magnetization

As a numerical validation of (2.70), a comparison is made between the instantaneous torque values computed through such formulas and by FE analysis on the sample machines with characteristic data given in Table IV (again 4 and 12 poles machines). The FEA simulation is performed through successive magnetostatic analyses where the rotor is moved in synchronism with stator currents and with the *d* axis in quadrature with the stator field. The comparison, shown in Figure 40, highlights again that, with the proposed approach, the instantaneous torque can be very accurately predicted.

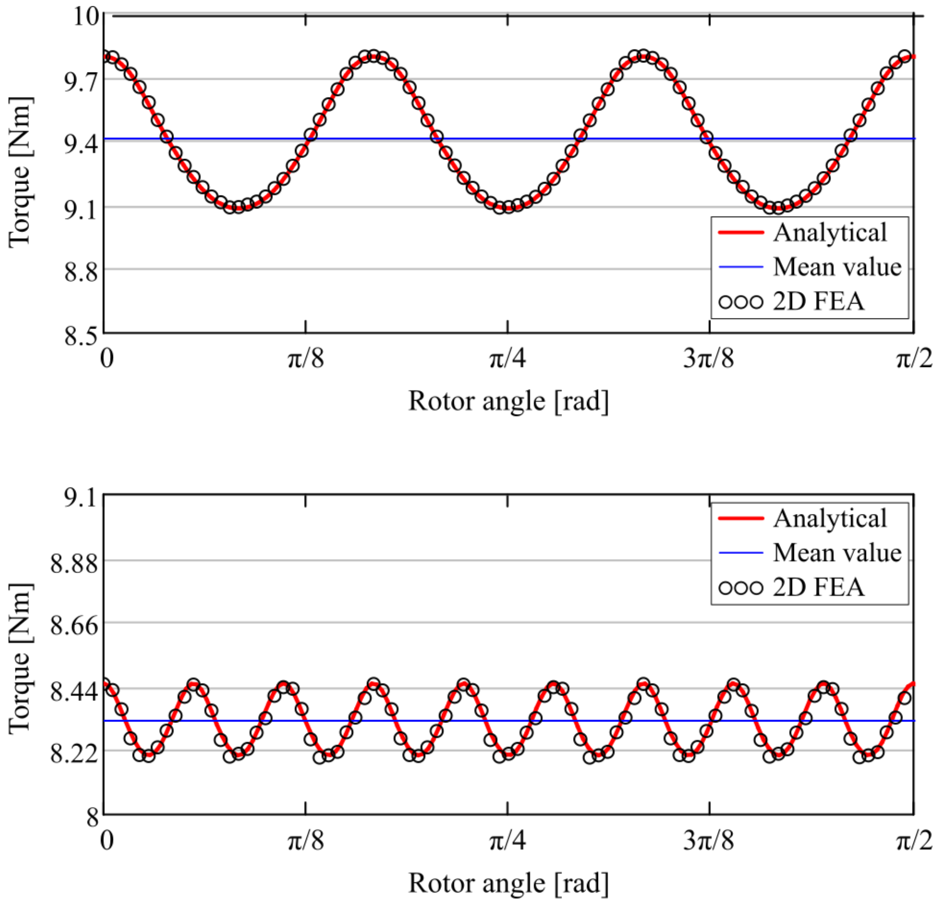

Figure 40: Torque waveforms and average value for the 12-poles machine with continuous radial magnetized magnets

Also the machine model with continuous radial magnetized permanent magnets proposed in [2] can be therefore used as a fast computationally efficient alternative to FE analysis. The diagram in Figure 40 also clarifies how the non-sinusoidal stator winding distribution, although in presence of sinusoidal current versus-time waveform, gives rise to a non-negligible torque ripple amplitude.

As a concluding remark, it is observed that the torque distribution evaluated with 2.70 and shown in Figure 40 is almost the same as the one evaluated with 2.63 for the segmented radial magnetization pattern. This result confirms the fact that the continuous radial magnetization is well represented using also parallel magnetized blocks (in this case we have 3 magnet blocks per pole).

2.2.4 COMPUTATION OF THE MACHINE BACK-EMF

In this section, the same approach used in 2.2.2 to compute the output torque, is applied to obtain explicit analytical formulas for the no-load back-EMF.

For this purpose, it is observed that, according to all the magnetization patterns taken into account (Figure 15), the rotor permanent magnets are composed of uniformly-magnetized blocks. To facilitate computations, let us consider a set of $2p$ magnet blocks displaced by π/p mechanical radians apart (Figure 41), i.e. with their axes placed at the angular positions:

$$\Theta + m\frac{\pi}{p} \tag{2.74}$$

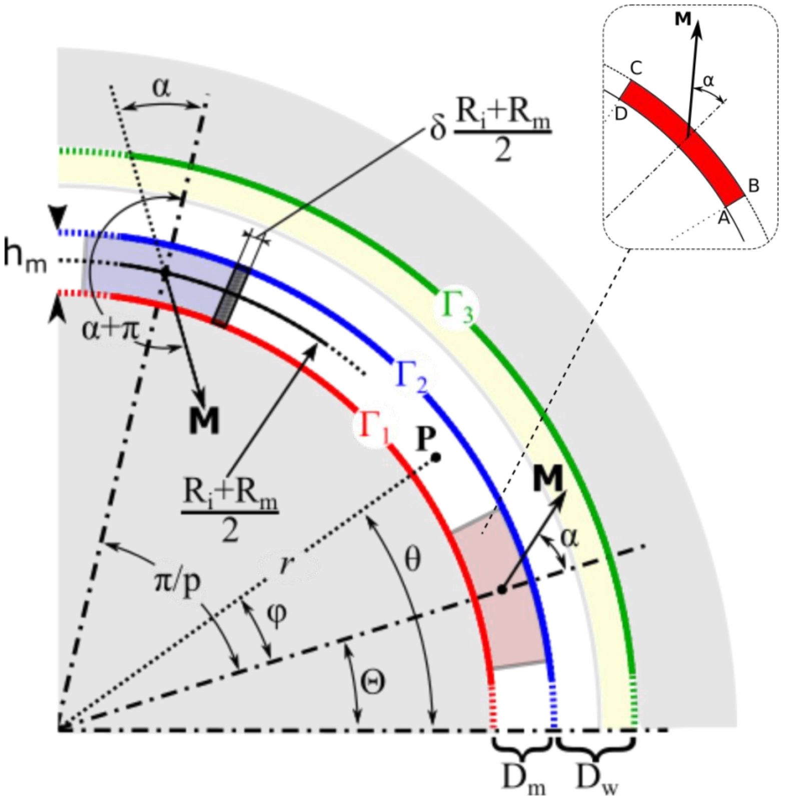

Figure 41: Two magnet blocks displaced by one pole pitch. The set of 2p magnet blocks displaced by π/p mechanical radians around the rotor surface is referred to as a "group" of magnet blocks.

where $m = 0, 1, \dots\ 2p - 1$ and Θ is the position of the first block of the set. Let us call this set of $2p$ blocks "a group".

As it can be argued from Figure 15, regardless of the magnetization pattern the magnetization vectors of magnet blocks displaced by π/p mechanical radians are shifted by 180° (Figure 41). So, calling α the magnetization angle (with respect to the magnet block axis) of the first magnet block (that placed at $\Theta = \theta$), the m^{th} block of the group will have its magnetization placed at $\alpha + m\pi$ radians with respect to its axis, with $m = 0, 1, \dots, 2p - 1$.

For the sake of convenience, we shall also introduce a new angular coordinate φ measured from the axis of the first block of the group to a generic point *P* (Figure 41). So, this point *P* will be identified with the couple of polar coordinates (r, φ) being:

$$\varphi = \theta - \Theta \qquad 2.75$$

The first step to evaluate the entire machine back-emf is to evaluate the vector potential distribution $\Phi(r,\theta)$ due to a "group" of magnets.

2.2.4.1 Vector potential distribution due to a group of magnet blocks

The vector potential $\Phi(r,\theta)$ produced by a group of permanent magnet blocks can be written as:

$$\Phi(r,\varphi) = \begin{cases} \Phi_m(r,\varphi) & \text{if } R_i < r < R_m \\ \Phi_w(r,\varphi) & \text{if } R_m < r < R_2 \end{cases} \qquad 2.76$$

where $\Phi_m(r,\theta)$ is the vector potential in the permanent magnet region (subdomain D_m in Figure 41) and $\Phi_w(r,\theta)$ is the vector potential in the rest of the magnetic air-gap region (subdomain D_w in Figure 41), which, in particular, includes the stator windings. These two functions must satisfy the following elliptic equations:

$$\nabla \Phi_m = \frac{1}{r}\frac{\partial}{\partial r}\left(r\frac{\partial \Phi_m}{\partial r}\right) + \frac{1}{r^2}\frac{\partial^2 \Phi_m}{\partial^2 \varphi} = j(\varphi,\alpha) \qquad 2.77$$

$$\nabla \Phi_w = \frac{1}{r}\frac{\partial}{\partial r}\left(r\frac{\partial \Phi_w}{\partial r}\right) + \frac{1}{r^2}\frac{\partial^2 \Phi_w}{\partial^2 \varphi} = 0 \qquad 2.78$$

where $j(\varphi,\alpha)$ is the current density due to the equivalent currents (2.33, 2.34) distributed along the radial borders of the magnet blocks (segments AB and CD, Figure 31a). The equivalent currents densities (2.35, 2.36), distributed along the circumferential block borders (arcs AD and BC, Figure 31a) will be accounted for when setting the boundary conditions along the circumferences Γ_1 and Γ_2 (Figure 41) to solve (2.77 and 2.78).

Determination of the equivalent current density $j(\varphi,\alpha)$ in the permanent magnet region

To determine the current density function $j(\varphi,\alpha)$ in (2.77), we first assume that the radial magnet borders AB and CD of each magnet blocks (on which the linear current densities K_{AB} and K_{CD} given by (2.33, 2.34) are placed have a finite angular thickness δ in the circumferential direction (Figure 41). The segments AB and CD can be then approximated by rectangles of height h_m and width $\delta(R_i + R_m)/2$ as reported in Figure 41. In the rectangle around the segment AB a current equal to $h_m\, K_{AB}$ flows, so the current density in it will be:

$$J_{AB}(\alpha) = \frac{h_m K_{AB}(\alpha)}{h_m\,\delta\frac{R_i + R_m}{2}} = \frac{2K_{AB}(\alpha)}{\delta(R_i + R_m)} \qquad 2.79$$

Similarly, in the rectangle around the segment CD a current equal to $h_m\, K_{CD}$ flows, so the current density in it will be:

$$J_{CD}(\alpha) = \frac{h_m K_{CD}(\alpha)}{h_m\,\delta\frac{R_i + R_m}{2}} = \frac{2K_{CD}(\alpha)}{\delta(R_i + R_m)} \qquad 2.80$$

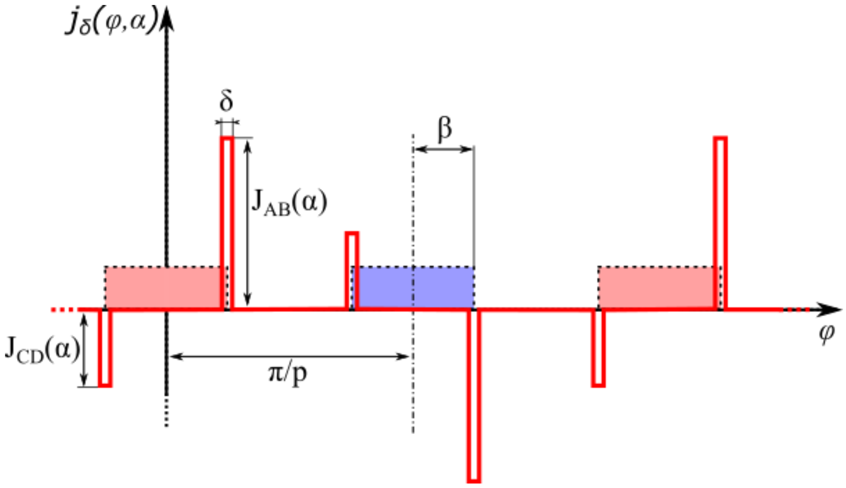

Figure 42: Current density, as a function of the angular coordinate φ, produced in the permanent magnet region by a group of magnet blocks displaced by π/p mechanical radians, under the hypothesis that the magnet blocks have radial borders (AB and CD) of finite thickness δ.

At this point, it is clear that a current density function $j_\delta(\varphi,\alpha)$ as plotted in Figure 42 can describe the current density distribution in the permanent magnet region ($R_i < r < R_m$). This function can be expressed in Fourier series as:

$$j_\delta(\varphi,\alpha) = \sum_{n=1,3,5,...} \frac{4}{n\pi} \sin\left(\frac{np\delta}{2}\right)\left[J_{AB}(\alpha)\cos(pn(\varphi-\beta)) + J_{CD}(\alpha)\cos(pn(\varphi+\beta))\right]$$
$$= \sum_{n=1,3,5..} \frac{8}{n\pi\delta(R_i+R_m)} \sin\left(\frac{np\delta}{2}\right)\left[K_{AB}(\alpha)\cos(pn(\varphi-\beta)) + K_{CD}(\alpha)\cos(pn(\varphi+\beta))\right] \tag{2.81}$$

To consider that segments AB and CD have infinitesimal thickness, we can now compute the limit of (2.81) for δ tending to zero, which gives:

$$j(\varphi,\alpha) = \lim_{\delta\to 0} j_\delta(\varphi,\alpha) =$$
$$\sum_{n=1,3,5...} \frac{4p}{\pi(R_i+R_m)}\left[K_{AB}(\alpha)\cos(pn(\varphi-\beta)) + K_{DC}(\alpha)\cos(pn(\varphi+\beta))\right] = \tag{2.82}$$
$$= \sum_{n=1,3,5...} \frac{4pM}{\pi(R_i+R_m)}\left[\cos(\alpha-\beta)\cos(pn(\varphi+\beta)) - \cos(\alpha+\beta)\cos(pn(\varphi-\beta))\right]$$

where the expressions (2.33, 2.34) for K_{AB} and K_{DC} have been used. We some algebraic manipulations, this can be put into the more convenient form:

$$j(\varphi,\alpha) = \sum_{n=1,3,5...} a_n(\alpha)\cos(np\varphi) + b_n(\alpha)\sin(np\varphi) \tag{2.83}$$

where:

$$a_n(\alpha) = \frac{4p}{\pi(R_i+R_m)}[K_{AB}(\alpha)+K_{DC}(\alpha)]\cos(np\beta)$$
$$= \frac{4pM}{\pi(R_i+R_m)}[\cos(\alpha-\beta)-\cos(\alpha+\beta)]\sin(np\beta) \qquad 2.84$$
$$= \frac{8pM}{\pi(R_i+R_m)}\sin(\alpha)\sin(\beta)\sin(np\beta)$$

and:

$$b_n(\alpha) = \frac{4p}{\pi(R_i+R_m)}[K_{AB}(\alpha)-K_{DC}(\alpha)]\sin(np\beta)$$
$$= -\frac{4pM}{\pi(R_i+R_m)}[\cos(\alpha-\beta)+\cos(\alpha+\beta)]\sin(np\beta) \qquad 2.85$$
$$= -\frac{8pM}{\pi(R_i+R_m)}\cos(\alpha)\cos(\beta)\sin(np\beta)$$

Expression of the equivalent current density along circumferences Γ_1 and Γ_2

The equivalent current density distributed along the straight magnet block borders (segments AB and CD, Figure 31) has been included in the function $j(\varphi,\alpha)$ as explained above. The linear current densities K_{AD} and K_{BC} given by (2.35, 2.36) and placed on the curved magnet block borders (arcs AD and BC, Figure 41) result in appropriate linear currents distributed along the circumferences Γ_1 and Γ_2. Analytically, the linear current distributions on Γ_1 and Γ_2 are respectively:

$$\lambda_1(\theta,\Theta,\alpha) = \sum_{m=0}^{2p-1}\left\{\mathrm{bool}\left(\Theta+m\tfrac{\pi}{p}-\beta\le\theta\le\Theta+m\tfrac{\pi}{p}+\beta\right)\times K_{AD}\left(\theta,\Theta+m\tfrac{\pi}{p},\alpha+m\pi\right)\right\} \qquad 2.86$$

and:

$$\lambda_2(\theta,\Theta,\alpha) = \sum_{m=0}^{2p-1}\left\{\mathrm{bool}\left(\Theta+m\tfrac{\pi}{p}-\beta\le\theta\le\Theta+m\tfrac{\pi}{p}+\beta\right)\times K_{BC}\left(\theta,\Theta+m\tfrac{\pi}{p},\alpha+m\pi\right)\right. \qquad 2.87$$

where bool (·) is, the Boolean function returning 1 or 0 depending on whether the argument is true or false, respectively; furthermore, in (2.87) the property has been used that magnet blocks displaced by π/p mechanical radians have their magnetization vectors rotated by 180°. Using the angular variable φ given by (2.75) and considering the expressions (2.35, 2.36) for K_{AD} and K_{BC}, (2.86, 2.87) can be rewritten as:

$$\lambda_1(\varphi,\alpha) = \sum_{m=0}^{2p-1}\left\{\mathrm{bool}\left(m\tfrac{\pi}{p}-\beta\le\varphi\le m\tfrac{\pi}{p}+\beta\right)\times M\sin\left(\alpha-\varphi+m\pi+m\tfrac{\pi}{p}\right)\right. \qquad 2.88$$

$$\lambda_2(\varphi,\alpha)=-\sum_{m=0}^{2p-1}\left\{\text{bool}\left(m\tfrac{\pi}{p}-\beta\le\varphi\le m\tfrac{\pi}{p}+\beta\right)\times M\sin\left(\alpha-\varphi+m\pi+m\tfrac{\pi}{p}\right)\right\}=-\lambda_1(\varphi,\alpha) \quad 2.89$$

These functions can be expressed using Fourier expansion:

$$\lambda_1(\varphi,\alpha)=-\lambda_2(\varphi,\alpha)=\sum_{n=1,3,5...}c_n(\alpha)\cos(np\varphi)+d_n(\alpha)\sin(np\varphi) \quad 2.90$$

where:

$$c(\alpha)_n=\frac{4pM\sin(\alpha)}{\pi}\frac{np\ \sin(np\beta)\cos(\beta)-\cos(np\beta)\sin(\beta)}{n^2p^2-1} \quad 2.91$$

$$d(\alpha)_n=\frac{4pM\cos(\alpha)}{\pi}\frac{np\ \cos(np\beta)\sin(\beta)-\sin(np\beta)\cos(\beta)}{n^2p^2-1} \quad 2.92$$

The Fourier coefficients (2.91, 2.92) become singular for *n*=1 and *p*=1. In the case of *p*=1 (two-pole machines), the coefficients $c(\alpha)_n$ and $d(\alpha)_n$ can be computed as the limit of (2.91, 2.92) for n tending to 1, i.e.

$$c(\alpha)_1=\lim_{\substack{n\to1\\p=1}}c(\alpha)_n=\frac{M}{\pi}\sin(\alpha)[(2\beta+\sin(2\beta)] \quad 2.93$$

$$d(\alpha)_1=\lim_{\substack{n\to1\\p=1}}d(\alpha)_n=-\frac{M}{\pi}\cos(\alpha)[(2\beta-\sin(2\beta)] \quad 2.94$$

The equivalent linear current densities (2.90) will be used to set appropriate boundary conditions along the circumferences Γ_1 and Γ_2 for the solution of the vector potential elliptic differential equations (2.77, 2.78).

Solution for the vector potential

In the solution of (2.77, 2.78) with the separation of variables method, the functions 2.76 are assumed in the following form:

$$\begin{aligned}\Phi_m(r,\varphi,\alpha)=\sum_{n=1,2,...}&\left\{\frac{r^2}{4-n^2p^2}\left[a_n(\alpha)\cos(np\varphi)+b_n(\alpha)\cos(np\varphi)\right]+\right.\\&\left.+\left[U_n^+(\alpha)r^{np}+U_n^-(\alpha)_n r^{-np}\right]\sin(np\varphi)+\left[V_n^+(\alpha)r^{np}+V_n^-(\alpha)_n r^{-np}\right]\cos(np\varphi)\right\}\end{aligned} \quad 2.95$$

and

$$\begin{aligned}\Phi_w(r,\varphi,\alpha)=&\left[X_n^+(\alpha)r^{np}+X_n^-(\alpha)_n r^{-np}\right]\sin(np\varphi)+\\&\left[Y_n^+(\alpha)r^{np}+Y_n^-(\alpha)_n r^{-np}\right]\cos(np\varphi)\end{aligned} \quad 2.96$$

where the coefficients $a_n(\alpha)$ and $b_n(\alpha)$ are those defined by (2.84, 2.85).

With this choice, it can be easily checked by direct symbolic substitution that $\nabla\Phi_m = j(\varphi,\alpha)$ is satisfied for any values of the parameters $U_n^+(\alpha), V_n^+(\alpha), U_n^-(\alpha), V_n^-(\alpha)$ in (2.95). These parameters, along with the others appearing in (2.96), namely $X_n^+(\alpha), Y_n^+(\alpha), X_n^-(\alpha), Y_n^-(\alpha)$ need to be determined by imposing suitable boundary conditions. For this purpose, it will be considered that the radial and tangential flux density components in a generic point of the permanent magnet region D_m are respectively given by:

$$\frac{1}{r}\frac{\partial\Phi_m(r,\varphi,\alpha)}{\partial\varphi}, -\frac{\partial\Phi_m(r,\varphi,\alpha)}{\partial r} \qquad 2.97$$

while the radial and tangential flux density components in a generic point of the domain D_w shown in Figure 41 are respectively given by:

$$\frac{1}{r}\frac{\partial\Phi_w(r,\varphi,\alpha)}{\partial\varphi}, -\frac{\partial\Phi_w(r,\varphi,\alpha)}{\partial r} \qquad 2.98$$

The first boundary condition results from the fact that the tangential magnetic field component along the circumference Γ_1 $(r = R_i)$ must be equal to the linear current density λ_1 given by (2.87). In symbols:

$$-\frac{1}{\mu_0}\left.\frac{\partial\Phi_m(r,\varphi,\alpha)}{\partial r}\right|_{r=R_i} = \lambda_1(\varphi,\alpha) \qquad \forall\varphi,\alpha \qquad 2.99$$

By substituting (2.95) and (2.90) into (2.99) and equaling the coefficients of $\cos(np\varphi)$ and $\sin(np\varphi)$, two linear equations are obtained in the unknowns $U_n^+(\alpha), V_n^+(\alpha), U_n^-(\alpha), V_n^-(\alpha)$ for any *n*=1,3,5….

The second boundary condition results from imposing the continuity of the radial flux density across the circumference Γ_2 $(r = R_m)$; in symbols:

$$\frac{1}{R_m}\frac{\partial\Phi_m(R_m,\varphi,\alpha)}{\partial\varphi} = \frac{1}{R_m}\frac{\partial\Phi_w(R_m,\varphi,\alpha)}{\partial\varphi} \qquad \forall\varphi,\alpha \qquad 2.100$$

By substituting (2.95) and (2.96) into (2.100) and equaling the coefficients of $\cos(np\varphi)$ and $\sin(np\varphi)$, two linear equations are obtained in the unknowns $X_n^+(\alpha), Y_n^+(\alpha), X_n^-(\alpha), Y_n^-(\alpha)$ for any n.

The third boundary condition results from imposing that the tangential magnetic field must have a discontinuity equal to the linear current density λ_2 across the circumference Γ_2 $(r = R_m)$; in symbols:

$$-\frac{1}{\mu_0}\left.\frac{\partial\Phi_w(r,\varphi,\alpha)}{\partial r}\right|_{r=R_m} - \left[-\frac{1}{\mu_0}\left.\frac{\partial\Phi_m(r,\varphi,\alpha)}{\partial r}\right|_{r=R_m}\right] = \lambda_2(\varphi,\alpha) \qquad \forall\varphi,\alpha \qquad 2.101$$

By substituting (2.95), (2.96) and (2.90) into (2.101) and equaling the coefficients of $\cos(np\varphi)$ and $\sin(np\varphi)$, two linear equations are obtained from (2.93) in the unknowns $U_n^+(\alpha), V_n^+(\alpha), U_n^-(\alpha), V_n^-(\alpha), X_n^+(\alpha), Y_n^+(\alpha), X_n^-(\alpha), Y_n^-(\alpha)$ for any *n*.

The fourth boundary condition results from imposing that the tangential flux density component along the circumference Γ_3 $(r = R_2)$ must be zero. In symbols:

$$-\left.\frac{\partial \Phi_w(r,\varphi,\alpha)}{\partial r}\right|_{r=R_2} = 0 \;\forall \varphi,\alpha \qquad 2.102$$

By substituting (2.96) into (2.102) and setting the coefficients of $\cos(np\varphi)$ and $\sin(np\varphi)$ to zero, two linear equations are obtained in the unknowns $U_n^+(\alpha), V_n^+(\alpha), U_n^-(\alpha), V_n^-(\alpha)$, $X_n^+(\alpha), Y_n^+(\alpha), X_n^-(\alpha), Y_n^-(\alpha)$ for any *n*.

In conclusion, the four boundary conditions (2.99-2.102) result in a system of eight linear equations in the unknown parameters $U_n^+(\alpha), V_n^+(\alpha), U_n^-(\alpha), V_n^-(\alpha), X_n^+(\alpha), Y_n^+(\alpha), X_n^-(\alpha), Y_n^-(\alpha)$ for any *n*=1, 3, 5, …. This system of equations can be symbolically solved making the vector potentials Φ_m and Φ_w fully known from (2.95-2.96). Out of the two potentials Φ_m and Φ_w, only the latter will be used in the following to compute flux linkages and back-EMF's. Hence, for the sake of simplicity, only the explicit expressions for parameters $X_n^+(\alpha), Y_n^+(\alpha), X_n^-(\alpha), Y_n^-(\alpha)$ which are needed to compute Φ_w, are given next. For all values of p different from 2, these parameters can be expressed as follows:

$$X_n^+(\alpha) = R_2^{2np}\left[\frac{b_n(\alpha)F_n(\alpha)}{n^2p^2-4} - d_n(\alpha)G_n(\alpha)\right] \qquad 2.103$$

$$X_n^-(\alpha) = \frac{b_n(\alpha)F_n(\alpha)}{n^2p^2-4} - d_n(\alpha)G_n(\alpha) \qquad 2.104$$

$$Y_n^+(\alpha) = R_2^{2np}\left[\frac{a_n(\alpha)F_n(\alpha)}{n^2p^2-4} - c_n(\alpha)G_n(\alpha)\right] \qquad 2.105$$

$$Y_n^-(\alpha) = \frac{a_n(\alpha)F_n(\alpha)}{n^2p^2-4} - c_n(\alpha)G_n(\alpha) \qquad 2.106$$

with the functions $F_n(\alpha)$ and $G_n(\alpha)$ given by:

$$F_n(\alpha) = \frac{2R_m^{2np+2} - 4R_i^{np+2}R_m^{np} + 2R_i^{2np}R_m^2 - R_m^{2np+2}np + R_i^{2np}R_m^2 np}{2R_m^{np}np(R_2^{2np} - R_i^{2np})} \qquad 2.107$$

$$G_n(\alpha) = \frac{R_m^{2np+1} + R_i^{2np}R_m - 2R_i^{np+1}R_m^{np}}{2R_m^{np}np(R_2^{2np} - R_i^{2np})} \qquad 2.108$$

The expressions (2.103-2.106) become singular when $np = 2$. This can happen only when *p*=2 (four-pole machine) and *n*=1. In the case of *p*=2, these coefficients can be computed as the limits of (2.103-2.106) for *n* tending to 1. This gives:

$$X_1^+(\alpha) = \lim_{\substack{n\to 1\\ p=2}} X_n^+(\alpha) = R_2^4\left[b_1(\alpha)\overline{F}(\alpha) - d_1(\alpha)G_1(\alpha)\right] \qquad 2.109$$

$$X_1^-(\alpha) = \lim_{\substack{n\to 1\\ p=2}} X_n^-(\alpha) = b_1(\alpha)\overline{F}(\alpha) - d_1(\alpha)G_1(\alpha) \qquad 2.110$$

$$Y_1^+(\alpha) = \lim_{\substack{n\to 1 \\ p=2}} Y_n^+(\alpha) = R_2^4\left[a_1(\alpha)\overline{F}(\alpha) - c_1(\alpha)G_1(\alpha)\right] \quad 2.111$$

$$Y_1^-(\alpha) = \lim_{\substack{n\to 1 \\ p=2}} Y_n^-(\alpha) = a_1(\alpha)\overline{F}(\alpha) - c_1(\alpha)G_1(\alpha) \quad 2.112$$

where:

$$\overline{F}(\alpha) = \frac{4R_i^4 \ln(R_i / R_m) + R_i^4 - R_m^4}{16(R_2^4 - R_i^4)} \quad 2.113$$

2.2.4.2 Calculation of the phase flux linkage

Once the vector potential Φ_w produced by a group of magnet blocks has been determined as shown in the previous subsection, the flux linkage of one stator phase (e.g. phase *a*) can be easily found by integrating the vector potential over the coils of this phase. The phase *a* includes 2*p* phase belts, each spanning $\pi/3p$ mechanical radians, the first of which is placed between $\theta = \frac{\pi}{6p}$ and $\theta = -\frac{\pi}{6p}$ (Figure 31a). The flux linkage λ_{group} produced by the group of magnet blocks when the first magnet block is placed at $\theta = \Theta$ is then:

$$\lambda_{group}(\Theta,\alpha) = \frac{2pL}{S_{pb}} \int_{-\frac{\pi}{6p}}^{\frac{\pi}{6p}} \int_{R_1}^{R_2} \Phi_w(r,\theta-\Theta,\alpha)\, r\, dr\, d\theta \quad 2.114$$

where L is the core length, S_{pb} is the cross-sectional area of a phase belt, S_{pb} can be easily computed and expressed as:

$$S_{pb} = \tfrac{\pi}{6p}\left(R_2^{\,2} - R_1^{\,2}\right) \quad 2.115$$

Equation (2.75) has been used in (2.96) to work with the angular coordinate θ and the coefficient 2*p* in (2.114) accounts for the presence of 2*p* phase belts for the phase *a*.

The symbolic integration of (2.114), based on expression (2.96) for the vector potential, yields:

$$\lambda_{group}(\Theta,\alpha) =$$
$$\frac{L}{S_{pb}} \sum_n \sin\left(\tfrac{n\pi}{6}\right)\left\{\sin(\Theta np)\left[C_n^- X_n^-(\alpha) + C_n^+ X_n^+(\alpha)\right] + \cos(\Theta np)\left[C_n^- Y_n^-(\alpha) + C_n^+ Y_n^+(\alpha)\right]\right\} \quad 2.116$$

The constants C_n^+ and C_n^- are:

$$C_n^+ = 2\frac{R_2^{\,np+2} - R_1^{\,np+2}}{np(np+2)} \quad 2.117$$

$$C_n^- = \begin{cases} 2\dfrac{R_1^{\,2} R_2^{\,np} - R_1^{\,np} R_2^{\,2}}{R_1^{\,np} R_2^{\,np} np(np-2)} & \text{if } np \neq 2 \\ \ln(R_2 / R_1) & \text{if } p = 2 \wedge n = 1 \end{cases} \quad 2.118$$

The total flux linkage of phase *a* results from summing the contributions of all the magnet block groups. This sum is to be differently accomplished depending on the magnetization pattern. The three cases are addressed in the next sub-section.

Parallel magnetization

In case of parallel magnetization, there is only one magnet block (spanning 2β mechanical radians) per pole and the value of α is set equal to zero. Hence the flux linkage for the parallel magnetization can be computed as:

$$\lambda_{par}(\Theta) = \lambda_{group}(\Theta,\ 0) \qquad 2.119$$

Radial segmented magnetization

For the radial magnetization with segmented magnets, we assume to have again N_{bp} blocks per pole, each spanning 2β, with the permanent magnet span s_m, such that these quantities satisfy (2.61). Furthermore, the angle α is again set equal to zero. Hence the flux linkage can be computed as:

$$\lambda_{seg}(\Theta) = \sum_{b=0}^{N_{bp}-1} \lambda_{group}\left(\Theta - \frac{\pi s_m}{2p} + \beta(2b+1),\ 0\right) \qquad 2.120$$

Halbach magnetization

For the Halbach magnetization pattern, we assume to have N_{bp} magnet blocks per pole, each spanning 2β with these quantities satisfying (2.65). The angle α changes by steps equal to $2p\beta$ when moving from one block to the adjacent ones. Taking all this into account, the phase flux linkage for the Halbach array case is:

$$\lambda_{hal}(\Theta) = \sum_{b=0}^{N_{bp}-1} \lambda_{group}\left(\Theta - \frac{\pi}{2p} + \beta(2b+1),\ 2pb\beta - \frac{\pi}{2} + p\beta\right) \qquad 2.121$$

2.2.4.3 Back emf calculation

Assuming a synchronous machine operation with stator angular frequency ω, the following relationship holds:

$$\Theta = \frac{\omega}{p} t \qquad 2.122$$

The back-EMF e_{group} produced in the phase *a* by a magnet group can be computed by deriving the *a*-phase flux linkage with respect to the time:

$$e_{group}(t,\alpha) = \frac{d\Theta}{dt}\frac{d\lambda_{group}(\Theta,\alpha)}{d\Theta}\bigg|_{\Theta=\frac{\omega t}{p}} = \frac{\omega}{p}\frac{d\lambda_{group}(\Theta,\alpha)}{d\Theta}\bigg|_{\Theta=\frac{\omega t}{p}} \qquad 2.123$$

Substituting (2.116) in (2.123) we obtain:

$$e_{group}(t,\alpha) = \frac{L\omega}{S_{pb}}\sum_{n} n\sin\left(\tfrac{n\pi}{6}\right)\left\{\sin(\omega nt)\left[C_n^- X_n^-(\alpha) + C_n^+ X_n^+(\alpha)\right] - \cos(\omega nt)\left[C_n^- Y_n^-(\alpha) + C_n^+ Y_n^+(\alpha)\right]\right\} \qquad 2.124$$

At this point, using the same considerations as for the flux linkages in the previous subsection, the total back-EMF of a phase can be found by summing the contribution of all the magnet block groups.

Parallel magnetization:

For the parallel magnetization pattern, there is only one magnet block group so there is no sum to perform and the phase back-EMF is:

$$e_{par}(t) = e_{group}(t,0) \qquad 2.125$$

Radial segmented magnetization:

For the radial segmented magnetization pattern, we have.

$$e_{seg}(t) = \sum_{b=0}^{N_{bp}-1} e_{group}\left(t - \frac{\pi s_m}{2\omega} + \beta\frac{p}{\omega}(2b+1),\, 0\right) \qquad 2.126$$

Halbach magnetization:

For the halbach array topology the back emf can be expressed as follows, remembering that the magnetization angle α changes with the angular position θ:

$$e_{hal}(t) = \sum_{b=0}^{N_{bp}-1} e_{group}\left(t - \frac{\pi}{2\omega} + \beta\frac{p}{\omega}(2b+1),\, 2pb\beta - \frac{\pi}{2} + p\beta\right) \qquad 2.127$$

2.2.5 FEA ASSESSMENT FOR THE BACK-EMF EVALUATION

Similarly, to what has been done for the torque computation, also the no-load back-EMF calculation formulas derived in 2.2.4 are assessed by comparison with FEA simulations. As example case studies for the assessment the 4-pole and 12-pole machines, whose data are given in Table IV (repeated below). In this case, it is necessary to set the stator currents to zero in the simulations and derive the back-emf from the phase flux linkage. The comparison between the back-EMF versus time waveforms obtained by FEA and with the proposed analytical approach is given in Figure 43, showing a good agreement for all the number of poles and magnetization patterns considered.

Table IV: Geometric ad electrical data of the (4-pole and 12-pole) machines used for FEA simulations

Permanent magnet coercivity	850 kA
Permanent magnet relative permeability	1.04
Stator maximum current density	4 A/mm^2
Winding fill factor k_{fill}	1
R_i	47.5 mm
R_2	62 mm
g	1 mm
h_m	10.5 mm
h_w	3 mm
L	80 mm
s_m for parallel and radial magnetization	0.95
N_{bp} for parallel magnetization	1
N_{bp} for radial magnetization	3
N_{bp} for Halbach magnetization	15

As regards the computational efficiency, Table VI summarizes the time taken by FEA and by the analytical procedure to compute the back EMF of the four-pole machine for a given rotor position (or instant of time). As for the torque, computations are performed with the two methods on the same computer and using the calculation tools indicated in Table VI. It can be seen that a significant saving is achieved using the analytical approach, which can result in an important advantage in all cases where the computation is to be repeated hundreds or thousands of times.

Table VI: Comparison of back-emf computation times with fea and analytical techniques

Method	**Tool**	**Computation time**
FEA	FEMM© v.4.2	1 m
Analytical	Mathcad© v.15	Less than 0.5 s

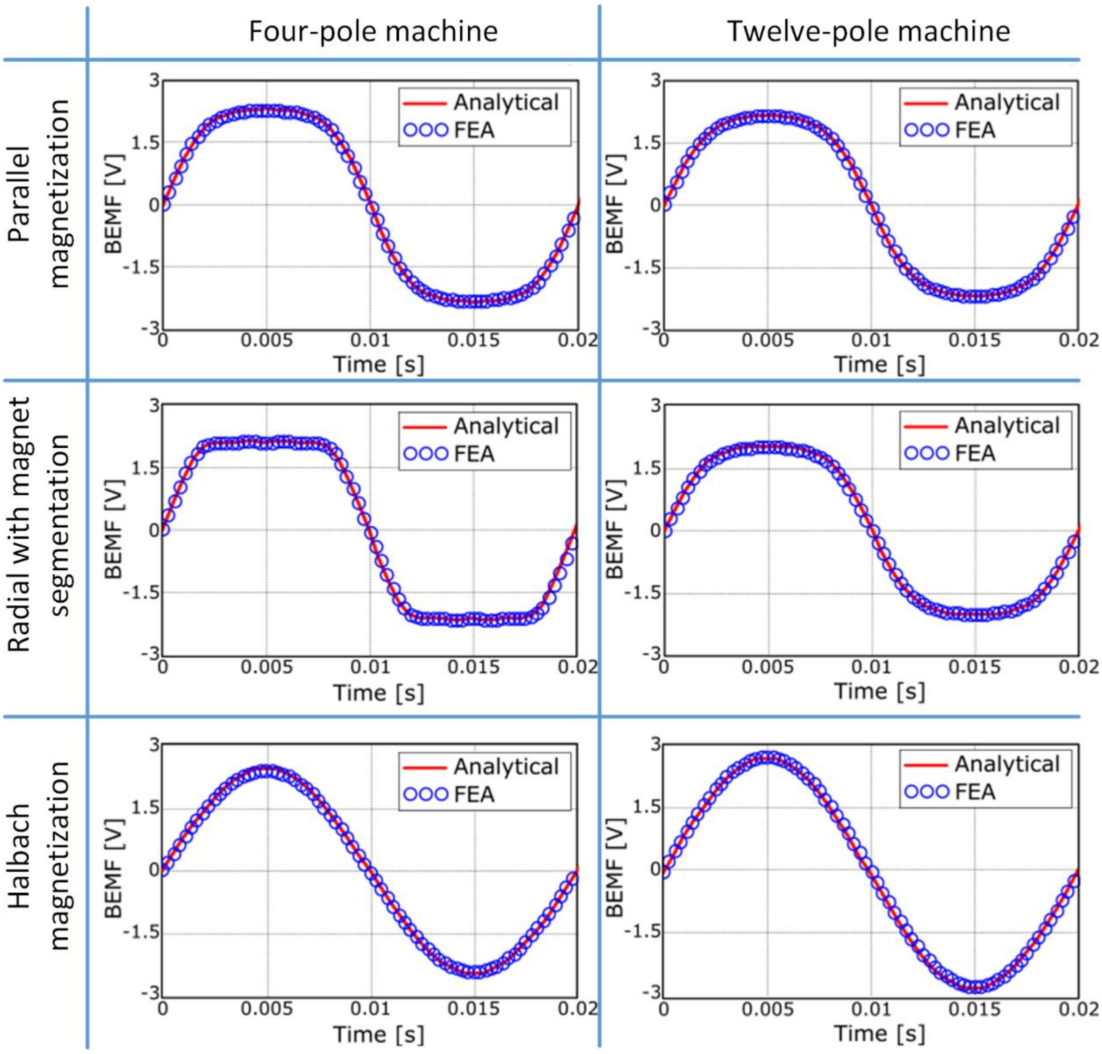

Figure 43: Comparison of the no-load back-EMF waveforms obtained by FEA and with the proposed analytical technique for the 4-pole and 12-pole example machines featuring different magnetization patterns.

2.3 APPLICATION EXAMPLE OF PERFORMANCE INVESTIGATION IN SLOTLESS SPM MACHINES

2.3.1 SUMMARIZED ALGORITHM PROCEDURE FOR THE TORQUE AND BACK EMF COMPUTATION

In this subsection, the algorithmic procedure for the computation of the torque and of the back-EMF according to the proposed analytical method is summarized. This is done through the block diagrams given in Figure 44. In the block diagram, the equations to be used for the computation of the various quantities are indicated and the input parameters required for the overall computation are highlighted. It is noted that not all the input parameters are always independent of one another, the relationships among parameters changing based on the magnetization pattern.

For example, in case of radial magnetization with segmented permanent magnets, the parameters s_m, β, p and N_{bp} must obey to (2.61); for the Halbach magnetization pattern, the parameters α, p and N_{bp} must satisfy the constraint (2.65).

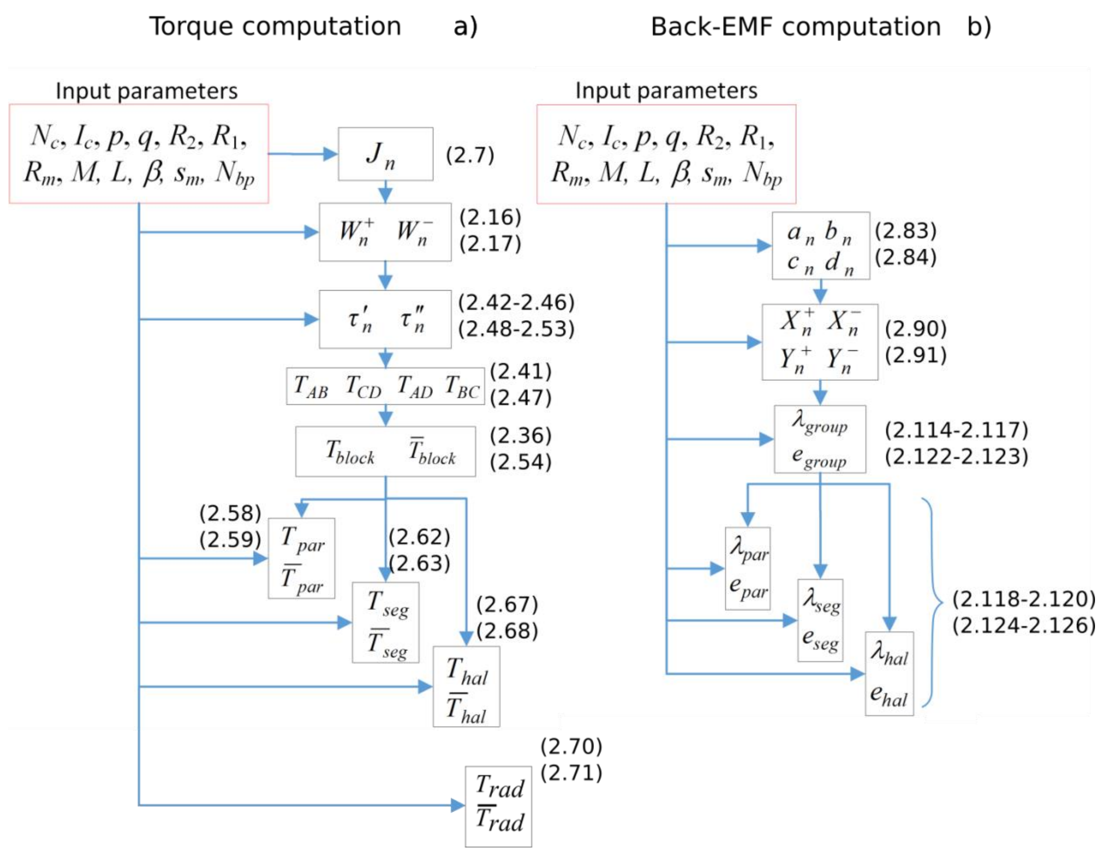

Figure 44: a) Block diagram illustrating the algorithm for the analytical computation of the torque, b) Block diagram illustrating the algorithm for the analytical computation of the back-EMF.

2.3.2 Application example with FEA assessment

The availability of an explicit torque expression as a function of the machine parameters makes it particularly easy to study the dependency of the torque on any characteristic dimension (or set of dimensions) that needs to be chosen in the design. This is better explained and summarized in Figure 44a where the torque evaluation process, as a function of input parameters, is shown.

Table VII: Constraints and variables for the optimization process

Permanent magnet coercivity	850 kA
Permanent magnet relative permeability	1.04
Stator maximum current density	4 A/mm^2
Winding fill factor k_{fill}	1
R_i	47.5 mm
R_2	62 mm
g	1 mm
h_m	variable
h_w	variable
L	80 mm
s_m for parallel and radial magnetization	0.95
N_{bp} for parallel magnetization	1
N_{bp} for radial magnetization	3
N_{bp} for Halbach magnetization	15

As an example of a design optimization scenario for the general cross section shown in Figure 45, let us suppose that we are interested in finding the h_w/h_m ratio that leads to the maximum average torque, while all the other parameters (including the gap width) are maintained unchanged. For this purpose, let us consider all the parameters in Table VII where all the constants and variables are reported. The magnet and winding heights are changed so that their sum is identically equal to:

$$h_m + h_w = R_2 - R_i - g = 13.5\,\mathrm{mm} \qquad 2.128$$

Two example designs satisfying the condition are shown in Figure 45 for the sake of clarity.

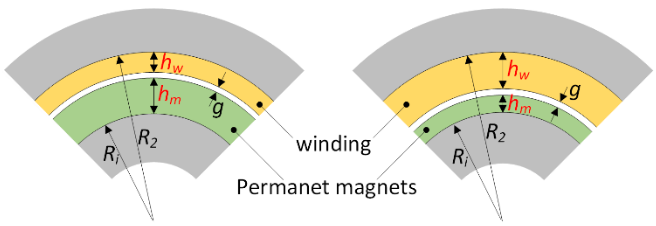

Figure 45: Two example schematic cross section differing from the permanent magnet height (h_m) and stator winding thickness (h_w) while all the other parameters are the same

By using the analytical expressions for the average torque derived in 2.2.2, it is possible to plot the curves shown in Figure 46. In the figure, the average torque is instantaneously obtained for different numbers of poles (4 and 12), for different magnetization patterns (parallel, radial segmented, Halbach) and for different dimensions h_w, h_m. The values obtained analytically are compared to those resulting from 2D FEA showing a good agreement.

The diagrams given in Figure 46 show that:

- In the 4-pole machine, the Halbach magnetization gives lower torques than the other magnetization patterns for any h_m/h_w ratio; conversely, in the 12-pole machine the Halbach magnetization gives higher torques than the others for $h_w < 8\ \mathrm{mm}$, while for larger winding thicknesses the other two patterns prevail.
- In both the 4-pole and 12-pole machines the maximum torque is achieved when h_w and h_m are practically equal, i.e. both between 6 mm and 7 mm. Conversely, if the Halbach magnetization is used, the maximum average torque is achieved when the winding thickness is slightly lower than the permanent magnet thickness.

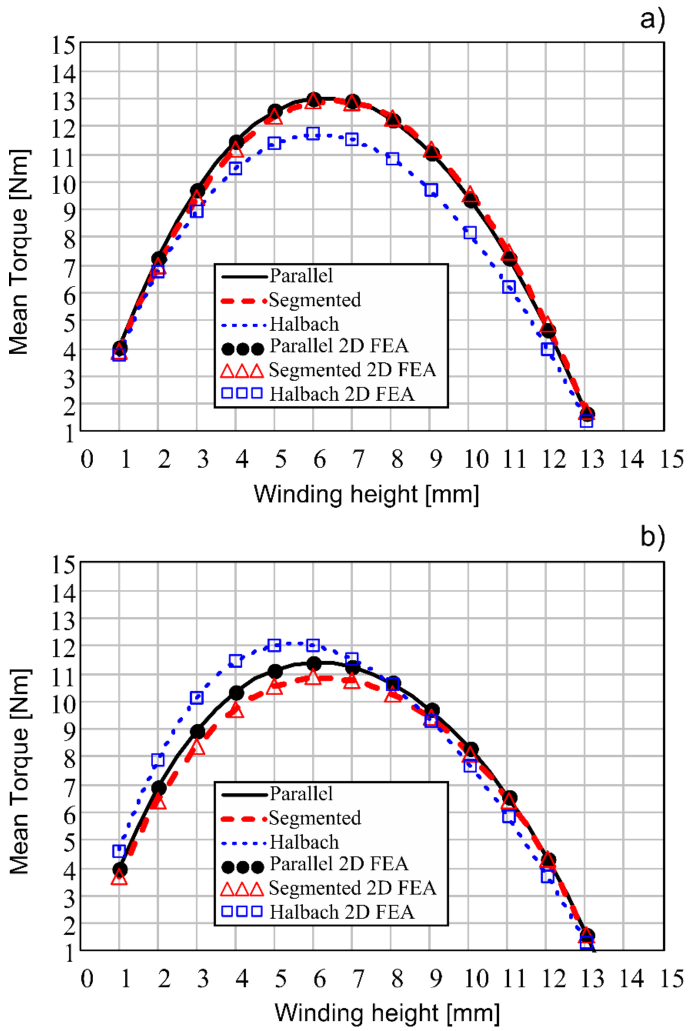

Figure 46: Average torque as a function of the winding height for various magnetization patterns, according to FEA and the analytical calculation, for (a) the four-pole machine; (b) the twelve-pole machine.

2.4 SIZING EQUATIONS FOR SLOTLESS SPM MACHINES WITH DIFFERENT ROTORS

Slotless SPM machines are often considered as the best fitting topology in those applications where very high efficiency and cogging-torque-free performance is needed. The optimal sizing of a slotless SPM machine can be performed following different approaches. The typical methodology employs FEA simulations to explore various design solution if search for the optimum with respect to a given objective function (or set or objective functions) and subject to a given set of constraints. The FEA method is effective, accurate, but time consuming. In the previous parts of this thesis, a fully-analytical performance evaluation approach has been proposed. Of course, these analytical formulas can be used instead of FEA to determine an optimal configuration with respect to an objective function (saving much time especially when many designs have to be investigated). In this section, another sizing approach is proposed, without any third-party optimization software.

This method is fundamentally based on the analytical expression of the average torque (2.60, 2.64, 2.69, 2.72) of the slotless SPM machine as a function of the various design parameters. The expressions have been implemented in two different cases, depending on whether the stator current density or the joule loss per unit of air-gap surface is treated as a fixed quantity. In both cases, some examples are provided of how the proposed equation can be employed to optimize the slotless SPM machine cross section with no need for FEA simulations.

2.4.1 STATOR WINDING AND PERMANENT MAGNET SIZING FOR A GIVEN STATOR CURRENT DENSITY

In this section an extension of the investigation reported in 2.3 is proposed. As done in the previous analysis, the current density in the stator winding is assumed constant. Regarding the machine geometric characteristics these are reported in table VII.

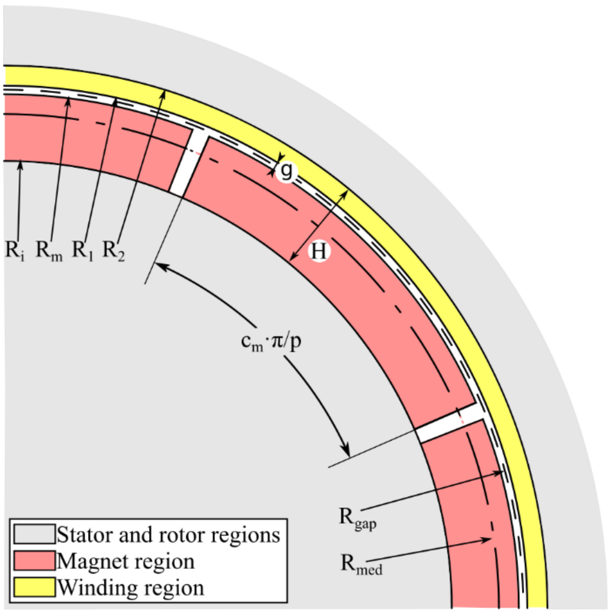

Figure 47: Slotless SPM machine cross section with main dimensional data required for the optimization process

In addition to what has been already observed in 2.3, let us note that the machine cross-sectional overall structure is characterized by the magnetic gap width H and by the radius R_{med} of the circumference placed in the middle of the air gap (Figure 47). Furthermore, the mechanical air-gap g should be defined, taking into account the possible need for retaining sleeves or other structures to be mounted for permanent magnet retention. It is noted that fixing H and R_{med} is equivalent to fixing the radii R_i and R_2 as:

$$R_i = R_{med} - H/2$$
$$R_2 = R_{med} + H/2 \qquad 2.129$$

Regarding the current density fundamental amplitude J_p, the rms value of the current density in the winding is linked to the maximum value by a $\sqrt{2}$ factor, so we will refer to rms value J of the electrical current density. In addition, in a practical example, the current is not uniformly distributed over the winding cross section but is constrained to flow through conductors so the winding fill factor (k_{fill}) cannot be one (usual values of the winding fill factor are from 0.6 to 0.75).

At this point, the problem naturally rises of finding the permanent-magnet and the stator winding thicknesses which lead to the maximum torque for a given set of parameters *H*, R_{med} and *g*. In a more formalized and compact way, the problem is to find the radius R_{gap} (which is the mean mechanical air-gap radius) such as to maximize the torque computed with (2.60, 2.64, 2.69, 2.72) when *J* is selected. This optimization process is proposed for the slotless SPM machine with all the rotor magnetization patterns (parallel, radial segmented, Halbach, radial continuous).

Looking at Figure 47, it is clear that once R_{gap} is fixed, also the radii R_m and R_1 are determined as:

$$R_m = R_{gap} - G/2$$
$$R_1 = R_{gap} + G/2 \qquad 2.130$$

The problem can be visualized by plotting the torque *T* given by (2.60, 2.64, 2.69, 2.72) as a function of R_{gap}, which can feasibly vary in the range (2.131) as shown in Figure 48.

$$R_1 + g/2 < R_{gap} < R_2 - g/2 \qquad 2.131$$

From Figure 48 it is clear that, when $R_{gap} = R_i + G/2$ the torque is zero because the permanent magnet thickness degenerates to zero; similarly, for $R_{gap} = R_2 - g/2$ the torque becomes zero as the winding thickness degenerates to zero. For intermediate values of R_{gap}, the permanent magnet and the winding have different thicknesses depending on this variable (large values indicate a prevalence of permanent magnets and small values denote a prevalence of the winding). The value of R_{gap} for which the torque becomes maximum indicates the optimal distribution between the magnet and the winding. The situation shown in Figure 48 denotes that the torque profile as a function of R_{gap} is strongly dependent on the number of poles and the machine configuration. In particular, the maximum torque for the machine design that represents the left part of the figure (R_i=47.5mm, R_2=62mm, *g*=1mm) is obtainable imposing almost always a mean value of R_{gap} except from Halbach array magnetization pattern where in some cases the maximum point moves to a larger magnet optimal design (larger R_{gap}). Considering the “right” part of the figure, it is clear that the maximum torque point is generally obtainable with a higher R_{gap} compared to the "left" design and this value generally increases with the number of poles.

Final considerations can be made in the sense that the slotless SPM machine performance estimation cannot be done without an analytical or FEA approach, because there is a strong and generally unpredictable dependence on machine architecture and input design parameters.

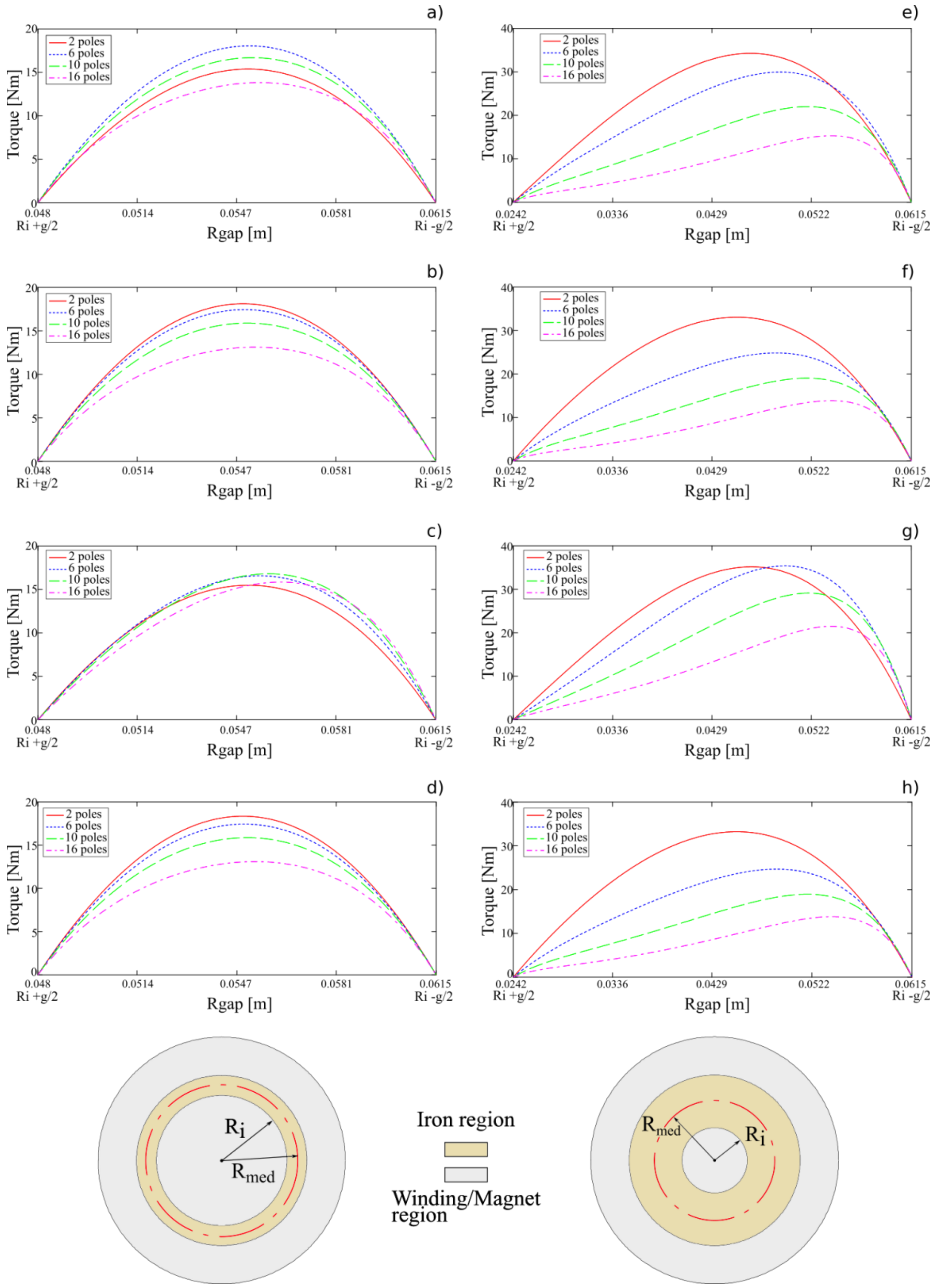

Figure 48: Torque vs R_{gap} for two different machine configurations ($left$: $R_i = 47.5mm, R_2 = 62mm, g = 1mm$), ($Right$: $Ri = 23.75mm, R2 = 62mm, g = 1mm$): a), e): Parallel magnetization b), f): Radial segmented magnetization c), g): Halbach array magnetization d), h): Continuous radial magnetization

2.4.2 SIZING EQUATION FOR A GIVEN JOULE POWER LOSS PER UNIT OF HEAT-EXCHANGE SURFACE

The sizing approach presented in the previous sections suffers from the shortcoming that the current density J (or J_p) appearing in the formulas is not a known fixed quantity, but is something actually involved in the sizing process, in many cases. In the dimensioning of the machine, the most reasonable and effective approach is to suitably fix the power dissipation per unit of heat-exchange surface as this quantity is closely connected with the temperature rise of the winding [20].

As usually done with slotted machines [20], the heat exchange surface is identified with the stator bore surface as the interface between the winding region and the air-gap region. For a slotless machine, it is also reasonable to consider the heat-exchange surface as the inner stator winding surface, which is the cylindrical surface S_{gap} of radius R_1. Through this surface the power loss P_{loss} arising in the winding flows into the air gap, so the specific power loss per unit of surface is:

$$P_{J,S}^{gap} = \frac{P_{loss}}{S_{gap}} \qquad 2.132$$

where the joule losses generated by the stator can be expressed as follows:

$$P_{loss} = \frac{1}{\gamma_c}\pi\left(R_2^{\,2} - R_1^{\,2}\right)Lk_{fill}\sigma^2 = \frac{\pi}{\gamma_c k_{fill}}\left(R_2^{\,2} - R_1^{\,2}\right)LJ^2 \qquad 2.133$$

$$with: \quad k_{fill} \cdot \sigma = J$$

where γ_c is the electrical conductivity of the winding conductors, and:

$$S_{gap} = 2\pi\, R_1\, L \qquad 2.134$$

the specific power $P_{J,S}^{gap}$ is related to the winding temperature T_w rise over the air-gap temperature T_{gap} through the relationship:

$$P_{J,S}^{gap} = \alpha_{gap-w}\left(T_w - T_{gap}\right) \qquad 2.135$$

α_{gap-w} is the heat transfer coefficient between the air-gap and the winding.

Of course, a significant heat flow also occurs from the winding into the back iron and in this case the heat exchange surface is to be identified with the external winding cylindrical surface of radius R_2 (Figure 47) and the specific power loss per unit of surface is in this case:

$$P_{J,S}^{yoke} = \frac{P_{loss}}{S_{yoke}} \qquad 2.136$$

where P_{loss} is again given by 2.133 and S_{yoke} is:

$$S_{yoke} = 2\pi\, R_2\, L \qquad 2.137$$

The specific power $P_{J,S}^{yoke}$ is related to the winding temperature (T_w) rise over the air-gap temperature T_{yoke} through the relationship:

$$P_{J,S}^{yoke} = \alpha_{yoke-w}\left(T_w - T_{yoke}\right) \tag{2.138}$$

α_{yoke-w} being the heat transfer coefficient (by conduction) between the winding and the back iron.

Consistently with what is usually done in the study and dimensioning of slotted rotating machines [20], the specific power loss flow per unit of gap surface (2.132) is considered in the following. Using (2.133-2.134) this becomes:

$$P_{J,S}^{gap} = \frac{J^2}{2\gamma_c k_{fill}} \frac{R_2^{\,2} - R_1^{\,2}}{R_1} \tag{2.139}$$

In this equation, it is possible to fix $P_{J,S}^{gap}$ based on thermal considerations or analyses and the current density J is thereby determined as:

$$J = \sqrt{\frac{2P_{J,S}^{gap} R_1 \gamma_c k_{fill}}{R_2^{\,2} - R_1^{\,2}}} \tag{2.140}$$

It is very important to remember that the relationship between J and σ is: $J = k_{fill}\,\sigma$. Considering this fact and substituting 2.140 in 2.8 and following the Figure 44-procedure it is possible to evaluate the average output torque for a given specific power loss flow per unit of gap surface.

2.4.2.1 Example of optimal sizing

In this chapter, two examples are provided on how this approach can be used to optimally size the cross section of an SPM slotless machine with different rotor magnetization patterns.

The constant parameters assumed in the optimization are listed in Table VIII with their relevant values. In particular, the specific loss per unit of gap surface $P_{J,S}^{gap}$ is assumed to be defined based on thermal considerations (i.e. considering the equivalent thermal network of the machine). It is also noted that the outer winding radius, R_2, is also treated as a constant, fixed at 60 mm, for example due to a maximum size constraint. Finally, the gap width G is fixed as well (equal to 1 mm) for both mechanical and ventilation reasons.

Table VIII: Constant parameters assumed in the optimization

$\boldsymbol{P_{j,s}^{gap}}$	830 W/m^2
γ_c	56 MS/m
k_{fill}	0.7
M	850×10^3 A/m
c_m	0.85
R_2	60 mm
g	1 mm

The two radii R_i, R_m, which univocally determine the winding and the permanent magnet thickness (Figure 47), are taken as the optimization variables. Since the gap width is fixed, the value of R_m also determines R_1 as:

$$R_1 = R_m + G \qquad 2.141$$

The objective function is to be suitably chosen at this point. A reasonable and very common target in this sense is to obtain a given torque per unit of machine length (*T/L*) using the minimum possible amount of permanent magnets (which are the most expensive component in the machine construction), i.e. with the minimum permanent magnet cross section. The permanent magnet cross section is given by:

$$A_{magnet} = \pi\left(R_m^{\ 2} - R_i^{\ 2}\right)c_m \qquad 2.142$$

So, the optimization problem can be formulated saying that we want to find the radii R_i, R_m such as to satisfy a torque per unit of length constraint and minimizing the magnet volume imposing a given specific loss per unit of gap surface ($P_{J,S}^{gap}$).

The torque per unit of length, for a given $P_{J,S}^{gap}$ can be evaluated using (2.60, 2.64, 2.69, 2.72) with (2.140) imposing also unitary length for the model.

The problem can be numerically solved and solution examples are next provided for two slotless SPM machines, one with four poles (*p*=2) and the other with eight poles (*p*=4), both characterized by the common data given in Table VIII.

The optimization results are shown in Figure 49 and Figure 50 which plots the optimal radii R_i and R_m required to obtain a given torque over length ratio *T/L* minimizing the magnet cross section, while the outer winding radius R_2 is maintained constant at 60 mm. It can be seen that, as the *T/L* ratio increases, the magnetic air-gap width grows, with a growth of both the stator winding and permanent magnet thickness in all the rotor magnetization pattern architectures.

What can be noticed, however, is how the rate of increase of the magnet thickness is higher in the eighth pole machines than in the four pole machines, while, conversely, the rate of increase of the winding thickness is higher in the four pole machine than in the eighth poles one. This fact occurs for all the magnetization patterns except from the Halbach array. In this case the magnet thickness increase, for a given torque per unit length, is higher in the four poles machine. The winding thickness tendency is the same for all magnetization patterns.

This can be easily seen from Figure 51, which clearly shows that, for any given *T/L* ratio, the optimal four pole machine requires more winding thickness and less magnet thickness than the eighth-pole one (except from the Halbach where the four-pole machine requires more both magnet and winding thickness than the eighth-pole one).

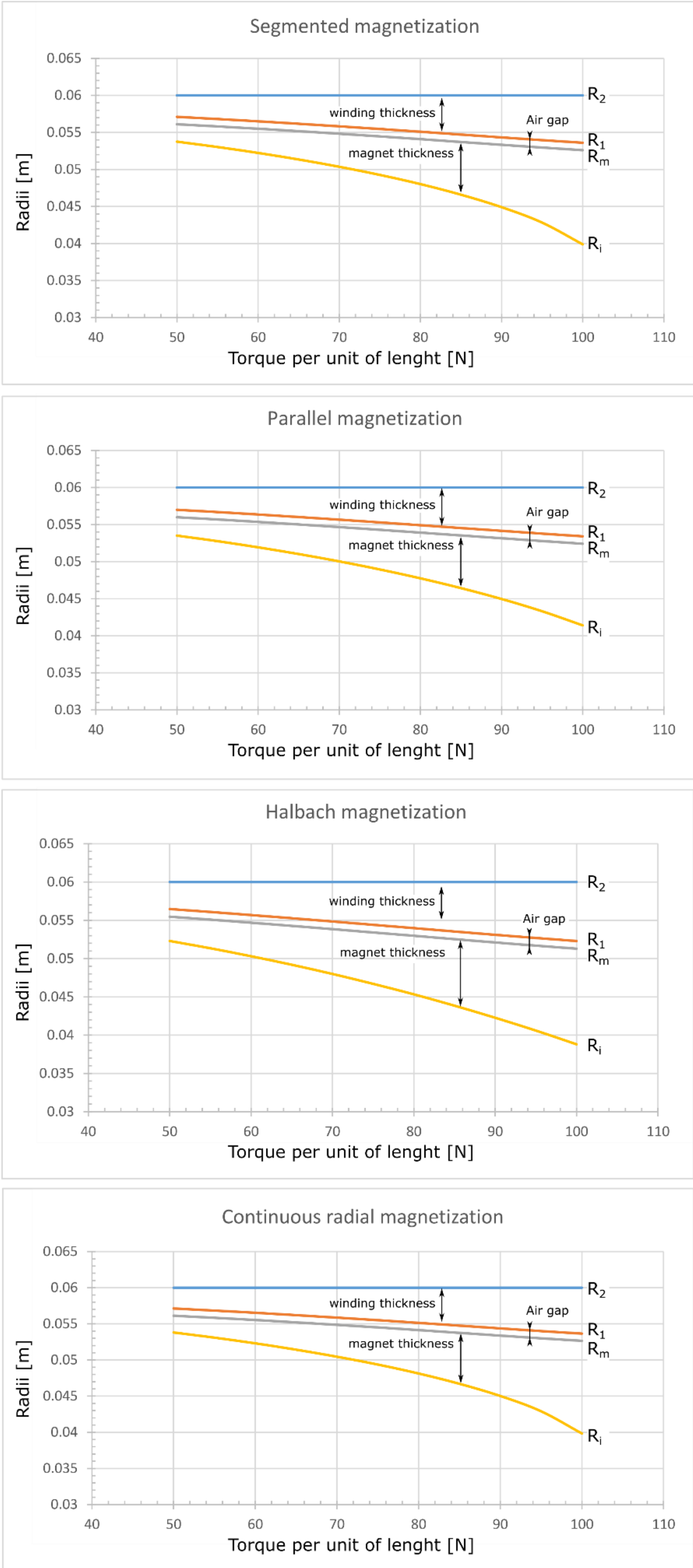

Figure 49: Optimization results in terms of radii R_i and R_m which minimize permanent magnet cross section to achieve a given torque per length output, in the case of a four pole machine with different magnetization patterns

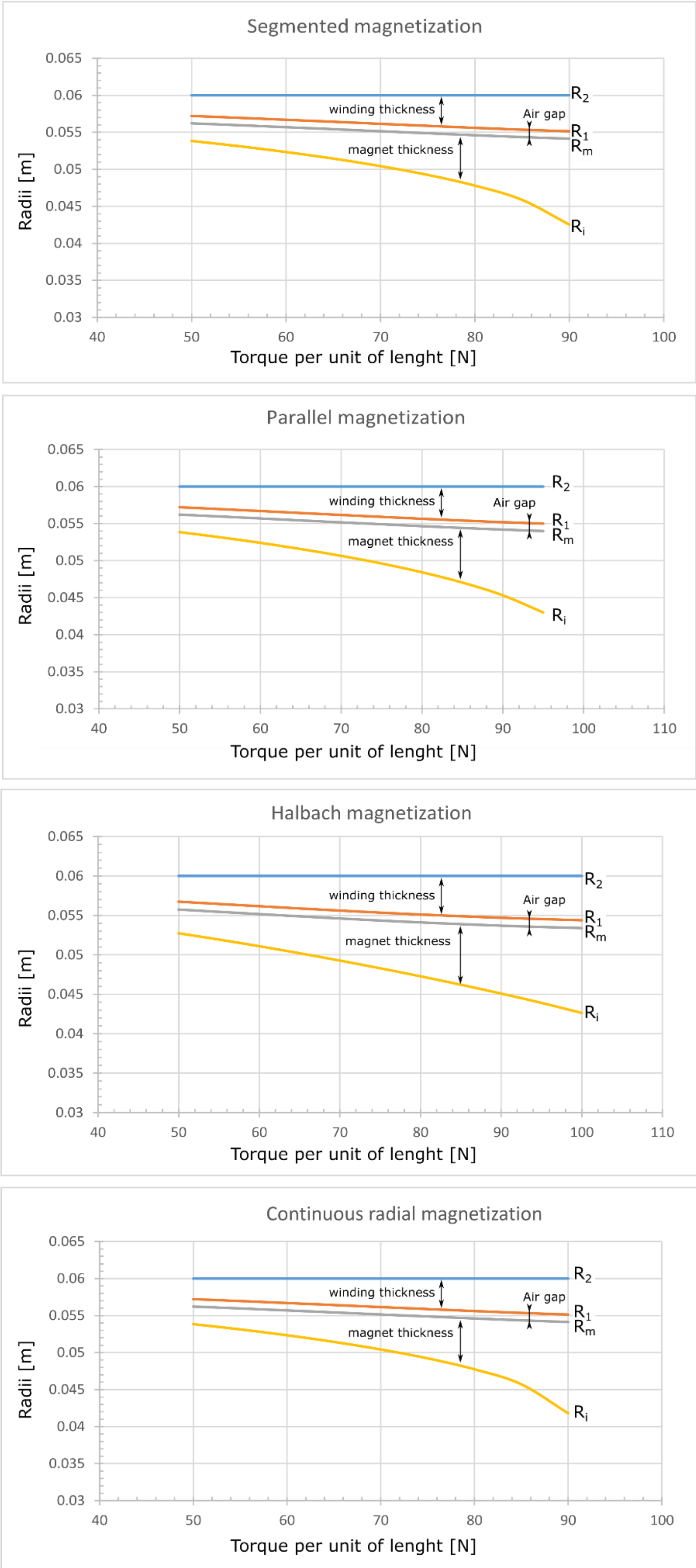

Figure 50: Optimization results in terms of radii R_i and R_m which minimize permanent magnet cross section to achieve a given torque per length output, in the case of an eight pole machine with different magnetization patterns

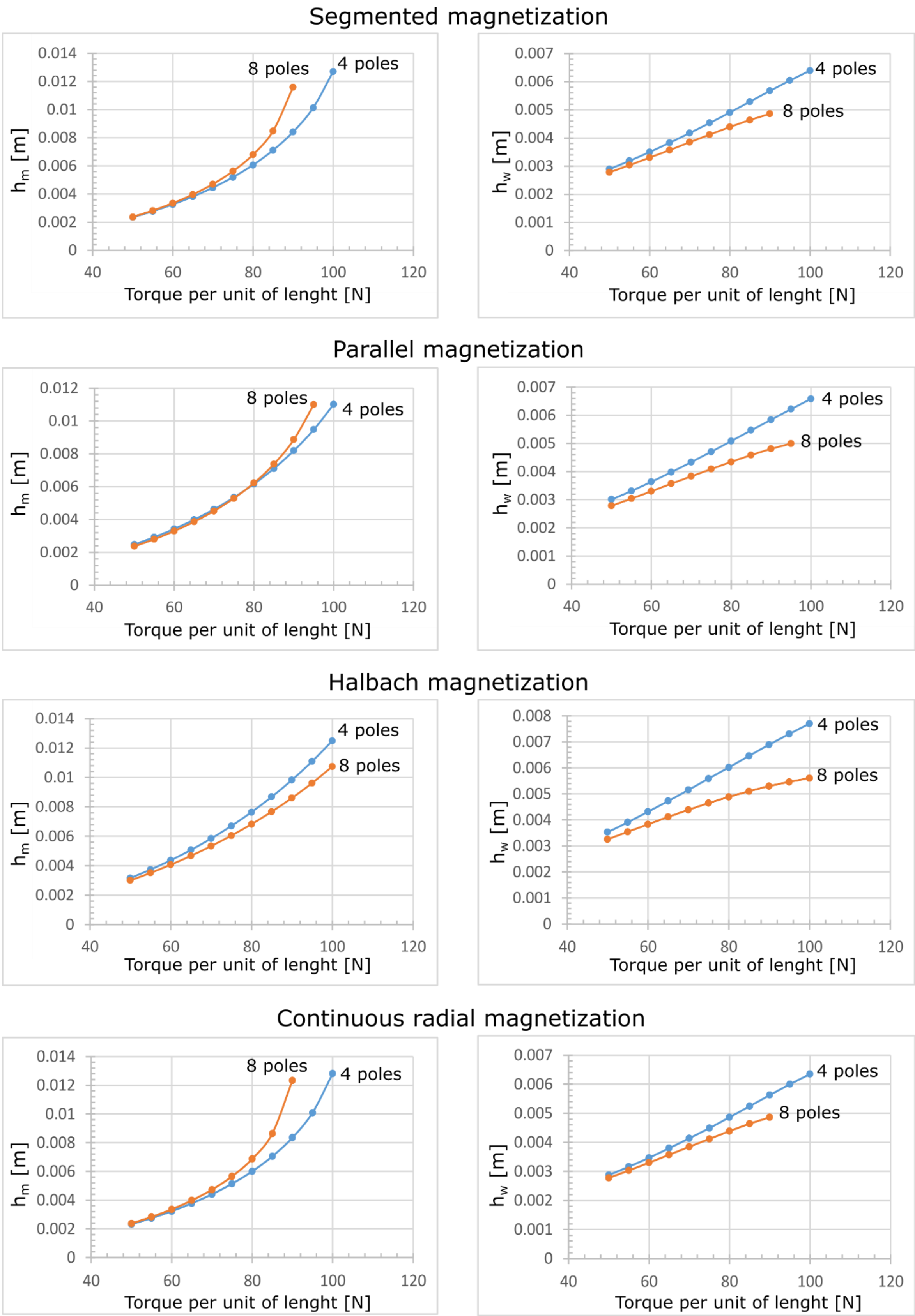

Figure 51: Optimization results in terms of winding and magnet thicknesses required to minimize permanent magnet cross section to achieve a given torque per length output, in the case of a four pole machine and of an eighth pole machine with different magnetization patterns.

2.4.3 Final remarks

As final remarks, we can observe that the optimal sizing of a slotless SPM machine can be performed following different approaches. The typical methodology employs FEA simulations to explore various design solution in search for the optimum with respect to a given objective function (or set or objective functions) and subject to a given set of constraints. The FEA method is effective, accurate, but time consuming. In this section, a fully-analytical sizing method has been proposed. It is fundamentally based on the analytical expression of the average torque of the slotless SPM machine as a function of the various design parameters (chapter 2.2.2).

The torque evaluation procedure (Figure 44a) has been implemented in two main forms depending on whether the stator current density or the joule loss per unit of air-gap surface is treated as a fixed quantity. In both cases, some examples have been provided of how the proposed method can be employed to optimize the slotless SPM machine cross section with no need for FEA simulations or complicated magnetic field solutions.

2.5 REFERENCES

[1] A. Tessarolo; M. Bortolozzi; C. Bruzzese, "Explicit Torque and back-EMF Expressions for Slotless Surface Permanent-Magnet Machines with Different Magnetization Patterns," in IEEE Transactions on Magnetics, vol. PP, no.99, pp.1-1

[2] A. Tessarolo, L. Branz and C. Bruzzese, "A compact analytical expression for the load torque in Surface Permanent-Magnet machines with slotless stator design," Electrical Machines Design Control and Diagnosis (WEMDCD), 2013 IEEE Workshop on, Paris, 2013, pp. 8-17.

[3] A. Tessarolo, M. Bortolozzi, M. Mezzarobba, “On the Validity of the Harmonic Superposition Principle for Computing Rotor Eddy Current Losses in Permanent Magnet Machines”, International Conference on Electrical Machines, ICEM 2012, Marseille, 2-5 Sept. 2012, pp. 1369-1373.

[4] A. Tessarolo, L. Branz, M. Bortolozzi, “Analytical calculation of the no-load flux density in the stator core of slotless SPM machines”, IEEE International Symposium on Compatibility and Power Electronics, IEEE CPE 2013, Ljubljana, Slovenia, 5-7 June 2013.

[5] F. Luise, A. Tessarolo, F. Agnolet, S. Pieri, M. Scalabrin and P. Raffin, “A High-Performance 640-kW 10.000-rpm Halbach-Array PM Slotless Motor with Active Magnetic Bearings. Part I: Preliminary and Detailed Design”, 2014 International Symposium on Power Electronics, Electrical Drives, Automation and Motion (SPEEDAM), pp. 1237-1244, 18-20 June 2014.

[6] F. Luise, A. Tessarolo, F. Agnolet, S. Pieri, M. Scalabrin and P. Raffin, “A High-Performance 640-kW 10.000-rpm Halbach-Array PM Slotless Motor with Active Magnetic Bearings. Part I: Manufacturing and Testing”, 2014 International Symposium on Power Electronics, Electrical Drives, Automation and Motion (SPEEDAM), pp. 1245-1250, 18-20 June 2014.

[7] Tessarolo, A.; Luise, F.; Raffin, P.; Venuti, V.; “Multi-objective design optimization of a surface permanent-magnet slotless alternator for small power wind generation," Clean Electrical Power (ICCEP), 2011 International Conference on, vol., no., pp.371-376, 14-16 June 2011.

[8] Zhu, Z.Q.; Howe, D.; Chan, C.C.; "Improved analytical model for predicting the magnetic field distribution in brushless permanent- magnet machines," Magnetics, IEEE Transactions on, vol.38, no.1, pp.229-238, Jan 2002.D

[9] Atallah, K.; Zi Qiang Zhu; Howe, D.; "Armature reaction field and winding inductances of slotless permanent-magnet brushless machines," Magnetics, IEEE Transactions on, vol.34, no.5, pp.3737- 3744, Sep 1998.

[10]Pfister, P.-D.; Perriard, Y.; "Slotless Permanent-Magnet Machines: General Analytical Magnetic Field Calculation," Magnetics, IEEE Transactions on, vol.47, no.6, pp.1739-1752, June 2011.

[11]Luise, F.; Tessarolo, A.; Piera, S.; Raffin, P.; Di Chiara, M.; Agnolet, F.; Calabrian, M.; "Design and technology solutions for high- efficiency high-speed motors,” Electrical Machines (ICEM), 2012 Ext International Conference on, vol., no., pp.157-163, 2-5 Sept. 2012.

[12]P.-D. Pfister, Y. Perriard, “Very-High-Speed Slotless Permanent- Magnet Motors: Analytical Modeling, Optimization, Design, and Torque Measurement Methods”, IEEE Transactions on Industrial Electronics, vol.57, no.1, pp.296-303, Jan. 2010.

[13]R.P. Praveen, M.H. Ravichandran, V.T.S. Acharya, V.P.J. Raj, G. Madhu, G.R. Bindu, “A Novel Slotless Halbach-Array Permanent- Magnet Brushless DC Motor for Spacecraft Applications”, IEEE Transactions on Industrial Electronics, vol.59, no.9, pp.3553-3560, Sept. 2012.

[14]L. Schwager, A. Tüysüz,C. Zwyssig, J. W. Kolar; “Modeling and Comparison of Machine and Converter Losses for PWM and PAM in High-Speed Drives”, IEEE Transactions on industry applications, VOL. 50, NO. 2, march/april 2014
[15]N. Bianchi, S. Bolognani and F. Luise, "Analysis and design of a brushless motor for high speed operation," Electric Machines and Drives Conference, 2003. IEMDC'03. IEEE International, 2003, pp. 44-51 vol.1.
[16]N. Bianchi, S. Bolognani and F. Luise, "Potentials and limits of high speed PM motors," 38th IAS Annual Meeting on Conference Record of the Industry Applications Conference, 2003., 2003, pp. 1918-1925 vol.3.
[17]A. Tessarolo; F. Agnolet; F. Luise; M. Mezzarobba, “Use of Time- Harmonic Finite-Element Analysis to Compute Stator Winding Eddy-Current Losses Due to Rotor Motion in Surface Permanent- Magnet Machines,” Energy Conversion, IEEE Transactions on, vol.27, no.3, pp.670-679, Sept. 2012.
[18]A. Rahideh, T. Korakianitis, “Analytical magnetic field distribution of slotless brushless PM motors. Part 2: Open-circuit field and torque calculations”, IET Electric Power Applications, vol. 6, no. 9, pp. 639-651, November 2012.
[19]A. Rahideh, M. Mardaneh, T. Korakianitis, “Analytical 2-D Calculations of Torque, Inductance, and Back-EMF for Brushless Slotless Machines With Surface Inset Magnets", IEEE Transactions on Magnetics, vol. 49, no. 8, pp. 4873-4884, Aug. 2013.
[20]A. Tessarolo, M. De Martin, D. Diffen, M. Branz, M. Bailoni, “Practical Assessment of Homothetic Dimensioning Criteria for Induction Motors”, IET Power Electronics, Machines and Drives Conference, PEMD 2014, Manchester, UK, 8-10 April 2014, paper ID 0519.

3 ANALYTICAL COMPUTATION OF END-COIL LEAKAGE INDUCTANCE IN CONCENTRIC WINDINGS

For the reliable dynamic modeling of electric machines, it is essential that their mathematical model is determined and that the model parameters are identified with sufficient accuracy. One of the challenges in the model parameter computation is constituted by the evaluation of leakage inductances associated to the flux leakage around end coils. In fact, this leakage flux follows complicated 3D paths which are difficult to capture unless very time-consuming 3D FEA tools are employed. These 3D FEA calculations may take hours to produce a result, so their employment in the frame of design optimization processes can be even unfeasible. Relatively fast computation techniques are already available in the literature to compute end-coil leakage inductances for some end coil windings by discretizing the end coil geometry into elementary straight elements and by applying Neumann integrals and the method of mirror images to evaluate mutual inductances between end turns. The investigations being carried out in this chapter focus on a new fully analytical method that is able to estimate end coil leakage inductance with no need for geometry discretization. The method applies to specific end coil geometries, which can be however encountered in a variety of electric machines, such as in the excitation winding of wound-field round-rotor generators [1], in stator slotless windings [2], and in some concentrated-coil stator winding [3].

3.1 INTRODUCTION ON END COIL LEAKAGE INDUCTANCE EVALUATION PROBLEM

The computation of end-coil leakage inductance is a challenge in the analysis and simulation of electric machines due to the complicated 3D distribution of leakage fluxes in the winding overhang region. Such flux distribution can be studied using 3D Finite Element Analysis (FEA) which, however, is a very resource-consuming method [4],[5]. Some authors have tried to work out a parametric calculation approach for concentrated-coil end-turn leakage inductance computation based on a large amount of 3D and 2D FEA simulations [5][6].

Purely analytical-numerical algorithms, not requiring any FEA, have been proposed in the literature to estimate end coil leakage inductances of distributed windings based on solving Neumann integrals for mutual inductance computation [7] combined with the method of mirror images [8] to account for magnetic core effects [9]-[13]. When applied to the coil geometry of usual stator distributed windings, Neumann integrals do not allow for a symbolical solution [9][10][11]; their computation requires approximating each end coil as a set of elementary straight filaments [10][11][12], for which a closed-form solution of Neumann integrals is known [14]. This constitutes a significant complication because the mutual inductance between all pairs of coils results in the sum of a large number of terms [10][11]. Conversely, as theoretically investigated in [13], a fully-analytical solution to Neumann integrals can be derived when computing the end-coil leakage inductances of distributed concentric windings. In this chapter, the analytical formulations proposed in [13] are firstly verified by measurements on a small-scale laboratory setup; secondly, the validated equations are applied to the end-coil leakage inductance computation of the field windings in cylindrical-rotor synchronous machines [10], [15]. The method is, in particular, applied to a 4-pole 16-MVA medium-voltage wound-field round-rotor synchronous machine and analytical results are assessed by comparison with 3D FEA showing a satisfactory accordance. With respect to other computation techniques for end-coil leakage inductance, the proposed approach is very fast and flexible as it does not require any detailed geometry modeling, end-coil shape discretization and numerical integral solutions.

This thesis section is organized as follows: first of all, the analytical formula for mutual inductance computation between two generic end-coils is reported. Subsequently, these formulas are assessed both by measurements on a dedicated experimental equipment and by 3D FEA. After that, the validated formulas are applied to leakage inductance computation of the entire field winding referring to a 16-MVA synchronous machine for which analytical results are compared to 3D FEA computations. Finally, the chapter discusses the effect of a ferromagnetic shaft on the field winding end coil inductance.

3.1.1 EXAMPLES OF CONCENTRIC COIL WINDINGS

Three examples of concentric coil windings are shown in Figure 52. They refer to the field winding of a round-rotor generator and to the stator windings of a DC machine.

Each end-turn of such windings can be modeled as a couple of straight conductors connected by a frontal circular arc (Figure 52a). An orthogonal coordinate system (*x, y, z*) is fixed having the *z*-axis aligned with the machine axis and the *xy* plane lying on the stator or rotor core terminal surface. The generic point *P* of the end-turn is thus identified by the radius vector **r** having spherical coordinates (r, θ, Φ) or cylindrical coordinates (r, θ, z) the second case is represented in Figure 53.

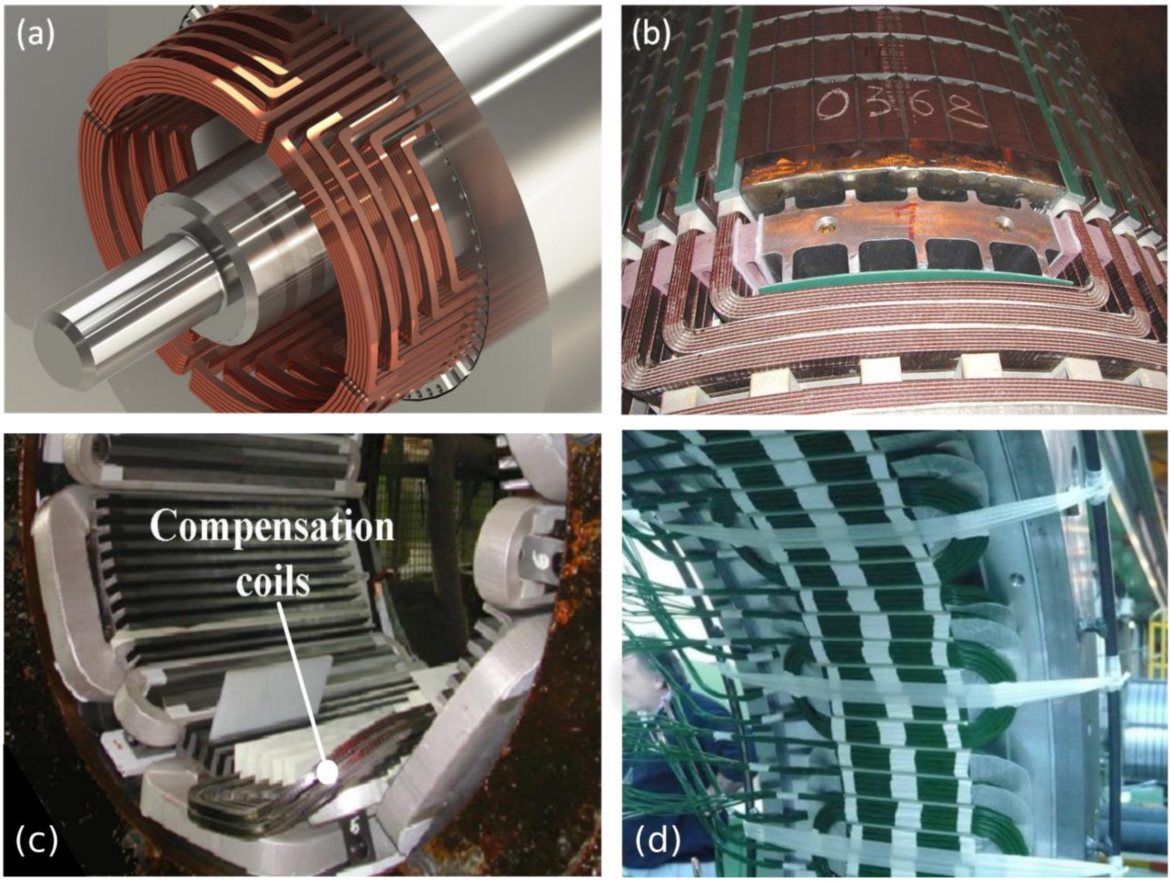

Figure 52: Examples of concentric windings in electric machines during manufacturing: (a) rendered 3D image of a round rotor synchronous machine field winding (b) Real image of a turbo-alternator rotor with visible rotor windings (c) Stator compensator windings of a dc machine (d) stator windings of a slotless SPM machine

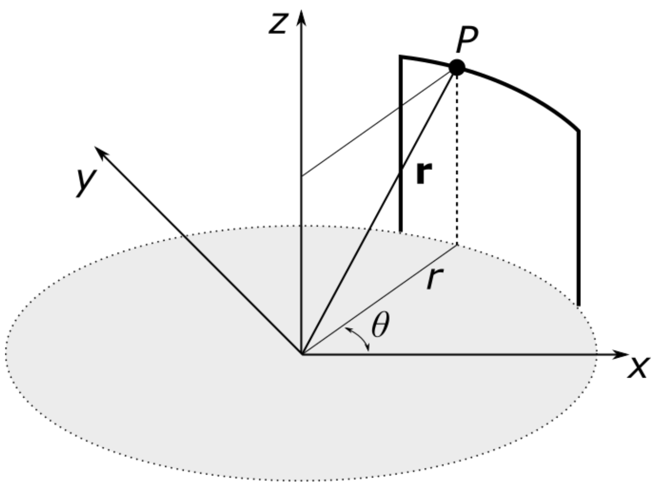

Figure 53: Model of a single end-turn with point P radius vector identified with cylindrical coordinate system

3.2 Analytical formula for the mutual inductance determination between two coils

As reported in the previous section, the coil shape taken into account is a sort of cylindrical section and that is a good representation of coils reported in Figure 52.

3.2.1 End coil geometric modeling

As a first step for determining the leakage inductance of this kind of end windings is the analytical calculation of the mutual inductance between two generic end turns, modeled as ideal filaments with infinitesimal cross section as shown in Figure 54. The geometric model of the two end turns is represented in Figure 54 with solid lines (curves ABCD, A'B'C'D', respectively), while dashed lines indicate fictitious conductors that need to be introduced for the mutual inductance computation through the method of mirror images.

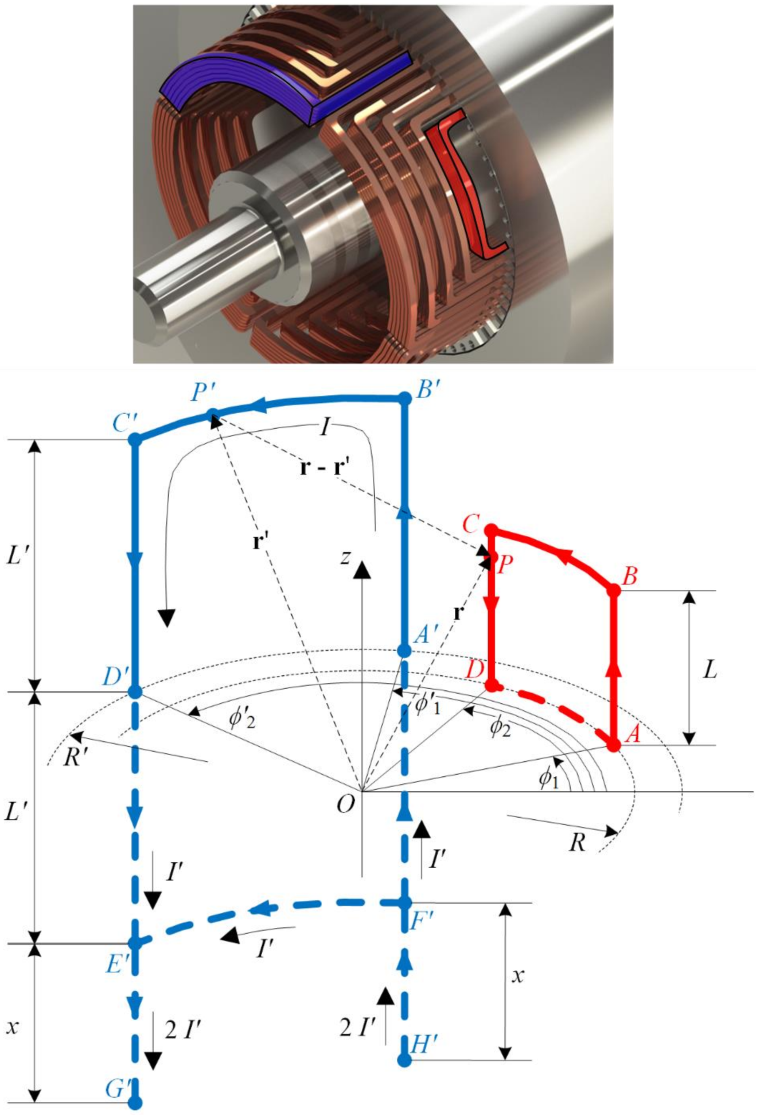

Figure 54: Geometric modeling of two end coils with a possible correspondence in a synchronous machine field. Dashed lines represent fictitious conductors used for the mutual inductance calculation (method of the images)

The approach followed to compute the mutual inductance is to impress a current I in one end turn ($A'B'C'D'$) and to compute the flux λ linked by the other end turn, i.e. the flux linked by the closed loop ABCD. The mutual inductance is hence derived as λ/I. In order to account for stator and rotor magnetic core effects through the method of mirror images, the finite fictitious conductors $D'E'$, $E'F'$ and $A'F'$, carrying the current I', are introduced [8], [10]. Moreover, the further fictitious conductors $E'G'$ and $F'H'$, carrying the current $2I'$, are used such that their length x tends to infinity.

The value of the ideal current I' depends on the relative magnetic permeability μ_r of the stator and rotor cores. In the following of this work the assumption will be made that the iron cores have infinite magnetic permeability ($\mu_r = \infty$) with respect to the air. Using this hypothesis, 1.68 leads to set $I' = I$, in fact, imposing the relative permeability of the air equal to one 1.68 can be rewritten as follows:

$$I' = I \cdot \frac{\mu_r - 1}{\mu_r + 1} \xRightarrow[if\ \mu_r \to \infty]{} I' = I \cdot \lim_{\mu_r \to \infty} \frac{\mu_r - 1}{\mu_r + 1} = I \qquad 3.1$$

The reason for adding the fictitious conductors shown in Figure 54 and the justification for the currents flowing through them are extensively explained in [8] and [10], where the method of mirror images is applied to the computation of electric machine end winding leakage inductance.

The infinitely permeable stator and rotor cores are approximated as the semi-space *z*<0 in the cylindrical coordinate system with origin *O* as shown in Figure 54. In such coordinate system, the proposed geometric modeling makes it possibly to univocally identify the shape of the two generic end coils through the set of parameters $\phi_1, \phi_2, R, L\ and\ \phi_1', \phi_2', R', L'$ respectively, hence the mutual inductance between these end coils will be indicated as:

$$M_{(\phi_1,\phi_2,L,R)-(\phi_1',\phi_2',L',R')} \qquad 3.2$$

3.2.2 Analytical expression through Neumann integrals

Making use of Neumann integrals [13], applied to the geometric model shown in Figure 54 leads to the following expression of the mutual inductance between the two end coils:

$$\begin{aligned} M_{(\phi_1,\phi_2,L,R)-(\phi'_1,\phi'_2,L',R')} = \frac{\mu_0}{4\pi}\Bigg\{ & \oint_{ABCD}\int_{A'B'C'D'} \frac{d\mathbf{r}\cdot d\mathbf{r}'}{|\mathbf{r}-\mathbf{r}'|} + \oint_{ABCD}\int_{D'E'} \frac{d\mathbf{r}\cdot d\mathbf{r}'}{|\mathbf{r}-\mathbf{r}'|} + \\ & + \oint_{ABCD}\int_{F'A'} \frac{d\mathbf{r}\cdot d\mathbf{r}'}{|\mathbf{r}-\mathbf{r}'|} + \oint_{ABCD}\int_{F'E'} \frac{d\mathbf{r}\cdot d\mathbf{r}'}{|\mathbf{r}-\mathbf{r}'|} + \\ & + 2\oint_{ABCD}\int_{E'G'} \frac{d\mathbf{r}\cdot d\mathbf{r}'}{|\mathbf{r}-\mathbf{r}'|} + 2\oint_{ABCD}\int_{H'F'} \frac{d\mathbf{r}\cdot d\mathbf{r}'}{|\mathbf{r}-\mathbf{r}'|} \Bigg\} \end{aligned} \qquad 3.3$$

In (3.3), $\mathbf{r}$ and $\mathbf{r}'$ are the vectors radii that identify two generic points lying on the two end turn models as shown in Figure 54 and integrals are performed over oriented paths (e.g. $D'E'$ indicates the oriented segment which begins at D' and ends at E').

Equation (3.3) can be rewritten as follows:

$$m_{ij} = \frac{\mu_0}{4\pi}\left(N_{str} + N_{arc} + N_{inf}\right) \tag{3.4}$$

where: N_{str} is the sum of Neumann integrals including straight segments of finite length; N_{arc} is the sum of Neumann integrals including circular arcs; and N_{inf} is the sum of Neumann integrals including straight segments whose length tends to infinity; in symbols:

$$N_{str} = \int_{AB\cup CD} \int_{F'B'\cup C'E'} \frac{d\mathbf{r} \times d\mathbf{r}'}{|\mathbf{r} - \mathbf{r}'|} \tag{3.5}$$

$$N_{arc} = \int_{BC\cup DA} \int_{B'C'\cup F'E'} \frac{d\mathbf{r} \times d\mathbf{r}'}{|\mathbf{r} - \mathbf{r}'|} \tag{3.6}$$

$$N_{inf} = 2\int_{AB\cup CD} \int_{E'G'\cup H'F'} \frac{d\mathbf{r} \times d\mathbf{r}'}{|\mathbf{r} - \mathbf{r}'|} \tag{3.7}$$

In the following section, a closed-form analytical expression for the terms (3.5-3.7) is provided based on the mathematical derivations detailed in [13].

3.2.2.1 *Terms accounting for finite straight elements*

The term N_{str} can be written as:

$$N_{str} = n_{str}(\phi_1, \phi_1') + n_{str}(\phi_2, \phi_2') - n_{str}(\phi_1, \phi_2') - n_{str}(\phi_2, \phi_1') \tag{3.8}$$

where the $n_{str}(x, y)$ is defined as follows:

$$n_{str}(x, y) = \left\{ \sum_{k=-1,1} \left\{ k(L' + kL)\operatorname{asinh}\left(\frac{L' + kL}{d(x, y)}\right) - k\sqrt{(L' + kL)^2 + d(x, y)^2} \right\} \right. \tag{3.9}$$

where $d(x, y)$ can be defined as follows:

$$d(x, y) = \sqrt{R^2 + R'^2 - 2RR'\cos(x - y)} \tag{3.10}$$

3.2.2.2 *Terms accounting for the circular arcs*

The term N_{arc} can be expressed as:

$$N_{arc} = n_{arc}(L, \theta, \theta') + n_{arc}(L, \theta, \pi - \theta') - n_{arc}\left(0, \tfrac{\pi}{2}, \theta'\right) - n_{arc}\left(0, \tfrac{\pi}{2}, \pi - \theta'\right) \tag{3.11}$$

where the function $n_{arc}(x, y)$ is defined by following formula:

$$n_{arc}(\ell, x, y) = \frac{RR'}{r_>(\ell)} \left\{ U + \sum_{n=1}^{+\infty} \left[\frac{r_<(\ell)}{r_>(\ell)}\right]^n \sum_{m=0}^{n} K_{n,m} P_n^m(\cos(x)) P_n^m(\cos(y)) V_m \right\} \tag{3.12}$$

And the angles θ and θ' are given by:

$$\theta = \mathrm{atan2}(L, R)\,,\ \theta' = \mathrm{atan2}(L', R') \qquad 3.13$$

In the formula number 3.12 the term $P_m^n(x)$ is the associated Legendre polynomial expression [16] and can be expressed as the following finite sum:

$$P_n^m(x) = \frac{(1-x^2)^{m/2}}{2^n} \sum_{k=0}^{\mathrm{floor}(n/2)} (-1)^{k+m} m! \binom{n}{k} \binom{2n-2k}{n} \binom{n-2k}{m} x^{n-2k-m} \qquad 3.14$$

the functions $r_<(\ell)$, $r_>(\ell)$ are given by:

$$\begin{aligned} r_>(\ell) &= \max\left(\sqrt{R^2+\ell^2}, \sqrt{R'^2+L'^2}\right) \\ r_<(\ell) &= \min\left(\sqrt{R^2+\ell^2}, \sqrt{R'^2+L'^2}\right) \end{aligned} \qquad 3.15$$

and the constants U, V_m, K_m, n are defined as follows:

$$K_{n,m} = \begin{cases} 1/2 & \text{if } m = 0 \\ (n-m)!/(n+m)! & \text{if } m \neq 0 \end{cases}$$

$$U = \sum_{j=0,1} \sum_{k=0,1} (-1)^{j+k} \cos(c_{j,k}) \qquad 3.16$$

$$V_m = \begin{cases} \displaystyle\sum_{j=0,1} \sum_{k=0,1} \sum_{q=-1,1} (-1)^{j+k} \frac{\cos[c_{j,k}(m+q)]}{(m+q)^2} & \text{if } m \neq 1 \\ \displaystyle\sum_{j=0,1} \sum_{k=0,1} (-1)^{j+k} \left[\frac{\cos^2(c_{j,k})}{2} + b_{j,k}\right] & \text{if } m = 1 \end{cases}$$

with:

$$\begin{aligned} c_{j,k} &= \phi_1 + j(\phi_2 - \phi_1) - [\phi_1' + k(\phi_2' - \phi_1')] \\ b_{j,k} &= [\phi_1 + j(\phi_2 - \phi_1)][\phi_1' + k(\phi_2' - \phi_1')] \end{aligned} \qquad 3.17$$

3.2.2.3 Terms accounting the infinite straight elements

The term N_{inf} in 3.4 can be expressed as:

$$N_{inf} = 2\left[n_{inf}(\phi_1, \phi_1', \phi_2') - n_{inf}(\phi_2, \phi_2', \phi_1')\right] \quad 3.18$$

where the function $n_{inf}(x, y, z)$ is defined as follows:

$$\begin{aligned} n_{inf}(x,y,z) = L \ln\left[\frac{d(x,z)}{d(x,y)}\right] + \sum_{k=0,1}\Bigg\{(-1)^k (kL+L')\left[\operatorname{asinh}\left(\frac{L'+kL}{d(x,y)}\right) - \operatorname{asinh}\left(\frac{L'+kL}{d(x,z)}\right)\right] + \\ -(-1)^k\left[\sqrt{(kL+L')^2 + d(x,y)^2} - \sqrt{(kL+L')^2 + d(x,z)^2}\right]\Bigg\} \end{aligned} \quad 3.19$$

It is clear that, based on the definitions (3.8, 3.11 and 3.18), these formulas have to be substituted into 3.4 to evaluate the mutual inductance between two general coils (in terms of position, opening and axial length as shown in Figure 54).

3.2.3 EXPERIMENTAL AND 3D FEA VALIDATION

In the previous Section, the fully analytical formulas have been provided to compute the mutual inductance $M_{(\phi_1,\phi_2,L,R)-(\phi_1',\phi_2',L',R')}$ between two infinitely-thin end turns characterized by parameters ϕ_1, ϕ_2, R, L and ϕ_1', ϕ_2', R', L' respectively, as illustrated in Figure 54. In this section, the mentioned formulas are assessed with two independent approaches, namely: by experiments on a dedicated laboratory set-up and by 3D FEA.

3.2.3.1 Experimental Validation

The experimental setup is built using the stator of an induction motor with a source coil (including N' turns) fixed to the stator bore as shown in Figure 55a (the characteristic data $N', \phi_1', \phi_2', R', L'$ of the source coil are given in Table I). A dummy rotor, made of a laminated silicon steel stack, is also built and a search coil (including *N* turns) is connected to its axis as shown in Figure 55b. The air gap width is 2 mm.

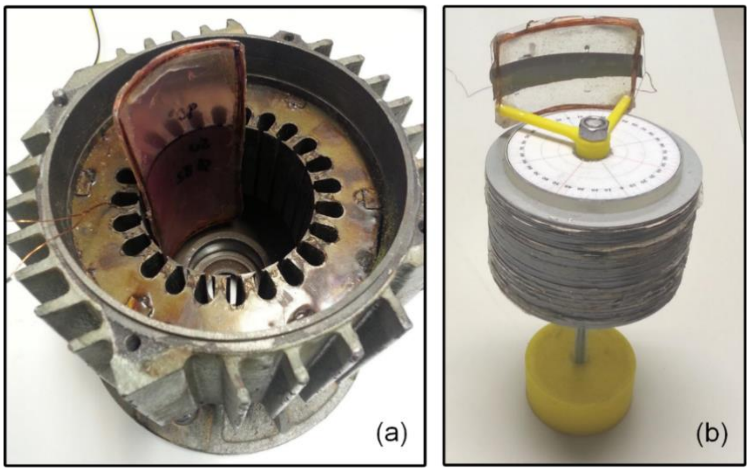

Figure 55: (a) Stator core and frame with the search coil fixed to the stator bore; (b) Dummy rotor core with the search coil fixed on its axis.

Table I: Characteristic dimensions of the end coils used for experimental validations

Source coil		**Search coil**	
L'	48 mm	L	35 mm
R'	41 mm	R	40 mm
$\phi'_2-\phi'_1$	90°	$\phi_2-\phi_1$	80°
N'	5	N	20

The search coil (whose characteristic data N, ϕ_1, ϕ_2, R, L are given also in Table I), can freely rotate around the rotor axis as illustrated in Figure 55b.

The entire assembly of the experimental setup is shown in Figure 56 for two possible angular positions of the search coil. From Figure 56 it can be also seen how the angular position of the search coil can be precisely identified by means of an angular graduated scale fixed to the dummy rotor stack.

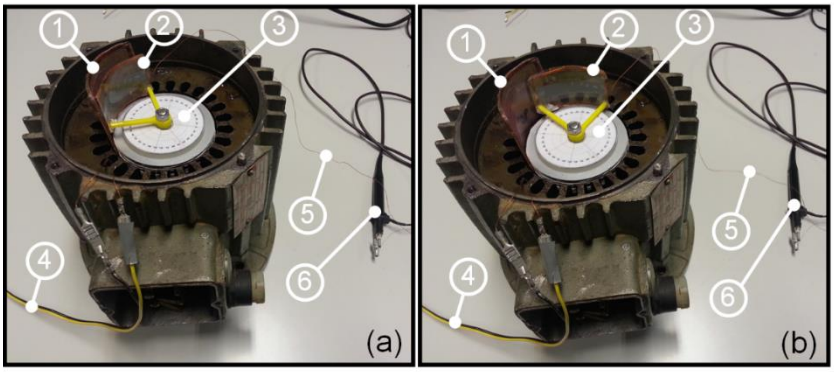

Figure 56: Experimental setup for the verification of mutual inductance calculation between end coils. The figure shows the equipment for two different positions (a) and (b) of the search coil

Each element of the experimental setup is described below referring to Figure 56 for the object identification:

Experimental setup elements
① Source coil
② Search coil
③ Graduated angular scale
④ Supply terminals of the source coil
⑤ Twisted terminals of the search coil
⑥ Voltage probe

For the experimental validation, the source coil is energized with a variable sinusoidal current I at a frequency f = 50 Hz and the electromotive force (EMF) E induced between the search coil terminals is measured. The measurement is repeated for various displacement angles α between the source and search coil axes and, for each measurement, the mutual inductance between the two end coils is computed as follows:

$$M_{test}(\alpha) = \frac{E}{2\pi\, f\, I} \tag{3.20}$$

The measurement is compared to the analytical calculation, that is:

$$M_{analyt}(\alpha) = M_{(\phi_1+\alpha,\phi_2+\alpha,L,R)-(\phi'_1,\phi'_2,L',R')} \times N \times N' \tag{3.21}$$

where N and N' are the number of turns for the search and source coils respectively.

The result of the comparison between the analytical and measurement results is provided in Figure 57 showing a satisfactory accordance.

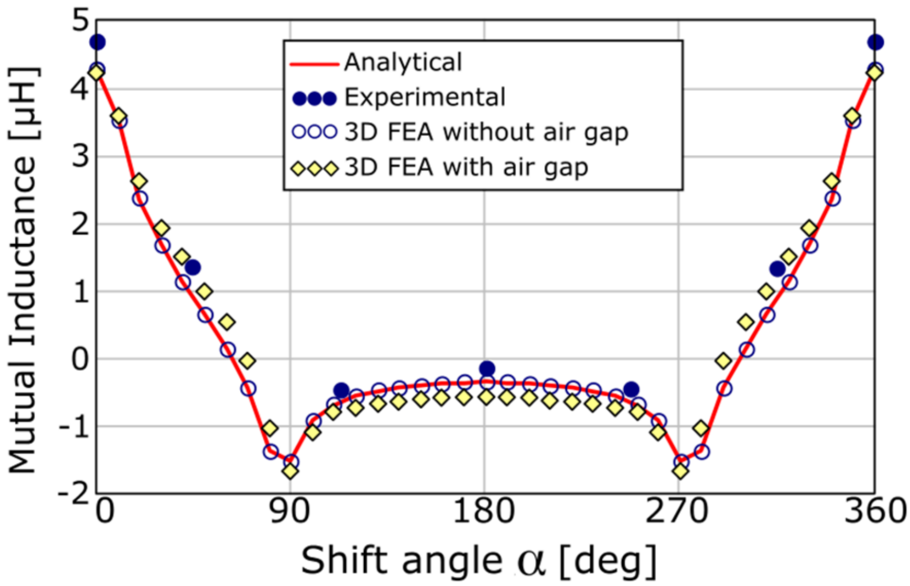

Figure 57: Comparison between mutual inductance values obtained analytically, experimentally and by 3D FEA.

3.2.3.2 3D FEA validation

A further validation is performed using 3D FEA based on the meshed model shown in Figure 58. The two end coils used in the experiment (Figure 55 and Figure 56) emerge from a circular ferromagnetic slab of ideally infinite relative magnetic permeability $\mu_r = 2 \cdot 10^5$) which represents the stator and rotor cores. While the source coil passes through the ferromagnetic slab, the search coil is modeled as a closed loop by adding the fictitious arc identified by "③" in Figure 58. The source coil (composed of N' turns) is then energized with a current I, while the flux λ linked by the search coil (composed of N turns) is computed by 3D FEA. The computation is repeated for different shift angles α between the two end coil axes and, in each case, the mutual inductance is derived as:

$$M_{FEA}(\alpha) = \frac{\lambda}{I} \qquad 3.22$$

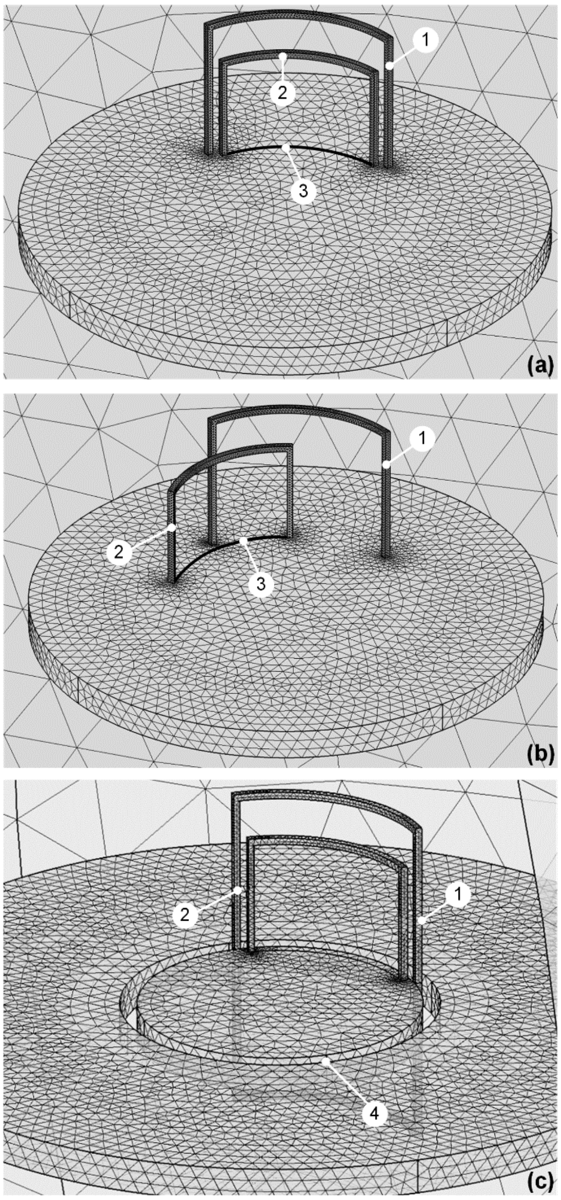

Figure 58: 3D model for FEA validation. 1 source coil; 2 search coil; 3 fictitious arc needed to make the search end coil a closed loop. 4 Air gap. (a) and (b) show the model with no air gap for two different shift angles α between the end coils; (c) shows the model with a 3-mm air gap.

Furthermore, the simulation is performed both on a model without air gap (Figure 58a and b) and on a model including an air gap with different possible widths (Figure 58c), in order to investigate the air gap influence on inductance calculation.

The mutual inductance as a function of the shift angle α computed by 3D FEA on the model with no air gap and on a model with 3 mm air-gap width is plotted in Figure 57 and can be seen to be in good agreement with the analytical prediction. The air gap actually affects mutual inductance values as it alters the spatial end-coil leakage field distribution, but the resulting errors are such that they do not invalidate the accuracy of the computation. By reducing the air gap width g in the 3D FEA model (in the experimental set-up g=2 mm), the results obtained by 3D FEA tend to converge to the analytically computed values, up to practically coinciding with them when the air gap vanishes (Figure 57).

The possibility to disregard air-gap effects while preserving an acceptable accuracy in end coil leakage inductance prediction is confirmed by various works [8],[10],[11] where, in spite of this approximation, a good accordance is achieved between measurements and calculations. Interesting attempts to include air-gap effects by means on suitable “virtual air-gap conductors” appear in some recent works [12], although lacking assessment by either experiments or 3D FEA simulations. The introduction of virtual air-gap conductors could be a possible way to further increase the accuracy of the method in future researches.

3.3 INDUCTANCE COMPUTATION FOR THE ENTIRE FIELD WINDING

In this section the problem is addressed to determine the end coil inductance of the entire field winding for a round-rotor synchronous machine with a number of poles equal to *P*. The structure of the field winding is illustrated in Figure 59 where it can be seen that each of the *P* poles includes *K* coils of different size. Each end coil is denoted as $C_{p,k}$ (with *p*=1...*P* and *k*=1...K) and is composed of N_k series-connected turns, each of length l_k.

The total end-coil inductance L_{tot} of the winding can be computed as follows [13]:

$$L_{tot} = 2\left[P \sum_{k=1..K} L_k + \sum_{\substack{p,p'=1..P \\ p\neq p'}} \sum_{\substack{k,k'=1..K \\ k\neq k'}} (-1)^{p+p'} M_{p,k,p',k'} \right] \qquad 3.23$$

where: the coefficient 2 is used to account for end coils at both rotor ends, L_k is the self-inductance of coil $C_{p,k}$ (which is independent of p) and $M_{p,k,p',k'}$ is the mutual inductance between two generic distinct coils $C_{p,k}$ and $C_{p',k'}$. The coefficient $(-1)^{p+p'}$ accounts for the fact that the field current reverses when we move from one field pole to the adjacent one.

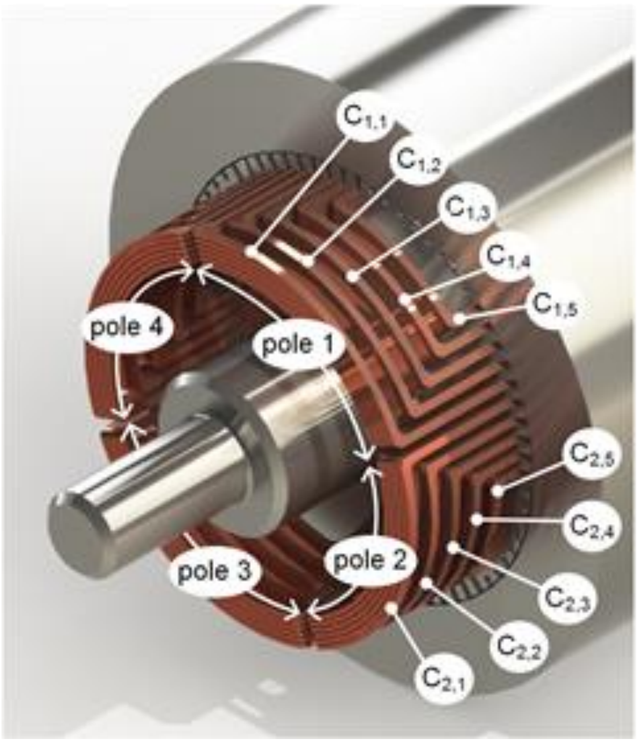

Figure 59: Illustration of a 4-pole field winding with five coils per pole. $C_{p,k}$ indicates the k-th coil of the p-th pole.

3.3.1 SELF-INDUCTANCE OF AN END COIL

In order to evaluate the total leakage inductance of the entire circuit it is necessary to calculate the self-inductance L_k of the generic $C_{p,k}$ coil. This quantity can be expressed as the sum of two contributions:

$$L_k = L_k^{(int)} + L_k^{(ext)} \qquad 3.24$$

where $L_k^{(int)}$ is the "internal inductance" [10] due to the flux crossing the conductors, and $L_k^{(ext)}$ is the "external inductance" due to the flux linked by the coil but not crossing the conductors. Following [10], the internal inductance is computed approximating the coil as a circular conductor, so that $L_k^{(int)}$ is independent of the coil cross section and only depends on the end coil length l_k as follows:

$$L_k^{(int)} = N_k^{\ 2} \frac{\mu_0}{8\pi} \cdot l_k \qquad 3.25$$

where the end coil length is easily computed based on its dimensions *L*, *R* and $\phi_1 - \phi_2$.

As regards the external self-inductance of the generic end coil $C_{p,k}$, it is computed following the procedure described in [11]. For this purpose, in each end coil $C_{p,k}$ two curves Γ_{pk} and $\Lambda_{p,k}$ are defined as illustrated in Figure 60 and in Figure 61.

Γ_{pk} is an open curve developing along the mean path of the end coil (Figure 60b), while $\Lambda_{p,k}$ is a closed loop that unfolds along the internal periphery of the end coil (Figure 60b, Figure 61). The internal inductance is then computed using the algorithms explained in chapter 3.2 where Γ_{pk} acts as the source turn (curve $A'B'C'D'$ in Figure 54) and $\Lambda_{p,k}$ acts as the search turn (closed curve ABCD in Figure 54). Hence:

$$L_k^{(ext)} = N_k^{\ 2} M_{\Lambda_{p,k} - \Gamma_{p,k}} \qquad 3.26$$

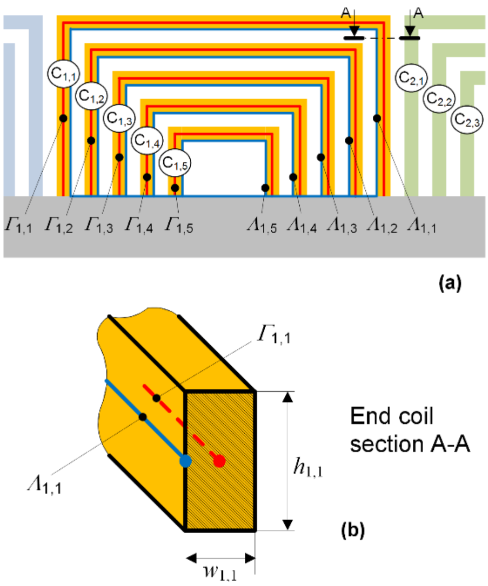

Figure 60: (a) End coils C_{11}, ..., $C_{1,5}$ of pole 1 and relevant curves Γ_{11}, ..., $\Gamma_{1,5}$ and Λ_{11}, ..., $\Lambda_{1,5}$. (b) Section A-A of end-coil $C_{1,1}$ illustrating the position of the auxiliary curves $\Gamma_{1,1}$ and $\Lambda_{1,1}$.

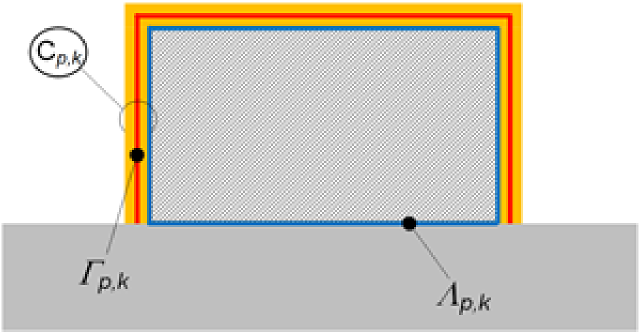

Figure 61: Detail of the two curves $\Gamma_{p,k}$ and $\Lambda_{p,k}$ associated with the end coil $C_{p,k}$ for the computation of the internal self-inductance L_k.

3.3.2 MUTUAL INDUCTANCE BETWEEN DISTINCT END-COILS

The mutual inductance between two distinct end coils $C_{p,k}$ and $C_{p',k'}$ (3.23) is computed using the algorithms given in chapter 3.2 where the source and search turns are the mean curves Γ_{pk} and $\Gamma_{p'k'}$ respectively placed in the middle of the two mentioned end coils. Hence:

$$M_{p,k,p',k'} = N_k N_{k'} M_{\Gamma_{p,k}-\Gamma_{p',k'}} \tag{3.27}$$

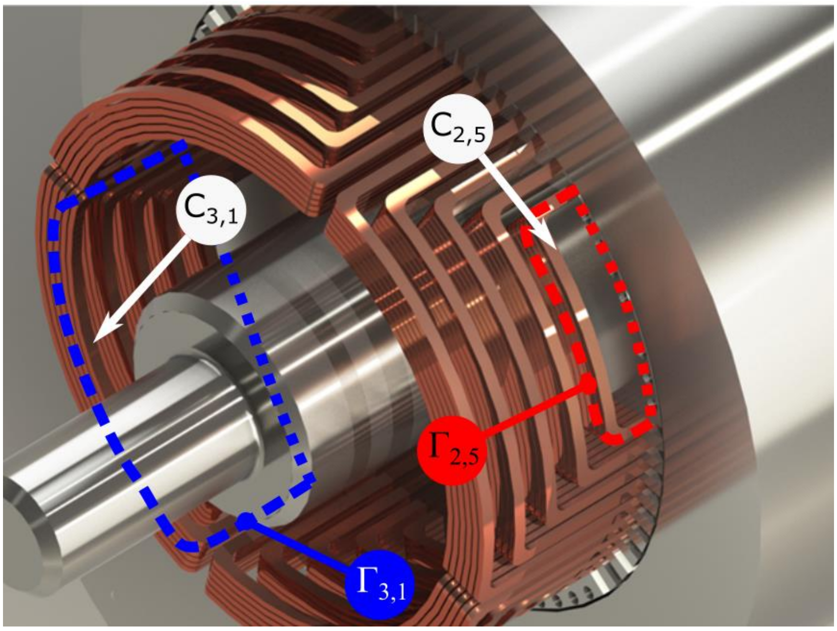

Figure 62:Example of $C_{p,k}$ and $C_{p',k'}$ identification in a concentric winding with their respective Γ_{pk} and $\Gamma_{p'k'}$ curves

3.3.3 APPLICATION EXAMPLE AND 3D FEA VALIDATION

The analytical procedure described in the previous chapter is herein applied to compute the end coil leakage inductance of a medium-voltage (MV) synchronous generator whose ratings are provided in the following Table II.

Table II: Ratings of the machine used for validation

Rated power	16.2 MVA
Rated voltage	11 kV
Number of poles	4
Rated speed	1500 r/min
Rated power factor	0.85
Rated efficiency	0.98

The field winding end coil structure is that shown in Figure 62. The detailed dimensions and number of turns of all individual end coils (including the auxiliary curves Γ_{pk} and $\Lambda_{p,k}$ associated to them as explained in Section 3.3.1) are provided in table III, which refers to the generic *p*-th pole of the machine (for the other poles, the data are the same). The nomenclature used in table III to identify dimensions is the same introduced in section 3.2 to characterize infinitely-thin end turns (for the sake of clarity the figure of the generic coils situation is reported again in Figure 63 in this section)

Regarding the end coil cross section dimensions (Figure 60b), all end coils share the following sizes: $w_{p,k} = 21\ mm,\ h_{p,k} = 84\ mm$ with: *p*=1...4 and *k*=1...5.

Table III: Dimensions and number of turns for the end coils of the p-th pole

Coil	N. of turns	Curve	*L* [mm]	*R* [mm]	$\phi_2 - \phi_1$ [deg]
$C_{p,1}$	$N_1 = 6$	$\Gamma_{p,1}$	248	410	85
		$\Lambda_{p,1}$	237	410	82
$C_{p,2}$	$N_2 = 6$	$\Gamma_{p,2}$	204	410	75
		$\Lambda_{p,2}$	193	410	72
$C_{p,3}$	$N_3 = 6$	$\Gamma_{p,3}$	160	410	65
		$\Lambda_{p,3}$	149	410	62
$C_{p,4}$	$N_4 = 6$	$\Gamma_{p,4}$	116	410	55
		$\Lambda_{p,4}$	105	410	52
$C_{p,5}$	$N_5 = 6$	$\Gamma_{p,5}$	72	410	45
		$\Lambda_{p,5}$	61	410	42

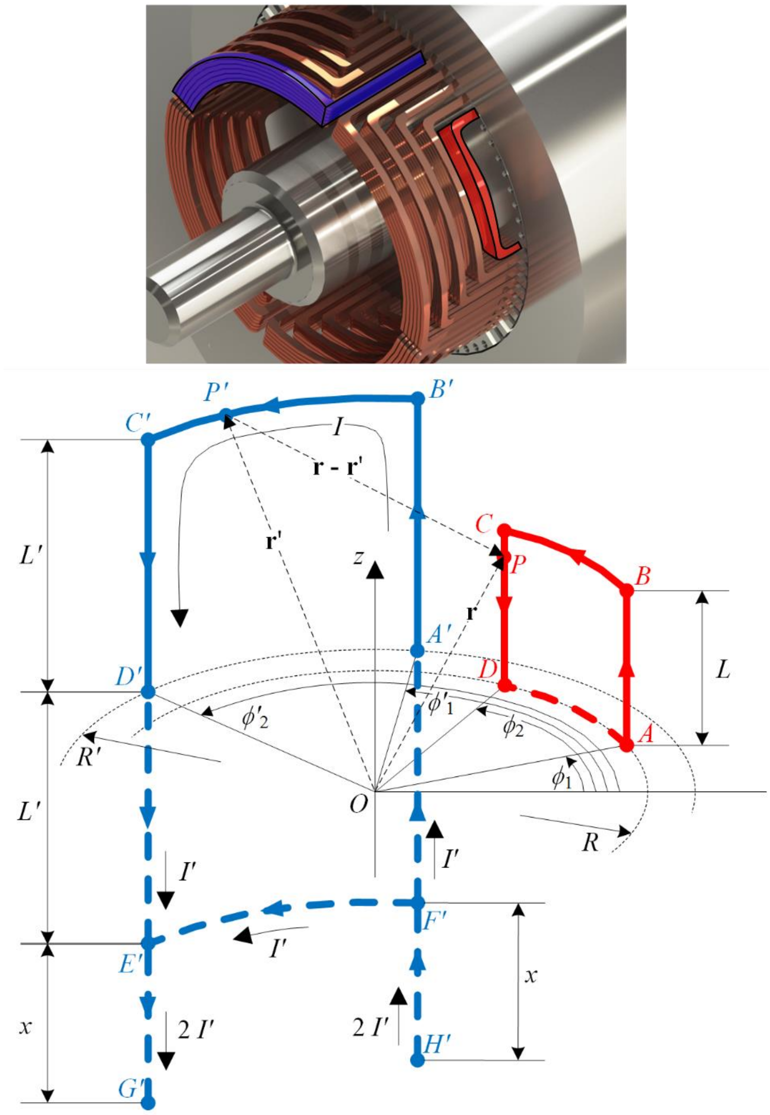

Figure 63: Geometric modeling of two end coils with a possible correspondence in a synchronous machine field.

For the purpose of a numerical validation, the machine has been modeled for 3D magneto-static FEA. The meshed model used for this purpose is shown in Figure 64 and does not have any damper winding. In order to assess the influence of ammortisseur circuits, which are generally mounted in the rotor, a time-harmonic 3D FEA simulation is also performed on a generator model equipped with damper windings as shown in Figure 65. This figure shows that front aluminum plates are used as end connections to short circuit damper bars. The same components also act as clamping plates for the rotor laminated stack. End plates and damper bars need to be modeled with a small mesh size because eddy currents occur in them when the field is supplied by an AC current.

For the magneto-static simulation, the field circuit is energized with its rated no-load DC current (0 Hz), while for the time-harmonic simulation the same current is applied with a frequency of 50 Hz. The magneto-static and time-harmonic FEA solutions in the core region are shown in Figure 66a-b, respectively. It can be seen that, in presence of an AC field supply, a reaction current (e.g. I_d in Figure 66b) is induced in rotor dampers such that it weakens the air-gap flux produced by the field current (e.g. If in Figure 66a-b) in accordance with Faraday-Lenz law. The leakage fluxes produced in the end region by the field current I_f and by the damper current I_d are qualitatively sketched in Figure 66c. It can be noticed that the end leakage flux φ_d due to the damper reaction current counteracts the end leakage flux φ_f due to the field current as it happens in the core region (Figure 66b). This is expected to result in a reduced field end-coil flux linkage when the damper is present and reactive.

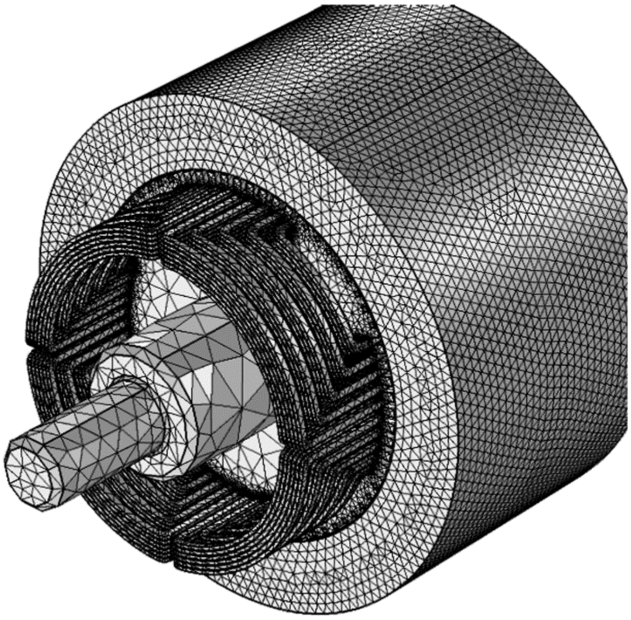

Figure 64: Generator meshed model (without damper cage) used for magneto-static 3D FEA.

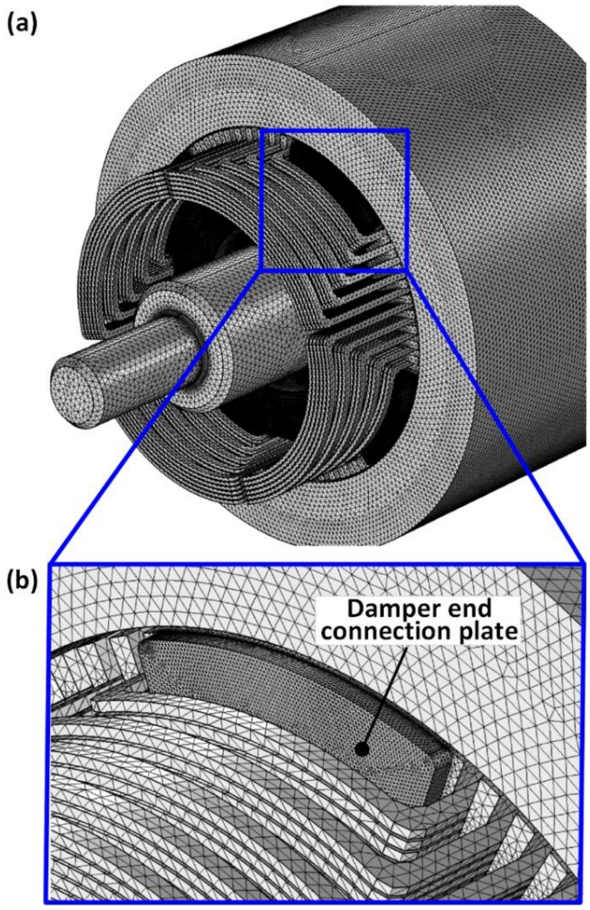

Figure 65: Generator meshed model (with damper cage) used for time-harmonic 3D FEA.

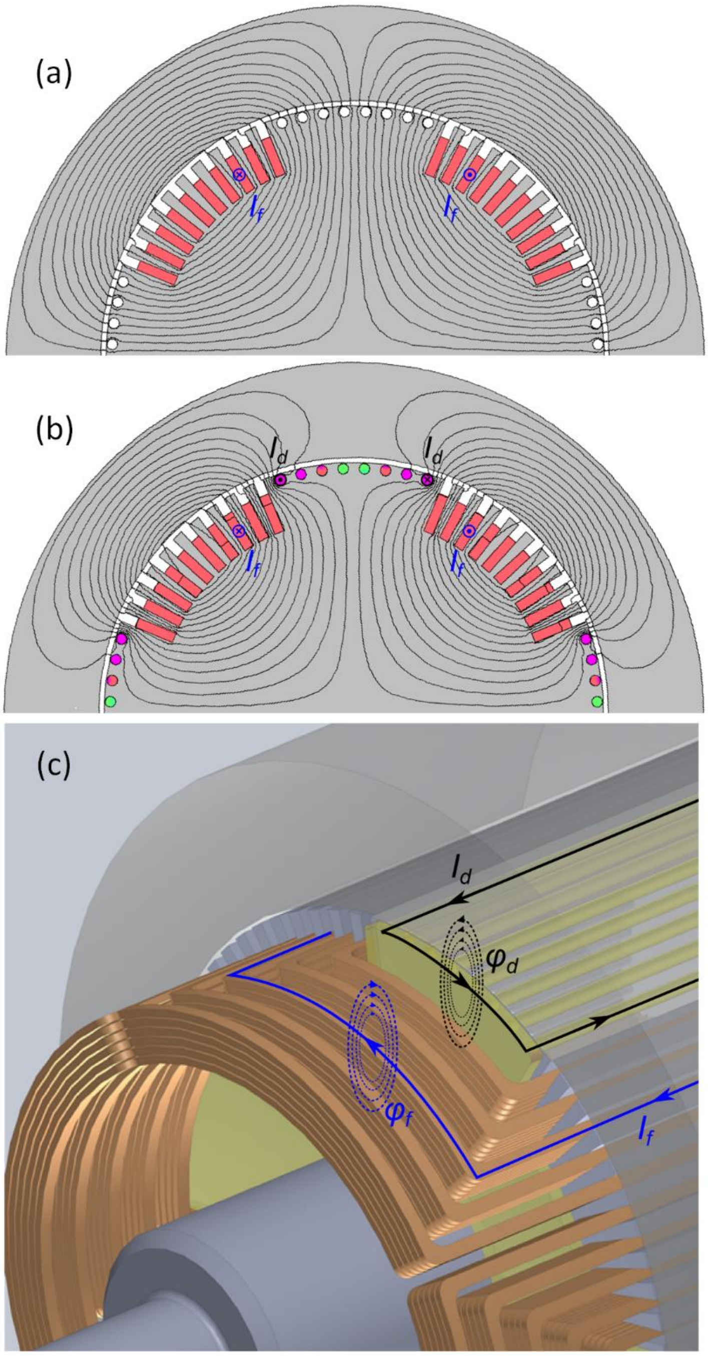

Figure 66: (a) Magneto-static solution in the core region. (b) Time-harmonic solution in the core region. (c) Schematic of field and damper currents with the relevant end leakage fluxes.

For both the magneto-static and the time-harmonic 3D FEA simulations, the field circuit end-coil leakage inductance is computed as:

$$\lambda_{field} / I_{field} \tag{3.28}$$

where λ_{field} is the peak value of the total flux linked by all the end coils (at both rotor ends) and I_{field} is the peak value of the field current. The results obtained are provided in Table IV.

Table IV: End coil leakage inductance computation results

Analytical method		1.53 mH
3D FEA	Magnetostatic (0 Hz)	1.57 mH
	Time-harmonic (50 Hz)	1.55 mH

The results shown in Table IV confirm that there is a slight reduction in the inductance obtained from the time-harmonic FEA as an effect of the end field due to damper reaction currents. However, the reduction is extremely small, proving that the end leakage flux produced by the reaction current in the damper end connection (schematically indicated as φ_d in Figure 66c) is very weakly linked by field-circuit end coils. It therefore appears that the damper cage does not have a significant influence on the field end-coil leakage inductance in the machine under study. However, this result is not claimed to be general as other kinds of damper cage construction (especially in regard to the end connection technology) may lead to different conclusions.

More importantly, what clearly appears from Table IV is that the leakage inductance value predicted analytically is in very good accordance with the results of 3D FEA simulations, with an estimation error in the order of 2%. This is consistent with the good agreement already found in the chapter 3.2 in both experimental and 3D FEA assessments. However, while in chapter 3.2 both the 3D FEA and the analytical model assumed an infinitesimal cross section for the end turns, in the validation example reported in this part the end coils have finite thickness and their actual rectangular cross section is approximated as circular so as to compute the internal leakage inductance according to (3.25). As already found by other authors [10], the approximation is demonstrated not to introduce a remarkable error since the internal inductance accounts for a small portion of the overall leakage inductance being evaluated. Moreover, in the 3D generator model shown in Figure 64 there is an air gap (whose width is 5 mm), which is not considered by the analytical model. In spite of this approximation, the analytical result exhibits a very good agreement with the 3D FEA simulation, confirming what has been already observed in chapter 3.2.3 about the possibility to neglect air-gap effects without significant errors in the field circuit end-coil leakage inductance computation.

A further simplification underlying the results in table IV is the fact that the analytical model disregards the ferromagnetic shaft which is included in the machine model for 3D FEA. This approximation is proved to introduce negligible errors, too, at least for the machine geometry under study (Figure 64). The effect of a ferromagnetic shaft of different possible diameters is studied in more detail and in more general terms in the following section.

3.3.4 FERROMAGNETIC SHAFT EFFECTS IN THE END WINDING LEAKAGE COMPUTATION

In order to investigate the influence of a ferromagnetic shaft on the field winding end coil inductance, the 3D model shown in Figure 67 is adopted. The situation is the same explored in 3.2 except that a ferromagnetic shaft of radius R_S is included. The mutual inductance is computed by 3D FEA between the two end coils shown in Figure 67, which are characterized by the data given in Table V. For clarity, the average Rm of the two end coil radii R and R' is introduced:

$$R_m = (R + R')/2 \qquad 3.29$$

Table V: Characteristic data for the end-winding coils

Source coil		Search coil	
L'	48 mm	L	35 mm
R'	41 mm	R	40 mm
$\phi'_2-\phi'_1$	90°	$\phi_2-\phi_1$	80°
N'	5	N	20

Figure 68 shows the mutual inductance between the two end coils as a function of their displacement angle α and for different shaft radii R_S. It can be seen that some non-negligible effect occurs when the shaft radius exceeds 40% of the mean end coil radius R_m.

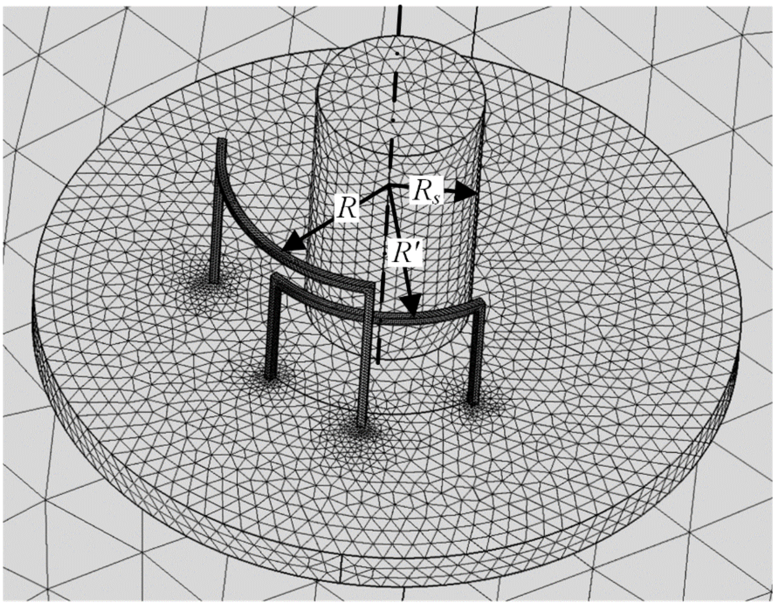

Figure 67: 3D model used to study shaft effects on the mutual inductance between end coils

The shaft effect on end coil leakage inductance values is further clarifier in Figure 69, where the mutual inductance between two end coils, fixed in a given mutual position with displacement angle α, is plotted versus the shaft radius.

In the case study addressed in Section 3.3.3 (Figure 65), the shaft radius is significantly smaller than 40% of the mean end coil radius, hence shaft effects can be reasonably neglected in the analytical calculations without introducing remarkable errors as proven by the good accordance found between computation and FEA results. For different geometries where the shaft is ferromagnetic and features a larger size compared to the mean field winding diameter, it may be possible that end coil leakage inductances can be influenced by the presence of the shaft to a larger extent and a 3D FEA simulation may be required for a more accurate estimation. Further studies on how to incorporate shaft effects in the analytical computation based on the method of mirror images are presently in progress.

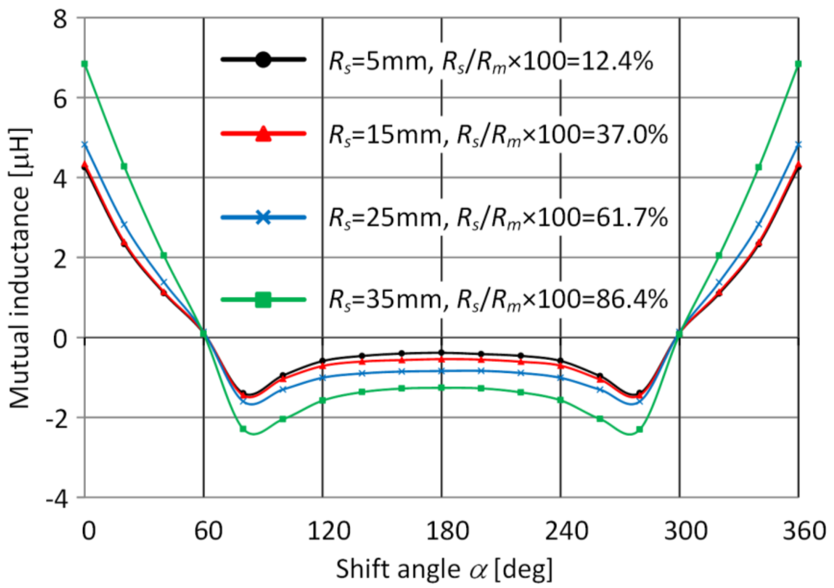

Figure 68: Mutual inductance between two end coils as a function of their relative displacement, for different ferromagnetic shaft radii.

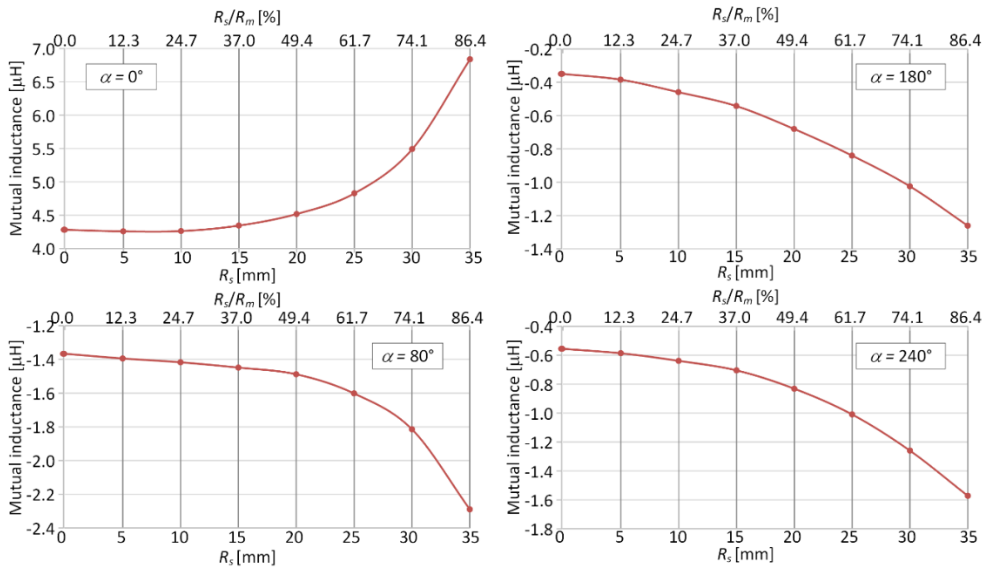

Figure 69: Mutual inductance between two end coils as a function of the ferromagnetic shaft radius, for different values of the relative displacement angle between end coils.

3.3.5 COMPARISON BETWEEN PROPOSED METHOD AND ANALYTICAL FORMULAS FOUNDED IN LITERATURE FOR THE END WINDING LEAKAGE INDUCTANCE COMPUTATION

The presented method for the computation of field-circuit end-coil leakage inductances is basically a fully-analytical version of the hybrid (numerical-analytical) technique proposed in [10]-[14], where end coils are discretized into elementary straight segments so as to compute their self and mutual inductances through Neumann integrals and the method of mirror images. Therefore, the level of accuracy achievable with the proposed method is essentially the same as for the method discussed in [10]-[14], the main advantage lying in the time and computation resource savings that result from a merely analytical approach where no domain discretization is required.

Approximated algebraic formulas can be found in the technical literature for a first-attempt guess of field circuit end-coil leakage inductances, as well. Examples can be found in [17], [18] where empirical expressions are provided based on experimentally-determined coefficients found through tests on reduced-scale simplified prototypes. As clearly stated in [17], however, these approximate formulas have poor reliability and are expected to significantly underestimate end coil leakage inductance actual values for full-scale synchronous machines. Just to give a numerical example, [19] proposes the following expression to estimate the field-circuit end-coil leakage inductance of cylindrical-rotor synchronous machines:

$$L_{tot} = P\,\mu_0\,N_{fp}\,W_{fc}\,l_p\,\lambda_{ef} \qquad 3.30$$

where P is the number of poles, N_{fp} is the number of field-winding slots per pole, W_{fc} is the number of turns per rotor slots, l_p is the total rotor length and λ_{ef} is a permeance coefficient. The evaluation of λ_{ef} is proposed as follows:

$$\lambda_{ef} = 0.2\tau_r / l_i \qquad 3.31$$

where τ_r is the average coil pitch for the field winding coils and li is the ideal core length [19]. In the case of the machine considered in chapter 3.3 for 3D FEA validation, we have:

- $P = 4$,
- $N_{fp} = 10$,
- $W_{fc} = 6$,
- $l_p = 1.6\ m$,
- $l_i = 1.48\ m$,
- $\tau_r = 0.93\ m$.

With such parameters, L_{tot} can be estimated using (3.30) ad results are shown in Table VI and also compared with previous analytical and 3D FEA results:

Table VI: End coil leakage inductance computation results

Analytical method	1.53 mH
3D FEA	1.57 mH
Simplified analytical	0.36 mH

As shown in Table VI it is clear that the formula founded in literature gives a significantly smaller value than the proposed method.

3.4 FINAL REMARKS AND CONCLUSIONS

In this chapter a fully analytical approach has been proposed for computing the end coil leakage inductance of the field winding in round-rotor synchronous machines. The proposed method descends from the analytical solution of Neumann integrals combined with the method of mirror images to account for stator and rotor magnetic core effects. As a first step, analytical formulas have been provided to compute the mutual inductance between single end turns and such formulas have been validated against both 3D FEA simulations and experimental measurements on a dedicated laboratory setup. Then, the validated equations have been used to compute the overall field winding end coil leakage inductance and computation results have been assessed by comparison with 3D FEA. Finally, the influence of a ferromagnetic shaft on the inductance computation has been investigated using 3D FEA. It has been demonstrated that, when the shaft radius is smaller than 40% of the mean winding radius, shaft effects can be disregarded with negligible errors. Further studies are presently in progress on how to account for the mentioned shaft effects in the analytical computation of field winding end coil leakage inductance.

3.5 REFERENCES

[1] D. Giulivo, M. Bortolozzi, M. De Martin, A. Tessarolo, “Improving the Fault Tolerance of Grid-Connected Synchronous Generators through Electromagnetic Design”, International Conference on Electrical Machines, ICEM 2014, Berlin, Germany, 2-5 Sept. 2014, pp. 2362-2366.

[2] A. Tessarolo, L. Branz, M. Bortolozzi, “Analytical calculation of the no-load flux density in the stator core of slotless SPM machines”, IEEE International Symposium on Compatibility and Power Electronics, IEEE CPE 2013, Ljubljana, Slovenia, 5-7 June 2013.

[3] A. Tessarolo, L. Branz, M. Bortolozzi, “Cogging torque fast computation method for surface permanent magnet machines based on winding function theory”, IEEE International Symposium on Compatibility and Power Electronics, IEEE CPE 2013, Ljubljana, Slovenia, 5-7 June 2013.

[4] K. C. Kim, H. W. Lee, Y. D. Chun, J. Lee, “Analysis of electromagnetic force distribution on end winding for motor reliance”, IEEE Trans. on Magnetics, vol. 41, no. 10, Oct. 2005, pp. 4072-4074.

[5] Taieb Brahimi, A. Foggia, G. Meunier, “End winding reactance computation using a 3D finite element program”, IEEE Trans. on Magnetics, vol. 29, no. 2, March 1993, pp. 1411-1414.

[6] T. Cox, F. Eastham, J. Proverbs, “End Turn Leakage Reactance of Concentrated Modular Winding Stators”, IEEE Transactions on Magnetics, vol.44, no.11, pp.4057-4061, Nov. 2008.

[7] F. W. Grover, Inductance Calculations, pp. 45-47, Dover Phoenix Editions, 2004.

[8] C. J. Carpenter, “The application of the method of images to machine end-winding fields”, Proceedings of IEE, vol. 107, pt. A, 1960, pp. 487-500.

[9] Y. Liang, X. Bian, H. Yu, L. Wu, B. Wang, “Analytical Algorithm for Strand End Leakage Reactance of Transposition Bar in AC Machine," IEEE Transactions on Energy Conversion, early access article.

[10] D. Ban, D. Zarko, I. Mandic, “Turbogenerator end-winding leakage inductance calculation using a 3-D analytical approach based on the solution of Neumann Integrals,” IEEE Transactions on Energy Conversion, vol.20, no.1, pp.98-105, March 2005.

[11] A. Tessarolo, F. Luise, “An Analytical-Numeric Method for Stator End-Coil Leakage Inductance Computation in Multi-Phase Electric Machines”, IEEE Industry Applications Society Annual Meeting, pp.1-8, 5-9, Oct. 2008.

[12] M. Freese, “Analytic calculation of turbo generator end winding inductances using Neumann’s formula”, International Symposium on Power Electronics Electrical Drives Automation and Motion, SPEEDAM 2010, pp. 1597-1602, 14-16 June 2010.

[13] A. Tessarolo, “Computing end-turn leakage inductance of concentric coil windings by asymptotical series approximation of Neumann integrals”, 2010 XIX International Conference on Electrical Machines (ICEM), pp.1-6, 6-8 Sept. 2010.

[14] G. A. Campbell, “Mutual inductances of circuits composed of straight wires”, Physical Review, vol. 5, 1915, pp. 452-458.

[15] A. Tessarolo, C. Bassi, “Stator Harmonic Currents in VSI-Fed Synchronous Motors With Multiple Three-Phase Armature Windings,” IEEE Transactions on Energy Conversion, vol.25, no.4, pp.974-982, Dec. 2010.

[16] G. B. Arfken, H. J. Weber, Mathematical Methods for Physicists, Academic Press, 2001, pp. 740-742, pp. 772-777, pp. 786-790.

[17] W. Schuisky, Berechnung elektrischer Maschinen, Verlag Springer, 1960.

[18]Weissheimer, Die Stirnstreuung der Synchronmaschinen. Arbeiten aus dem Elektrotechnischen Institut der Tecnischen Hochschule Karlsruhe, Band 5 (1927-1929).
[19]Ion Boldea, The Electric Generator Handbook, CRC Press, 2006.
[20]D. P. Kothari, I. J. Nagrath, Electric Machines, Tata McGraw-Hill,2006, pp. 288-289.

4 LEAKAGE INDUCTANCE DETERMINATION FROM NO-LOAD AND SHORT-CIRCUIT TESTS IN A MULTIPHASE SYNCHRONOUS MACHINE

The accurate determination of stator leakage inductances is presently an open issue in the analysis and testing of multiphase electric machines. Calculation methods are available which involve complicated and often poorly precise 3D analyses. Experimental determination techniques, using measurements on the wound stator with the rotor removed, are also possible but quite impractical as they need to be performed during machine manufacturing or require rotor withdrawal. In this chapter, a new approach is proposed to determine all the stator self and mutual leakage inductances of a nine-phase synchronous machine based on a minimal set (a couple) of magneto-static finite element (FE) simulations and on the measurements taken during no-load and short circuit routine tests. The procedure is applied to a wound-field salient pole nine-phase synchronous generator for validation, showing a good accordance with the results obtained from measurements on the machine with the rotor removed. A discussion is also proposed on the possibility to extend the presented procedure to other machine topologies.

4.1 INTRODUCTION ON LEAKAGE INDUCTANCE IN MULTIPHASE MACHINES

Multiphase synchronous machines are widely used today thanks to their well-known advantages over three-phase ones, in terms of performance, fault tolerance and flexibility of operation [1], [2]. In particular, an important multiphase machine design which is often taken into account is the nine-phase one. Example of nine-phase synchronous machines can be found in the field of power generation [3]-[5], permanent-magnet motor drives [6]-[8] and multi-motor applications [9].

In the analysis and testing of multiphase machines, a sufficiently accurate determination of their stator leakage inductances is still an open issue of some possible practical importance. Leakage inductances, in fact, can importantly impact on machine performance [10], especially in presence of time and space harmonics [11]-[14].

The problem of determining stator leakage inductances of electric machines from tests has been widely addressed in the technical literature. Experimental procedures are proposed for this purpose in [15] applying to three-phase induction motors based on impedance measurements on the machine with the rotor at stand-still. As regards three-phase synchronous machines, experimental methods are addressed in [16] to characterize their saturated *dq* model where the rotor is represented with a generic linear equivalent circuit [17]. Stator leakage inductances, together with the other *dq* model parameters, are identified in [16] based on standstill frequency response (SSFR) measurements suitably processed through genetic algorithms. Finally, some experimental procedures can be found in the literature to measure the end-coil and slot leakage inductances of multiphase machines based on dedicated tests to be conducted on the wound stator with the rotor removed combined with suitably calibrated Finite Element Analysis (FEA) simulations [18]-[21].

The work described in this chapter proposes a new alternative method to determine the overall stator leakage inductances of a nine-phase synchronous machine using the no-load and the short-circuit tests combined with a minimal set of FEA magneto-static simulations. The latter are used to identify magnetizing inductances as functions of the rotor position according to [22], which can be accomplished with only two magneto-static FEA simulations. The short circuit and no-load tests [18], on the other side, are used to record the no-load voltage and short-circuit current waveforms.

The basic idea of the proposed methodology is to derive the accurate mathematical model of the machine by identifying stator magnetizing inductances through FEA simulations as per [22] and treating leakage inductances as unknown parameters. On the machine model, transformed through the Vector Space Decomposition (VSD) technique [23], the condition is then imposed that the short circuit current waveform must equal the measured one when the rotor-produced back-emf equals the one recorded in the no-load test. This leads to a set of nonlinear algebraic equations from which the leakage inductances (unknowns) can be obtained. In the procedure, rotor circuit parameters are not involved and thereby do not need to be estimated or measured.

Compared to [16], the proposed technique employs measurements which can be taken during usual no-load and sustained short-circuit acceptance tests [18] and does not require any frequency response characterization or processing. Furthermore, the work in [16] is tailored on three-phase machines, while this work necessarily addresses high-phase-order stator topologies as it exploits harmonic circulation currents which specifically occur in multiphase machines in sustained short-circuit conditions or under Voltage-Source Inverter (VSI) supply as discussed in [11][12][22]. On the other side, unlike the tests with the rotor removed [18]-[21], the presented approach does not require rotor withdrawal and can be therefore implemented on the built machine and not in the manufacturing stage.

The method described in the following sections is applied to the computation of the leakage inductances of a nine-phase salient-pole synchronous machine prototype. The results are compared to those obtained with more traditional approaches based on measurements on the machine with the rotor removed, showing a good accordance. The same experimental validation is repeated twice on the same machine equipped with two different rotors having identical geometry, but one with and the other without damper circuits. The tests with the two different rotors are shown to give practically the same results. This confirms that the proposed methodology is not affected by the presence of rotor circuits and does not require their characterization.

The chapter is organized as follows: in the next sub-section (4.2) the nine-phase machine model is presented in both phase variables and after VSD transformation; in section 0 the model is particularized to reproduce steady-state short-circuit conditions; in section 4.4 the algebraic equations are derived to identify stator leakage inductances from no-load and short-circuit test measurements; section 4.5 describes the application of the procedure to a nine-phase machine prototype (with and without rotor damper cage; in the sixth section the results are validated against the leakage inductance independently measurement [18] on the same machine with the rotor removed and a clarification is provided of why 2D FEA does not suffice, in general, for the purpose of an accurate estimation of leakage inductances; finally, the last section discusses the merits of the proposed approach and the possibility (presently under study) to extend it to other multiphase designs.

4.2 MULTIPHASE MACHINE MATHEMATICAL MODEL

The stator phases of a nine-phase machine are conventionally numbered from 0 to 8 and named as depicted in the diagrams shown in Figure 70 according to the scheme proposed in [11],[23]. It can be seen that, based on this convention, two subsequent phases are displaced by $\pi/9$

electrical radians. Phase voltages, flux linkages, currents and rotor-produced back-emf's are indicated as $v_0 \ldots v_8$, $\varphi_0 \ldots \varphi_8$, $i_0 \ldots i_8$, $e_0 \ldots e_8$, respectively.

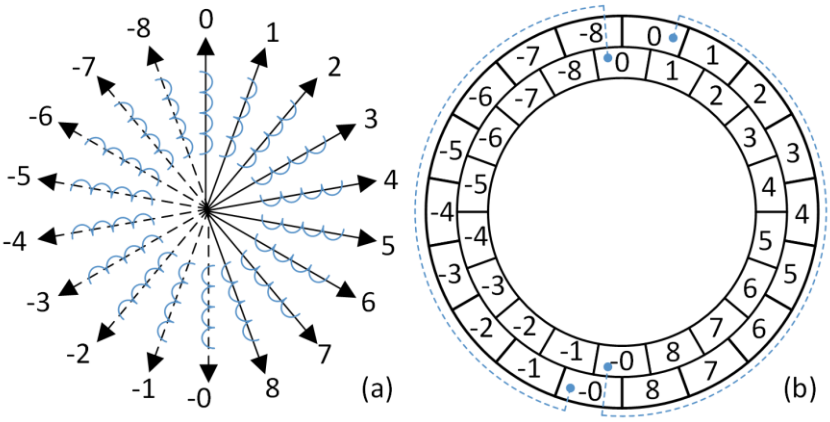

Figure 70: Phase numbering and arrangement for a two-pole nine-phase machine in the form of: (a) vector diagram; (b) phase belt arrangement in a two-layer short-pitch winding. The dashed line exemplifies the end-winding connections for phase "0".

4.2.1 MACHINE MODEL IN PHASE VARIABLES

The mathematical model of a nine-phase machine, expressed in phase variables (subscript ph) is:

$$\mathbf{v}_{ph} = r_s \mathbf{i}_{ph} + \tfrac{d}{dt}\boldsymbol{\varphi}_{ph} + \mathbf{e}_{ph} \qquad 4.1$$

where r_s is the phase resistance and:

$$\begin{aligned} \mathbf{v}_{ph} &= \begin{pmatrix} v_0 & v_1 & \cdots & v_8 \end{pmatrix}^t, \\ \boldsymbol{\varphi}_{ph} &= \begin{pmatrix} \varphi_0 & \varphi_1 & \cdots & \varphi_8 \end{pmatrix}^t, \\ \mathbf{i}_{ph} &= \begin{pmatrix} i_0 & i_1 & \cdots & i_8 \end{pmatrix}^t, \\ \mathbf{e}_{ph} &= \begin{pmatrix} e_0 & e_1 & \cdots & e_8 \end{pmatrix}^t. \end{aligned} \qquad 4.2$$

the flux linkage vector can be expressed as:

$$\boldsymbol{\varphi}_{ph} = \left(\mathbf{L}_{ph} + \mathbf{M}_{ph}\right)\mathbf{i}_{ph} \qquad 4.3$$

where $\mathbf{L}_{ph}$, $\mathbf{M}_{ph}$ are the leakage inductance and magnetizing inductance matrices, respectively. Under the assumption that leakage inductances do not vary with the rotor position [24], $\mathbf{L}_{ph}$ takes the following form:

$$\mathbf{L}_{ph} = \begin{pmatrix} l_0 & l_1 & l_2 & l_3 & l_4 & -l_4 & -l_3 & -l_2 & -l_1 \\ l_1 & l_0 & l_1 & l_2 & l_3 & l_4 & -l_4 & -l_3 & -l_2 \\ l_2 & l_1 & l_0 & l_1 & l_2 & l_3 & l_4 & -l_4 & -l_3 \\ l_3 & l_2 & l_1 & l_0 & l_1 & l_2 & l_3 & l_4 & -l_4 \\ l_4 & l_3 & l_2 & l_1 & l_0 & l_1 & l_2 & l_3 & l_4 \\ -l_4 & l_4 & l_3 & l_2 & l_1 & l_0 & l_1 & l_2 & l_3 \\ -l_3 & -l_4 & l_4 & l_3 & l_2 & l_1 & l_0 & l_1 & l_2 \\ -l_2 & -l_3 & -l_4 & l_4 & l_3 & l_2 & l_1 & l_0 & l_1 \\ -l_1 & -l_2 & -l_3 & -l_4 & l_4 & l_3 & l_2 & l_1 & l_0 \end{pmatrix} \qquad 4.4$$

where l_0 indicates the leakage self-inductance of a phase and l_j (with *j* standing for a generic integer number between 1 and 4) represents the mutual leakage inductance between two phases displaced by $\boldsymbol{j}\frac{\boldsymbol{\pi}}{\mathbf{9}}$ electrical radians. The five independent inductances $l_0, l_1, l_2, l_3\ l_4$ are the five unknown parameters which have to be identified.

The matrix $\mathbf{M_{ph}}$, on the other side, can be written as:

$$\mathbf{M}_{ph}(\theta) = \begin{pmatrix} m_{0,0}(\theta) & m_{0,1}(\theta) & \cdots & m_{0,8}(\theta) \\ m_{1,0}(\theta) & m_{1,1}(\theta) & \cdots & m_{1,8}(\theta) \\ \vdots & \vdots & \ddots & \vdots \\ m_{8,0}(\theta) & m_{8,1}(\theta) & \cdots & m_{8,8}(\theta) \end{pmatrix} \qquad 4.5$$

where $m_{i,j}$ is the mutual inductance (due to the air-gap flux) between phases *i* and *j* ($i, j = 0, 1, \dots, 8$) and, in particular, $m_{j,j}$ indicates the self-inductance (due to the air-gap flux) of phase *j*. Such inductances depend on the rotor position in case of salient-pole machines and can be expressed as follows [22]:

$$m_{i,j}(\theta) = \frac{\pi R L \mu_0}{2} \left\{ \begin{array}{l} \sum\limits_{r,s=1,3,5,7,9} F_s W_r P_{s+r} \cos[(si+rj)\alpha - (s+r)\theta] + \\ + \sum\limits_{\substack{r,s=1,3,5,7,9 \\ r \neq s}} F_s W_r P_{|s-r|} \cos[(si-rj)\alpha - (s-r)\theta] + \\ + \sum\limits_{s=1,3,5,7,9} F_s W_s P_0 \cos[s(i-j)\alpha] \end{array} \right\} \qquad 4.6$$

where R is the mean air-gap radius, $\alpha = \pi/9$ is the phase progression, L is the machine core length, μ_0 is the magnetic permeability of the air and F_s, W_r, P_k (with s, r, k being integer indices) are Fourier coefficients that can be found as explained in [22] from two magneto-static FEA simulations. In 4.6, the first nine odd space harmonics are considered for inclusion in the machine model, as they generally have the highest amplitude [24][25]. More space harmonics cannot be included in the model because this would result in a time-varying inductance matrix after application of the VSD transform [24][25] as discussed in the next section.

4.2.2 MACHINE MODEL AFTER VECTOR SPACE DECOMPOSITION

The VSD is a particular transformation which enables to express the machine model in the form of a linear differential equation with time-invariant parameters [2]. For a nine-phase machine, the VSD can be achieved by defining the following real-valued 9x9 transformation matrices:

$$\mathbf{C}=\sqrt{\tfrac{2}{9}}\left(\begin{array}{cccccc} 1 & \cos(\alpha) & \cos(2\alpha) & \cos(3\alpha) & \cdots & \cos(8\alpha) \\ 0 & \sin(\alpha) & \sin(2\alpha) & \sin(3\alpha) & \cdots & \sin(8\alpha) \\ \hline 1 & \cos(3\alpha) & \cos(6\alpha) & \cos(9\alpha) & \cdots & \cos(24\alpha) \\ 0 & \sin(3\alpha) & \sin(6\alpha) & \sin(9\alpha) & \cdots & \sin(24\alpha) \\ \hline 1 & \cos(5\alpha) & \cos(10\alpha) & \cos(15\alpha) & \cdots & \cos(40\alpha) \\ 0 & \sin(5\alpha) & \sin(10\alpha) & \sin(15\alpha) & \cdots & \sin(40\alpha) \\ \hline 1 & \cos(7\alpha) & \cos(14\alpha) & \cos(21\alpha) & \cdots & \cos(56\alpha) \\ 0 & \sin(7\alpha) & \sin(14\alpha) & \sin(21\alpha) & \cdots & \sin(56\alpha) \\ \hline \frac{1}{\sqrt{2}} & \frac{1}{\sqrt{2}}\cos(9\alpha) & \frac{1}{\sqrt{2}}\cos(18\alpha) & \frac{1}{\sqrt{2}}\cos(27\alpha) & \cdots & \frac{1}{\sqrt{2}}\cos(72\alpha) \end{array}\right) \qquad 4.7$$

$$\mathbf{P}(\theta)=\begin{pmatrix} \mathbf{P}_1(\theta) & \mathbf{0}_{2\times2} & \mathbf{0}_{2\times2} & \mathbf{0}_{2\times2} & \mathbf{0}_{2\times1} \\ \mathbf{0}_{2\times2} & \mathbf{P}_3(\theta) & \mathbf{0}_{2\times2} & \mathbf{0}_{2\times2} & \mathbf{0}_{2\times1} \\ \mathbf{0}_{2\times2} & \mathbf{0}_{2\times2} & \mathbf{P}_5(\theta) & \mathbf{0}_{2\times2} & \mathbf{0}_{2\times1} \\ \mathbf{0}_{2\times2} & \mathbf{0}_{2\times2} & \mathbf{0}_{2\times2} & \mathbf{P}_7(\theta) & \mathbf{0}_{2\times1} \\ \mathbf{0}_{1\times2} & \mathbf{0}_{1\times2} & \mathbf{0}_{1\times2} & \mathbf{0}_{1\times2} & 1 \end{pmatrix} \qquad 4.8$$

where $\mathbf{0}_{2\times2}$ is the 2×2 null matrix and:

$$\mathbf{P}_h(\theta)=\begin{pmatrix} \cos(h\theta) & \sin(h\theta) \\ -\sin(h\theta) & \cos(h\theta) \end{pmatrix}, \quad \mathbf{0}_{2\times1}=\mathbf{0}_{1\times2}{}^{t}=\begin{pmatrix} 0 \\ 0 \end{pmatrix} \qquad 4.9$$

for any integer $h \in \{1, 3, 5, 7\}$.

The overall transformation matrix is defined as:

$$\mathbf{T}(\theta)=\mathbf{P}(\theta)\mathbf{C} \qquad 4.10$$

by a symbolic math tool, it can be easily checked that the following identities hold for $\mathbf{T}(\theta)$:

$$\mathbf{T}(\theta)\mathbf{T}(\theta)^{t}=\mathbf{I}_9 \qquad 4.11$$

$$\mathbf{J}=\mathbf{T}(\theta)\left[\tfrac{d}{d\theta}\mathbf{T}(\theta)^{t}\right]=\begin{pmatrix} \mathbf{J}_2 & \mathbf{0}_{2\times2} & \mathbf{0}_{2\times2} & \mathbf{0}_{2\times2} & \mathbf{0}_{2\times1} \\ \mathbf{0}_{2\times2} & 3\mathbf{J}_2 & \mathbf{0}_{2\times2} & \mathbf{0}_{2\times2} & \mathbf{0}_{2\times1} \\ \mathbf{0}_{2\times2} & \mathbf{0}_{2\times2} & 5\mathbf{J}_2 & \mathbf{0}_{2\times2} & \mathbf{0}_{2\times1} \\ \mathbf{0}_{2\times2} & \mathbf{0}_{2\times2} & \mathbf{0}_{2\times2} & 7\mathbf{J}_2 & \mathbf{0}_{2\times1} \\ \mathbf{0}_{1\times2} & \mathbf{0}_{1\times2} & \mathbf{0}_{1\times2} & \mathbf{0}_{1\times2} & 0 \end{pmatrix} \qquad 4.12$$

where $\mathbf{I}_9$ is the 9×9 identity matrix and:

$$\mathbf{J}_2 = \begin{pmatrix} 0 & -1 \\ 1 & 0 \end{pmatrix} \tag{4.13}$$

By applying $\mathbf{T}(\theta)$ to the phase variables 4.2 we obtain the transformed current, voltage, flux linkage and rotor-produced back-emf vector variables as follows:

$$\mathbf{v}_{vsd} = \mathbf{T}\mathbf{v}_{ph},\ \boldsymbol{\varphi}_{vsd} = \mathbf{T}\boldsymbol{\varphi}_{ph},\ \mathbf{i}_{vsd} = \mathbf{T}\mathbf{i}_{ph},\ \mathbf{e}_{vsd} = \mathbf{T}\mathbf{e}_{ph} \tag{4.14}$$

where:

$$\mathbf{v}_{vsd} = \left(v_{d1} \quad v_{q1} \mid v_{d3} \quad v_{q3} \mid v_{d5} \quad v_{q5} \mid v_{d7} \quad v_{q7} \mid v_9 \right)^t \tag{4.15}$$

$$\boldsymbol{\varphi}_{vsd} = \left(\varphi_{d1} \quad \varphi_{q1} \mid \varphi_{d3} \quad \varphi_{q3} \mid \varphi_{d5} \quad \varphi_{q5} \mid \varphi_{d7} \quad \varphi_{q7} \mid \varphi_9 \right)^t \tag{4.16}$$

$$\mathbf{i}_{vsd} = \left(i_{d1} \quad i_{q1} \mid i_{d3} \quad i_{q3} \mid i_{d5} \quad i_{q5} \mid i_{d7} \quad i_{q7} \mid i_9 \right)^t \tag{4.17}$$

$$\mathbf{e}_{vsd} = \left(e_{d1} \quad e_{q1} \mid e_{d3} \quad e_{q3} \mid e_{d5} \quad e_{q5} \mid e_{d7} \quad e_{q7} \mid e_9 \right)^t \tag{4.18}$$

matrices $\boldsymbol{L}_{ph}$, $\boldsymbol{M}_{ph}$ are also transformed as follows:

$$\mathbf{L}_{vsd} = \mathbf{T}\mathbf{L}_{ph}\mathbf{T}^t,\ \mathbf{M}_{vsd} = \mathbf{T}\mathbf{M}_{ph}\mathbf{T}^t \tag{4.19}$$

by left-multiplying both the members of 4.1 by $\mathbf{T}$ and using 4.14, 4.19 together with the identities 4.10-4.12 we can finally write:

$$\mathbf{v}_{vsd} = r_s\mathbf{i}_{vsd} + \omega\mathbf{J}\left(\mathbf{L}_{vsd} + \mathbf{M}_{vsd}\right)\mathbf{i}_{vsd} + \left(\mathbf{L}_{vsd} + \mathbf{M}_{vsd}\right)\tfrac{d}{dt}\mathbf{i}_{vsd} + \mathbf{e}_{vsd} \tag{4.20}$$

which is the sought differential equation representing the machine constant-parameter model in VSD variables. The explicit expression of the constant matrices $\mathbf{L}_{vsd}$, $\mathbf{M}_{vsd}$ can be found from [19] and, with a symbolic math tool, they can be easily checked to be:

$$\mathbf{L}_{vsd} = \begin{pmatrix} \mathbf{I}_2\lambda_1 & \mathbf{0}_{2\times2} & \mathbf{0}_{2\times2} & \mathbf{0}_{2\times2} & \mathbf{0}_{2\times1} \\ \mathbf{0}_{2\times2} & \mathbf{I}_2\lambda_3 & \mathbf{0}_{2\times2} & \mathbf{0}_{2\times2} & \mathbf{0}_{2\times1} \\ \mathbf{0}_{2\times2} & \mathbf{0}_{2\times2} & \mathbf{I}_2\lambda_5 & \mathbf{0}_{2\times2} & \mathbf{0}_{2\times1} \\ \mathbf{0}_{2\times2} & \mathbf{0}_{2\times2} & \mathbf{0}_{2\times2} & \mathbf{I}_2\lambda_7 & \mathbf{0}_{2\times1} \\ \mathbf{0}_{1\times2} & \mathbf{0}_{1\times2} & \mathbf{0}_{1\times2} & \mathbf{0}_{1\times2} & \lambda_9 \end{pmatrix} \tag{4.21}$$

$$\mathbf{M}_{vsd} = \begin{pmatrix} \mathbf{\Gamma}_{1,1} & \mathbf{\Gamma}_{1,3} & \mathbf{\Gamma}_{1,5} & \mathbf{\Gamma}_{1,7} & \mathbf{0}_{2\times1} \\ \mathbf{\Gamma}_{1,3} & \mathbf{\Gamma}_{3,3} & \mathbf{\Gamma}_{3,5} & \mathbf{\Gamma}_{3,7} & \mathbf{0}_{2\times1} \\ \mathbf{\Gamma}_{1,5} & \mathbf{\Gamma}_{3,5} & \mathbf{\Gamma}_{5,5} & \mathbf{\Gamma}_{5,7} & \mathbf{0}_{2\times1} \\ \mathbf{\Gamma}_{1,7} & \mathbf{\Gamma}_{3,7} & \mathbf{\Gamma}_{5,7} & \mathbf{\Gamma}_{7,7} & \mathbf{0}_{2\times1} \\ \mathbf{0}_{1\times2} & \mathbf{0}_{1\times2} & \mathbf{0}_{1\times2} & \mathbf{0}_{1\times2} & 0 \end{pmatrix} \qquad 4.22$$

where: $\mathbf{I}_2$ is the 2×2 identity matrix, parameters $\lambda_1, \lambda_3, \lambda_5, \lambda_7, \lambda_9$ in 4.21 can be expressed in terms of the phase leakage inductances l_0, l_1, l_2, l_3, l_4 as:

$$\lambda_h = l_0 + 2\sum_{k=1,2,3,4} l_k \cos\left(hk\tfrac{\pi}{9}\right), \quad h \in \{1, 3, 5, 7, 9\} \qquad 4.23$$

and the $\mathbf{\Gamma}_{i,j}$ sub-matrices in 4.22 take the following form:

$$\begin{aligned} \mathbf{\Gamma}_{i,j} = \frac{9\pi RL\mu_0}{4}\Bigg[&\begin{pmatrix} F_i W_j \left(P_{|i-j|} + P_{i+j}\right) & 0 \\ 0 & F_i W_j \left(P_{|i-j|} - P_{i+j}\right) \end{pmatrix} + \\ &\delta_{i,j}\begin{pmatrix} F_i W_i P_0 & 0 \\ 0 & F_i W_i P_0 \end{pmatrix}\Bigg] \text{ with } \quad i, j \in \{1, 3, 5, 7, 9\} \end{aligned} \qquad 4.24$$

where $i, j \in \{1,3,5,7\}$ and F_s, W_r, P_k are the Fourier coefficients appearing in 4.6 and computed as per [22], with $\delta_{i,j}$ standing for Kronecker symbol:

$$\delta_{i,j} = \begin{cases} 1 & \text{if } i = j \\ 0 & \text{if } i \neq j \end{cases} \qquad 4.25$$

4.3 Model particularization in steady-state short-circuit conditions

The machine model derived in the previous section through VSD can be particularized to the case of machine operation in steady-state (sustained) short-circuit conditions, as represented in Figure 71a in case of a wound-field synchronous machine. In Figure 71, $i_0, i_1, \ldots, i_8$ denote the nine phase currents when the machine operates at an electrical speed ω in steady-state short-circuit conditions with a field current i_f. With the same field current i_f and at the same speed ω, the phase back-emf's $e_1, e_2, \ldots, e_8$ are induced in stator phases at no load (Figure 71b).

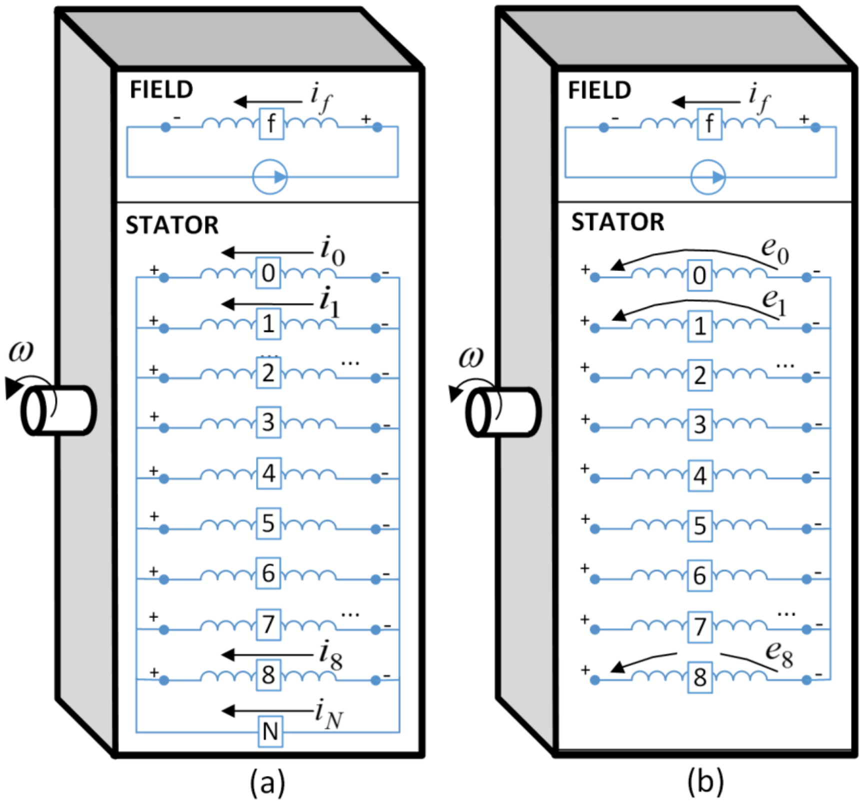

Figure 71: Stator phases and rotor field circuit (a) in short circuit conditions; (b) at no-load conditions.

At steady-state, the short circuit currents and back-emfs can be written as follows:

$$i_j(t) = \left[\mathbf{i}_{ph}(t)\right]_j = \sum_{k=1,3,5,7,9} I_k \cos\left[k\left(\omega t - \tfrac{\pi}{9} j\right) + \phi_k\right] \tag{4.26}$$

$$e_j(t) = \left[\mathbf{e}_{ph}(t)\right]_j = -\sum_{k=1,3,5,7,9} E_k \sin\left[k\left(\omega t - \tfrac{\pi}{9} j\right)\right] \tag{4.27}$$

where $j \in \{0,1,..,8\}$ is the phase index and $k \in \{1,3,5,7,9\}$ is the harmonic order; the terminal voltage is imposed to be zero on each stator phase due to the neutral connection indicated with the letter "N" in Figure 71a. In 4.26-4.27, harmonic components up to the ninth order have been considered. By transforming 4.26, 4.27 through 4.14 we obtain:

$$\mathbf{i}_{vsd} = \tfrac{3}{\sqrt{2}} \begin{pmatrix} I_1 \cos\phi_1 \\ I_1 \sin\phi_1 \\ \hline I_3 \cos\phi_3 \\ I_3 \sin\phi_3 \\ \hline I_5 \cos\phi_5 \\ I_5 \sin\phi_5 \\ \hline I_7 \cos\phi_7 \\ I_7 \sin\phi_7 \\ \hline \sqrt{2} I_9 \cos(9\omega t + \phi_9) \end{pmatrix}, \quad \mathbf{e}_{vsd} = \tfrac{3}{\sqrt{2}} \begin{pmatrix} 0 \\ E_1 \\ \hline 0 \\ E_3 \\ \hline 0 \\ E_5 \\ \hline 0 \\ E_7 \\ \hline \sqrt{2} E_9 \cos(9\omega t) \end{pmatrix} \tag{4.28}$$

In steady-state short-circuit conditions, the transformed machine equation 4.20 yields ($v_{vsd} = 0$):

$$-\mathbf{e}_{vsd} = r_s \mathbf{i}_{vsd} + \omega \mathbf{J}(\mathbf{L}_{vsd} + \mathbf{M}_{vsd})\mathbf{i}_{vsd} + (\mathbf{L}_{vsd} + \mathbf{M}_{vsd})\tfrac{d}{dt}\mathbf{i}_{vsd} \tag{4.29}$$

it can be noted that all the elements of the transformed current and back-emf vectors 4.28 are constant except for the last one (accounting for the ninth harmonic), which is time dependent. In particular, we can write:

$$\tfrac{d}{dt}\mathbf{i}_{vsd} = \begin{pmatrix} 0 \\ \vdots \\ 0 \\ -27\omega I_9 \sin(9\omega t + \phi_9) \end{pmatrix} \tag{4.30}$$

Furthermore, from 4.21-4.22 and considering 4.30, we can write:

$$(\mathbf{L}_{vsd} + \mathbf{M}_{vsd})\tfrac{d}{dt}\mathbf{i}_{vsd} = \begin{pmatrix} 0 \\ \vdots \\ 0 \\ -27\omega \lambda_9 I_9 \sin(9\omega t + \phi_9) \end{pmatrix} \tag{4.31}$$

$$\omega \mathbf{J}(\mathbf{L}_{vsd} + \mathbf{M}_{vsd})\mathbf{i}_{vsd} = \begin{pmatrix} * \\ \vdots \\ * \\ 0 \end{pmatrix} \tag{4.32}$$

where the symbol “*” denotes a number which is, in general, different from zero.

4.4 Leakage inductance identification from open-circuit and short-circuit tests

In order to identify leakage inductances, a short circuit test is performed on the machine arranged according to the scheme shown in Figure 71a at electrical speed ω and with a field current i_f; a no-load test (Figure 71b) is also performed on the machine at the same electrical speed ω and with the same field current if. In the short circuit test, one phase current (e.g. i0) is recorded and its Fourier series coefficients I_1, I_3, I_5, I_7, I_9 are extracted from the measurement. Moreover, the no-load voltage of one phase (e.g. e0) is recorded in the no-load test and its Fourier series coefficients E_1, E_3, E_5, E_7, E_9 are extracted from the measurement. In this way, the transformed current and back-emf vectors 4.28 are known except for the phase angles $\phi_1, \phi_3, \phi_5, \phi_7, \phi_9$.

The idea is therefore to use the measured Fourier coefficients E_1, E_3, E_5, E_7, E_9 and I_1, I_3, I_5, I_7, I_9 to identify the leakage inductance matrix L_{vsd} 4.21 in 4.29 and, from the knowledge of parameters $\lambda_1, \lambda_3, \lambda_5, \lambda_7, \lambda_9$, to finally determine the physical stator leakage inductances l_0, l_1, l_2, l_3, l_4 through 4.23.

For this purpose, based on 4.30-4.32 we can observe that 4.29 is equivalent to the system of the following two equations ("~" denotes reduced-order matrices and vectors):

$$\begin{cases} -\tilde{\mathbf{e}}_{vsd} = r_s \tilde{\mathbf{i}}_{vsd} + \omega \tilde{\mathbf{J}} \left(\tilde{\mathbf{L}}_{vsd} + \tilde{\mathbf{M}}_{vsd} \right) \tilde{\mathbf{i}}_{vsd} \\ -E_9 \cos(9\omega t) = r_s I_9 \cos(9\omega t + \phi_9) - 9\omega\lambda_9 I_9 \sin(9\omega t + \phi_9) \end{cases} \qquad 4.33$$

where:

$$\tilde{\mathbf{i}}_{vsd} = \tfrac{3}{\sqrt{2}} \begin{pmatrix} I_1 \cos\phi_1 \\ I_1 \sin\phi_1 \\ \hline I_3 \cos\phi_3 \\ I_3 \sin\phi_3 \\ \hline I_5 \cos\phi_5 \\ I_5 \sin\phi_5 \\ \hline I_7 \cos\phi_7 \\ I_7 \sin\phi_7 \end{pmatrix}, \quad \tilde{\mathbf{e}}_{vsd} = \tfrac{3}{\sqrt{2}} \begin{pmatrix} 0 \\ E_1 \\ \hline 0 \\ E_3 \\ \hline 0 \\ E_5 \\ \hline 0 \\ E_7 \end{pmatrix} \qquad 4.34$$

$$\tilde{\mathbf{L}}_{vsd} = \begin{pmatrix} \mathbf{I}_2\lambda_1 & \mathbf{0}_{2\times2} & \mathbf{0}_{2\times2} & \mathbf{0}_{2\times2} \\ \mathbf{0}_{2\times2} & \mathbf{I}_2\lambda_3 & \mathbf{0}_{2\times2} & \mathbf{0}_{2\times2} \\ \mathbf{0}_{2\times2} & \mathbf{0}_{2\times2} & \mathbf{I}_2\lambda_5 & \mathbf{0}_{2\times2} \\ \mathbf{0}_{2\times2} & \mathbf{0}_{2\times2} & \mathbf{0}_{2\times2} & \mathbf{I}_2\lambda_7 \end{pmatrix}, \quad \tilde{\mathbf{M}}_{vsd} = \begin{pmatrix} \mathbf{\Gamma}_{1,1} & \mathbf{\Gamma}_{1,3} & \mathbf{\Gamma}_{1,5} & \mathbf{\Gamma}_{1,7} \\ \mathbf{\Gamma}_{1,3} & \mathbf{\Gamma}_{3,3} & \mathbf{\Gamma}_{3,5} & \mathbf{\Gamma}_{3,7} \\ \mathbf{\Gamma}_{1,5} & \mathbf{\Gamma}_{3,5} & \mathbf{\Gamma}_{5,5} & \mathbf{\Gamma}_{5,7} \\ \mathbf{\Gamma}_{1,7} & \mathbf{\Gamma}_{3,7} & \mathbf{\Gamma}_{5,7} & \mathbf{\Gamma}_{7,7} \end{pmatrix} \qquad 4.35$$

the first equation in 4.33 will be used to determine the unknown coefficients $\lambda_1, \lambda_3, \lambda_5, \lambda_7$ (4.4.1), the second to determine the coefficient λ_9 (4.4.2) and, finally, the leakage inductances l_0, l_1, l_2, l_3, l_4 will be obtained from $\lambda_1, \lambda_3, \lambda_5, \lambda_7, \lambda_9$ (4.4.3).

4.4.1 DETERMINATION OF $\lambda_1, \lambda_3, \lambda_5, \lambda_7$

The first (matrix) equation in 4.33 can be put in the following form:

$$\mathbf{F}(\lambda_1,\lambda_3,\lambda_5,\lambda_7)\,\tilde{\mathbf{e}}_{vsd} = \tilde{\mathbf{i}}_{vsd} \qquad 4.36$$

where

$$\mathbf{F}(\lambda_1,\lambda_3,\lambda_5,\lambda_7) = -\left\{r_s\mathbf{I}_8 + \omega\tilde{\mathbf{J}}\left(\tilde{\mathbf{L}}_{vsd} + \tilde{\mathbf{M}}_{vsd}\right)\right\}^{-1}. \qquad 4.37$$

Pointing out that the matrix **F** depends on the four unknown parameters $\lambda_1, \lambda_3, \lambda_5, \lambda_7$ included in $\tilde{\mathbf{L}}_{vsd}$. At this point, we introduce the auxiliary constant matrices:

$$\mathbf{U}_1 = \begin{pmatrix} \mathbf{I}_2 \\ \mathbf{0}_{2\times2} \\ \mathbf{0}_{2\times2} \\ \mathbf{0}_{2\times2} \end{pmatrix}, \quad \mathbf{U}_3 = \begin{pmatrix} \mathbf{0}_{2\times2} \\ \mathbf{I}_2 \\ \mathbf{0}_{2\times2} \\ \mathbf{0}_{2\times2} \end{pmatrix}, \quad \mathbf{U}_5 = \begin{pmatrix} \mathbf{0}_{2\times2} \\ \mathbf{0}_{2\times2} \\ \mathbf{I}_2 \\ \mathbf{0}_{2\times2} \end{pmatrix}, \quad \mathbf{U}_7 = \begin{pmatrix} \mathbf{0}_{2\times2} \\ \mathbf{0}_{2\times2} \\ \mathbf{0}_{2\times2} \\ \mathbf{I}_2 \end{pmatrix} \qquad 4.38$$

By left-multiplying 4.37 by the transposed matrices 4.38 we obtain:

$$\mathbf{U}_k{}^t\mathbf{F}(\lambda_1,\lambda_3,\lambda_5,\lambda_7)\,\tilde{\mathbf{e}}_{vsd} = \mathbf{U}_k{}^t\tilde{\mathbf{i}}_{vsd} = \begin{pmatrix} I_k\cos\phi_k \\ I_k\sin\phi_k \end{pmatrix} \qquad 4.39$$

for any $k \in \{1,3,5,7\}$. Hence:

$$\begin{aligned}
&\left[\mathbf{U}_k{}^t\mathbf{F}(\lambda_1,\lambda_3,\lambda_5,\lambda_7)\,\tilde{\mathbf{e}}_{vsd}\right]^t\left[\mathbf{U}_k{}^t\mathbf{F}(\lambda_1,\lambda_3,\lambda_5,\lambda_7)\,\tilde{\mathbf{e}}_{vsd}\right] = \\
&= \tilde{\mathbf{e}}_{vsd}{}^t\mathbf{F}(\lambda_1,\lambda_3,\lambda_5,\lambda_7)^t\,\mathbf{U}_k\mathbf{U}_k{}^t\mathbf{F}(\lambda_1,\lambda_3,\lambda_5,\lambda_7)\,\tilde{\mathbf{e}}_{vsd} = \\
&= \tilde{\mathbf{e}}_{vsd}{}^t\mathbf{F}(\lambda_1,\lambda_3,\lambda_5,\lambda_7)^t\mathbf{E}_k\mathbf{F}(\lambda_1,\lambda_3,\lambda_5,\lambda_7)\,\tilde{\mathbf{e}}_{vsd} = \\
&= \begin{pmatrix} I_k\cos\phi_k \\ I_k\sin\phi_k \end{pmatrix}^t\begin{pmatrix} I_k\cos\phi_k \\ I_k\sin\phi_k \end{pmatrix} = I_k{}^2
\end{aligned} \qquad 4.40$$

where

$$\mathbf{E}_k = \begin{pmatrix} \mathbf{I}_2\delta_{1,k} & \mathbf{0}_{2\times2} & \mathbf{0}_{2\times2} & \mathbf{0}_{2\times2} \\ \mathbf{0}_{2\times2} & \mathbf{I}_2\delta_{3,k} & \mathbf{0}_{2\times2} & \mathbf{0}_{2\times2} \\ \mathbf{0}_{2\times2} & \mathbf{0}_{2\times2} & \mathbf{I}_2\delta_{5,k} & \mathbf{0}_{2\times2} \\ \mathbf{0}_{2\times2} & \mathbf{0}_{2\times2} & \mathbf{0}_{2\times2} & \mathbf{I}_2\delta_{7,k} \end{pmatrix} \qquad 4.41$$

being $\delta_{i,j}$ Kronecker symbol defined by 4.25.

In conclusion, 4.40 yields the following set of equations:

$$\begin{cases} \tilde{\mathbf{e}}_{vsd}{}^t \mathbf{F}(\lambda_1,\lambda_3,\lambda_5,\lambda_7)^t \mathbf{E}_1 \mathbf{F}(\lambda_1,\lambda_3,\lambda_5,\lambda_7)\, \tilde{\mathbf{e}}_{vsd} = I_1{}^2 \\ \tilde{\mathbf{e}}_{vsd}{}^t \mathbf{F}(\lambda_1,\lambda_3,\lambda_5,\lambda_7)^t \mathbf{E}_3 \mathbf{F}(\lambda_1,\lambda_3,\lambda_5,\lambda_7)\, \tilde{\mathbf{e}}_{vsd} = I_3{}^2 \\ \tilde{\mathbf{e}}_{vsd}{}^t \mathbf{F}(\lambda_1,\lambda_3,\lambda_5,\lambda_7)^t \mathbf{E}_5 \mathbf{F}(\lambda_1,\lambda_3,\lambda_5,\lambda_7)\, \tilde{\mathbf{e}}_{vsd} = I_5{}^2 \\ \tilde{\mathbf{e}}_{vsd}{}^t \mathbf{F}(\lambda_1,\lambda_3,\lambda_5,\lambda_7)^t \mathbf{E}_7 \mathbf{F}(\lambda_1,\lambda_3,\lambda_5,\lambda_7)\, \tilde{\mathbf{e}}_{vsd} = I_7{}^2 \end{cases} \tag{4.42}$$

which is a system of four nonlinear equations in the four unknowns $\lambda_1, \lambda_3, \lambda_5, \lambda_7$. The system can be solved numerically, e.g. with conjugate gradient method [26].

4.4.2 DETERMINATION OF λ_9

The parameter λ_9 can be determined from the second equation in the system 4.33. We can define the quantity:

$$Z_9 = \sqrt{r_s{}^2 + (9\omega\lambda_9)^2} \tag{4.43}$$

and the angle ψ_9 such that:

$$\cos\psi_9 = \frac{r_s}{Z_9}, \quad \sin\psi_9 = \frac{9\omega\lambda_9}{Z_9} \tag{4.44}$$

By dividing both members of the second equation in system 4.33 by Z_9 we obtain:

$$\begin{aligned} -\frac{E_9}{Z_9}\cos(9\omega t) &= \frac{r_s}{Z_9} I_9 \cos(9\omega t + \phi_9) - \frac{9\omega\lambda_9}{Z_9} I_9 \sin(9\omega t + \phi_9) = \\ &= I_9 \cos(\psi_9)\cos(9\omega t + \phi_9) - I_9 \sin(\psi_9)\sin(9\omega t + \phi_9) = \\ &= I_9 \cos(9\omega t + \phi_9 + \psi_9) \end{aligned} \tag{4.45}$$

In order for the first and last member of 4.45 to be equal, the following identities must hold:

$$\phi_9 + \psi_9 = \pi \tag{4.46}$$

$$Z_9 = \frac{E_9}{I_9} \tag{4.47}$$

Considering the expression 4.43 for Z_9, 4.47 implies:

$$\lambda_9 = \frac{\sqrt{(E_9 / I_9)^2 - r_s{}^2}}{9\omega} \tag{4.48}$$

which gives the value of the parameter λ_9.

4.4.3 DETERMINATION OF l_0, l_1, l_2, l_3, l_4

Once parameters $\lambda_1, \lambda_3, \lambda_5, \lambda_7, \lambda_9$ are known, the physical leakage inductances l_0, l_1, l_2, l_3, l_4 can be determined based on the linear relationship 4.23, which can be written in matrix form as follows:

$$(\lambda_1 \quad \lambda_3 \quad \lambda_5 \quad \lambda_7 \quad \lambda_9)^t = \mathbf{A}(l_0 \quad l_1 \quad l_2 \quad l_3 \quad l_4)^t \Rightarrow \qquad 4.49$$

$$\Rightarrow (l_0 \quad l_1 \quad l_2 \quad l_3 \quad l_4)^t = \mathbf{A}^{-1}(\lambda_1 \quad \lambda_3 \quad \lambda_5 \quad \lambda_7 \quad \lambda_9)^t \qquad 4.50$$

where the matrix $\mathbf{A}$ is given by 4.51 and is certainly invertible as its determinant is equal to $|\boldsymbol{A}| = 243$.

$$\mathbf{A} = \begin{pmatrix} 1 & 2\cos(\alpha) & 2\cos(2\alpha) & 2\cos(3\alpha) & 2\cos(4\alpha) \\ 1 & 2\cos(3\alpha) & 2\cos(6\alpha) & 2\cos(9\alpha) & 2\cos(12\alpha) \\ 1 & 2\cos(5\alpha) & 2\cos(10\alpha) & 2\cos(15\alpha) & 2\cos(20\alpha) \\ 1 & 2\cos(7\alpha) & 2\cos(14\alpha) & 2\cos(21\alpha) & 2\cos(28\alpha) \\ 1 & 2\cos(9\alpha) & 2\cos(18\alpha) & 2\cos(27\alpha) & 2\cos(36\alpha) \end{pmatrix} \qquad 4.51$$

4.5 PRACTICAL APPLICATION EXAMPLE

In order to illustrate and assess the proposed procedure the nine-phase generator shown in Figure 72 and in Figure 73 is used. Its ratings are reported in Table I and its main electromagnetic design data are provided in Table II.

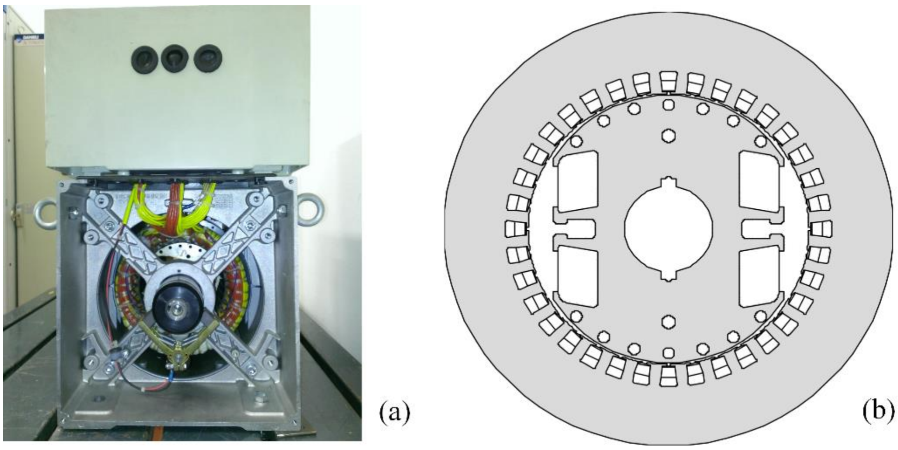

Figure 72: Generator used for testing (a) picture (b) cross section

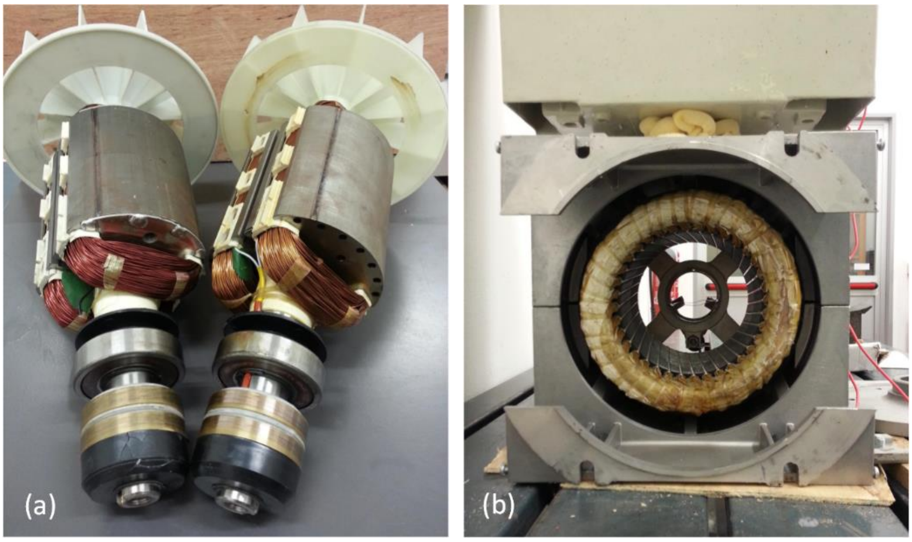

Figure 73: Pictures of: (a) the two rotors used for testing (with and without damper cage), (b) stator with the rotor removed

<u>*Table I: Machine ratings*</u>

Rated power	21 kVA
Rated power factor	0.8
Rated speed	3000 rpm
Number of poles	2

<u>*Table II: Electromagnetic design data*</u>

Core length	150 mm
Stator bore inner radius, R_s	75 mm
Minimum air-gap width, g	0.8 mm
Number of stator slots	36
Number of turns per stator coil, N_c	21
Coil pitch, γ	$(16/18)\pi$
Number parallel paths per phase, b	1
Number of excitation winding turns	540
Number of slots/pole/phase, q	2
Mean air-gap radius, R	37.1 mm
Stator phase resistance at 20°C, r_s	1.86 Ω

The application of the proposed procedure to the machine selected for testing includes the steps described in the previous chapters.

4.5.1 COMPUTATION OF MAGNETIZING INDUCTANCE PARAMETERS

The first step consists of computing the magnetizing inductances $m_{i,j}(\theta)$ in the Fourier series expansion form given by 4.6. The procedure described in [22] is adopted, which enables one to identify all the Fourier coefficients F_s, W_r, P_k based on some analytical formulas and through a couple of magneto-static FEA simulations. More precisely, coefficients W_r are computed as:

$$W_r = \frac{4}{\pi}\frac{N_c}{b}\frac{\sin(r\gamma/2)\sin(\alpha_s qr/2)}{r\sin(\alpha_s r/2)} \qquad 4.52$$

where:

$$\alpha_s = \pi/(9q) \qquad 4.53$$

being: N_c the number of stator turns per coil, b the number of parallel paths per phase, γ the coil pitch in electrical radians, q the number of slots per pole per phase, α_s the slot pitch in electrical radians.

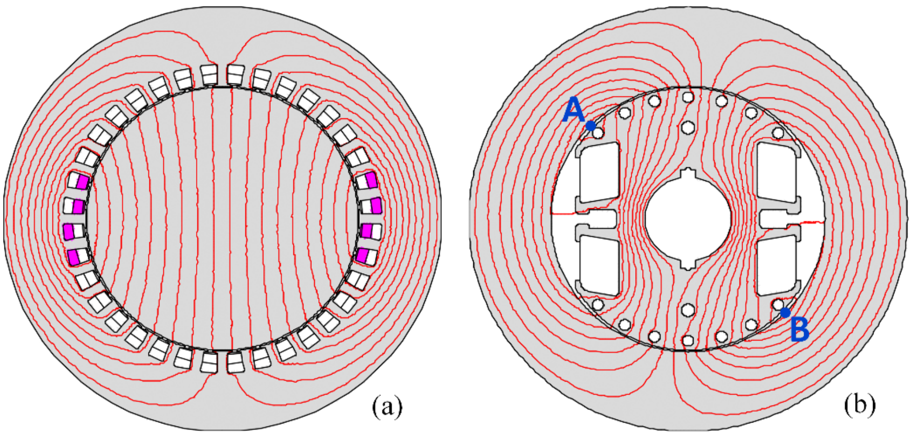

Figure 74: Results of FEA simulations needed for magnetizing inductance identification

As regards coefficients F_s, P_k, they are derived, based on [22], from the post-processing of the two FEA simulations shown in Figure 74. In particular:

- The model used in Figure 74a features the same stator as that of the real machine, while the rotor is replaced by a round one so as to have a uniform air-gap g equal to the minimum air-gap of the real machine. The model is energized by imposing an arbitrary current in one stator phase and then the radial magnetic field along the mean air-gap circumference is obtained and post-processed as discussed in [22] to obtain coefficients F_s.
- The model shown in Figure 74b includes a slotless stator core with a bore radius R_s and a rotor geometry which are the same as for the real machine. The model is energized with the two punctual ideal conductors marked as A and B in Figure 74b; the resulting radial magnetic field is then computed and post-processed as discussed in [22] to determine coefficients P_k.

The non-dimensional coefficients F_s, W_r, P_k obtained for the first (significant) values of indices *s, r, k* are reported in Table III and Table IV.

Table III: Values of Fourier coefficients F_s and W_s

s or *r*	1	3	5	7	9
F_s	45.97	−13.62	5.73	−1.977	4.245×10^{-3}
W_r	52.463	−14.9	6.231	−2.14	0

Table IV: Values of Fourier coefficients P_k

k	P_k	*k*	P_k	*k*	P_k	*k*	P_k	*k*	P_k
0	0.442	4	0.025	8	0.050	12	$3.3\cdot10^{-3}$	16	−0.012
2	0.446	6	0.019	10	−0.020	14	0.021	18	$1.1\cdot10^{-3}$

The knowledge of parameters F_s, W_r, P_k leads to fully identify the magnetizing self and mutual inductances given by 4.6 and to fully determine the magnetizing inductance $\widetilde{\mathbf{M}}_{vsd}$ through its submatrices $\widetilde{\mathbf{\Gamma}}_{i,j}$ given by 4.24.

4.5.2 NO LOAD AND SHORT CIRCUIT TESTS

The following step is to perform the no-load and the sustained short circuit tests on the built machine [18]. It is essential that both these tests are conducted at the same speed ω and with the same excitation current i_f. Furthermore, during the short-circuit test, the phase terminals need not only to be shorted, but also connected to the star point through a negligible-impedance wire indicated with letter "*N*" in Figure 71a. This is necessary to let the third and ninth current harmonics flow in machine phases.

In the no-load test, the open-circuit voltage waveform across a machine phase is recorded. For example, on the machine shown in Figure 72 and Figure 73 the no-load test is conducted at 1500 rpm ($\omega = 157\ \mathrm{rad/s}$) with a DC field excitation current $i_f = 1.58\ \mathrm{A}$ and the waveform shown in Figure 75 is recorded. By spectral analysis of the recorded waveform, the back-emf Fourier coefficients E_k $(k = 1, 3, \dots, 9)$ appearing in 4.27 and 4.28 are obtained. Their values are given in Table V.

Table V: Fourier coefficients E_k and I_k from the no-load and short-circuit tests

k	1	3	5	7	9
E_k (V)	124.4	−26.7	−1.9	−3.1	$5.1\cdot10^{-3}$
$\mid I_k \mid$ (A)	2.06	1.23	0.62	0.57	$2.3\cdot10^{-3}$

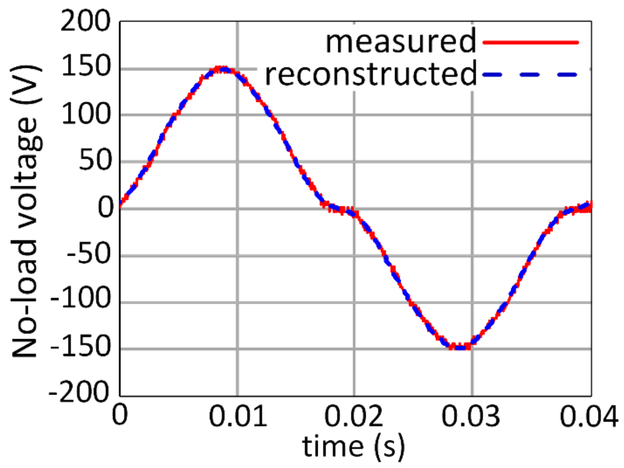

Figure 75: Open-circuit voltage waveform recorded on the test machine at 1500 rpm with a field excitation current of 1.58 A. The reconstructed waveform uses Fourier coefficients given in Table V.

In the short-circuit test, the current waveform is recorded and then analyzed to identify the magnitudes of coefficients I_k $(k = 1, 3, \dots, 9)$ appearing in 4.26 and 4.28. Their values are given in Table V. The recorded waveform and its reconstruction are shown in Figure 76.

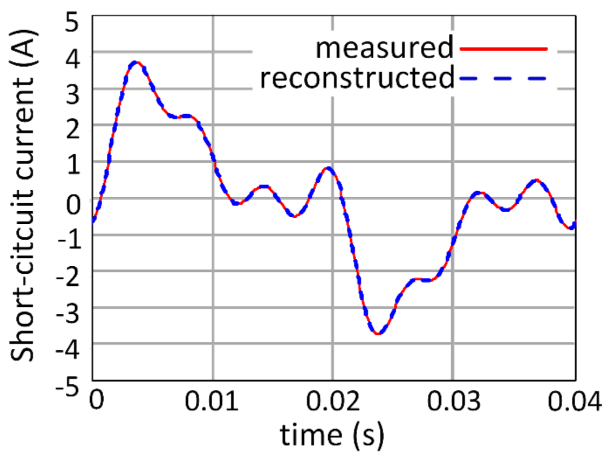

Figure 76: Short-circuit current waveform recorded in the sustained short circuit test at 1500 rpm with a field excitation current of 1.58 A. The reconstructed waveform uses Fourier coefficients given in Table V.

It is worth noting that the transformed back-emf vector $\mathbf{e}_{vsd}$ in 4.28 is fully identified from the no-load test through the computation of coefficients E_k, while the short circuit current vector $\mathbf{i}_{vsd}$ in 4.28 is not completely known because, from the short-circuit test, the magnitudes of coefficients I_k can be easily determined while the phase angles ϕ_k are undetermined. The reason for this is illustrated in Figure 77 which highlights that the back-emf fundamental is certainly aligned with the q axis (consistently with 4.27 and 4.28), while the fundamental of the short circuit current is shifted by ϕ_1 with respect to the *d*-axis (consistently with 4.26 and 4.28) and by $\pi - \phi_1$ with respect to the fundamental of the back-emf; however, in the short circuit test, neither the rotor position (i.e. the *d*-axis position) nor the back-emf signal are available, hence ϕ_1 remains undetermined together with the other phase angles $\phi_3, \phi_5, \phi_7, \phi_9$.

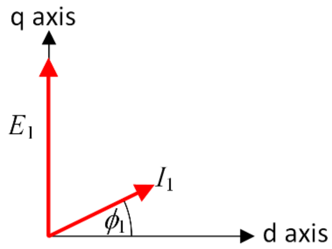

Figure 77: Phasor diagram for the back-emf and short circuit current fundamentals in the machine dq *reference frame.*

4.5.3 Identification of parameters λ_1, λ_3, λ_5, λ_7, λ_9

4.5.3.1 Parameters λ_1, λ_3, λ_5, λ_7

Based on the no-load and short circuit tests, the vector $\tilde{\mathbf{e}}_{vsd}$ in 4.34 is known as well as the values of $|I_1|, |I_3|, |I_5|, |I_7|$. On the other side, the matrix $\tilde{\mathbf{M}}_{vsd}$ is also fully identified as described in 4.5.1 and therefore, supposing that also the stator phase resistance r_s is known (Table II), the matrix **F** defined by 4.37 is a function of the only unknown parameters $\lambda_1, \lambda_3, \lambda_5, \lambda_7$. As a result, the set of equations in 4.42 is a nonlinear system in the only unknowns $\lambda_1, \lambda_3, \lambda_5, \lambda_7$. This system can be solved with numerical methods [26]. In the case of the test machine considered in this chapter, the numerical solution 4.42, performed with the conjugate gradient method, gives the results shown in Table VI. The same table also shows the initial guess values of the unknowns used for the numerical solution of 4.42.

Table VI: Parameters λ_1, λ_3, λ_5, λ_7

	λ_1	λ_3	λ_5	λ_7	λ_9
Initial guess (mH)	10	10	10	10	—
Identified values (mH)	7.78	1.92	0.88	1.16	0.85

4.5.3.2 Parameter $\boldsymbol{\lambda_9}$

The identification of the parameter λ_9 does not require any numerical procedure as it can be performed by means of 4.48 using the measured voltage and current components E_9 and $|I_9|$ (Table V) and the phase resistance r_s (Table II). This gives the value of λ_9 given in Table VI.

4.5.3.3 Parameter identification check

Once all the five values $\lambda_1, \lambda_3, \lambda_5, \lambda_7, \lambda_9$ are determined, all the parameters of the machine model in VSD coordinates are known. It is then possible to check the correctness of the parameter identification by computing the short circuit current from 4.29, which gives the block-scheme diagram shown in Figure 78. As a solution, the phase short circuit current vector $\mathbf{i}_{ph}$ is obtained at steady-state.

One phase current is plotted in Figure 79 and shown to almost perfectly match the measured current waveform. The same figure also shows the current waveform obtained by setting the parameters $\lambda_1, \lambda_3, \lambda_5, \lambda_7, \lambda_9$ equal to their initial-guess values (Table VI). It can be seen that the latter waveform strongly differs from the measured one. This confirms the importance of the leakage parameters $\lambda_1, \lambda_3, \lambda_5, \lambda_7, \lambda_9$ in determining the short circuit current waveform and proves that the identified values (Table VI) have been correctly determined.

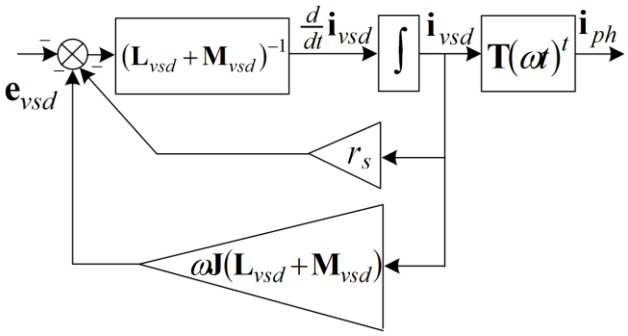

Figure 78: . Block diagram for the computation of the short circuit current in phase variables $\boldsymbol{i}_{ph}$.

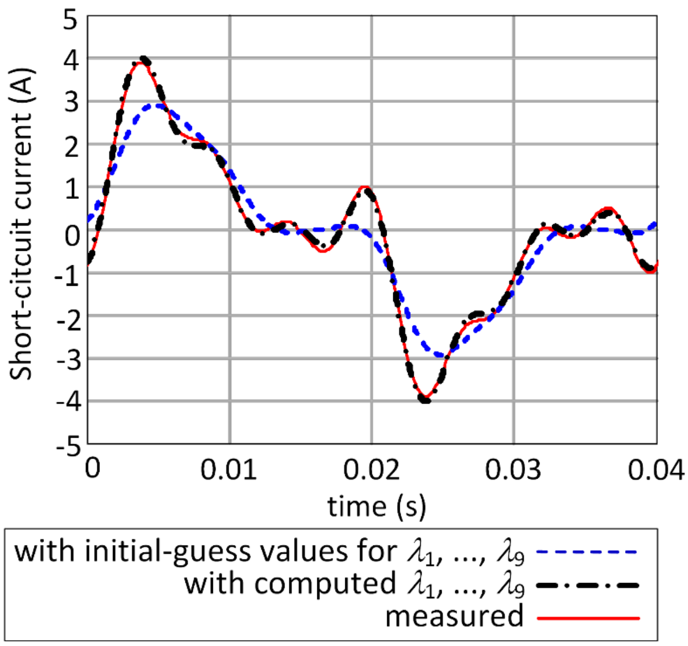

Figure 79: Short circuit current waveform: measured; before leakage inductance identification; after leakage inductance identification.

4.5.3.4 Computation of physical phase leakage inductances

As a final step, the physical self and mutual leakage inductances l_0, l_1, l_2, l_3, l_4 are determined by solution of the linear system 4.50. The numerical values obtained are given in Table VII, which shows the result of the stator leakage inductance identification procedure when the two kinds of rotors shown in Figure 73a (one with and the other without the damper cage) are used in the no-load and short circuit tests.

Table VII: Stator Physical leakage inductances l_0, l_1, l_2, l_3, l_4 (mH) identified with two different kinds of rotor

Rotor type	l_0	l_1	l_2	l_3	l_4
Without dampers	2.70	1.52	1.06	0.57	0.08
With dampers	2.75	1.47	1.09	0.60	0.08

Table VII demonstrates that the presence of rotor circuits does not significantly impacts on the results of the stator leakage inductance identification procedure.

The independency of stator leakage identification results on the rotor circuits is important as it justifies the usage of a machine model (Sections 4.2, 0) where no rotor-related parameters are used and where only the no-load back-emf appears.

The reason why rotor circuits do not impact on the proposed identification procedure is theoretically simple to justify. In fact, the no-load voltage is the same regardless of whether the rotor is equipped or not with a damper cage. Furthermore, the significant harmonics which appear in the short circuit current (with orders from 3 to 9) are known to not produce any resultant air-gap flux since their magneto-motive force fields mutually cancel out [2],[11] and [13]. Hence, neglecting the current harmonics with higher harmonic orders than the ninth, the damper cage during the short circuit test does not react, if present, and therefore the overall machine behaves as if the dampers were not present. This has been also experimentally validated in [27].

4.6 EXPERIMENTAL VALIDATIONS AND COMPARISON WITH FEA RESULTS

4.6.1 EXPERIMENTAL VALIDATIONS AGAINST MEASUREMENTS ON THE MACHINE WITH THE ROTOR REMOVED

The stator leakage inductance identification method proposed in this chapter is not easy to validate experimentally due to the lack of well-established methods or standards for the measurement of stator leakage inductances. The most reliable alternative way to perform such measurement to be used for comparison has been derived from the test with the rotor removed proposed in [18] for stator leakage inductance determination in three-phase machines. The same procedure has been already adopted in [19] for determining the stator end-coil leakage inductance of a three-phase turbo-alternator and in [20]-[21] for the experimental determination of end-coil [20] and end-coil plus slot [21] leakage inductances of machines with various phase counts.

This experimental procedure is applied to the test generator shown in Figure 73 and Figure 74. This leads to measure the physical inductance values l_0, l_1, l_2, l_3, l_4 given in the histogram shown in the Figure 80. In the diagram, the direct measurements obtained from the test with the rotor removed are compared to the values obtained with the methodology proposed in this chapter (sections 4.4 and 4.5). It can be seen that a satisfactory matching is achieved.

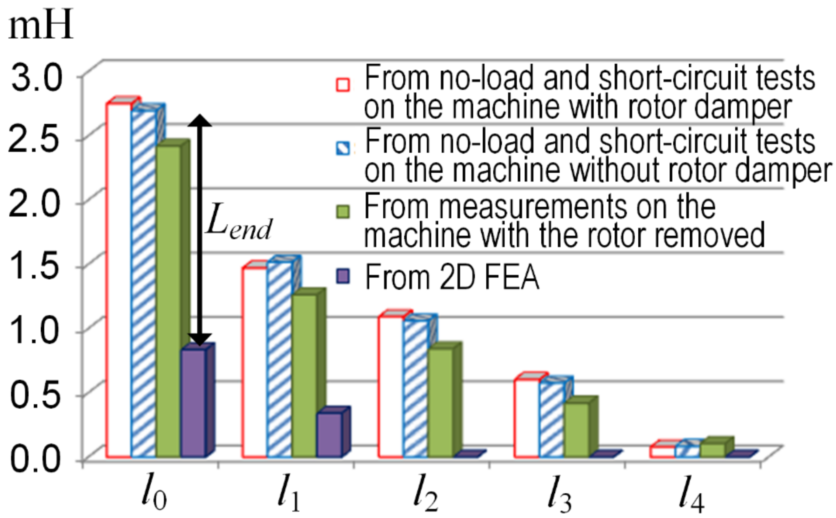

Figure 80: Physical leakage inductance values obtained from the proposed identification method (on the machine with and without the rotor damper cage), from measurements on the machine with the rotor removed and from 2D FEA.

4.6.2 Comparison with FEA results

It is reasonable to investigate if 2D FEA, which is used to determine magnetizing inductances, could be effectively used for a full calculation of leakage inductances as well. For this purpose, inductances are calculated for the machine under test through 2D FEA by segregating the leakage terms $l_0, l_1 .. l_4$ from the magnetizing ones $m_{i,j}(\theta)$ according to the definitions provided in Section 4.2.1.

4.6.2.1 Leakage inductance computation by FEA

The procedure followed is illustrated in Figure 81 where the mutual inductance between phases "0" and "6" is taken as an example: the phase "0" is energized with a given current I, while the other phases and the field circuit are at no load; then the total flux $\Lambda_6(\theta)$ linked by phase "6"as a function of the rotor positions θ is computed by FEA.

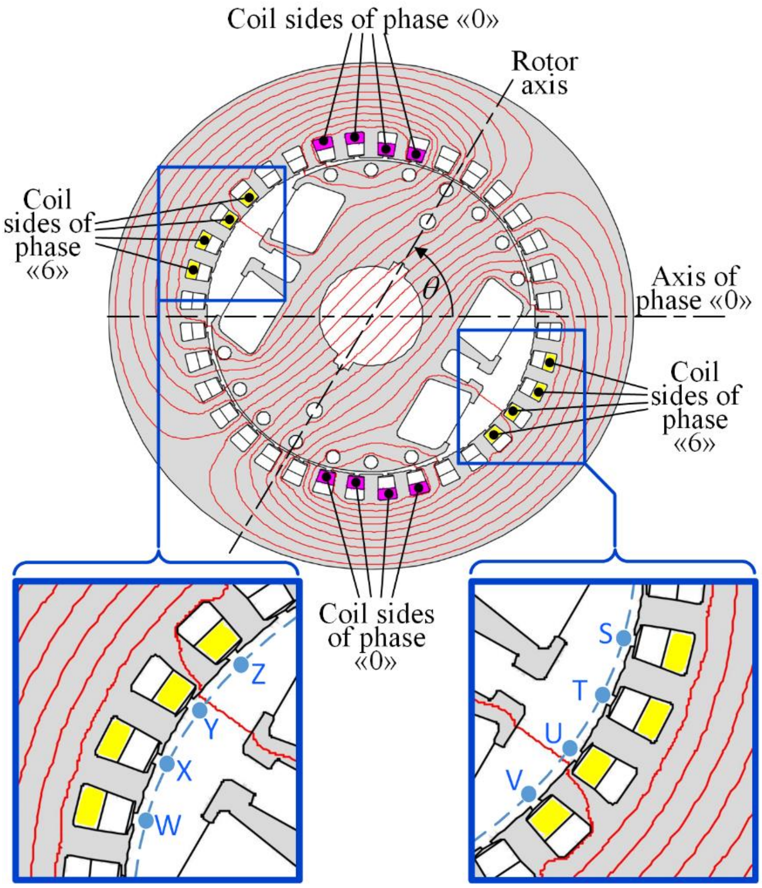

Figure 81: Schematic illustrating the computation of total and magnetizing mutual inductances between phases "0" and "6" by 2D FEA when the rotor is placed at ⍰ electrical radians with respect to the phase "0" axis.

This gives the total mutual inductance between phases "0" and "6", namely the quantity:

$$l_6 + m_{0,6}(\theta) = \Lambda_6 / I \qquad 4.54$$

In order to segregate the leakage inductance terms l_6, the magnetizing component $m_{0,6}(\theta)$ needs to be determined as well. This is done using the vector potential in the points S, T, U, V, W, X, Y, Z placed in the mean air-gap circumference of radius R in front of the slots including coils of phase "6", as shown in Figure 81. More precisely, $m_{0,6}(\theta)$ is computed as:

$$m_{0,6}(\theta)=L[A_S(\theta)+A_T(\theta)+A_U(\theta)+A_V(\theta)-A_W(\theta)-A_X(\theta)-A_Y(\theta)-A_Z(\theta)] \quad 4.55$$

where $A_S(\theta)$ is the vector potential, computed by FEA, at point S (Figure 81) when the rotor is at position θ and the same holds for the vector potentials in the other mentioned seven points.

The results of the inductance computations by 2D FEA are shown in Figure 82 in the form of self-inductance of phase “0” and mutual inductances between phase “0” and phases “1”, “2”, “3” and “4”. The mutual inductance between phase “0” and phases “5”, “6”, “7” and “8” are omitted as they can be obtained from the displayed diagrams using the relationship:

$$l_j + m_{0,j}(\theta) = -\left[l_{9-j} + m_{0,9-j}\left(\theta - \frac{\pi}{9} j\right)\right] \quad 4.56$$

which can be easily proved based on symmetry considerations and also based on the theory in Section 4.2.

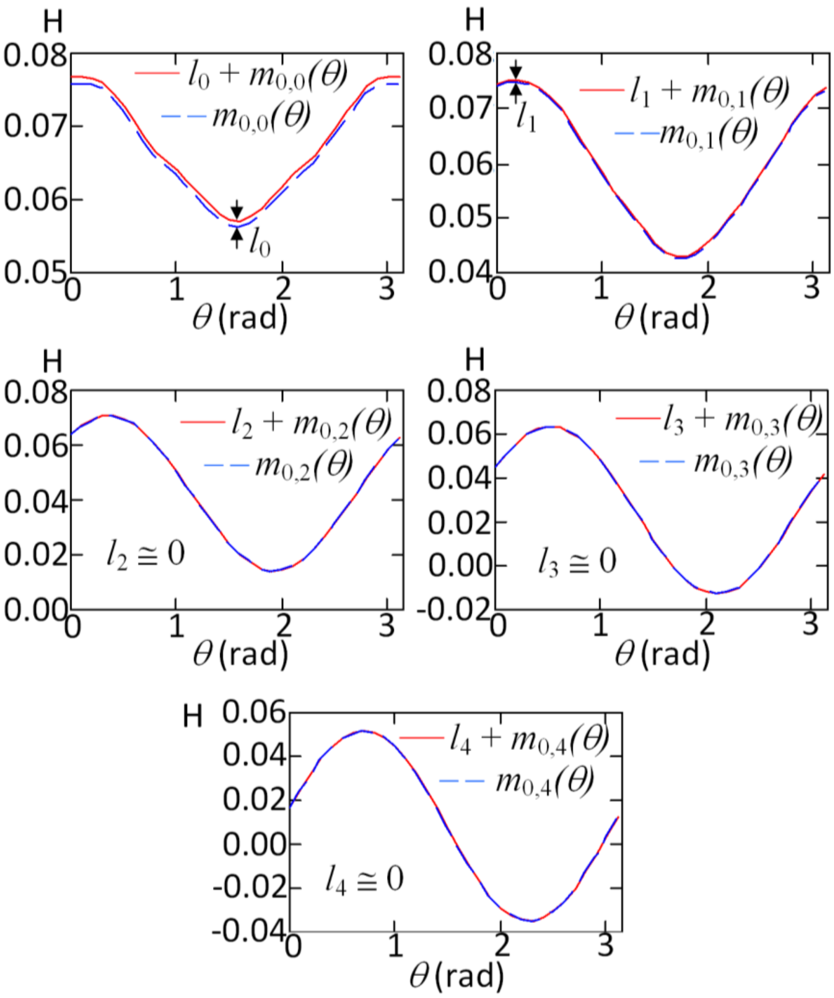

Figure 82: Inductance values as functions of the rotor position computed by 2D FEA.

From Figure 82 it can be seen that the only two leakage inductances which (according to 2D FEA) take non-negligible values compared to magnetizing terms are l_0 and l_1 This is due to the fact that the computed leakage inductances are essentially due to slot leakage flux (end-coil leakage phenomena not being captured by 2D FEA); hence, it is intuitively predictable that the only significant leakage inductances are the self-leakage inductance of each phase (l_0) and the mutual leakage inductance between adjacent phases (l_1), which have coil sides placed in the same slots [21].

The leakage inductances l_0, l_1, l_2, l_4 computed by 2D FEA with the procedure illustrated above are included in the histogram shown in Figure 80 for comparison with the same values obtained in other ways (i.e. from measurements on the machine with the rotor removed and from the post-processing of no-load and short-circuit tests). It can be seen that leakage inductance estimation by 2D FEA exhibits a very large error with respect to the other prediction methods. Hence, 2D FEA appears inadequate for the purpose of an accurate estimation of leakage inductances.

4.6.2.2 Interpretation of results and importance of end-coil effects

The discrepancies found in the estimation of the total leakage inductances by 2D FEA (Figure 80) are due to the fact that 2D FEA can well account for slot leakage effects, but is incapable of capturing end-coil leakage fluxes. As discussed and experimentally proven in previous works [21], the end-coil leakage inductance can be comparable to (or even larger than) the slot leakage one. This is particularly likely to occur in those machine configurations (e.g. some two-pole designs) where the length of end coils is comparable to (or larger than) the length of the straight coil portions embedded in the slots.

The fact that the error in the leakage inductance evaluation by 2D FEA is due to end coil effects is proven by a dedicated experiment on the nine-phase machine used for validation. The experiment is performed on the machine after rotor removal and consists of placing a pre-formed search coil (composed on $N_t = 2$ series-connected turns fixed on a plastic support) in the end-coil region as shown in the following figure.

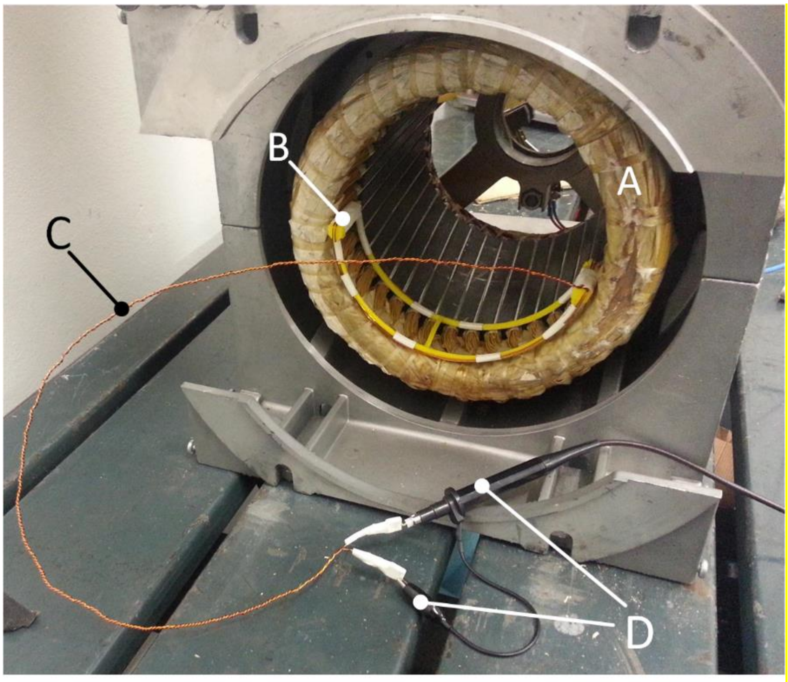

Figure 83: Experimental set-up for the assessment of end-coil contribution to phase leakage inductances. A–End coils. B–Search coil. C–Search coil terminals (twisted to avoid flux linkages outside the search coil). D–Voltage probe connected to the oscilloscope.

The angular span of the search coil in the circumferential direction is equal to the span of an end coil. The search coil terminals are connected to a voltage probe (Figure 83) to measure the induced no-load electromotive force (emf) E_t. At this point, the phase "0" of the machine is energized with a current $I_t = 8\ \mathrm{A\ rms}$ at a frequency $f_t = 50\ \mathrm{Hz}$ (with the other phases at no load) and the search coil is moved circumferentially into the position where it links the maximum leakage flux as shown in Figure 84, that is in the position where the emf in it is maximum. In this situation, the measured emf is $E_t = 0.108\text{ V rms}$ the flux linkage Λ_t of the search coil is evaluated as:

$$\Lambda_t = \frac{E_t}{2\pi\, f_t} = 3.44\times10^{-4}\ \text{wb rms} \qquad 4.57$$

From this measurement, the flux linkage Λ_{ec} due to the end coils of phase “0” on both machine sides is approximatively estimated as:

$$\Lambda_{ec} = \Lambda_t \frac{2N_c q}{N_t} = 0.0144\ \text{wb rms} \qquad 4.58$$

where: q and N_c are respectively the number of slots per pole per phase and the number of turns per coil for the machine; N_t is the number of turns in the search coil; the coefficient 2 at the numerator accounts for end coils being present on both machine sides.

Finally, the approximate estimation L_{end} of phase “0” self-inductance due to end coil leakage flux is derived dividing Λ_{ec} in 4.58 by the phase rms current I_t:

$$L_{end} = \frac{\Lambda_{ec}}{I_t} = 1.81\times10^{-3}\ \text{H} \qquad 4.59$$

The L_{end} value obtained in this way is reported in Figure 80 (arrow) showing that the magnitude of L_{end} well matches the “gap” between the phase self-leakage inductance estimated by FEA and the phase self-leakage inductance estimated by the other methods. This confirms that 2D FEA does not suffice for a complete and accurate estimation of leakage inductance as it cannot capture end coil leakage effects, which can be seen to be definitely non-negligible in some machine designs, such as in the two-pole machine prototype used.

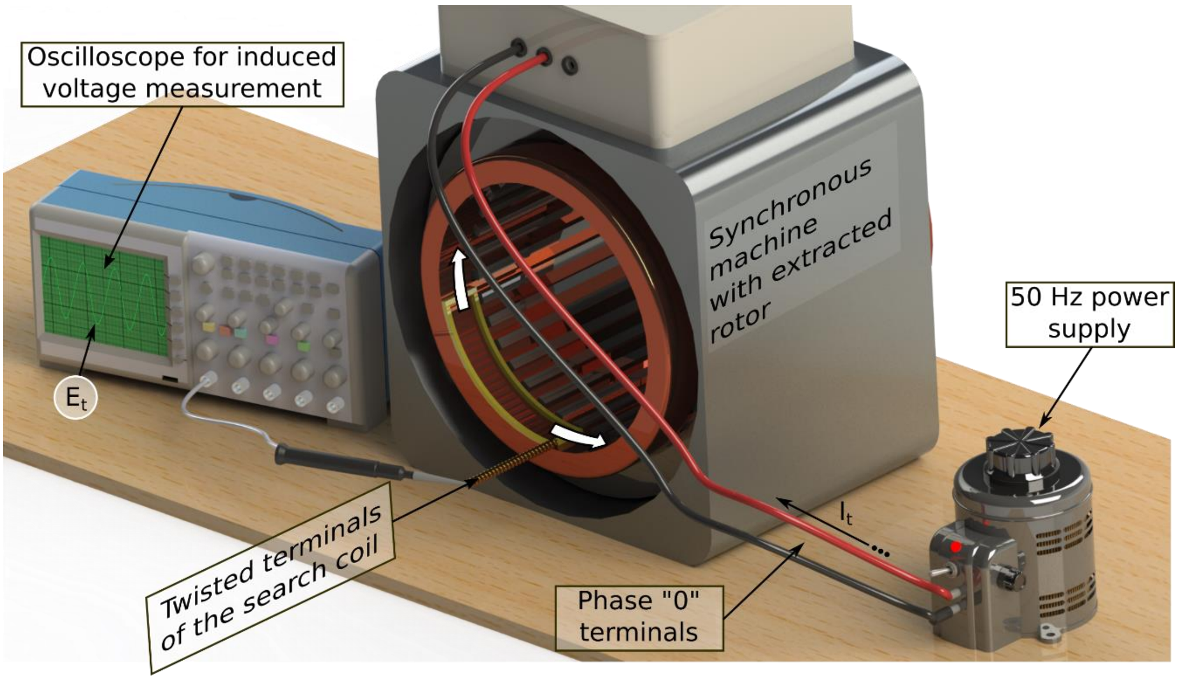

Figure 84: Experimental setup representation for the end winding leakage inductance estimation that underlines the procedure for the maximum linked flux position identification.

4.6.2.3 *Note on end coil leakage estimation by FEA*

Finally, a note is included regarding the possibility to estimate the end-coil leakage inductance portion (not captured by 2D FEA) resorting to alternative techniques.

Some hybrid numerical-analytical procedures have been proposed in literature and also in chapter 3 (for concentric windings), based on Neumann integrals and on the method of mirror images [19][20]. These techniques are well suited for turbo-alternators equipped with Roebel bars [19] and for winding designs based on preformed coils [20] and require that the end coil geometry is modeled and discretized into multiple straight elements for which an analytical solution of Neumann integrals can be found. Other kinds of stator designs (e.g. concentric windings), as shown in chapter 3, permit to find a solution for the end coil leakage determination problem without the straight segments coil.

An alternative method to compute end coil leakage inductances is the use of 3D FEA. This method is known to be extremely heavy and time-consuming from a computational view-point and, in addition to this drawback, it suffers from the major problem of being little effective when applied to certain kinds of stator windings. An example is just given by the wire-wound machine used for validations in this work: it can be seen from Figure 83 how, in this case, end coils, after emerging from the stator stack, do not remain separated as in the case of pre-formed coils, but join together into a sort of single “bundle” which develops around the stator circumference. Inside this bundle, for obvious constructive reasons, end coils overlap and are partly twisted together in order to implement a dual-layer short-pitch distributed winding scheme. It is quite apparent that modeling such geometry for 3D FEA would be practically impossible, in addition to probably giving unreliable results

In conclusion, it is deemed that 3D FEA for end-coil leakage inductance computation, although beneficial in some cases, still poses serious computational challenges and may be even unfeasible for certain machine designs. For this reason, it appears that a leakage inductance computation method fully based on FEA (2D and 3D) could not be proposed for general validity.

4.7 SOME CONCLUSIONS ABOUT THE LEAKAGE INDUCTANCE DETERMINATION

The work presented in this chapter may give rise to some points of discussion, regarding: its better practical applicability compared to alternative measurement techniques [18]-[21]; the possible extension of the method to electric machines with other number of phases (different from nine); the feasibility of a leakage inductance estimation procedure fully based on FEA simulations.

Regarding the former point, we can observe that the stator leakage inductance measurement methods used so far and based on tests with the rotor removed [18]-[21] can be applied to induction machines and not only to synchronous ones. On the other side, they need to be performed on the machine during manufacturing (i.e. before rotor mounting), while the proposed method can be applied to the built machine, based on measurements taken on such routine tests as the no-load and short circuit ones. It can be also objected that the proposed method, in addition to electrical measurements, requires some FEA. This, however, is normally required also for the measurements with the rotor removed to obtain sufficiently accurate results [19]-[21].

Regarding the possible extension of the method proposed in the chapter to electric machines with a different number of phases, this is actually under investigation. In particular, when dealing with machines with a relatively low number of phases (such as five or six), the main challenge originates from the fact that space harmonics (which are responsible for the short circuit current distortion) can be included in the VSD model up to a limited harmonic order [2]. This makes the VSD model little suitable and would make it necessary to work with the machine model in phase variables, so that the inductance identification procedure would not reduce to an algebraic problem as discussed in Section 4.4.

For machines with a high number of phases, on the other side, the same procedure described for the nine-phase case can be applied. However, some practical problems could arise in the accurate measurement of high-order harmonics (in the no-load voltage and short-circuit currents) which typically have very small amplitudes (as it can be seen in the nine-phase machine, too, for the ninth-order harmonics, Table V).

Finally, as regards the feasibility of a leakage inductance identification method fully based on FEA simulations, one should note that (as showed in 4.6) a purely 2D FEA approach cannot capture end-coil leakage inductances, which can account for a significant portion of the overall leakage inductances. On the other side, the use of 3D FEA as a complementary tool to predict end coil leakage inductances, poses major challenges in terms of computational burden and appears very little suited for some winding designs, like that of the wire-wound machine used as a validation platform in this work.

As a consequence, some experimental data appear necessary, in general, to fully accomplish leakage inductance identification and the experimental data obtained from open-circuit and sustained short circuit tests.

In conclusion the accurate determination of stator leakage inductances of multiphase machines from either computation or measurements is a challenging task due to the complicated spatial distribution of leakage flux paths. Measurement methods have been proposed in the literature using properly calibrated FE models and electrical measurements performed on the wound stator before rotor mounting. In this work, a new method is set forth to determine the stator self and mutual leakage inductances of a synchronous nine-phase machine based on two magneto-static analyses combined with measurements taken on the built machine during no-load and short-circuit routine tests. The magneto-static analyses are used to determine the magnetizing inductance matrix in the machine VSD model so that leakage inductances are left as the only unknown parameters in it. The harmonics detected in the no-load voltage and short circuit current waveforms are then used to identify such parameters through the numerical solution of a nonlinear algebraic system of equations. The proposed procedure has been experimentally applied and assessed on a nine-phase salient-pole wound-field machine comparing its results to the stator leakage inductances obtained from the conventional tests with the rotor removed. A satisfactory accordance has been found in the comparison. Further investigations are currently in progress to extend the proposed leakage inductance identification method to synchronous electric machines with a different number of phases.

4.8 References

[1] E. Levi, "Multiphase Electric Machines for Variable-Speed Applications", IEEE Trans. on Ind. Electron., vol. 55, no. 5, pp. 1893-1909, May 2008.

[2] E. Levi, R. Bojoi, F. Profumo, H.A. Toliyat, S. Williamson, "Multiphase induction motor drives - a technology status review", IET Electric Power Applications, no.4, pp.489-516, July 2007.

[3] J.L.F. van der Veen, L.J.J. Offringa, and A.J.A. Vandenput, "Minimising rotor losses in high-speed high-power permanent magnet synchronous generators with rectifier loads", Proc. Inst. Electr. Eng.—Electr. Power Appl., vol. 144, no. 5, pp. 1258–1266, Sep. 1997.

[4] J. Wang, R. Qu, and Y. Liu, "Comparison study of superconducting generators with multiphase armature windings for large-scale direct-drive wind turbines", IEEE Trans. Appl. Supercond., vol. 23, no. 3, article# 5201005, Jun. 2013.

[5] H.E. Jordan, R.C. Zowarka and S.B. Pratap, "Nine-Phase Armature Windings Design, Test, and Harmonic Analysis", IEEE Trans. on Magnetics, vol. 41, no. 1, Jan. 2005, pp. 299-302.

[6] E. Jung, H. Yoo, S. Sul, H. Choi, and Y. Choi, "A nine-phase permanent magnet motor drive system for an ultrahigh-speed elevator", IEEE Trans. Ind. Appl., vol. 48, no. 3, pp. 987–995, May/Jun. 2012.

[7] M. Ruba and D. Fodorean, "Analysis of fault-tolerant multiphase power converter for a nine-phase permanent magnet synchronous machine", IEEE Trans. Ind. Appl., vol. 48, no. 6, pp. 2092–2101, Nov./Dec. 2012.

[8] L. Parsa and T. Kim, "Reducing torque pulsation of multi-phase interior permanent magnet machines", 41st IAS Annu. Meeting, 2006, vol. 4, pp. 1978–1983.

[9] E. Levi, M. Jones, S. N. Vukosavic, and H. A. Toliyat, "Operating principles of a novel multiphase multimotor vector-controlled drive". IEEE Trans. Energy Convers., vol. 19, no. 3, pp. 508–517, Sep. 2004.

[10]P. Ponomarev, Y. Alexandrova, I. Petrov, P. Lindh, E. Lomonova, J. Pyrhonen, "Inductance Calculation of Tooth-Coil Permanent-Magnet Synchronous Machines", IEEE Transactions on Industrial Electronics, vol. 61, no. 11, pp. 5966-5973, Nov. 2014.

[11]A. Tessarolo, C. Bassi, "Stator Harmonic Currents in VSI-Fed Synchronous Motors with Multiple Three-Phase Armature Windings", IEEE Transactions on Energy Conversion, vol. 25, no. 4, pp. 974-982, Dec. 2010.

[12]D. Hadiouche, H. Razik, and A. Rezzoug, "On the modeling and design of dual-stator windings to minimize circulating harmonic currents for VSI-fed AC machines", IEEE Trans. Ind. Appl., vol. 40, no. 2, pp. 506–515, Mar./Apr. 2004.

[13]E. A. Klingshirn, "High phase order induction Motors−Part I−Description and theoretical considerations", IEEE Trans. Power Appar. Syst., vol. PAS-102, no. 1, pp. 47–53, Jan. 1983.

[14]E. A. Klingshirn, "High phase order induction motors–Part II– Experimental results," IEEE Trans. Power Appar. Syst., vol. PAS-102, no. 1, pp. 54–59, Jan. 1983.

[15]S.D. Sudhoff, D.C. Aliprantis, B.T. Kuhn, P.L. Chapman, "Experimental characterization procedure for use with an advanced induction machine model", IEEE Transactions on Energy Conversion, vol.18, no.1, pp.48.56, Mar 2003.

[16]D.C. Aliprantis, S.D. Sudhoff, B.T. Kuhn, "Experimental Characterization Procedure for a Synchronous Machine Model with Saturation and Arbitrary Rotor Network Representation", IEEE Transactions on Energy Conversion, vol.20, no.3, pp.595-603, Sept. 2005.

[17]D.C. Aliprantis, S.D. Sudhoff, B.T. Kuhn, "A Synchronous Machine Model with Saturation and Arbitrary Rotor Network Representation", IEEE Transactions on Energy Conversion, vol.20, no.3, pp.584-594, Sept. 2005.

[18]Rotating Electrical Machines, Part 4: Methods for Determining Synchronous Machine Quantities from Tests, IEC 34–4 Standard, 2008, pp. 22-24, 33-34, 52-53.

[19]D. Ban, D. Zarko, I. Mandic, "Turbogenerator end-winding leakage inductance calculation using a 3-D analytical approach based on the solution of Neumann Integrals", IEEE Transactions on Energy Conversion, vol. 20, no. 1, pp.98-105, March 2005.

[20]A. Tessarolo, F. Luise, "An Analytical-Numeric Method for Stator End-Coil Leakage Inductance Computation in Multi-Phase Electric Machines", IEEE Industry Applications Society Annual Meeting 2008, IAS '08, vol., no., pp.1,8, 5-9 Oct. 2008A.

[21]Tessarolo and D. Giulivo, "Analytical methods for the accurate computation of stator leakage inductances in multiphase synchronous machines", Int. Symp. Power Electron., Electr. Drives, Autom. Motion, Pisa, Italy, Jun. 14–16, 2010, pp. 845–852.

[22]A. Tessarolo, "Accurate Computation of Multiphase Synchronous Machine Inductances Based on Winding Function Theory", IEEE Transactions on Energy Conversion, vol.27, no.4, pp.895,904, Dec. 2012.

[23]A. Tessarolo, "On the modeling of poly-phase electric machines through Vector-Space Decomposition: Theoretical considerations", International Conference on Power Engineering, Energy and Electrical Drives, 2009. POWERENG '09, pp.519-523, 18-20 March 2009.

[24]J. Figuroa, J. Cros, and P. Viarouge, "Generalized transformations for polyphase phase-modulation motors", IEEE Trans. Energy Convers., vol. 21, no. 2, pp. 332-341, Jun. 2006.

[25]A. Pereira, C.C. Scharlau, L.F.A. Pereira, J.F. Haffner, "General Model of a Five-Phase Induction Machine Allowing for Harmonics in the Air Gap Field," IEEE Transactions on Energy Conversion, vol.21, no.4, pp.891,899, Dec. 2006.

[26]W. Winston, Operations Research: Applications and Algorithms, Wadsworth, 1994.

[27]M. Mezzarobba, L. Spangaro, A. Tessarolo, "Experimental evaluation of damper circuit influence on the performance of multiphase synchronous generators feeding multiple rectifiers", 2011 International Conference on Power Engineering, Energy and Electrical Drives (POWERENG), 11-13 May 2011.

5 Fault tolerance improvements through special electromagnetic design issues

The increasing complexity of electric grids including renewable sources causes significant impacts in terms of power quality. This implies that new generators are to be designed so that they can withstand larger and larger disturbances in the amplitude and frequency of the grid to which they are connected. This purpose can be attained by appropriate provisions in the generator electromagnetic design. In this chapter, some case studies will be presented comparing the transient stability performance of possible alternative electromagnetic designs of a 4.7-MVA 6-kV for power station based on an Organic Rankine Cycle. The fault-tolerance capabilities of the alternative design solutions are assessed through lumped-parameter simulations in the Matlab-Simulink environment used to predict machine compliance with typical transient functional requirements.

5.1 Introduction on Grid-Connected synchronous machines systems

Due to the increasing importance and wide-spread diffusion of renewable sources, a noticeable increase has been taking place over the last few years in the electric energy production from distributed generation. The impact of distributed generation on the distribution network, due to its unpredictable nature, gives rise to various issues in terms of quality, stability and safe operation of the electric power system. European countries have had to regulate the connection criteria to distribution network. In Italy, for example, technical regulations for electrical connection to MV and LV networks (CEI 0-16, 0-21) have been updated and impose some operating restrictions to generation systems to guarantee network stability [1]-[3].

This chapter aims at investigating the behavior of a synchronous generator connected to a distributed generation power system and to illustrate the impact of different possible design solutions in the operation during heavy transient conditions [4]-[8]. The analysis has been performed with a Matlab-Simulink simulation model that enabled to check generator response to some certain network disturbance cases. The case under study refers to a co-generation system based on a particular Rankine cycle known as ORC (Organic Rankine Cycle). The organic-fluid Rankine cycle is similar to the one used in conventional steam turbines except for the fluid being used that, in this case, is an organic fluid. ORC plants allow for simultaneous generation of thermal and electric energy and constitute a well-established renewable source in the biomass and geothermal energy fields. However, a large employment of the same technology is to be expected in the solar and heat recovery as well.

As a case study investigated in this chapter, a synchronous generator has been considered which is expected to comply with some given operating requirements defined by CEI 0-16 standard [1]-[3]. The possibility to achieve the compliance with these mentioned requirements by acting on generator design has been evaluated.

In particular, the following conditions are taken into account:

- Short circuit for 700 ms followed by full voltage restore
- 30% voltage dip lasting 150 ms
- Low-voltage fault ride-through

- Change in grid frequency from 50 Hz to 51.5 Hz with a simultaneous 15% voltage drop.

With respect to the third requirement (Low Voltage fault Ride Through, LVRT), it is illustrated in Figure 85 the production plant shall remain connected to the network when the grid voltage undergoes a change having according to the time diagram shown in Figure 85, which can be due to either a fault or to a sudden voltage drop. The new network standards tend to force the requirements to keep the connection withstanding the fault and guaranteeing the power availability after the fault. As a rule, the fundamental requirement is that for 70% voltage drops the generator protection system shall not activate before 150 ms.

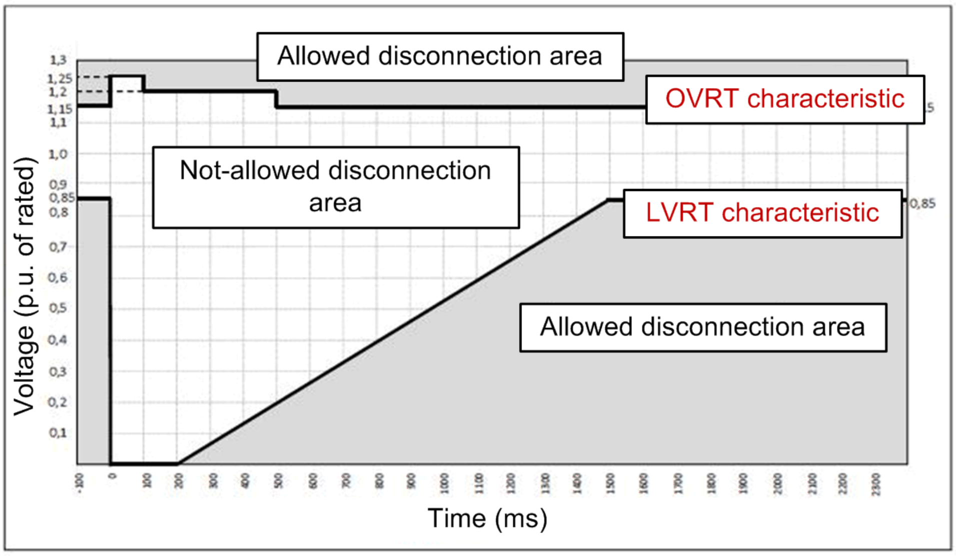

Figure 85: Low voltage and over voltage ride-through characteristic

5.2 PROPOSED GENERATOR DESIGN ALTERNATIVES

Two alternative generator designs are taken into account and compared to assess their different response to the fault or disturbance events described in the previous chapter. In both cases, the technology used features a four-pole salient-rotor synchronous generator with laminated wound rotor [9]-[11]. The two designs are indicated as “N” (normal) and “P” (plus): the normal design N corresponds to a conventional machine dimensioned to thermally match the steady-state operating point disregarding transient requirements; design P aims at endowing the machine with the required transient capabilities. The two designs share the same ratings, which are given in Table I.

The design quantities relevant to the two solutions are given in Table II. Rotor design is the same and the only significant difference can be recognized in the core length, which is significantly larger in the P design. Therefore, in order to have the same rated voltage, the number of turns per coil is accordingly reduced in design P. Another difference is in the full-load field current, which is lower in the P design meaning an oversized rotor circuit. As a consequence of the oversized dimensioning, the P design also features a higher short-circuit ratio [9].

The transient behavior of a synchronous machine mainly depends on equivalent circuit parameters. These are given in Table III and Table IV for the two design alternatives, in per unit with respect to a base impedance equal to 7.70 Ω.

Table I: Machine ratings

Rated power (kVA)	4678
Rated voltage (V)	6000
Rated frequency (Hz)	50
Number of poles	4
Rated power factor	0.9

Table II: Machine design quantities

	Design *N*	**Design *P***
Stator external diameter (mm)	1200	1200
Rotor outer diameter (mm)	788	788
Number of stator slots	72	72
Number of parallel ways per phase	4	4
Number of turns per coil	12	8
Core length (mm)	830	1200
Full-load field current (A)	186	142
Short circuit ratio	0.386	0.612

Table III: Machine equivalent circuit parameters in p.u.

	Design N	**Design P**
Phase resistance	0.00896	0.00453
Stator leakage reactance	0.139	0.0748
d-axis magnetizing inductance, X_{md}	2.57	1.65
q-axis magnetizing inductance, X_{mq}	1.31	0.843
Stator-referred field resistance	0.00208	0.00118
Stator-referred field leakage reactance, X_f	0.284	0.179
Stator-referred d-axis damper leakage resistance	0.0228	0.0134
Stator-referred d-axis damper leakage reactance, X_{kd}	0.149	0.0863
Stator-referred q-axis damper leakage resistance	0.0275	0.0155
Stator-referred q-axis damper leakage reactance, X_{kq}	0.192	0.106

Table IV: Transient and subtransient reactances in p.u.

	Design N	**Design P**
X_d''	0.233	0.169
X_q''	0.307	0.131
X_d'	0.394	0.236
X_q'	1.451	0.918
X_d	2.71	1.72

As regards equivalent circuit parameters, we can have a better idea of their impact on the machine transient behavior by computing the transient (X_d', X_q') and sub transient reactances (X_d'', X_q''), as follows [9], [11]:

$$X_d'' = \frac{1}{\frac{1}{X_d} + \frac{1}{X_{kd}} + \frac{1}{X_f}} \qquad 5.1$$

$$X_q'' = \frac{1}{\frac{1}{X_q} + \frac{1}{X_{kq}}} \qquad 5.2$$

$$X_d' = \frac{1}{\frac{1}{X_d} + \frac{1}{X_f}} \qquad 5.3$$

$$X_q' = X_q \qquad 5.4$$

The resulting numerical values are given in Table IV and show that the P-design exhibits lower values of transient and sub-transient reactances. From a transient behavior viewpoint, this has a double effect: on one side, it tends to increase the peak value of short circuit currents, which can be a harmful effect; on the other side, it increases the synchronizing torque of the machine, which means a more robust (more stable) behavior during heavy transients. In fact, for the short-circuit peak current $I_{ss\text{-}peak}$ and the transient and sub-transient stabilizing torques (T_s', T_s'') we can write [9]:

$$T_s' \propto \frac{1}{X_d'}, \; T_s'' \propto \frac{1}{X_d''} \qquad 5.5$$

$$I_{ss,peak} \propto \frac{1}{X_d''} \qquad 5.6$$

It is therefore clear that the P design, having lower values of X_d'', is expected to be more resilient to possible pole slip or out-of-synchronism faults.

In Figure 86 the "capability" curves are shown for the two proposed designs [6]. From such curves, it is possible to see how the P design has a much larger under-excitation stability margin compared to the N design. Moreover, the P design exhibits a larger thermal margin in the over-excitation region which allows to force the rotor field current for a longer time if needed for stability reinforcement. The maximum limit in under-excitation (absorbed reactive power) in

Figure 86 is determined by the SCR (short-circuit ratio) and corresponds to the maximum load angle allowed under safe conditions.

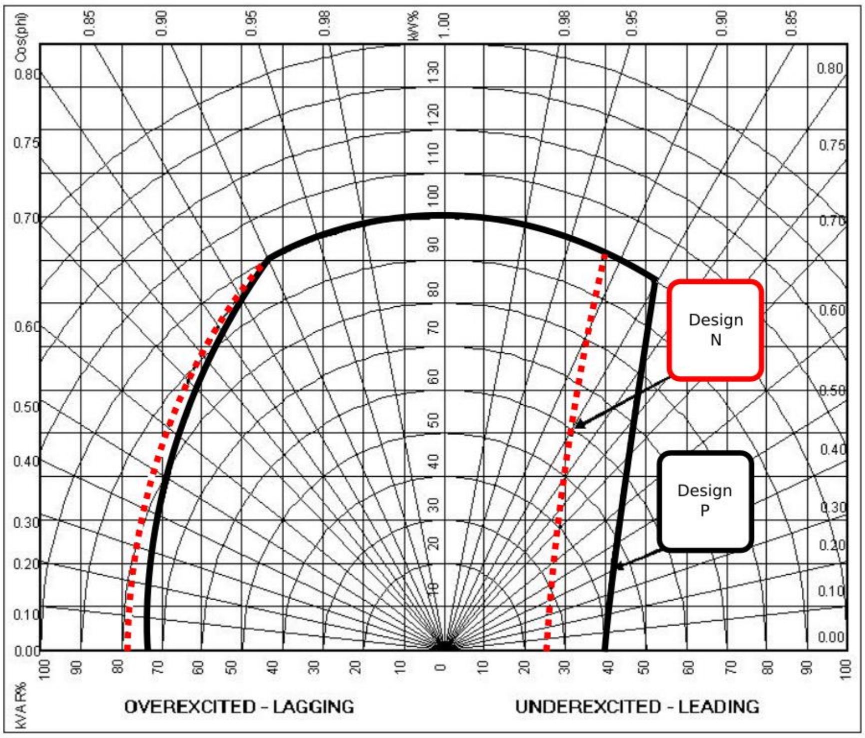

Figure 86: Capability curves for both P and N designs

5.3 NUMERICAL SIMULATIONS

In order to assess the dynamic characteristics of the two designs, the synchronous machine has been modeled in the Matlab-Simulink environment along with its AVR and speed regulator associated to the prime mover.

As anticipated in section 5.1, four case studies have been taken into account for the simulation and are described in the following sections.

5.3.1 SUDDEN SHORT CIRCUIT

As a first fault scenario, a sudden three-phase short circuit is applied to machine terminals starting from 0.9 p.u. load operation. The short circuit fault is cleared at t=2.7 s, when the full voltage is restored. The transient of the two machines are reported in Figure 87, Figure 88 and Figure 89, where index “p” and “n” respectively denote the P (plus) and N (normal) designs. In particular, from Figure 89_ one can see that the machine with P design exhibits a higher peak fault current, as can be expected due to the lower synchronous reactance (Table IV). Furthermore, after fault clearance, we can observe that the P machine is capable of resynchronization with the grid, while the N machine loses synchronism and enters an unstable operation state.

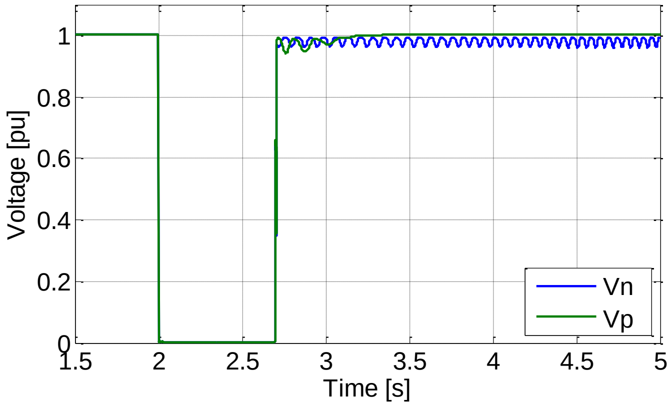

Figure 87: Voltage transients following a short circuit at t=2 s.

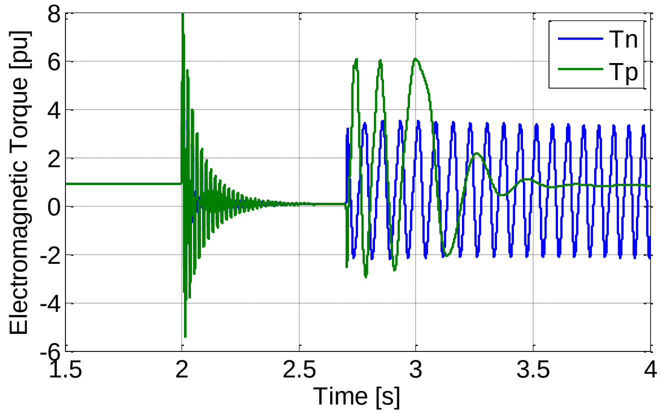

Figure 88: Torque transients following a short circuit at t=2 s

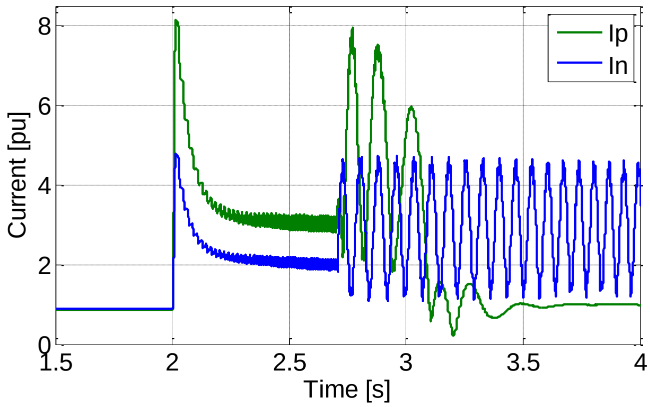

Figure 89: Phase current transients following a short circuit at t=2 s.

5.3.2 Voltage Dip

As a second study case, the grid voltage is supposed to abruptly decrease by 30% at t=2 s and then return to its rated value after 150 ms. The transients following such voltage dip event are illustrated in Figure 90, Figure 91 and in Figure 92. Simulations show that in both design variants the generator maintains the grid synchronization throughout the voltage dip. Again, due to the lower subtransient reactances, the plus design exhibits higher fault current and torque peaks but, due to shorter time constants, it leads to a slightly faster resynchronization.

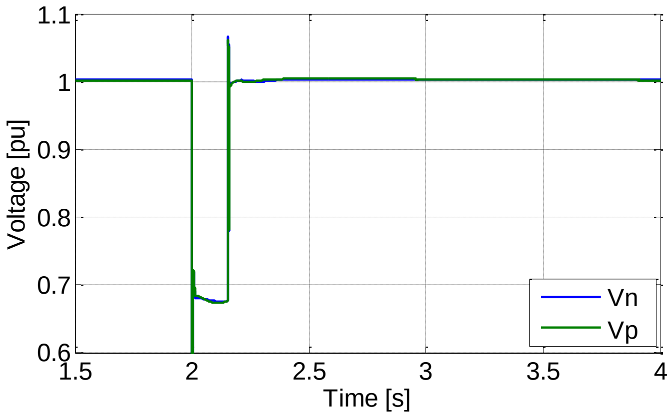

Figure 90: Voltage transients following a 30% voltage dip at t=2 s

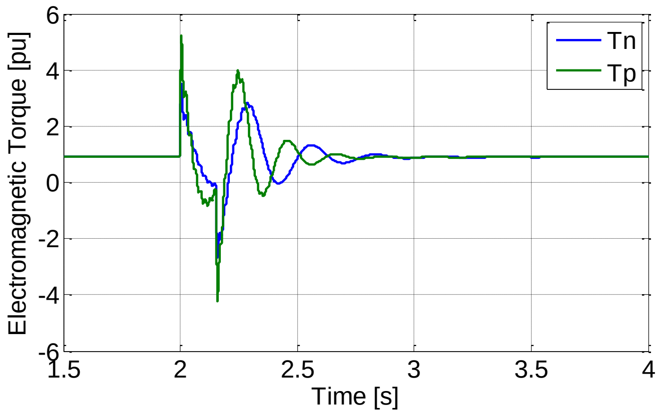

Figure 91: Torque transients following a 30% voltage dip at t=2 s

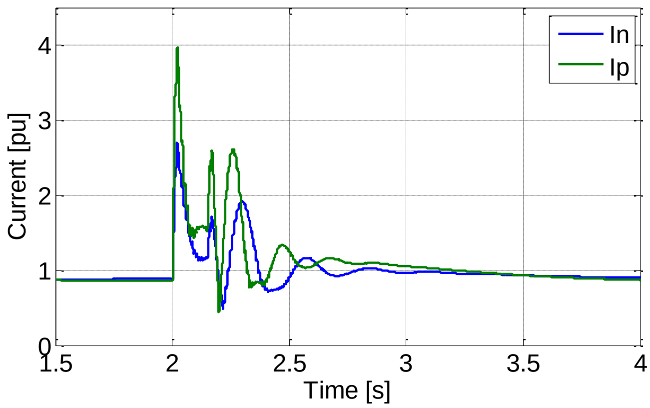

Figure 92: Phase current transients following a 30% voltage dip at t=2 s.

5.3.3 LOW-VOLTAGE RIDE-THROUGH

As a third study case, a low-voltage ride-through (LVRT) as described in 5.1 has been simulated assuming that, at t = 2 s, the voltage abruptly decays to zero and then returns to its initial value with a ramp as illustrated in Figure 93 (the voltage ramp has been approximated with a sequence of discrete steps). Figure 94 and Figure 95 show machine transients in terms of torque and current. In particular, the current diagram confirms that the plus design features larger current peak due to the lower reactance values but proves able to resynchronize, while the N design loses synchronism.

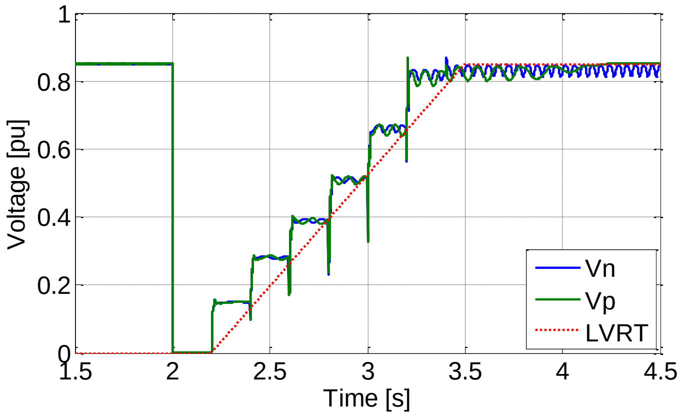

Figure 93: Voltage transient associated with a LVRT.

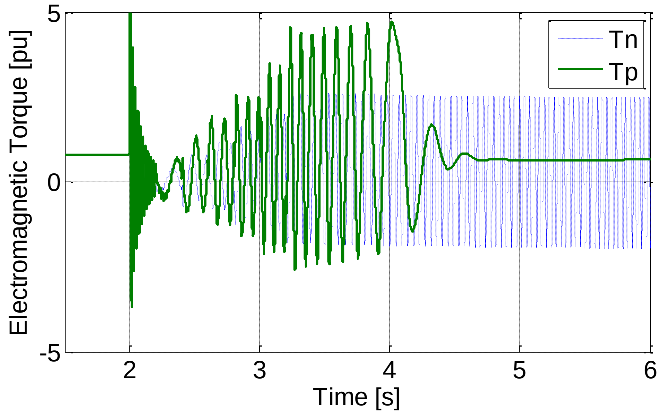

Figure 94: Torque transients following LVRT event at t *= 2s.*

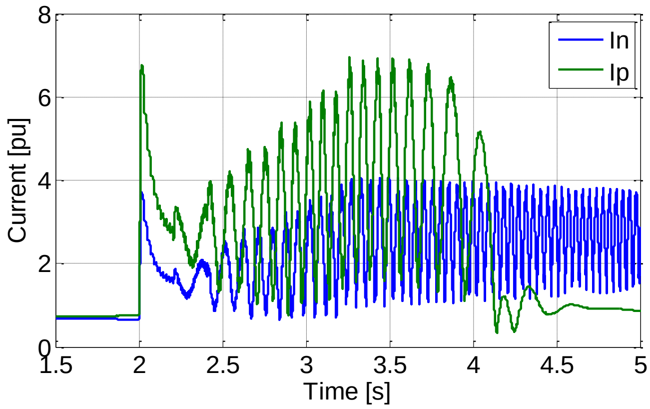

Figure 95: Phase current transients following a LVRT event at t = 2s.

5.3.4 GRID FREQUENCY AND VOLTAGE STEPWISE CHANGE

Finally, a stepwise change is applied in grid voltage and frequency at instant *t*=2 s. The grid voltage decreases by 15% while the grid frequency increases from 50 Hz to 51.5 Hz at the same time. These changes are maintained permanently. Transients resulting from the simulation are provided in Figure 96, Figure 97 and in Figure 98. We can observe that the generator, in both designs, proves capable of resynchronization. The peak values of current and torques are higher with the P design, which is also capable of a faster resynchronization due to smaller time constants.

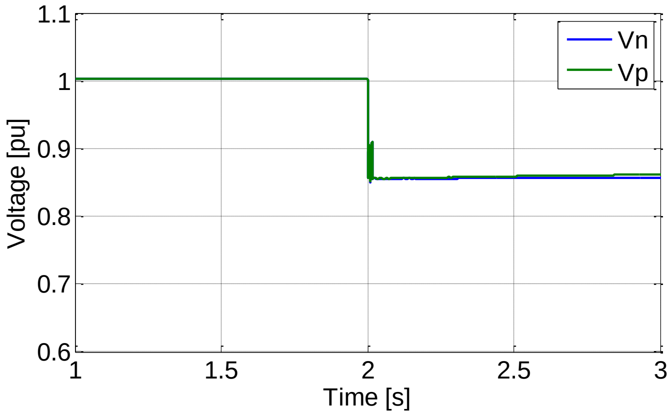

Figure 96: Voltage transient associated with a 15% voltage drop and frequency increase from 50 Hz to 51.5 Hz at t=2 s.

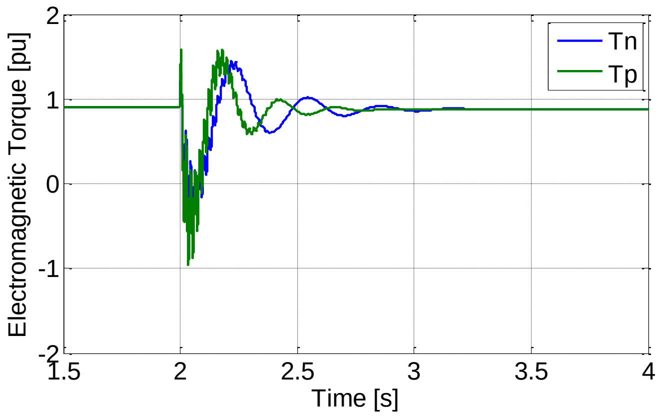

Figure 97: Torque transients following a 15% voltage drop and frequency increase from 50 Hz to 51.5 Hz at t=2 s.

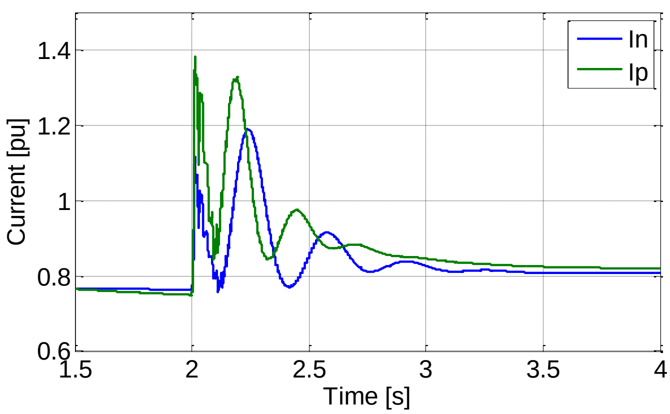

Figure 98: Phase current transients following a 15% voltage drop and frequency increase from 50 Hz to 51.5 Hz at t=2 s.

5.4 CONCLUDING REMARKS

The regulations governing the connection of a generator to the grid define a set of criteria and procedures to prevent supply disturbances and to ensure safety continuity and safety conditions. In this chapter, it has been shown how it can be possible to act on the electromagnetic design of a synchronous generator to make it capable of withstanding some of the most significant disturbances or malfunctions associated to the grid to which it is connected. This issue is of key importance especially for electric generators connected to distributed generation grids, where the power quality can be very poor and significant voltage and frequency stability issues are known to possibly occur. For this purpose, two design versions of the same synchronous generator have been compared by means of numerical transient simulations, considering some typical case studies recommended for consideration by the present power system management standards, namely temporary short circuit events, voltage dips, stepwise voltage and frequency changes. The main design provision adopted to improve generator resilience and fault tolerance with respect these grid-related power quality issues consists substantially oversizing it to reduce the transient and sub-transient reactances. Therefore, simulations have shown how the improved generator design actually exhibits a higher resilience to desynchronization or pole-slipping events thanks to the larger synchronizing torque that it can develop during transients; on the other side, the lower transient and subtransient reactances of the improved design lead to higher peak values for both transient currents and torques.

5.5 References

[1] CEI, "CEI 0-16: Technical rules for active and passive load connection to HV and MV distribution grids", CEI Italian Standard, Dec. 2012

[2] CEI, "CEI 0-21: Technical rules for active and passive load connection to LV distribution grids", CEI Italian Standard, June 2012.

[3] ANSI/IEEE Std 242-2001, *IEEE Recommended practice for protection and co-ordination of industrial and commercial power systems*, 2001

[4] M. Amini, M. Sanaye-Pasand, M.-T. Nabavi, M. Davarpanah, A. Asadi, "Generators loss of field and its effect on voltage stability in power systems", *The international Conference on Electrical Engineering*, 2008

[5] L. Yan-ling, G. Bao-jun, L. Cui-cui, T. Da-jun, Z. Zhi-qiang, "Analysis of high-voltage generator stator windings sudden three-phase short-circuit and loss of excitation fault", *International Conference on Sustainable Power Generation and Supply, 2009. SUPERGEN '09*, April 2009.

[6] Murdoch, and G.E. Boukarim, M.J. D'Antonio and R.A. Lawson, "Generator over excitation capability and excitation system limiters", *IEEE Power Engineering Society Winter Meeting, 2001*, pp.215-220 vol.1, 28 Jan-1 Feb 2001.

[7] R. J. Best, D. J. Morrow, and P. A. Crossley, "Out-of-Phase Synchronization of a Small Alternator", *IEEE Power Engineering Society General Meeting, 2007.* 24-28 June 2007.

[8] P. C. Krause U. C. Hollopeter D. M. Triezenberg, P. A. Rusche, "Shaft torques during out-of-phase synchronization", *IEEE Transactions on Power Apparatus and Systems*, VOL. PAS-96, no. 4, July/August 1977.

[9] C. Concordia, *Synchronous Machine Theory and Performance*, Hoboken, NJ Wiley, 1951

[10]J.H. Walker, *Large Synchronous Machines: Design, Manufacture and Operation*, Oxford, U.K.: Clarendon, 1981

[11]E. Fitzgerald and C. Kingsly, Jr., *Electrical Machinery*. New York, McCraw-Hill.

6 ANALYSIS OF ASYMMETRICAL SHORT CIRCUITS DOWNSTREAM OF 12 PULSE DIODE RECTIFIER FED BY A DOUBLE THREE PHASE SYNCHRONOUS MACHINE

DC power generation for MVDC grids is in the easiest way realized by a cascade connection of a synchronous generator and a diode rectifier. Due to large peak fault currents, including oscillating transient components, it is important to know in depth the short circuit behavior of diode rectifiers, mainly during the first moments after the fault. This is helpful to be able to perform a suitable sizing of the system and its protections. In order to obtain an accurate estimation of the transient short circuit current, models for software simulation of 6-pulse and 12-pulse DC generator systems have been implemented. This work shows the validation of such models by the comparison of simulation results with experimental tests.

6.1 BRIEF INTRODUCTION ON DC SYSTEMS

DC power generation for DC smart grids, DC shipboard power systems, DC traction systems is realized by a cascade connection of an AC generator and an AC/DC converter. DC machines are not considered owing to their well-known drawbacks related to commutator, brushes and sliding contacts.

Different kinds of AC machines [1]-[5] and AC/DC converters can be used [2]-[6], however one of the easiest and well proven solution is to employ a synchronous machine with a diode rectifier [2] and, possibly, a cascade-connected chopper on its output [3], [4].

While power converters composed of controlled semiconductor devices are able to limit and interrupt fault currents, diode bridges cannot break them. Indeed, short circuit currents downstream of diode rectifiers are a critical issue, owing to the large peak value of their transient oscillating component. Actually, the current peak, which occurs in the first few tens of milliseconds after the fault, reaches a typical amplitude in the order of tens of times the short circuit steady state current. It is therefore necessary to size the system and its protections in order to cope with such events with the required reliability level. For the reasons mentioned above it is important to accurately predict the short circuit behavior of diode rectifiers, mainly during the first moments after the fault. Few works approaching this problem can be found in the literature [7]-[11]. Among these the most significant are [7] and [8]. The problem is investigated for 6-pulse rectifiers supplying DC railway power systems and a model for computer simulation is developed in [7]. Transient and steady state behavior after a short circuit fault on the DC side of 6 and 12-pulse diode rectifiers supplied by three-winding transformers is well described through an analytical model in [8]. Simulation results for 24-pulse rectifiers are reported in [9]-[11]. In [9] the 24-pulse rectifier is directly supplied by a 12-phase synchronous generator while in [10], [11] it is supplied by two three-winding transformers. The adoption of a dual three-phase alternator in combination with a double-rectifier configuration provides the system with intrinsic redundancy, as a reduced power supply can be guaranteed in case of fault in either of the two bridges. Therefore, it is useful to investigate the behavior of the system in case of asymmetrical short circuit, that is when the short circuit occurs at the output terminals of one of the two three-phase diode bridges. However, in the cited works only symmetrical short circuits are analyzed. Moreover, no results of experimental tests are shown.

In the following chapters the short circuit behavior of a generation system composed of a 6-pulse diode rectifier directly supplied by a three-phase synchronous machine is considered first. Secondly, as a key point of the analysis, the asymmetrical short circuit will be analyzed of a generation system composed of two series-connected diode bridges directly supplied by a double three-phase synchronous machine, like the one described in [2]. The aim of the work is the implementation of models for software simulation of the system in order to obtain an accurate estimation of the transient short circuit current. This is very useful to perform a suitable sizing of the system. All the models are validated comparing simulation results with experimental tests.

6.2 System and tests description

The DC generators systems considered here are composed by the series connection of a synchronous machine and a diode rectifier. Two possible structures are analyzed. The first one is shown in Figure 99a and is constituted by a three phase synchronous machine (SM) supplying a three phase diode bridge. The second one is shown in Figure 99b and is composed of a synchronous machine (SM) endowed with two three-phase stator windings, each one supplying a three-phase diode bridge. The output terminals of the two diode bridges are series connected to form a 12-pulse diode rectifier. Two short circuit tests are carried out, the first one for the DC generator system sketched again in Figure 99a and the second one for the DC generator system sketched in Figure 99b.

In the first test the output terminals of the DC generator are short-circuited by closing the switch S. In the second test the switch *S* of Figure 99b is closed in order to produce an asymmetrical fault by the short circuit of the upper diode bridge output terminals.

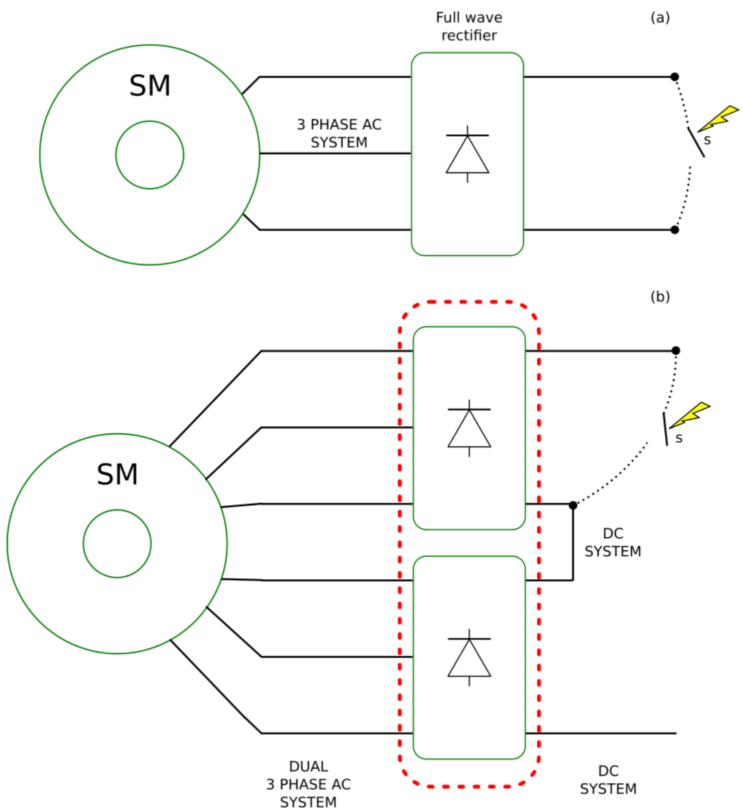

Figure 99: Schemes of two possible different configurations for a DC generator system. (a) composed of a three-phase generator connected with a full wave rectifier (b) composed by double three phase generator and a 12-pulse diode rectifier

6.3 System model and experimental setup

The system model is implemented in the Simulink environment and takes advantage of models either available from the Simulink SimPowerSystem tool or specifically built on purpose. The model of the system represented in Figure 99a is implemented by connecting a Synchronous Machine Fundamental block with a Universal Bridge block. The model of the system sketched in Figure 99b, shown in Figure 100, is implemented connecting a Double Three Phase Synchronous Machine Fundamental block with two Universal Bridge blocks. The Double Three Phase Synchronous Machine Fundamental block is implemented *ad hoc* as it is not available as a predefined component. The machine is modeled based on its complete nine-order electromagnetic model written in multiple Park's and Clark's coordinates in the synchronous reference frame. A damper winding on both *d* and *q* axes and the excitation field circuit on the *d*-axis has been included. A detailed description of the mathematical model structure and parameters can be found in [12]

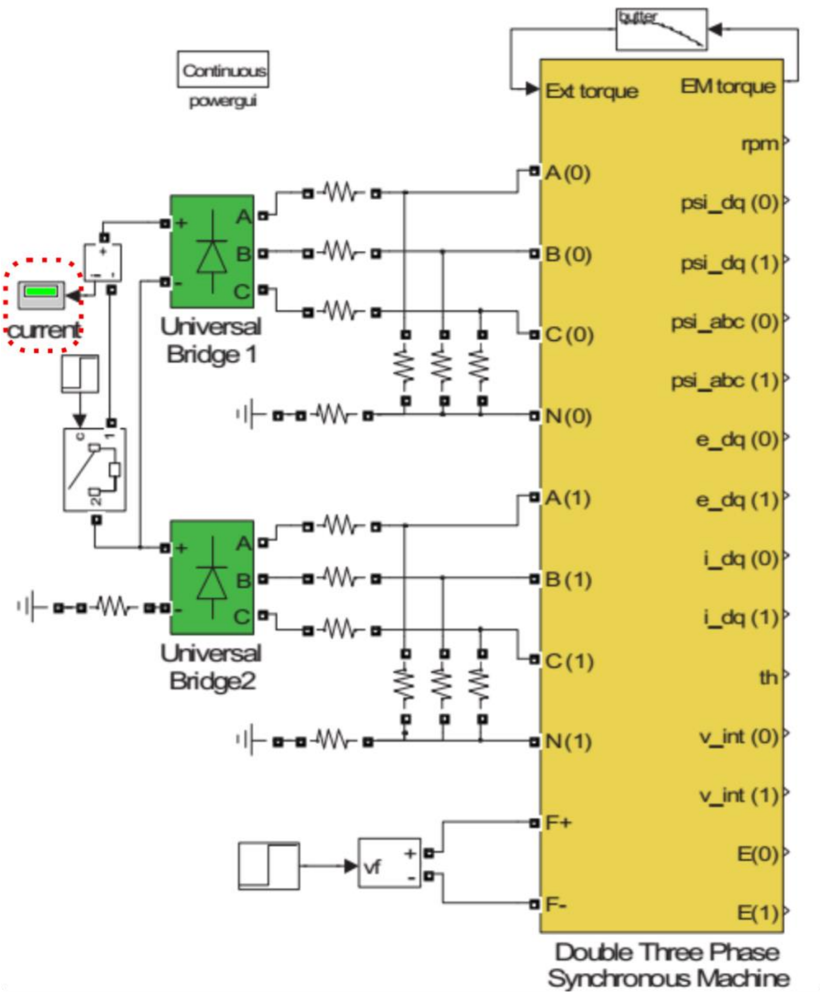

Figure 100: Simulink model of the DC generator composed by the custom made double three phase generator model and the 12 pulse rectifier SimPowerSystem standard model

Experimental tests are carried out on a test bench with the reconfigurable 21 kVA, 50 Hz multiphase machine shown in Figure 101. The machine rotor is composed by two poles and no damper winding. At first the machine was configured as a three-phase machine ($V_n = 760\ \mathrm{V}, I_n = 16.2\ \mathrm{A}$) in order to test a DC generator system with the structure sketched in Figure 99. Afterwards the machine was configured as a double three-phase machine ($V_n = 380\ \mathrm{V}, I_n = 16.2\ \mathrm{A}$) in order to test a DC generator system with the structure represented in Figure 99.

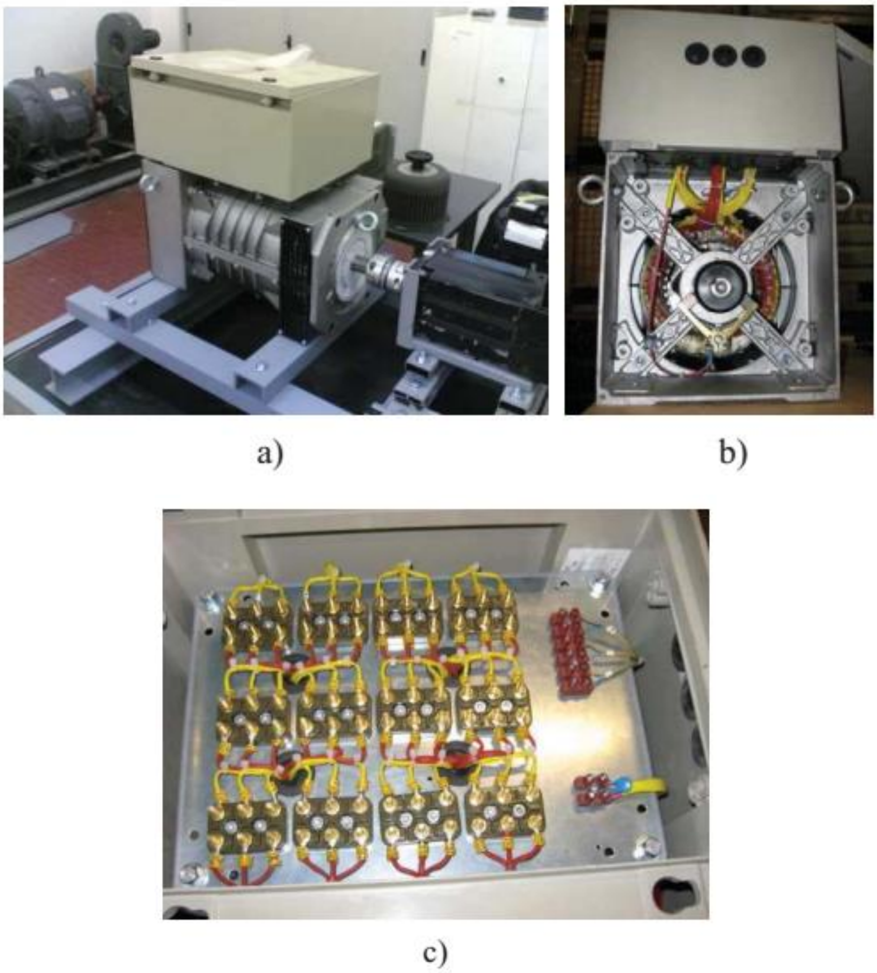

Figure 101: Test bench with reconfigurable multiphase machine prototype; a) Synchronous reconfigurable machine; b) internal view of the prototype showing connections between stator coils and terminal box leads; c) terminal box where all stator coils are individually connected to an accessible lead for winding reconfiguration.

All the needed parameters of the machine in its three-phase and double three-phase configurations were deduced by short circuit tests together with the tests described in [13].

As an example, the Figure 102 shows the current of one phase of the double three-phase machine registered during a short circuit test. Starting from no load conditions (line-to-line voltage =120V) then one of the three phase systems of the machine is short circuited while the other is left in no load conditions. In the figure it can be seen that the currents obtained by a laboratory test and by a simulation with the described model are more or less the same so it is possible to say that the model can faithfully reproduce the real behavior of the machine.

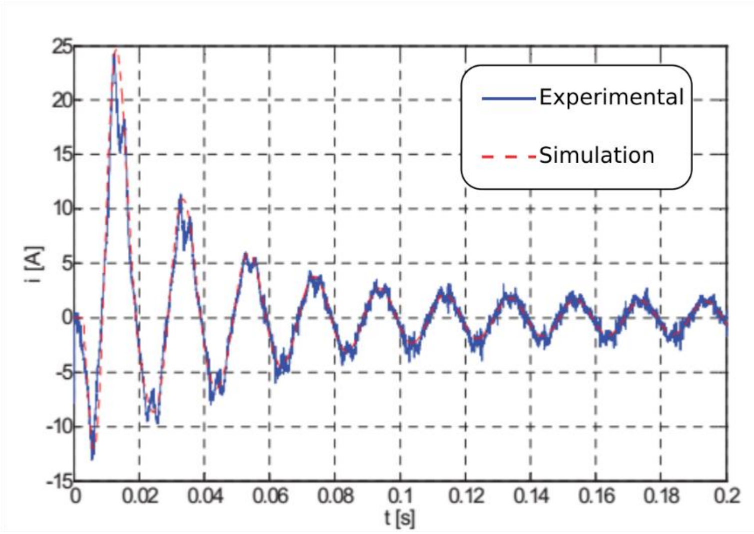

Figure 102: Three phase Short circuit current in the double three phase synchronous generator under analysis

6.4 SIMULATION AND EXPERIMENTAL RESULTS

The first test was performed on the system of Figure 99a Starting from no load conditions at different values of V_{dc}, then the switch S is closed to cause a short circuit at the output terminals of the DC generator. The output current of the DC generator obtained by simulations and experimental tests with initial voltages of $V_{dc} = 250$ V and $V_{dc} = 510$ V are shown in Figure 103 a and b respectively. The matching between simulation and experimental results is good and confirms the system behavior and current waveform expected according to [7] and [8].

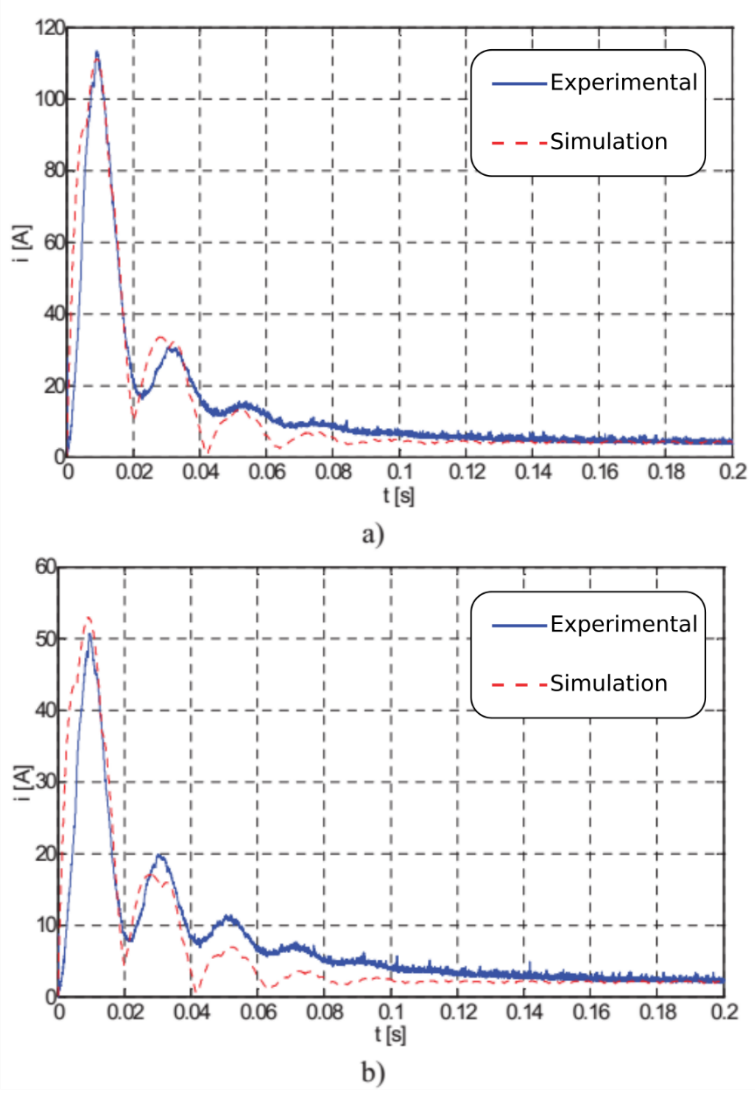

Figure 103: Short circuit output current of a 6-pulse diode rectifier supplied by a three phase synchronous machine with: a) initial voltage equal to 250 V and b) initial voltage equal to 510 *V*

The second test was performed on the system shown in Figure 99b starting from no load conditions, then the switch S is closed to cause an asymmetrical short circuit at the output terminals of the DC generator. The short circuit currents obtained by simulations and experimental tests carried out with initial voltages of $V_{dc} = 250$ V and $V_{dc} = 450$ V ($V_{dc} = V_{dc1} + V_{dc2}$) are shown in Figure 104a and b respectively. Also in this case, simulation and experimental results show a good matching. It is worth to point out that the DC voltage after the fault (which is not shown because less significant for the purposes of this work) is close to zero because it is very low also in the unfaulty bridge owing to the demagnetizing action of the short-circuit current. In order to allow a degraded service, it is necessary to clear the fault as soon as possible so that the output voltage of the unfaulty bridge is recovered. In this way the DC generator can still work supplying half of its nominal power at reduced voltage or, properly overexciting it, even at nominal voltage (provided that voltage sizing of the machine and diode bridges is suited).

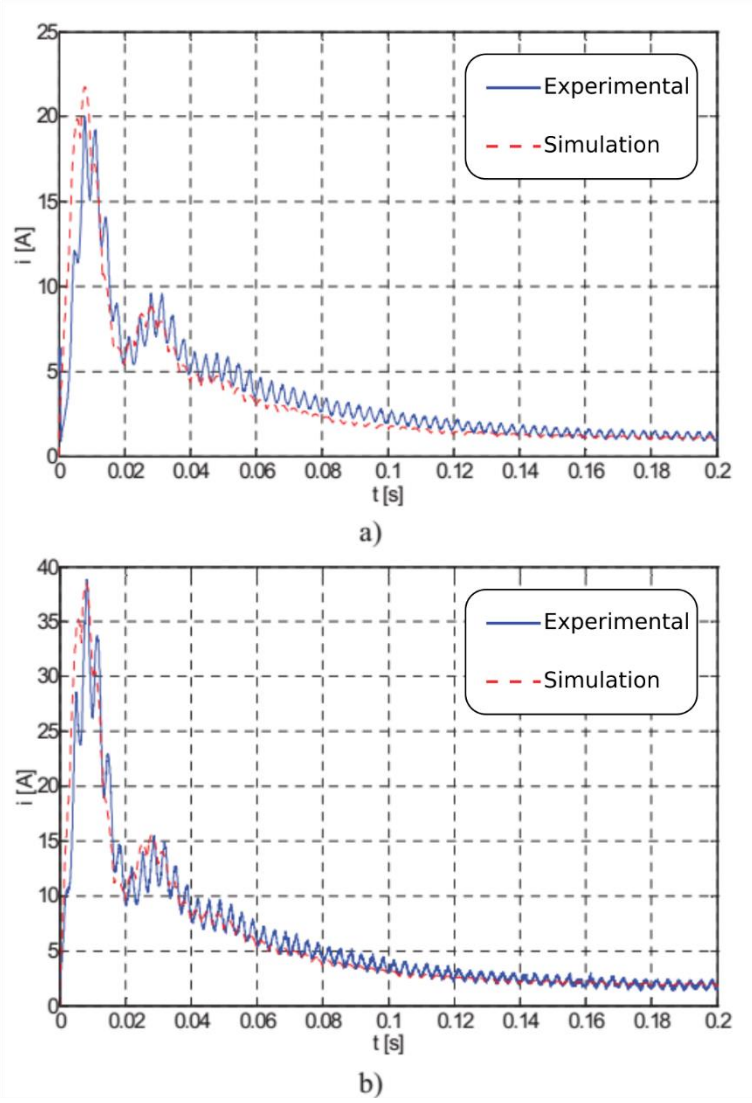

Figure 104: Short circuit output current of a 12-pulse diode rectifier supplied by a double three phase synchronous machine

6.5 CONCLUDING REMARKS

DC generator systems composed by diode rectifiers cascaded to synchronous generators have many positive features such as simplicity, reliability, efficiency and cost. This makes them the first choice for power supply of MVDC power systems. However, short circuits at their output terminals cause transient DC currents with an oscillating component at the same frequency as the AC voltage. The absence of zero crossing and the presence of a large current peak immediately after the fault (as shown by charts) make it quite challenging to suitably size and protect the system in case of faults.

It is therefore important to be able to predict the short circuit behavior of the system. For this reason, accurate models for numeric simulations were implemented and tested. Comparison of currents and voltages obtained by simulations and the corresponding ones registered during experimental tests demonstrates that the implemented models give the possibility to predict the transient short circuit current with the accuracy required by protection and sizing purposes.

6.6 REFERENCES

[1] A. Tessarolo, S. Castellan, R. Menis, G. Sulligoi. “Electric Generation Technologies for All-Electric Ships with Medium-Voltage DC Power Distribution Systems”, Proc. of Electric Ship Technologies Symposium, pp. 275 - 281, Arlington (VA - USA), 22 – 24 April 2013.

[2] G. Sulligoi, A. Tessarolo, V. Benucci, M. Baret, A. Rebora, A. Taffone. “Modeling, Simulation, and Experimental Validation of a Generation System for Medium-Voltage DC Integrated Power Systems”, IEEE Transactions on Industry Application, Vol. 46, No. 4, pp.1304-1310, July/August 2010.

[3] G. Sulligoi, A. Tessarolo, V. Benucci, A. Millerani Trapani, M. Baret, F. Luise. “Design, Implementation and Testing of a Ship-Board Medium-Voltage DC Generation System Based on a Ultra-High Speed 12- Phase Alternator”, Proc. of IEEE Electric Ship Technology Symposium (ESTS), pp. 388-395, Alexandria (Virginia - USA), 10-13 April 2011.

[4] M. Aizza, D. Bosich, S. Castellan, R. Menis, G. Sulligoi, A. Tessarolo. “Coordinated speed and voltage regulation of a dc power generation system based on a wound field split-phase generator supplying multiple rectifiers”, Proc. of the 6th IET International Conference on Power Electronics, Machines and Drives (PEMD), Bristol (UK), 27-29 March 2012.

[5] T. Ahmed, K. Nishida, M. Nakaoka. “A novel standalone induction generator system for AC and DC power generation”, IEEE Transactions on Industry Applications, Vol. 43, No. 6, pp. 1465 – 1474, November / December 2007.

[6] P. Kollensperger, C. Meyer, U. Schwarzer, S. Schroder, R. W. De Doncker. “High-power converter systems for high-speed generators”, Proc. of European Conference on Power Electronics and Applications, Dresden (Germany), 10-15 September 2005.

[7] J.C. Brown, J. Allan, B. Mellitt. “Six-pulse three-phase rectifier bridge models for calculating closeup and remote short circuit transients on DC supplied railways”, IEE Proceedings-B, Vol. 138, No. 6, pp. 303-310, November 1991.

[8] P. Pozzobon. “Transient and Steady-State Short-Circuit Currents in Rectifiers for DC Traction Supply”, IEEE Transactions on Vehicular Technology, Vol. 47, No. 4, pp. 1390-1404, November 1998.

[9] M. Fang, L. Fu, Z. Ye. “Transient DC Side Short Circuit Currents of 12-phase Generator-Rectifier System”, Proc. of International Conference on Electrical Machines and Systems (ICEMS), pp. 16-19, Wuhan (China), 17-20 October 2008.

[10] J.L. Zhang, X.Y. Feng K. Li, J. Zheng, D. Huang. “Mode of Short-circuit state operation in 24-pulse uncontrolled bridge rectifier”, Proc. of International Conference on Electrical Machines and Systems (ICEMS), Tokyo (Japan), 15-18 November 2009.

[11] J.L. Zhang, X.Y. Feng, K. Li, J. Zheng, D. Huang. “Closeup and remote short circuit transient calculation model on DC traction power supply system with 24-pulse rectifier”, Proc. of International Conference on Electrical Machines and Systems (ICEMS), pp. 97-101, Incheon (South Korea), 10-13 October 2010.

[12] A. Tessarolo, S. Castellan. “Analytical and circuital modeling of commutation transients in phase-split synchronous motors supplied by multiple load commutated inverters,” Proc. of 18th International Conference on electrical Machines (ICEM), Vilamoura, (Portugal), September, 2008.

[13] A. Tessarolo, S. Castellan, R. Menis, G. Ferrari. “On the Modeling of Commutation Transients in Split-Phase Synchronous Motors Supplied by Multiple Load Commutated Inverters”, IEEE Transactions on Industrial Electronics, Vol. 57, No. 1, pp. 35-43, January 2010.